Collective dynamics and rheology of phoretic suspensions under external mechanical and chemical forcings

Prathmesh Vinze

INSTITUT POLYTECHNIQUE DE PARIS

NNT : 2024IPPAX085

Thèse de doctorat

Collective dynamics and rheology of phoretic suspensions under external mechanical and chemical forcings

Thèse de doctorat de l'Institut Polytechnique de Paris
préparée à l'École polytechnique

École doctorale n°000 Thèse de doctorat de l'Institut Polytechnique de Paris
préparée à l'École Polytechnique (EDIPP)
Spécialité de doctorat : Mécanique des fluides et des solides, acoustique

Thèse présentée et soutenue à Palaiseau, le 12 September 2024, par

PRATHMESH VINZE

Composition du Jury :

Eric Clement Professor, Sorbonne University (Laboratoire Physique et mécanique des milieux Hétérogènes)	Président
Holger Stark Professor, Technische Universität Berlin (Institut für Theoretische Physik)	Rapporteur
Cecile Cottin-Bizonne Directrice de recherche, Université Lyon 1 (Institut Lumière Matière)	Rapporteur
Sara Jabbari-Farouji Professor, University of Amsterdam (Institute of Theoretical Physiscs)	Examinatrice
Thomas Bickel Professor, University of Bordeaux (Laboratoire Ondes et Matière d'Aquitaine)	Examinateur
Sébastien Michelin Professor, Ecole Polytechnique (LadHyX)	Directeur de thèse

INSTITUT POLYTECHNIQUE DE PARIS

DOCTORAL THESIS

LABORATOIRE D'HYDRODYNAMIQUE, ECOLE POLYTECHNIQUE

Collective dynamics and rheology of phoretic suspensions under external mechanical and chemical forcings

Author
Prathmesh VINZE

Supervisor
Prof. Sebastien MICHELIN

Jury members
Prof. Holger STARK (*Rapporteur*)
Prof. Cecile COTTIN-BIZONNE (*Rapporteur*)
Prof. Eric CLEMENT (*Examinateur*)
Prof. Thomas BICKEL (*Examinateur*)
Prof. Sara JABBARI-FAROUJI (*Examinatrice*)

Resume

La matière active est composée d'unités individuelles qui injectent de l'énergie dans le système, ce qui conduit à des dynamiques collectives non triviales. Quelques exemples courants à des échelles macroscopiques sont les motifs créés par un vol d'oiseaux, un banc de poissons, un troupeau de moutons, etc. Des dynamiques collectives similaires sont également observées à l'échelle microscopique chez les microswimmers artificiels et biologiques, tels que les bactéries, les algues, les spermatozoïdes, etc. Ici, nous concentrons notre attention sur les microswimmers phorétiques appelés particules de Janus. Ce sont des particules sphériques asymétriquement recouvertes d'un catalyseur chimique, ce qui entraîne des gradients de surface tangentiels des espèces produites ou consommées. Ce gradient provoque l'écoulement du fluide à travers la surface des particules, entraînant l'auto-propulsion de ces particules. Elles peuvent interagir à la fois par le champ d'écoulement et le champ de soluté, donnant lieu à la formation de motifs spatiotemporels complexes (comme la formation d'astres). Des expériences rhéologiques récentes révèlent que la suspension de ces microswimmers influence fortement la réponse rhéologique de la suspension et conduit en fait à une diminution de la viscosité effective de la suspension. Dans la première partie de cette thèse, nous analysons numériquement, en utilisant un modèle cinétique de continuum, les dynamiques et la réponse au cisaillement de suspensions diluées et confinées de particules phorétiques autochemotactiques, qui se réorientent et dérivent vers les solutés chimiques libérés par leurs voisins. Nous montrons qu'une distribution transitoire stable en 1D, causée par l'effet de confinement, est une caractéristique commune aux intensités de confinement et de taux de cisaillement considérées. Cet état en 1D est stable pour un confinement fort et est donc observé dans les dynamiques à long terme dans des canaux suffisamment étroits. Pour des canaux plus larges, l'état transitoire devient instable face aux perturbations axiales dues à l'instabilité chimiotactique, ce qui conduit à la formation d'agrégats de particules le long des parois du canal. Leur agencement et leurs dynamiques relatifs sont déterminés par l'influence relative de l'intensité du cisaillement et de la chimiotaxie, ainsi que par l'état critique des dynamiques de suspension et des écoulements induits par les particules. Dans un second temps, l'effet de rétroaction sur l'écoulement et la viscosité effective de la suspension auto-organisée est pris en compte. Nous montrons que l'écoulement induit et, par conséquent, son comportement rhéologique dépendent fortement du régime d'auto-organisation, et donc de l'interaction entre le confinement, le cisaillement et la chimiotaxie. La deuxième partie de la thèse se concentre sur le contrôle des dynamiques de suspension à l'aide de signaux chimiques induits par des parois actives afin de réduire la viscosité effective pour des confinements plus forts. Nous montrons que même si l'activité uniforme des parois joue un rôle crucial dans la détermination de l'épaisseur de la couche limite de particules, elle ne peut pas déclencher une instabilité chimiotactique. En revanche, une activité non uniforme des parois, telle qu'une distribution en escalier, peut induire un gradient chimique horizontal plus fort qui déclenche une instabilité chimiotactique, conduisant à une diminution significative de la viscosité effective. Cependant, imposer une activité et un cisaillement simultanément présente des limites à des taux de cisaillement modérés, où l'instabilité chimiotactique ne peut pas se développer dans l'ensemble du domaine. Pour résoudre ce problème, nous proposons une stratégie plus robuste qui étend la région de réduction de la viscosité à des confinements plus élevés. Ces résultats fournissent des informations importantes pour la conception de stratégies efficaces de contrôle de la viscosité des suspensions basées sur des signaux chimiques et mécaniques.

Keywords:Suspension phorétique, rhéologie des suspensions, dynamiques collectives, fluides actifs

Abstract

Active matter is composed of individual units that inject energy into the system leading to non-trivial collective dynamics. Some common examples at macroscopic scales are the patterns created by a flock of birds, a school of fish, a herd of sheep, etc. Similar collective dynamics are also observed at the microscopic scale for artificial and biological microswimmers such as bacteria, algae, spermatozoa, etc. Here, we focus our attention on phoretic microswimmers called Janus particles. These are spherical particles asymmetrically coated with a chemical catalyst resulting in tangential surface gradients of the species produced or consumed. This gradient drives the flow of fluid across the surface of the particles, leading to self-propulsion of the particles. These particles can interact through both the flow field and the solute field, giving rise to the formation of complex spatiotemporal patterns (such as the formation of asters). Recent rheological experiments reveal that the suspension of such microswimmers strongly influences the rheological response of the suspension and actually leads to a decrease in the effective viscosity of the suspension. In the first part of the thesis, we numerically analyze using a continuum kinetic model the dynamics and shear response of dilute and confined suspensions of autochemotactic phoretic particles, which reorient and drift towards chemical solutes released by their neighbors. We show that a 1D transient stable distribution driven by the confinement effect is a common feature at the considered confinement and shear rate intensities. This 1D state is stable for strong confinement and is therefore observed in the long-term dynamics in sufficiently narrow channels. For wider channels, the transient state becomes unstable to axial perturbations due to chemotactic instability, leading to the formation of particle aggregates along the channel walls. Their relative arrangement and dynamics are determined by the relative influence of shear intensity and chemotaxis and by the critical state of suspension dynamics and particle-induced flows. In a second step, the feedback effect on the flow and effective viscosity of the self-organized suspension is considered. We show that the induced flow and, consequently, its rheological behavior strongly depends on the self-organization regime, and thus on the interplay of confinement, shear, and chemotaxis.The second part of the thesis focuses on controlling suspension dynamics using chemical signals induced by active walls in order to reduce the effective viscosity for stronger confinements. We show that even though uniform wall activity plays a crucial role in determining the particle boundary layer thickness, it cannot trigger chemotactic instability. On the other hand, non-uniform wall activity such as a staircase distribution can induce a stronger horizontal chemical gradient that triggers chemotactic instability leading to a significant decrease in effective viscosity. However, imposing activity and shear simultaneously has limitations at moderate shear rates, where chemotactic instability cannot develop in the entire domain. To address this issue, we propose a more robust strategy that extends the viscosity reduction region to higher confinements. These results provide important information for the design of effective suspension viscosity control strategies based on chemical and mechanical signals.

Keywords: Phoretic suspension, suspension rheology, collective dynamics, active fluids

Acknowledgments

It brings me a deep sense of satisfaction to express my gratitude to those who, whether directly or indirectly, contributed to the completion of this thesis. While I will do my best to recognize everyone for their support, I am aware that I may not be able to fully capture all the help I received.

First and foremost, I am extremely grateful to my thesis supervisor Prof. Sebastien Michelin for giving me the opportunity to come to France and work under his guidance. During this time I learned the importance of objective and critical evaluation of ourselves and our theories for high quality research. I feel that the three years that I spent with my thesis advisor was not enough to learn everything from him and I hope to keep learning from him in the future. Secondly, I thank my jury members, Prof. Cecile Cottin-Bizonne, Prof. Holger Stark, Prof. Eric Clement, Prof. Thomas Bickel and Prof. Sara Jabbari Firouji for accepting to be a part of my doctoral jury and for the insightful questions, suggestions and remarks during my defense.

I extend my gratitude to all LadHyX members as well. I made some good friends here particularly my office mates. I shared extremely interesting conversation ranging from science to sports and even geopolitics with them. I sincerely thank Nikhil, Daniel, Vladimir, Antoine, Zhao Dong, Francisco, for the wonderful memories. I also thank Chris and the LadHyX climbing group Agathe, Yassine, Antoine, Sophie, Nikhil, Rishabh, Daniel for introducing me to the world of rock climbing. I have great memories of the rock climbing sessions and of course post session drinks. Another close friend that I made during this time was Rishabh. We have spent countless hours playing and learning chess at the Orsay chess club. It was also because of him that I attended the Paris Olympics.

The thesis would not have completed without the help from the administrative staff at LadHyX. Sandrine was my first contact at LadHyX who helped me start my journey at LadHyX, she was always helpful and I sincerely thank her. During my stay at LadHyX, I frequently bugged Toai for technical help and he was always extremely friendly and helpful. Although I did not frequently engage with Caroline, Magdalena, Melanie and Antoine, they were always willing to help and I extend my gratitude.

Finally, I thank my parents and my brother who believed in my interests and provided complete moral and emotional support during my time away from home. Similarly I extend my gratitude to my close friends Ish and Chiranjeet for their emotional support and for helping me get through difficult phases. I also thank my previous advisors Prof. Pushpavanam and Prof. Vellingiri who introduced me to this great field of transport phenomena and who inspired me to become a researcher.

Contents

1 Introduction **15**
- 1.1 Active matter and its importance . . . 15
  - 1.1.1 Biological microswimmers and their collective dynamics . . . 17
  - 1.1.2 Designing artificial swimmers . . . 19
  - 1.1.3 Why is controlling self-organisation important? . . . 23
- 1.2 Effect of external forcings on self-organisation . . . 24
  - 1.2.1 Effect of boundary on dynamics of microswimmers and its suspension . . . 24
  - 1.2.2 Effect of external field forcing . . . 25
  - 1.2.3 Effect of background flow on collective dynamics . . . 28
- 1.3 Complex rheology of a microswimmer suspensions . . . 28
  - 1.3.1 Rheology of bacterial suspensions . . . 29
  - 1.3.2 Physical mechanism and mathematical model . . . 30
- 1.4 Conclusion and structure of thesis . . . 32

2 Modeling dynamics of microswimmers and active suspensions **35**
- 2.1 Fundamentals of Microhydrodynamics . . . 36
  - 2.1.1 Stokes Flow and its properties . . . 36
  - 2.1.2 Fundamental solutions of Stokes flow . . . 38
- 2.2 Modeling Biological and artificial self-propulsion . . . 39
  - 2.2.1 Mathematical modelling for biological locomotion . . . 39
  - 2.2.2 Externally driven phoretic motion . . . 41
  - 2.2.3 Self-propulsion via- self-diffusiophoresis . . . 43
  - 2.2.4 Chemotaxis of phoretic swimmers . . . 45
- 2.3 Fundamentals of Kinetic Modelling . . . 46
  - 2.3.1 Continuous description of a suspension . . . 46
  - 2.3.2 Deriving the Focker-Planck equation . . . 47
  - 2.3.3 Reduced distribution and correlation functions . . . 49
- 2.4 Kinetic modelling of microswimmer suspensions: A review . . . 51
  - 2.4.1 Hydrodynamic instability . . . 51
  - 2.4.2 Chemotactic Instability . . . 53
- 2.5 Conclusion . . . 57

3 Self-organization of phoretic suspension in confined shear flows **59**
- 3.1 Introduction . . . 60
- 3.2 Modeling dilute suspensions of sheared phoretic particles . . . 61
  - 3.2.1 Physical model . . . 61
  - 3.2.2 Dimensionless equations . . . 64
- 3.3 Numerical Framework . . . 65
  - 3.3.1 Stokes Solver . . . 65
  - 3.3.2 Time marching scheme . . . 67
  - 3.3.3 Selection of the physical parameter values . . . 69
- 3.4 Self-organisation dynamics . . . 70
  - 3.4.1 Overview of the suspension dynamics . . . 71

3.4.2 Short term dynamics . . . 71
3.4.3 Long term dynamics . . . 72
3.4.4 Linear Stability of the 1D equilibrium: a minimal model . . . 77
3.5 Rheology of phoretic suspensions . . . 80
3.5.1 Defining an effective viscosity . . . 80
3.5.2 Induced Flow . . . 81
3.5.3 A simplified model for the induced flows . . . 83
3.5.4 Time evolution of the effective viscosity . . . 85
3.6 Conclusions . . . 87

4 Control of collective dynamics and rheology of phoretic suspensions using chemically active walls 89
4.1 Introduction . . . 90
4.2 Kinetic model for externally forced phoretic suspension . . . 92
4.2.1 Dimensionless Equations . . . 92
4.2.2 Numerical Scheme . . . 93
4.3 Case of spatially constant distribution of wall activity . . . 94
4.4 Triggering chemotactic instability using spatially varying wall activity . . . 97
4.4.1 Suspension dynamics in the presence of step-like activity distribution at a wall 97
4.4.2 Effect of magnitude and coverage of wall activity on suspension dynamics . 100
4.4.3 Limitations to this strategy . . . 101
4.5 An improved pre-conditioned strategy . . . 103
4.5.1 Self-organisation and rheology of phoretic suspensions for improved control strategy . . . 105
4.5.2 Phase diagrams for collective and rheological behaviour following S2 strategy . . . 107
4.6 Conclusion . . . 109

5 Conclusions and perspectives 111
5.1 Summary and general remarks . . . 111
5.2 Ongoing work and future perspectives . . . 112

A Chebyshev tau method 117

B Reduced order equations 119

C Simplification of the fluid forcing 121

D Adjoint state method 123
D.1 Linearised equations . . . 123
D.2 Adjoint fields and their governing equations . . . 124

List of Figures

1.1 Some common examples of collective behaviour shown by various species. (Left top) Ant colony undergoing a circular spiral motion (Image courtesy India Today). (Right top) A strongly ordered herd of sheep (Image courtesy iStock). (Left bottom) A flock of starlings showing complex patterns (Image taken from CGTN YouTube channel). (Right bottom) Collective behaviour of a school of sardine fish (Image courtesy Scubashooters). 16

1.2 (a) A dense bacterial (*B.subtilis*) suspension with the induced flow shown using yellow arrows. (b) Streamlines (black) and vorticity field evaluated using the PIV data. (c) Distribution of tracer particles showing turbulent-like characteristics. (d) Streamlines (black) and vorticity field were obtained using the modified Toner-Tu continuum model. Images adapted from the paper by Dunkel and co-workers [1]. . 18

1.3 (Top) Field emission scanning electron microscopy image of a magnetic helical swimmer with the scale bar equal to 4 μm. (Bottom) Schematic showing the self-propulsion mechanism. Using continuously rotating magnetic field B perpendicular to microswimmer orientation, a misalignment angle between the field and the thin magnetic head induces a magnetic torque τ that rotates the magnetic head resulting in propulsion of the microswimmer. The direction of self-propulsion can be controlled by changing the direction of magnetic field. Images adapted from ref. [2] 20

1.4 (Left) The trajectory of an active drop showing large persistence length compared to drop size. Image taken from [3]. (Right) Steady swimming velocity of the drop as a function of Peclet number. The inset images illustrate the solute field around the drop for particular value of Peclet number indicated on top. Image adapted from [4] 21

1.5 (Left) Scanning electron microscope image showing a band of rod-shaped Janus particles with gold and platinum halves. Image adapted from [5]). (Right) Schematic showing the charged self-diffusiophoretic mechanism for self-propulsion of Janus rod. Image adapted from ref. [6] 22

1.6 (Left) Schematic showing the self-propulsion mechanism for a Janus particle with reduction of H_2O_2 taking place on the Pt coated half. Image adapted from ref. [7]. (Right) Trajectories of colloidal particles (top panel) and Janus particles (bottom panel) overlayed to match the starting point to show enhanced effective diffusion of Janus particles due to self-propulsion. Image adapted from ref. [8]. 22

1.7 (Left) Targeted transport of colloidal particles using 6 linear arrays of confined bacteria. The induced flow created by the bacteria transports colloidal particles towards the center of the structure. (Right) Transport of 2 μm silica particles using (a)linear, (b) spiral and (c) square arrays of confined bacteria. The red and blue symbols represent the starting and final position of the colloidal particle, respectively. The cavities are at 40^o to the local tangent of the structures. The scale bar for both images equals 10 μm. Images adapted from ref. [9] 23

1.8 (Left) Racetrack set-up of Wioland et al. [10] experiments for self-organisation of *E.coli* suspension in the presence of confinement. The large green arrow shows the unidirectional motion of the induced flow, while the smaller green arrows inside the channel show the distribution of the induced flow. (Right) Self-organisation of the suspension for varying $(30, 60, 90\ \mu m)$ confinement strength showing a continuous transition from a 2D turbulent-like state to a 1D state with an average induced flow profile adjacent to each panel. Images adapted from ref. [10]. 26

1.9 Light-driven control of phototactic algae. (Left) Trajectories of *Chlamydomonas reinhardtii* using the superimposition of 10 images in a pressure-driven flow in the (a)absence and (b) presence of light source. (Right) The schematic shows the algae's focusing mechanism depending on the direction of the light source. Image adapted from ref. [11]. 26

1.10 (Left) Experimental setup used by Gachelin and co-workers [12] to measure the effective rheology of bacterial suspension using a Y-shaped microchannel. (Right) Schematic showing the experimental set-up adapted from ref. [13] 29

1.11 (Left) Shear stress response of an *E.coli* suspension placed in a Taylor Couette device. Variation of effective viscosity (defined as the ratio of hydrodynamic stress to shear rate) at various shear rates shows a significant reduction of effective viscosity of the suspension at low shear rates. (Right) Variation of effective viscosity as a function of shear rate for various suspension densities. Increasing bacterial density results in a reduction of the low-shear plateau region. Images reused from ref. [14]. 30

1.12 Schematic illustrating the basic mechanism for effective viscosity modification for passive rods and pusher and puller swimmers in a simple shear flow. The purple arrows illustrate the induced flow corresponding to each particle, which is responsible for modifying the suspension's effective viscosity. The elongated particles are aligned along the direction of shear flow. Image adapted from ref. [15] 31

2.1 Fundamental singularities of the Stokes flow. (Left) Stokeslet : Flow field around a spherical particle settling under external force. (Center) Rotlet : Flow field around a particle rotating with an angular velocity. (Right) Stresslet: Flow field around a particle under extensional flow. 39

2.2 (Top panel) Experimental flow field of swimming (Left) *Chlamydomonas*(image adapted from Ref. [16]) (center) *Paramecium* [image adapted from Ref. [17]] and *E.coli* (image adapted from ref. [18]) [Drescher et.al 2010]. (Bottom panel) Schematic of the mathematical model of the corresponding swimmer. 39

2.3 Flow field around a puller, neutral and pusher squirmer in (top panel) Lab frame and (bottom panel) Particle's frame. 41

2.4 Schematic of Diffusiophoretic propulsion driven by external solute gradient. Solute interaction over a small thickness results in a flow close to the particle surface. . . . 42

2.5 (Left) SEM image of a Silica-based Janus Particle adapted from ref. [19]. (Right) The solute field around the Janus particle, with a black arrow indicating self-propulsion direction. Image adapted from ref. [20] 43

2.6 Schematic of the hydrodynamic instability mechanism for a suspension of pusher swimmers. The elongated microswimmer aligns along the extensional component of the perturbed flow (shown by black arrows) which results in enhancing the velocity perturbation due to the induced flow of the bacteria (illustrated by red arrows). This results in the growth of the instability.Image adapted from ref [21]. 52

2.7 (Top) Run and tumble mechanism for self-propulsion of a bacteria (bottom) Chemotactic behaviour of bacteria undergoing the run and tumble swimming. Image adapted from ref. [22] 54

2.8 Schematic of final state of the suspension for different limits.(left) In the phoretic limit, the particles are drifted towards the higher solute regions (formed due to higher particle density as the particles act as sources) in addition to its self-propulsion resulting in aggregation without polarisation. (center) In the chemotactic limit, the particles have the ability to reorient along the local solute gradient resulting in formation of asters. (right) In contrast in the anti-chemotactic limit, the system undergoes fixed oscillation with the aggregates oscillating in the physical domain. The two arrows point the transition between the two extremes in one cycle. 55

3.1 Problem Schematic. A dilute suspension of Janus particle placed between two flat walls. The walls move opposite to each other to establish a simple shear flow . . . 62
3.2 Figure depicting the overview of self-organisation of the current system. Identification of three different regimes based on shear rate and confinement. Strong shear or strong confinement tends to stabilise the 1D state. 71
3.3 Short-term particle (top) and solute distribution (bottom) obtained for $\zeta = 1, \gamma = 0.25$. The black arrows(bottom) represent the local polarisation direction and magnitude of the particles. 72
3.4 1D profiles of the solute and particle concentrations, and streamwise and wall-normal components of the particle polarisation in the transient regime. The 1D profiles are for $\zeta = 1, \gamma = 0.25$. 72
3.5 Long-term dynamics of the chemotactic suspension for varying relative shear rate γ and degree of confinement $\zeta = (\hat{H}\hat{N}\hat{R}^2)^{-1}$. Colours indicate the nature of the particle distribution: 1D (blue) and 2D (orange). Different symbols are used for steady (square) and unsteady (triangle) regimes. 73
3.6 1D boundary layer chemotactic destabilisation: a small disturbance in the particle distribution along the wall and the particles' activity introduce a local increase in solute concentration (green colour) and a small horizontal bias of the orientation of neighboring particles that start swimming toward and accumulating in this solute-rich region. 73
3.7 (Left) Long term particle distribution for $\zeta = 1$ and in the absence of external flow (top) and for $\gamma = 0.025$ (bottom) . (Right) Schematic representation of the opposite-walls aggregates in the absence of background flow (top) and for weak shear flow (bottom). The black arrows represent the local polarisation of the particles, white arrows show the direction of background advection and green arrow indicate the direction of chemotactic bias (reorientation). 74
3.8 (Left) Evolution of the particle density in time over a period of the relative motion of aggregates on opposite walls for $\gamma = 0.125$ and $\zeta = 1$. (Right) Corresponding schematic representation of the position of the particles' aggregates. 75
3.9 (Left) Evolution of the steady minimum offset between aggregates on opposite walls($\Delta/\lambda x$) with the shear intensity(with λ representing the wavelength of the most unstable mode), in the limit of weak shear and $\zeta = 1$. (Centre) Time evolution of $\Delta x(t)/\lambda$ for the unsteady regime at $\zeta = 1$ and sufficiently large shear forcing($\gamma = 0.125$) with λ representing the wavelength of the most unstable mode. (Right) Evolution with the shear rate intensity of the time period of the oscillations in the relative positioning of aggregates on the opposite walls for $\zeta = 1$. 76
3.10 Particle distribution (left) and solute concentration (right) observed in the strongly confined regime ($\zeta = 2$) for low and high shear rates. 76
3.11 Comparisson between the 1D steady states obtained by solving 1D version of the reduced order equations to the full simulation for $\zeta = 1$ and $\gamma = 1.5$. 78
3.12 (Left) Linear growth rate($Re(\sigma)$) as a function of background shear and degree of confinement. (Right) Frequency($Im(\sigma)$) of the most unstable mode as a function of background shear and degree of confinement. The black curve is the neutral stability curve separating the stable region from the unstable region. 78

3.13 Comparison of the phase plot obtained via the linear stability analysis (referred to as SA in the legend) with the phase plot obtained using the full simulation (referred to as FS in the legend)Red squares represent unstable 1D state while the blue circles represent the stable 1D state. 79

3.14 (Left) The steady state particle distribution and (right) real part of the eigenmodes of the particle density and solute distribution corresponding to the most unstable mode. 80

3.15 Streamlines of the induced flow for 2D steady state for $\gamma = 0$(top) and $\gamma = 0.0167$(bottom). 82

3.16 Evolution in time of particle density distribution and induced flow streamlines over a period of the unsteady regime, (i) $t = 0$, (ii) $t \sim T/4$, (iii) $t \sim T/2$ and (iv) $t \sim 3T/4$ with $\gamma = 0.125, \zeta = 1$. 82

3.17 (Left) Induced Flow field for the 1D symmetric flow for 1D steady state regime with $\gamma = 0.125, \zeta = 1.33$, inset shows the driving force due to active stress exerted by the particles. 83

3.18 Illustration of the fluid flow for 2D symmetric case. The white arrows show the direction of horizontal fluid forcing, and the black arrow shows particle polarization. The fluid forcing changes direction at a point t equidistant from the aggregates in the same wall due to a change in horizontal polarization. 85

3.19 Schematic showing asymmetrical horizontal forcing which leads to two vortices with the same direction of rotation. Green arrows show the relative dominant flow forcing resulting in the two vortex flows shown in green. The relative increase in the flow forcing is due to the orientation bias created to due to the presence of aggregate on the opposite wall. 85

3.20 Time evolution of effective viscosity($\eta_r = \eta_{hydro} + \eta_{act}$) for 2D unsteady (top) state and 2D steady state(centre) and 1D steady state (bottom) for parametric values $\gamma = 0.125, \zeta = 1$(top), $\gamma = 0.025, \zeta = 1$(centre) and $\gamma = 2, \zeta = 1$. 86

3.21 $\langle u_d \rangle_y$ (average disturbance velocity profile) for the 2D particle distribution with top aggregate displaced right (left) of bottom aggregate and (right) top aggregate displaced to the left of bottom aggregate for $\gamma = 0.125, \zeta = 1$ (Unsteady regime). 86

3.22 Net flow(averaged along the flow direction) compared to the imposed flow for (left) shear rates 0.125 (unsteady regime) and (right) 0.025 (steady regime) and $\zeta = 1$ at viscosity minima for the 2D unsteady state. 87

3.23 (Left)Variation of effective viscosity with respect to background shear rate for different degrees of confinement(ζ). (Right) Long term effective viscosity(η_r) on shear rate(γ) - confinement space(ζ). The range of the colour axis is modified such that the effective viscosity below -1 is all coloured identically as the data points are highly skewed for weak shear rates and weak confinement. Rough boundaries are drawn for the different long term regimes for respective shear rate and strength of confinement. Golden boundary indicates long term 1D steady state, orange boundary indicate long term 2D steady state and brown boundary indicate long term 2D unsteady state. 87

4.1 (a) Control of migration of electrophoretic particles based on the direction of electric field which controls the direction of the slip velocity shown by blue arrow and the red arrow represents the direction of fluid flow (Image adapted from ref. [23]). (b) (Top panel) uniform distribution of photactic bacteria in pressure driven flow. (bottom panel) focussed stream of phototactic bacteria in the presence of a light source (image adapted from ref. [11]). (c) Phase diagram showing distinct behaviour (pearling and continuous jet) of magnetotactic bacteria (image adapted from ref. [24]). 91

4.2 (Top left) Particle distribution across the channel width for $\zeta = 1.33, \gamma = 0$ for $A_1 = 0.1$. (Top right) The corresponding solute distribution across the channel width.(Bottom left) Particle distribution across the channel width for $\zeta = 1.33, \gamma = 0$ for $A_1 = -0.1$. (Bottom right) The corresponding solute distribution across the channel width. 95
4.3 Distribution of (Left to right) particle, solute, polarization and vertical solute gradient across the channel width for Dirichlet condition $C = 0$ at the walls for $\zeta = 1.33, \gamma = 0$. 95
4.4 (Top) Particle distribution in the long term in the presence of active wall (shown by red strip) producing solute at fixed rate with black arrows illustrating the local average orientation of the particles for $\gamma = 0, \zeta = 1.33$. (Bottom) Streamlines of the induced flow with the background color representing the strength of the induced flow. 98
4.5 Temporal evolution of the particle density distribution in the channel for $\zeta = 1.33, \gamma = 0.015$. The red strip shows the location of wall activity (externally driven solute consumption). The presence of wall activity triggers the particle aggregation at the transition (visible in the center panel). The chemotactic instability is triggered on both the walls and results in a 2D like state. 99
4.6 (Left) Temporal evolution of the net effective viscosity (η_r) and the two components (η_{hydro}, η_{act}) for half active wall and $\zeta = 1.33, \gamma = 0.015$. (Right) Comparison between the temporal evolution of the effective viscosity for half active wall (black) and quarter active wall (magenta). 99
4.7 (Left) Effective viscosity dependence on the magnitude of wall activity. Inset shows the particle distribution for respective regions. (Right) Maximum horizontal solute gradient induced as a function of magnitude of wall activity. 101
4.8 Comparison between the particle distribution for $A_w = 0.5$ and $A_w = 0.25$ for $\zeta = 1.33, \gamma = 0.015$. The black arrows represent the local average orientation of the particles. 101
4.9 (Top) Instantaneous particle distribution across the channel for half active wall and $\zeta = 1.33, \gamma = 0.1$. The black arrows depict the local particle polarization. (Bottom)The induced flow in the channel with the background color reflecting the strength of the flow. 102
4.10 (Left) Horizontal solute gradient at the inert wall and (right) Solute distribution in the channel for different strength of solute advection. 102
4.11 (Left) Effective viscosity for the fixed flux step-like distribution of the wall activity for $\zeta = 1.33$ following the S2 strategy. (Right) Time evolution of the effective viscosity for the two schemes for $\zeta = 1.33, \gamma = 0.3$. S1 represents the scheme where both activity and background shear imposed at the same time and throughout the run. S2 represents the second scheme where first the wall activity is introduced, and then shear is introduced after removing the activity. 103
4.12 Particle and solute distribution on the active wall for a preconditioned suspension with $\gamma = 0, \zeta = 1.33$ at t=100 and 500. The overlap between the two curves show that the 2D particle distribution is a steady state. 104
4.13 The 2D particle distribution after switching off the wall activity for $\zeta = 1.33, \gamma = 0$ following the S2 strategy. The suspension remains in this 2D state even after switching off the wall activity. 105
4.14 (Top) Particle distribution with the particle polarization shown by black arrows for $\zeta = 1.33, \gamma = 0.1$ after switching off the wall activity and imposing background shear. (Bottom) Induced flow with the background contour showing the strength of induced flow after switching off the wall activity and imposing background shear. . 106
4.15 Progression of the particle distribution for strongly confined condition ($\zeta = 2, \gamma = 0$). The 2D state slowly relaxes into the 1D state as the particle flux towards the aggregate is unable to balance the outward flux due to orientation diffusion. 107

4.16 Comparison of the phase map between the wall active case (left) with the original phase map obtained for inert walls (right). The region marked with green border corresponds to the 2D state achieved with the help of wall activity. 108
4.17 (Left) The effective viscosity on the ζ-γ space with wall activity. (Right) Relative fractional change in effective viscosity after introduction of activity. 109

5.1 Summary of the suspension dynamics in pressure driven flow. Image adapted from [25] 114
5.2 Schematic of experimental set-up to verify our results of chapter 4 115

C.1 Time evolution of spatial mean polarization magnitude and maximum $|\nabla_x C|$ for weak confinement case. The plateau region corresponds to the 1D transient state and the long-term periodic behaviour corresponds to the long-term unsteady 2D state. The plots are for $\gamma = 0.125, \zeta = 1$. 121
C.2 Comparison between disturbance velocity field due (top)total active stress and (bottom)only the pusher signature of active stress for $\gamma = 0.125, \zeta = 1, t = 1325$. The colour bar represents the particle density in the domain. 122
C.3 Horizontal and vertical fluid forcing for the two terms of Eq. 3.62 for $\gamma = 0.125, \zeta = 1, t = 1500$. The forcing field is shown on equally spaced grid points instead of the Chebyshev-Fourier grid so that the regions of strong forcing (very close to the walls) are visible. Both effects have the same pattern of contribution to the driving force. . 122

List of Tables

3.1 Dimensional parameters of the system together with their typical order of magnitude in experiments and references where such an estimate can be drawn from. 69
3.2 Distinctive characteristics of the long-term dynamics of the chemotactic suspension for different level of confinement and background shear forcing. 71

Chapter 1

Introduction

Contents

1.1 Active matter and its importance 15
1.1.1 Biological microswimmers and their collective dynamics 17
1.1.2 Designing artificial swimmers 19
1.1.3 Why is controlling self-organisation important? 23
1.2 Effect of external forcings on self-organisation 24
1.2.1 Effect of boundary on dynamics of microswimmers and its suspension . . 24
1.2.2 Effect of external field forcing 25
1.2.3 Effect of background flow on collective dynamics 28
1.3 Complex rheology of a microswimmer suspensions 28
1.3.1 Rheology of bacterial suspensions 29
1.3.2 Physical mechanism and mathematical model 30
1.4 Conclusion and structure of thesis 32

Overview

This chapter aims to introduce the readers to the active matter field, which has recently gained significant research interest due to its unique intersection with soft matter physics, applied mathematics, fluid mechanics and biophysics. The first section defines active matter and, with the help of a wide variety of examples, demonstrates the abundance of active matter at various lengthscales. This helps identify the unique features in active matter systems, leading to fundamental questions that must be answered when describing the behaviour of active systems. The universality of active matter and the potential engineering applications form the primary motivation for studying such systems. Controlling the collective behaviour of such a system becomes essential for designing any potential application devices. Focusing on designing control strategies, the following section discusses the response of microswimmer suspensions to external cues such as the presence of boundaries, background flow and external gradients. This is followed by experimental results showing evidence of unusual rheological behaviour due to the active stress exerted by the microswimmer. The distribution of active stress and, consequently, the rheological behaviour depends directly on the suspensions' self-organisation, which points to the importance of controlling the self-organisation of the microswimmer suspensions. Finally, the chapter ends with concluding remarks and an overview of the thesis structure.

1.1 Active matter and its importance

Matter composed of many individual units which exploit available free energy (often chemical) into individual mechanical energy, which drives its autonomous motion, is broadly categorised as

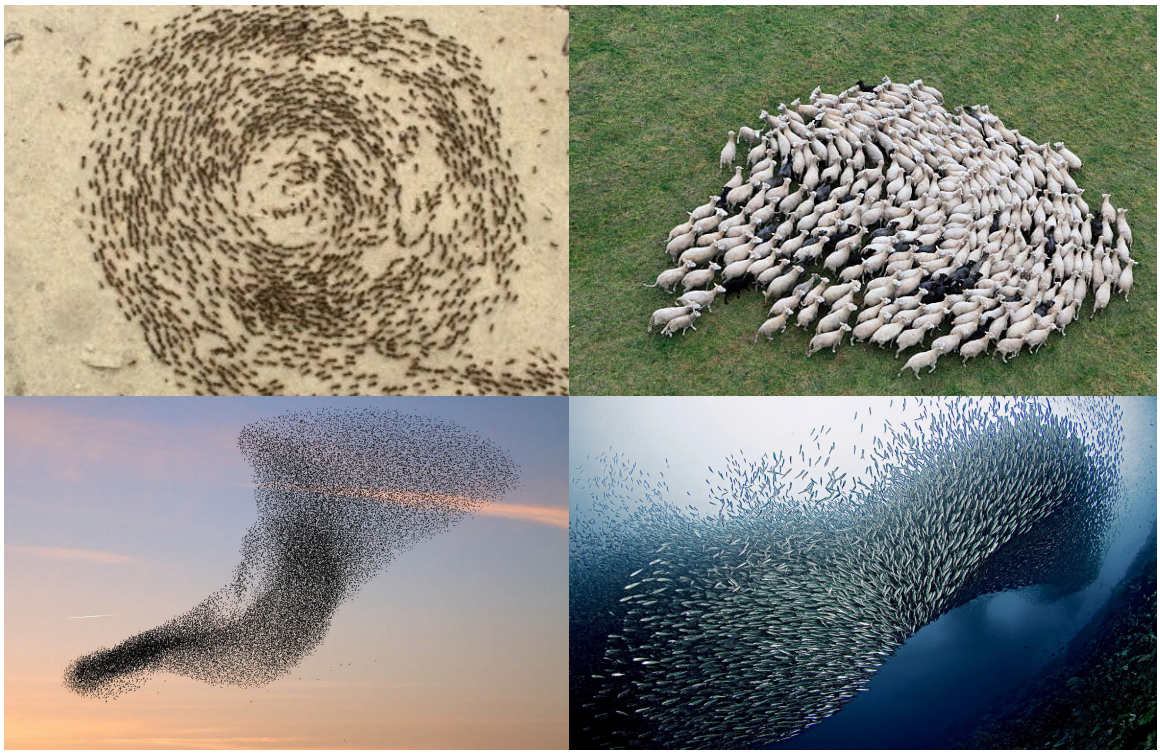

Figure 1.1: Some common examples of collective behaviour shown by various species. (Left top) Ant colony undergoing a circular spiral motion (Image courtesy India Today). (Right top) A strongly ordered herd of sheep (Image courtesy iStock). (Left bottom) A flock of starlings showing complex patterns (Image taken from CGTN YouTube channel). (Right bottom) Collective behaviour of a school of sardine fish (Image courtesy Scubashooters).

active matter [26, 27]. The continuous injection of energy drives such systems away from the thermal equilibrium, and therefore, such systems are said to be in *out of equillibrium* state [26]. This broad definition of active matter covers a wide range of systems with characteristic lengthscales ranging from a few nanometers (the motion of microtubules/actin in the cytoskeleton [28, 29]) to several meters (flocks of birds [30], fish school [31] animal herds [32]). Active matter systems are known to show rich, intriguing collective dynamics, including emergent structures [33], wave propagation [34], pattern formation [28] on scales much larger than individual units, etc., as a result of interactions. We now discuss a few examples to familiarize the readers with active systems and their unique features.

We begin by examining the dynamics of a group of ants, as shown in Fig. 1.1. In certain conditions, ants have been reported to show curious collective dynamics where the ant colony moves in a spiral shape for long times [35]. Naturally, the first question that arises is what leads to this behaviour. One possible answer to this question is that perhaps the ants follow the ant in front of it. In such cases, the collective dynamics can lead to a never-ending cycle if a path crosses itself. This can be fatal to the ant colony as the ants keep moving until they die of exhaustion [35]. This was explored recently [36, 37] using a model of reinforced random walks and random walks with memory where they found solutions that resemble such spiral. A second important feature of this collective behaviour is its striking order. The second natural question arises: what leads to such an ordered system? In this system, the order state is because each ant follows the ant's motion in front. Similarly, some sheep act as a leader with others following them [38, 39], which plays a major role in the collective dynamics of a sheep herd. As a result, similar strongly polarized states are observed for sheep herds, as shown in Fig. 1.1.

Next, we move on to a more familiar example of the dynamics of a flock of birds (such as starlings), which moves as a collective, making complex patterns as shown in Fig.1.1. Similar collective dynamics are also observed in other species, such as schools of fish, as shown in Fig. 1.1.

Observing these complex dynamics, a few questions that arise naturally are: i) What drives such collective dynamics? ii) What interactions lead to such rich dynamics? iii) Which factors decide the size of the group? etc.

Researchers from various fields have attempted to understand why certain organisms show complex collective dynamics [40]. The possible explanations include i) predator protection, ii) increased swimming efficiency, iii) increased foraging, etc. Organisms moving as a collective result in the *predator confusion effect* [41], where it becomes difficult for the predator to focus on an individual prey with a large number of moving targets as demonstrated by Millinski and Heller [40] in 1978. As a result, the chances of survival for the prey increase, which is one of the possible reasons why the species make complex collective dynamics. Collective motion of the group also reduces the drag on the individual units. As a result, the energy consumption may be reduced by up to 20% compared to its isolated motion [42]. Cyclists also often use this strategy to reduce drag and save energy [43]. Collective motion of the group has also been shown to increase the efficiency of locating food sources, as demonstrated by Pitcher and coworkers [44]. A balance between intragroup stress and intergroup food competition determines the size of the group. Large groups result in higher intragroup competition, whereas small groups reduce foraging efficiency [45]. For instance, Pride and co-workers [46] studied fecal cortisol levels in ring-tailed lemurs to measure stress levels in the population. They reported that an optimal group size of 10-20 lemurs resulted in the lowest cortisol levels, indicating the optimal group size.

At the center of the complex collective dynamics are the interactions between the individual units, and therefore, it is natural to ask how these individual units interact. A group of fish,birds or any other animal usually interact visually such that each unit changes its orientation to face along the average of its nearest neighbour. Additionally, if the animals come too close to each other, they change their direction, to avoid collision. Among the earliest models were the Vicsek [47] and Toner and Tu [48] models proposed by Tamás Vicsek and Toner and Tu in 1995. In the Viscek model, the individual units are considered point-sized with a constant speed with the rule that each unit aligns itself with its neighbours within a distance l_p in the presence of noise. A large noise results in an unaligned state where the individual units, on average, are not aligned, and therefore, the collective dynamics is similar to Brownian motion. In contrast, a global collective motion emerges, breaking the orientation symmetry in the limit of weak noise, which closely resembles experimental observations. On the other hand, Toner & Tu proposed a stochastic continuum model based on symmetry arguments to describe the flocking behaviour. Bertin and coworkers [49] recently derived these equations by coarse-graining the Vicsek model, thereby providing explicit expressions between the microscopic parameters and the macroscopic parameters used in the Toner-Tu model.

The above examples fall under the category of *dry active matter* where the individual units either do not disturb the hydrodynamic field or the disturbances are short-ranged. As a result, the hydrodynamic interactions between the individual units are negligible, and the collective dynamics can be solely described by conserving the number of units [26]. In contrast, long-ranged hydrodynamic interactions become important for *wet active matter* systems in certain situations, such as in a bacterial suspension [26]. Here, the individual units (e.g. bacteria) exert hydrodynamical stresses on the fluid, which induces fluid flows, which interact with the surrounding bacteria. This coupling results in collective dynamics on lengthscales much larger than individual bacteria. Therefore, solving the hydrodynamic equations and describing the collective dynamics simultaneously becomes important in such cases. The following subsection discusses the swimming dynamics of biological microswimmers and their collective dynamics due to hydrodynamic stresses.

1.1.1 Biological microswimmers and their collective dynamics

Due to the small size of microswimmers, the viscous effect dominates the swimming dynamics characterised by a low *Reynolds number*. As a result, the inertia-based swimming techniques fail at the microscale and symmetry breaking becomes essential for swimming at small scales [50]. A microorganism breaks this symmetry using appendages called cilia/flagella. For instance, a bacterium such as *E.coli* rotates its rigid helical appendage using cellular motors at the rear end [51]. This

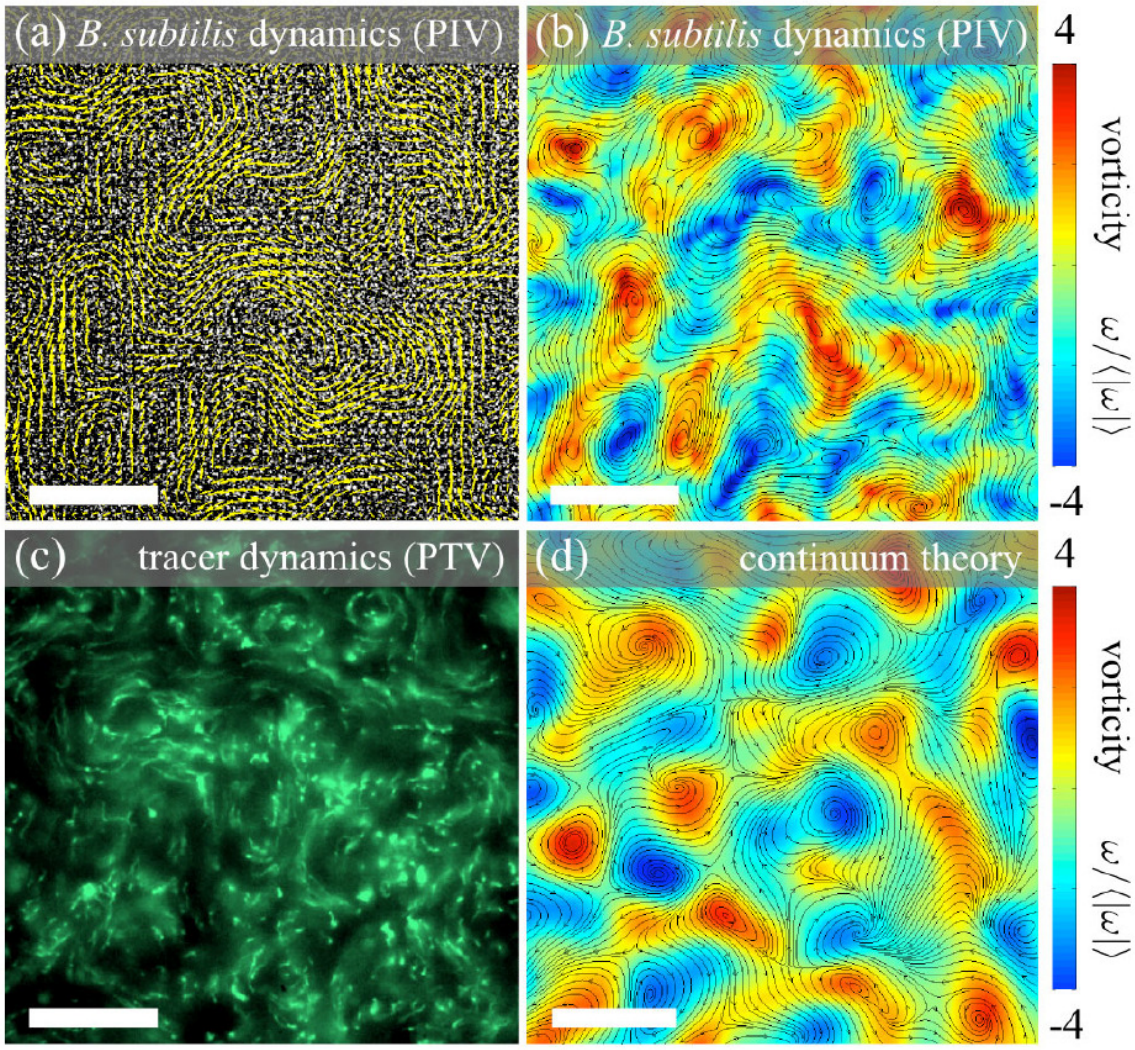

Figure 1.2: (a) A dense bacterial (*B.subtilis*) suspension with the induced flow shown using yellow arrows. (b) Streamlines (black) and vorticity field evaluated using the PIV data. (c) Distribution of tracer particles showing turbulent-like characteristics. (d) Streamlines (black) and vorticity field were obtained using the modified Toner-Tu continuum model. Images adapted from the paper by Dunkel and co-workers [1].

rotational motion leads to the swimming thrust required for self-propulsion [52]. In contrast, algae such as *Chlamydomonas reinhardtii* whips the appendages in the front to pull in the fluid from the front for self-propulsion, similar to a breaststroke motion executed by a human swimmer. These different self-propulsion strategies result in different hydrodynamic stress that the swimmers exert on the fluid. Consequently, the induced flow fields are different for these two categories of swimmers, which has significant consequences on the collective dynamics [53]. We discuss more about this in Sec. 2.2.1 in chapter 2.

The consequence of the microscopic self-propulsion on the flow field can be expressed as a series of decaying harmonics. A force dipole corresponds to the slowest decaying harmonic; therefore, the induced flow of a swimmer is often approximated with a force dipole, decaying as $1/r^2$ where r is the distance between a point in space and the bacteria. In a dilute bacterial suspension, the bacteria interact via this long-ranged hydrodynamical signature, which can lead to complex turbulent-like behaviour as shown in Fig. 1.2. Note that turbulence is usually associated with high Reynolds dynamics. Therefore, it is surprising to observe such flow structures in inertia-less flows. It is important to note that we use the term "biological turbulence" due to its use in the literature [1, 54, 55]; however, the flow structures do not strictly fall under turbulent flows as some essential characteristics of turbulence (such as energy cascades) are absent in these flows.

Mendelson and co-workers [56] were among the first to study the collective motion of *B.subtilis* (body length$\sim$ 5 μm, self-propulsion velocity $\sim$ 10-30 μm/s) in a thin liquid film over an agar surface. They reported a correlated cell motion over lengthscales $\sim$ 10 times the body length of an individual bacterium. Furthermore, they reported enhanced diffusion of tracer colloidal particles of size 1 μm due to coherent collective motion in the form of vortices and jets. However, this experiment was conducted in the presence of a boundary, which has been reported to induce swarming of bacteria. A similar swarming behaviour was recently reported for a suspension of ram spermatozoa [57], where the authors used imaging techniques to track the flow field to show "turbulent-like" behaviour between the swimmer lengthscale and a well-defined integral length.

Wu and Libchaber [58] analyzed the collective dynamics of *E.coli* bacteria in a soap film with an approximate thickness of 10 μm. They reported a linearly increasing diffusivity of 10 μm colloidal particles (with Brownian diffusivity $\sim 0.1\ \mu m^2/s$) with increasing bacterial concentration, with the effective diffusivity reaching up to $100\ \mu m^2/s$ at $nL^3 \sim 90$ where n is the number density of the bacteria and L is the characteristic scale of the drop. Sokolov et al. [59] reported similar results for bacteria *B.subtilis*. Furthermore, they reported a smooth increasing root mean squared velocity of the bacteria with an increase in bacterial concentration over the range $n_a L^2 = 3 - 9$, where n_a is the number of bacteria per unit area, as the soap films were 2D. This suggests that coherent long-range flow structures are formed as the bacterial concentration rises, which increase the average diffusivity of both the bacteria and tracer particles [59].

Dombrowski and co-workers [60] reported similar large-scale coherent structures in a three-dimensional fluid domain. The experiment set-up consisted of a bacterial suspension of *B.subtilis* in a sessile drop of size $\sim$ 1 cm. Using imaging techniques with the help of passive particles, the authors showed that large-scale vertical flows are responsible for increasing the diffusivity of passive particles. Dunkel and co-workers [1] recently analyzed the bacterial suspension in closed three-dimensional microfluidic chambers while nearly simultaneously tracking both the motion of cells and the tracker as shown in Fig. 1.2. Furthermore, by modifying the Toner-Tu theory to include a fourth-order term corresponding to active stresses in the system, they qualitatively captured (Fig. 1.2) the suspension dynamics while reproducing the statistical features of the experimental data.

1.1.2 Designing artificial swimmers

At small scales, symmetry breaking is a necessary condition for any artificial swimmer to self-propel, as discussed earlier [50]. A biological microswimmer uses appendages to break this symmetry by rotating them using motors attached to its cell membrane [52]. Inspired from flagella based self-propulsion of the biological microswimmers, artificial microswimmers have been designed to

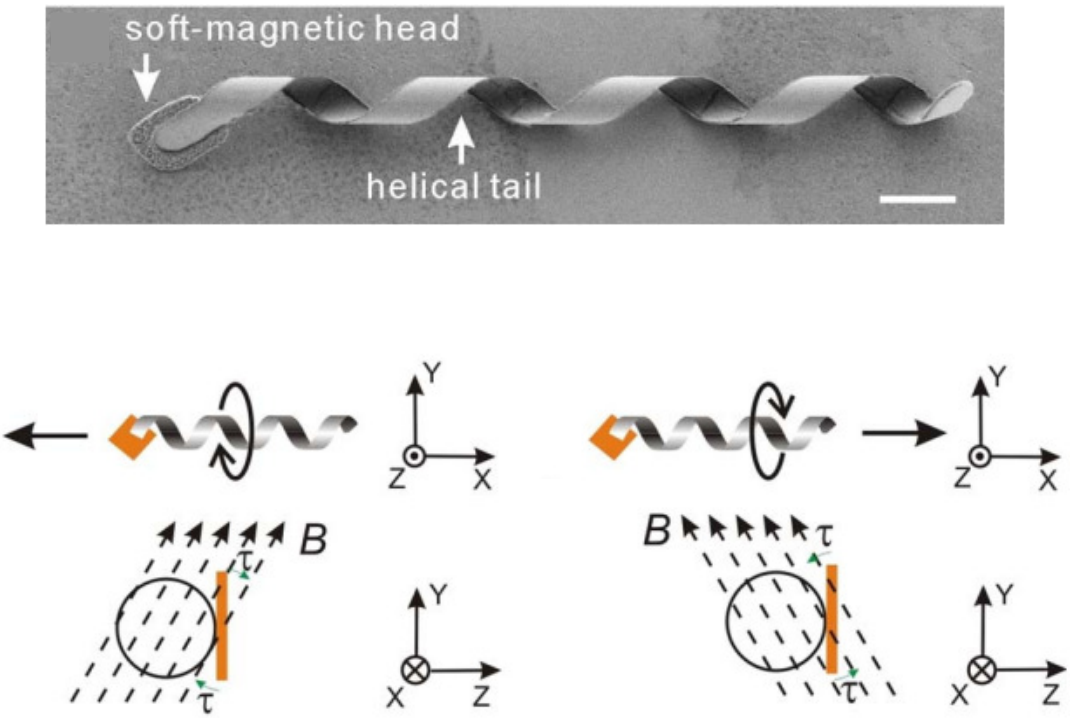

Figure 1.3: (Top) Field emission scanning electron microscopy image of a magnetic helical swimmer with the scale bar equal to 4 μm. (Bottom) Schematic showing the self-propulsion mechanism. Using continuously rotating magnetic field B perpendicular to microswimmer orientation, a misalignment angle between the field and the thin magnetic head induces a magnetic torque τ that rotates the magnetic head resulting in propulsion of the microswimmer. The direction of self-propulsion can be controlled by changing the direction of magnetic field. Images adapted from ref. [2]

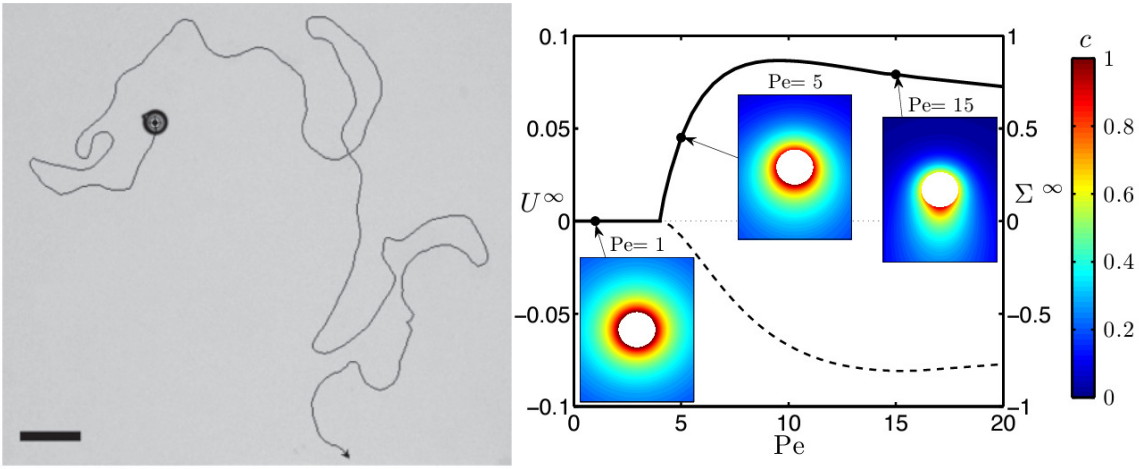

Figure 1.4: (Left) The trajectory of an active drop showing large persistence length compared to drop size. Image taken from [3]. (Right) Steady swimming velocity of the drop as a function of Peclet number. The inset images illustrate the solute field around the drop for particular value of Peclet number indicated on top. Image adapted from [4]

mimic the flagella rotation technique using external magnetic fields [2, 61, 62]. For instance, Zhang et al. [2] designed a microswimmer made up of a soft magnetic head and a helical tail resembling the flagella of a natural microswimmer as shown in Fig. 1.3. An external magnetic field drives the rotation of the microswimmer, which propels the microswimmer. Controlling the direction of the external magnetic field thus allows us to control the swimming direction as reversing the direction of the magnetic field results in rotation of the microswimmer in the opposite direction, as shown in fig. 1.3.

Quincke rollers are another example of an externally driven artificial swimmer. However, unlike the previous example, the self-propelling direction of such swimmers cannot be controlled using external fields as they pick a random swimming direction perpendicular to the applied magnetic field. These particles exploit the hydrodynamic interaction between a rotating particle and a boundary to self-propel [63–65]. These particles are synthesized using a weakly conducting dielectric material and are suspended in a dielectric liquid [63]. Upon application of an external electric field, such particles can spontaneously start rotating above a critical electric field, with the rotating speed increasing with increasing electric field strength. The spontaneous rotation near a boundary leads to levitation and self-propulsion of such colloidal particles [65]. Recent experimental works have shown precise control of single self-propelling particles and their collective dynamics, which makes this system very attractive for applications in the transport of microscale cargo [66].

Motivated by designing *intelligent motors*, researchers have proposed various strategies to achieve self-propulsion. Once such design exploits the physicochemical properties of the particle/drop to self-propel in viscous fluids. The fore-aft symmetry breaking, in this case, occurs either via an asymmetric design [8] or using an instability [3, 67].

In their seminal paper, Paxton and co-workers [68] showed that anisotropic catalysts' coverage of rodlike particles could also result in self-propulsion. They synthesized rod-shaped particles with a diameter of $\sim$ 37 µm with two halves of platinum and gold, each length $\sim$ 1 µm and utilized H_2O_2 as the fuel. These particles are known as *Janus* particles, named after the two-faced Greek god *Janus* [8]. H_2O_2 reduces on the gold surface to produce oxygen gas. At the same time, it oxidizes on the platinum surface to produce water. As a result, an asymmetric charge distribution is set up across the rod length, as shown in Fig. 1.5. This asymmetric charge distribution across the rod results in an electric field that drives a pressure-driven tangential flow near the particle surface due to *electrophoresis*. As the electric field is self-generated, this is also known as *self-electrophoresis*. Similarly, Forunier-Bidoz and co-workers [69] showed that Nickle-Gold rods also self-propel due to the same principle.

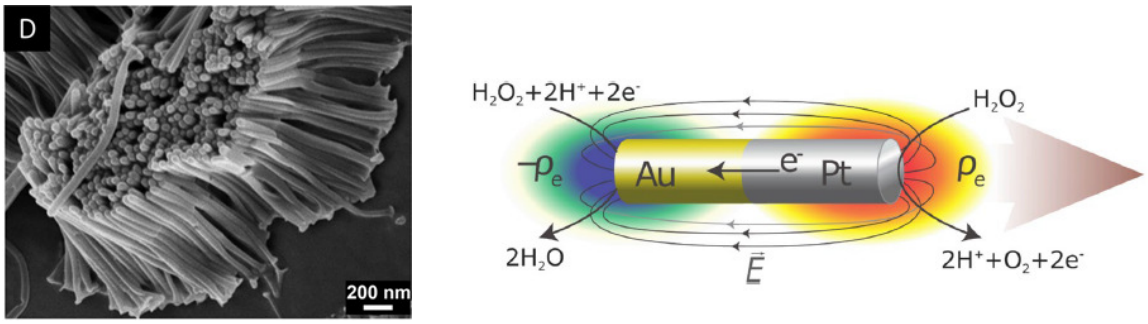

Figure 1.5: (Left) Scanning electron microscope image showing a band of rod-shaped Janus particles with gold and platinum halves. Image adapted from [5]). (Right) Schematic showing the charged self-diffusiophoretic mechanism for self-propulsion of Janus rod. Image adapted from ref. [6]

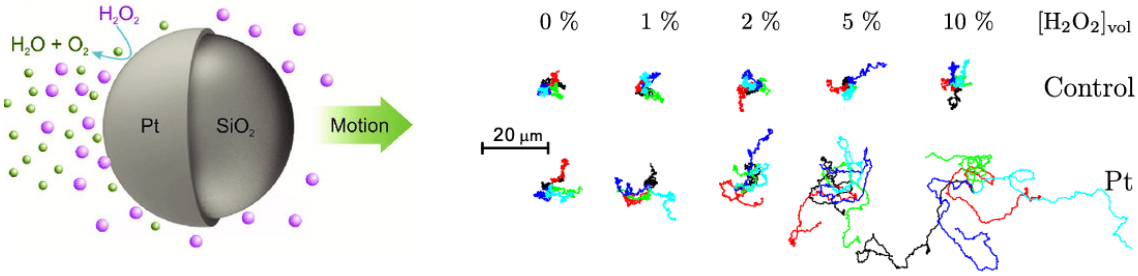

Figure 1.6: (Left) Schematic showing the self-propulsion mechanism for a Janus particle with reduction of H_2O_2 taking place on the *Pt* coated half. Image adapted from ref. [7]. (Right) Trajectories of colloidal particles (top panel) and Janus particles (bottom panel) overlayed to match the starting point to show enhanced effective diffusion of Janus particles due to self-propulsion. Image adapted from ref. [8].

Furthermore, spherical particles with chemically distinct halves have also been shown to self-propel, as demonstrated by Howse and cor-workers [8]. They coated polystyrene colloidal particles of size ~ 1.62 µm with platinum on one-half, and as a result, the reduction of H_2O_2 takes place only on the Platinum half. This generates a tangential chemical gradient at the particle surface, which drives fluid flow close to the particle surface, leading to the self-propulsion of the colloidal particles. In addition to the electrophoretic flow, the fluid flow close to the surface is driven due to the solute (O_2) concentration gradient, called *self-diffusiophoresis*. They showed that as the concentration of the fuel H_2O_2 increases, the effective diffusion of the particle increases due to self-propulsion, as illustrated in Fig. 1.6 (right). Instead of polystyrene, Silica particles have also been used to achieve self-propulsion by Ke and co-workers [70].

Moreover, neutral reactions have also been utilized to achieve self-propulsion via neutral self-diffusiophoresis. For instance, Pavlick et al. half-coated the surface of spherical silica colloids with a layer of gold and modified the silica surface using the Grubbs catalyst. The Grubbs catalyst on the silica face acts as a catalyst for a polymerization reaction. Consequently, a tangential solute gradient is generated due to an asymmetric reaction across the particle surface, which drives the flow due to diffusiophoresis. The neutral polymerization reaction ensures that the self-propulsion is driven solely by neutral self-diffusiophopresis. Recently, another example of neutral self-diffusiophoretic swimming was demonstrated by Gao et al. [71] using hydrazine as the fuel for iridium-based Janus particles.

The asymmetric chemical reaction can also be triggered using external signals such as ultraviolet light [72–74]. One of the reactions that has been exploited is the decomposition of silver chloride (AgCl) into silver and HCl in the presence of UV radiation as demonstrated by Ibele and co-workers [74]. The asymmetry can be based on asymmetric silver coating or asymmetric light

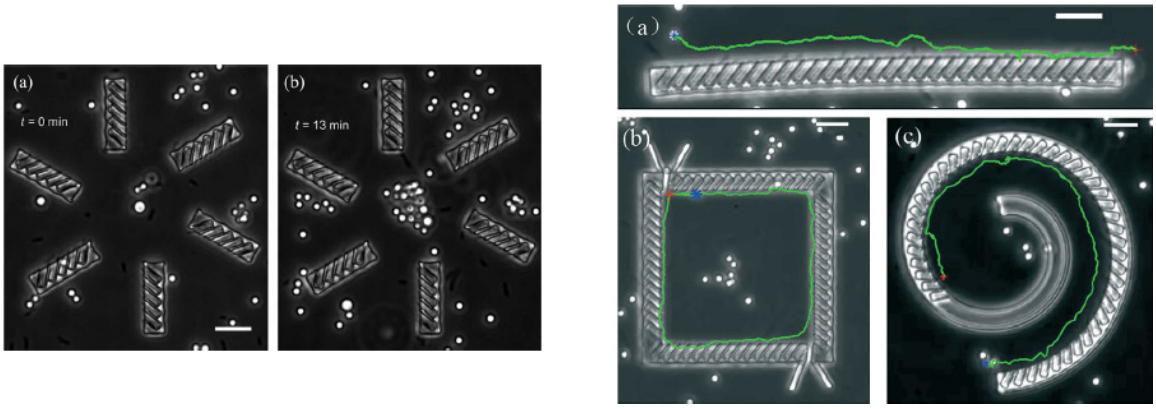

Figure 1.7: (Left) Targeted transport of colloidal particles using 6 linear arrays of confined bacteria. The induced flow created by the bacteria transports colloidal particles towards the center of the structure. (Right) Transport of 2 µm silica particles using (a)linear, (b) spiral and (c) square arrays of confined bacteria. The red and blue symbols represent the starting and final position of the colloidal particle, respectively. The cavities are at 40^o to the local tangent of the structures. The scale bar for both images equals 10 µm. Images adapted from ref. [9]

source. Still, the basic principles remain the same: an asymmetric chemical reaction leads to the formation of tangential gradients, which drive fluid flow close to the surface, resulting in the self-propulsion of the particle. Light illumination on asymmetrically metal-coated colloidal particles can also generate tangential thermal gradients [75–77], which drive surface flows similar to the diffusiophoretic flows, resulting in particle self-propulsion. These are termed *thermophoretic* self-propulsion arising due to *thermophoresis* [78]. However, these are relatively less common than self-diffusiophoretic and self-electrophoretic microswimmers.

Finally, for the case of active drops, the swimmer exploits the physicochemical "activity" (ability to exchange solute through the interface) along with interfacial flows created by chemical gradients [79]. Due to the isotropic nature of drops, the drop remains stationary in a diffusion-dominated regime. However, as the Peclet number increases (strength of advection to diffusion), the isotropic state becomes linearly unstable to small perturbations and the isotropic symmetry of solute concentration is broken (Fig. 1.4). As a result, a solute gradient is set up which drives interfacial Marangoni flows, resulting in self-propulsion of the drop as Izri et al. [67] demonstrated experimentally (see Fig. 1.4). Research on self-propelling drop dynamics has recently gained significant interest due to its simple design [79]. Another way to break the symmetry is by considering geometrically anisotropic particles. The simplest example is joining two isotropic particles of different sizes [80]. A chemical reaction occurs at a constant rate on the surface, creating a tangential gradient due to the asymmetric shape of the particle. Consequently, the particle self-propels using the slip velocity at the surface.

1.1.3 Why is controlling self-organisation important?

Active matter finds a unique position at a junction between applied mathematics, biophysics, and fluid mechanics, and it has recently garnered a lot of attention from different research communities. Physicists are interested in understanding such systems due to the unique *out of equilibrium* behaviour driven through active injection of energy of such systems. Therefore, studying active matter challenges traditional equilibrium-based frameworks and motivates the development of new theoretical approaches to describe and predict the behaviour of non-equilibrium systems. Developing theoretical models and computational tools to understand the dynamics of active systems also helps advance our theoretical understanding of complex systems and develop predictive models for their behaviour.

On the other hand, active systems are abundant in biological systems, such as during tissue growth [81], self-organisation of organelles inside a cell [82], survival strategies adopted by cell

colonies [83], etc. Understanding the mechanism behind self-organisation in different biological systems is of prime importance as it may help develop new strategies to control self-organisation based on a particular requirement. For instance, understanding how cancer cells aggregate and grow may help contain the growth of cancerous tissues, or understanding how epidemics spread in a population may help develop strategies to contain its spread. This illustrates the importance of understanding collective behaviour in active systems.

Furthermore, biological microswimmer suspensions exhibit rich collective behaviour to achieve complicated tasks. For instance, the collective swimming of spermatozoa plays a critical role during fertilization [84]; thus, understanding their collective dynamics can help design strategies for successful animal reproduction. Similarly, a collection of algae in water bodies has shown to induce large convective [85] eddies, which improves the mixing of nutrients in the water body crucial for the survival of marine species [86].

From an engineering point of view, studying such systems improves our understanding of transport at the microscale. This will result in the development of different techniques for wide applications, including designing directed drug delivery mechanisms [87], enhancing mixing at small scales [88], harvesting energy at small scales [89], etc. For instance, recently, Gao and co-workers [9] developed various strategies for controlling flows at the microscale using an array of confined bacteria. They confined *E.coli* into cuboid cavities and used them as basic building blocks to arrange in different patterns to achieve directed transport of passive colloids as shown in Fig. 1.7. An interesting question arises: instead of arranging the cavities, can we *control* their self-organisation so that collectively, the system can perform similar tasks? This will provide us with a way to actively control the flow instead of passive control by the fixed arrangements of the cavities. It is, therefore, essential to understand what drives their collective dynamics before we can attempt to control it.

Moreover, recent studies [12, 14, 90] have reported that microswimmer suspensions can alter the rheological properties of the fluid by exerting active stresses in the system. In a study conducted by Lopez et al. [14], they showed that a bacterial (*E.coli*) suspension could behave as a superfluid for high bacterial concentration. This suggests that bacterial suspensions may reduce the requirement of mechanical forcing in specific set-ups. Of course, instead of mechanical energy, chemical energy in the form of nutrients must be transported to maintain the activity of the bacteria. However, this provides a new path for potential applications where the *superfluid* nature may be exploited to reduce energy costs. The rheological response of a suspension depends strongly on its self-organization, as the induced active stresses depend on the distribution of the microswimmers. This shows a link between self-organization and fluid properties, which can be exploited to manipulate the rheological properties of the suspension at least in principle. Current work focuses on understanding the collective behaviour of phoretic particles and developing control strategies for potential applications (for example, as energy harvesters). In the next section, we discuss different strategies adopted in the literature to control the self-organisation of microswimmer suspensions.

1.2 Effect of external forcings on self-organisation

1.2.1 Effect of boundary on dynamics of microswimmers and its suspension

Suspensions of biological microswimmers encounter complex boundaries in various situations, such as bacterial movement in porous soil [91] or spermatozoa motion in the female reproductive tract [92]. The presence of wall boundaries has been shown to affect the dynamics of microswimmers both at the individual scale and the suspension scale [93, 94] due to i) no penetration condition and ii) no-slip condition imposed at the wall, which disturbs the hydrodynamic field generated by the microswimmer. This hydrodynamic-based interaction is known to strongly affect the dynamics of a single swimmer and the suspension dynamics. We first explore the effect of wall boundaries on an individual swimmer, followed by a discussion on the effect of wall boundaries on microswimmer suspensions.

It is well established now that microswimmers are attracted towards walls [95–99]. Earlier

works argued that this wall attraction had hydrodynamic origins and explained the attraction using the imaging system of flow singularities [97, 100]. They argued that for the no-slip condition at the wall to be satisfied, image singularities consisting of force dipole, source dipole and force quadrupole must be considered on the other side of the surface. These image singularities, in turn, have a net attractive effect on the swimmer [97]. Furthermore, the image singularities induce a torque on the swimmer, which leads to the swimmer's orientation being parallel to the surface. Hydrodynamic trapping is one among various reasons to explain the wall trapping of microswimmers. Another possible reason is based solely on kinetic arguments. [101]. The argument is as followed, as the boundaries are impermeable, a microswimmer moving towards the boundary is trapped until its orientation changes (due to tumble/ rotation diffusion). As a result the swimmer spends more time near the boundaries than in the bulk. We expand more on this in the later chapters.

Furthermore, the trajectories of the bacteria near a surface change significantly [52]. In bulk (away from the walls), bacteria show run-and-tumble dynamics where the trajectory of the bacteria follows a straight line between two tumbling events [52]. In contrast, in the presence of the wall, some bacteria move in a circular trajectory, as demonstrated by Berg and Turner [102] and Frymier and co-workers in 1995 [103]. This contrasting swimming behaviour is associated with the additional hydrodynamic force and its moment induced by the presence of a wall [104].

Now, we will proceed towards the effect of confinement on suspension dynamics; Wioland and co-workers [105] worked on a suspension of *Bacillus subtilis* bacteria in a drop of size $\sim$ 60-70 µm and height $\sim$ 25 µm surrounded by oil which supplied the oxygen needed for the bacteria. They demonstrated that a dense suspension of *Bacillus subtilis* self-organizes into a single stable vortex and radius of the drop below a critical value. They argued that the order in the bacterial suspension is driven by the interplay of boundary curvature and steric and hydrodynamic interactions between the bacteria, which were confirmed by a simple continuum model incorporating these effects. Beyond the critical size of the drop, the suspension showed bacterial turbulence previously reported for semi-infinite suspensions [60]. This showed that confinement dampens bacterial turbulence. Furthermore, they showed that upon imposing a weak shear, a thin layer of highly ordered bacteria develops close to the drop-oil interface, which swims opposite the background shear. Background shear rotates the bacteria to face upstream due to an additional torque. As a result, the bacteria move upstream at an angle close to the interface. This is called *rheotaxis* and is discussed in more detail in the next subsection. Lushi and co-workers [106] worked on a similar set-up and confirmed Wioland et al.'s finding experimentally and using a discrete model for bacterial dynamics. They showed that long-ranged hydrodynamic force is necessary for self-organization in this system.

In another study by Wioland et al. [10], a bacterial suspension was confined to a racetrack-like geometry to study the effect of strength of confinement on bacterial suspension as shown in Fig. 1.8 (left). Similar to the previous results, they demonstrated that increasing the confinement strength (width$\geq$ 45 µm) results in a transition from a 2D turbulent-like state to a 1D state as shown in Fig. 1.8. Furthermore, they showed that in this 1D state, the suspension induces a uni-directional flow with a parabolic flow profile on length scales much larger than individual bacteria, as shown in Fig. 1.8. The experimental results were reproduced using a discrete particle tracking model where the hydrodynamic interactions are captured by considering a force dipole at the location of the bacteria. This distribution of force dipoles drives the induced flow in the channel.

These various experimental and simulation studies show that the effect of confinement on a suspension of microswimmers is two-fold: i) the presence of a wall boundary acts as an attractor for the microswimmers, resulting in wall accumulation, and ii) The bacterial suspension can be stabilized into ordered fully state using confinement.

1.2.2 Effect of external field forcing

Both natural and synthetic microswimmers respond to external gradients of different fields such as light, gravity, solute concentration, etc., which plays a crucial role in the self-organisation of microswimmer suspensions. For instance, algae such as *Chlamydomonas reinhardtii* have evolved to detect gradients in light intensity to move towards higher light intensity to produce more energy

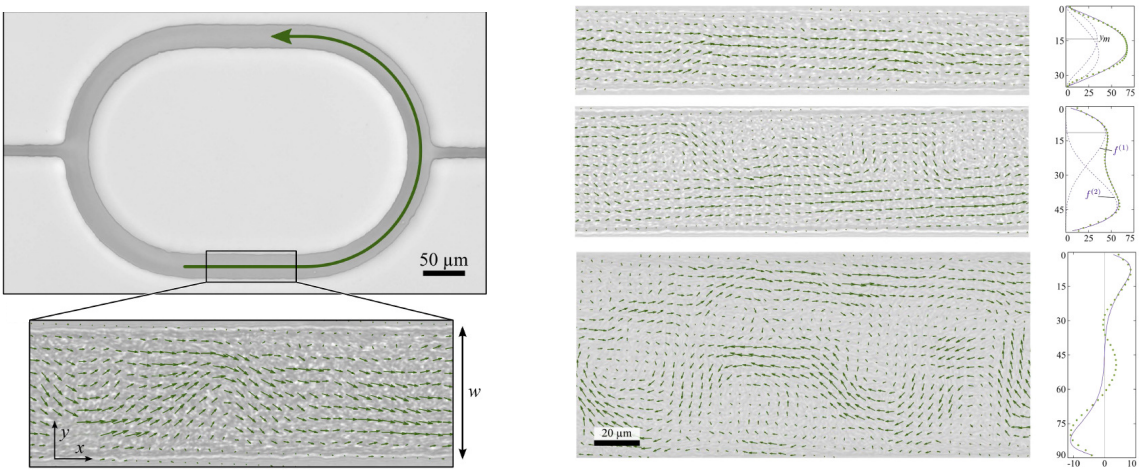

Figure 1.8: (Left) Racetrack set-up of Wioland et al. [10] experiments for self-organisation of *E.coli* suspension in the presence of confinement. The large green arrow shows the unidirectional motion of the induced flow, while the smaller green arrows inside the channel show the distribution of the induced flow. (Right) Self-organisation of the suspension for varying $(30, 60, 90\ \mu m)$ confinement strength showing a continuous transition from a 2D turbulent-like state to a 1D state with an average induced flow profile adjacent to each panel. Images adapted from ref. [10].

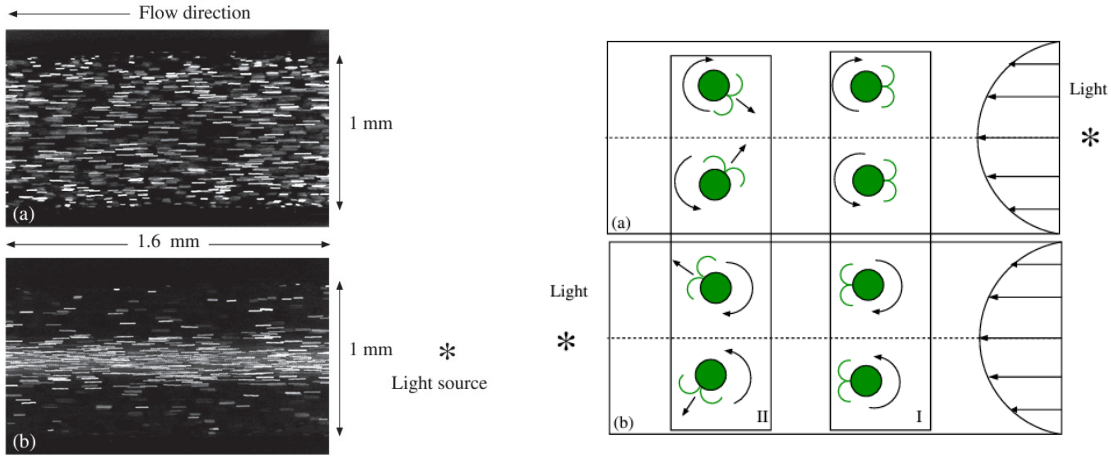

Figure 1.9: Light-driven control of phototactic algae. (Left) Trajectories of *Chlamydomonas reinhardtii* using the superimposition of 10 images in a pressure-driven flow in the (a)absence and (b) presence of light source. (Right) The schematic shows the algae's focusing mechanism depending on the direction of the light source. Image adapted from ref. [11].

via photosynthesis [107]. Consequently, if the light source is above the suspension, the algae moves against gravity and accumulates near the top surface. As *Chlamydomonas reinhardtii* are slightly heavier than water, this motion against gravity results in higher density "fluid" (highly concentrated region) on top of a less dense fluid (suspending fluid). Consequently, convective patterns are formed similar to the classic *Rayleigh-Taylor instability* [108, 109].

Another important example is the chemotactic response of some microorganisms. For instance, the response of immune cells to detect the location of foreign entities using the solute field produced by the invading entity [110]. This type of response is called chemotaxis, where the microswimmer responds to external solute concentration gradients. The response may be to the solute produced by different microswimmers (for example, mammalian spermatozoa and egg [111]) or between the same species (as reported in *E.coli* colonies). The latter is called auto-chemotaxis and generates complex patterns in microswimmer (both artificial [112] and natural [113]) suspensions.

While natural and artificial swimmers show auto-chemotactic behaviour, an important distinction exists between their chemotaxis mechanisms (discussed in more detail in the next chapter). Isolated natural microswimmers show run-and-tumble dynamics where the swimmer randomly changes its orientation (tumble) between straight runs [52]. By altering the tumbling frequency, a microorganism controls its motion in the presence of external gradients. In improving conditions, the tumbling frequency reduces, ensuring longer runs, while the frequency increases in harsher environments [83]. Consequently, the microorganism shows biased movement on longer timescales. In contrast, an artificial swimmer, such as a phoretic particle, responds to the external solute gradient due to its asymmetric chemical interaction with the surface [114]. As a result, the external gradient induces a rotational torque on the particle, leading to reorientation parallel/antiparallel to the chemical gradient [114, 115]. The next chapter discusses this mechanism and its modelling in more detail.

Response to external fields has also been observed in artificial systems; for instance, a suspension of phoretic particles has been reported to show dynamic clustering due to the chemotactic response of the Janus particles [116]. The clustering process is explained as follows: An individual phoretic particle acts as a source at the suspension scale and disturbs the solute field in the domain. The perturbed solute field interacts with other phoretic particles, and depending on the interaction of the solute with the particle surface, this can lead to attractive forces between the particles. The attraction has two components: i) a phoretic drift and ii) reorientation along with self-propulsion. Experimental studies have demonstrated that clustering is a dynamic process, that is, individually, the particles continuously leave and join the clusters due to thermal noise, and the cluster itself may rotate and self-propel. Furthermore, increasing the self-propulsion velocity increases the size of the clusters even in dense phoretic suspensions [117].

In addition to this auto-chemotactic phenomenon, the self-organisation of microswimmers can be externally controlled using external gradients. This was illustrated elegantly by Garcia and coworkers [11] who exploited light intensity to control their collective behaviour of algae *Chlamydomonas reinhardtii*. In their experimental set-up they pumped algae suspension through a channel in i) the presence of light and ii) its absence. They reported contrasting behaviour for the two cases, as shown in Fig. 1.9 (left). In the presence of light, the microswimmers move across the streamlines to focus in a band near the channel centerline in contrast to a uniform distribution in the absence of light. Furthermore, they showed that depending on the location of the light source (upstream/downstream), the microswimmers focus on the channel centerline or at the walls. The physical explanation behind this behaviour is as follows: the algae detect a gradient in light intensity and rotate towards a stronger intensity; simultaneously, the background flow rotates the swimmer clockwise in the upper and counterclockwise in the lower half. As a result, when the light source is upstream (downstream), a stable orientation of the microorganism is towards the channel center (wall). As a result, the algae swings towards the channel centerline (wall), resulting in cross-stream migration of the microswimmer.

1.2.3 Effect of background flow on collective dynamics

The effect of background flow on the swimmer is similar to that on a passive particle in that the swimmer experiences an additional drift due to advection and an additional torque due to background vorticity. Owing to small size of the swimmer, the background flow can be approximated locally as a linear flow composed of a linear superposition of uniform, extensional and pure rotation flow. As a result, the dynamics of a single isolated bacteria can be shown to be a linear superposition of active swimming and passive advection and rotation, similar to passive colloidal particles. Therefore, an isolated spherical microswimmer tumbles in a linear background flow in addition to its self-propulsion. This results in circular trajectories for a spherical microswimmer in shear flows [118]. In contrast, isolated elongated microswimmers (bacteria such as E.coli, Bacillus subtilis) follows a more complex trajectory, as the orientation dynamics of the particle follows dynamics similar to *Jeffrey orbits* where their orientation moves on a periodic orbit on the unit sphere [119].

Moreover, in non-linear flows such as Poiseuille, the non-uniform shear results in the orientation distribution of the particle depending on its position. When coupled with its self-propulsion, this spatial variation in orientation distribution leads to non-uniform particle concentration across the domain. This was elegantly demonstrated by Rusconi and co-workers [120] where they pumped a suspension of *Bacillus subtilis* in a microchannel to show accumulation of bacteria in high shear regions compared to a uniform distribution for dead cells. Intuitively, the trapping in the high-shear areas is due to stronger tumbling dynamics than in weak-shear regions. Consequently, the net swimming of bacteria in the high-shear areas is less compared to low-shear regions. Moreover, Rusconi and co-workers used Langevin equations with noise terms to model the shear-trapping behaviour of the microswimmers.

The bacteria swim upstream to the background flow in the presence of wall boundaries [121]. This phenomenon is called *rheotaxis*, which has been reported in various studies [121–124]. The upstream swimming is linked to the orientation dynamics of a microswimmer near a boundary coupled with the additional torque of the background flow. Due to no penetration condition at boundaries, the microswimmers are oriented vertically towards the wall without background flow. The shear flow introduces a torque on the swimmer, resulting in an equilibrium orientation upstream. Finally, due to its self-propulsion, the bacteria swim upstream. Note that due to the no-slip condition for the fluid at the wall, the advective effect on the bacteria is weaker, closer to the boundaries, and helps it swim upstream. Interestingly, the rheotactic behaviour is not just limited to elongated swimmers and has been reported for spherical Janus particles both in experiments [125, 126] and in simulations [25, 127].

A microswimmer also exerts hydrodynamic stresses on the fluid. As a result, microswimmers can respond to the externally forced background flow through active stress. In the next section, we focus on the rheological behaviour of a microswimmer suspension.

1.3 Complex rheology of a microswimmer suspensions

In this section, we explore the hydrodynamic response of a microswimmer suspension to external flows. However, before we move onto the rheology of "active" suspensions, it is important first to understand the rheological response of a passive suspension. However, we must first define the effective viscosity of a microswimmer suspension before proceeding further. The effective viscosity is defined as the bulk viscosity of the suspension if it were a continuum fluid [128]. Based on this definition, the effective viscosity for a dilute suspension (neglecting hydrodynamic interaction between the particles) was first derived by Einstein in 1906, which was corrected in 1911 [128] to

$$\mu_r = \mu_0 \left(1 + \frac{5}{2}\phi\right) \tag{1.1}$$

where ϕ is the particle concentration. This result has been verified experimentally in refs. [129, 130]. Furthermore, Batchelor [131] derived $O(\phi^2)$ correction for a suspension of spherical colloidal parti-

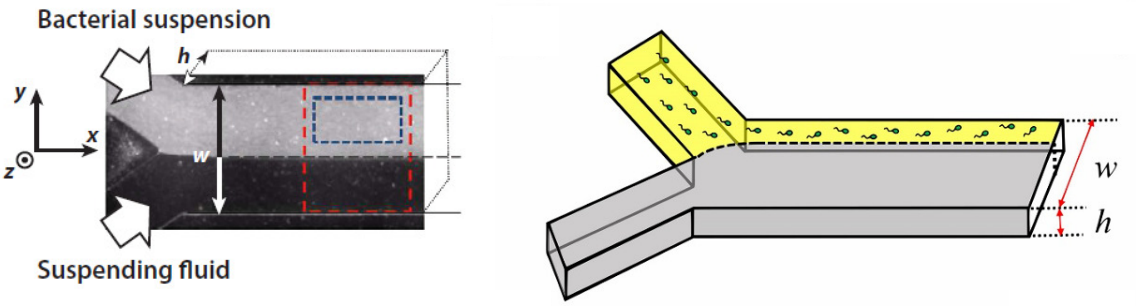

Figure 1.10: (Left) Experimental setup used by Gachelin and co-workers [12] to measure the effective rheology of bacterial suspension using a Y-shaped microchannel. (Right) Schematic showing the experimental set-up adapted from ref. [13]

cles using the "hydrodynamic renormalization" technique to show that the $O(\phi^2)$ contribution also increases the effective viscosity of the suspension. However, these results are valid for extremely dilute suspensions ($\phi < 0.1$). Increasing the suspensions' density results in a more complex nonlinear rise in the effective viscosity [128, 132] which is not the focus of the current work. For more details we refer our readers to a recent review on this topic by Guazzelli and Pouliguen [133].

The increase in effective viscosity has been demonstrated by both theory and experiments, which is understood as the consequence of the rigidity condition for the colloidal particles. As the particles are considered rigid, they do not deform to the extensional component of the background flow. As a result, the particles exert passive stress on the fluid, increasing the viscous dissipation. This suggests, more energy must be supplied externally to overcome this additional dissipation. This results in a higher effective viscosity of the suspension. As microswimmers exert active stresses on the fluid, it is expected that the rheological response of microswimmers to background flow could be different from passive particles.

We first begin by discussing experimental evidence for the strange rheological behaviour of a microswimmer suspension and then proceed towards understanding the rheological behaviour using modelling techniques.

1.3.1 Rheology of bacterial suspensions

Sokolov and Aronson [55] were among the earliest to determine the effective viscosity of a bacterial (*Bacillus subtilis*) suspension experimentally. They employed two techniques to infer the effective viscosity: i) by analyzing the unsteady decay time of a vortex generated using magnetic probes in the bacterial film and ii) by measuring the toque on a rotating magnetic particle immersed in the film. They reported a significant reduction in effective viscosity for dilute suspensions. However, an increase in effective viscosity was reported for concentrated suspensions [55].

Gachelin and co-workers [12] adopted a different technique to determine the effective viscosity where they pumped the bacterial (*E.coli*) suspension through a Y-shaped microfluidic channel along with a parallel co-flowing fluid, as shown in Fig. 1.10. This is a common technique used for measuring the viscosity of a Newtonian fluid using the deflection of the interface. Assuming a pure Poisuelle flow, the deflection can be related to the relative viscosity of the two fluids. They demonstrated that a dilute bacterial suspension has a lower effective viscosity than the suspending fluid. Furthermore, they showed the effective viscosity increases upon increasing the shear rate, reaching maxima beyond which it decreases. In other words, bacterial suspension shows a shear-thickening behaviour at lower shear rates in contrast to a shear-thinning regime at higher shear rates. More recently, Liu and co-workers [13] used a similar set-up to study the effect of strength of confinement on the rheology of bacterial suspensions. They showed that the confinement effect is dominant at low shear rates, reducing effective viscosity for increasing confinement.

Recently, Lopez and coworkers [14] used a Taylor–Couette rheometer to determine the effec-

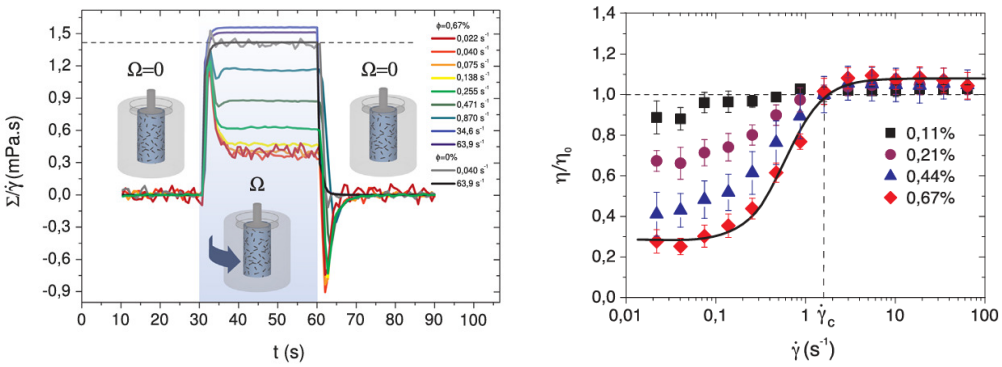

Figure 1.11: (Left) Shear stress response of an *E.coli* suspension placed in a Taylor Couette device. Variation of effective viscosity (defined as the ratio of hydrodynamic stress to shear rate) at various shear rates shows a significant reduction of effective viscosity of the suspension at low shear rates. (Right) Variation of effective viscosity as a function of shear rate for various suspension densities. Increasing bacterial density results in a reduction of the low-shear plateau region. Images reused from ref. [14].

tive viscosity of *E.coli* suspension. Similar to the results of Gachelin et al. [12], they reported effective viscosity reduction at low shear rates followed by an increase in effective viscosity, which flattens for higher shear rates as shown in Fig. 1.11. Interestingly, they demonstrated that the value of the plateau depends on the concentration of the bacterial suspension, which tends to be zero as the concentration increases. In other words, they showed a potential superfluid-like behaviour at high bacterial concentrations, suggesting that the external stress balances the active stress at high bacterial concentrations. Extending this work, Chui and co-workers [134] studied the effect of the viscosity of suspending fluid on the reduction of the effective viscosity of the suspension. Swimming dynamics of an isolated bacterium change in more viscous environments [135, 136], which is expected to alter the viscosity reduction of the suspension. This study showed that the transition to the superfluid state occurs when the rotational diffusion and shear rate are of similar strength, that is, when $Pe \sim O(1)$.

Rafai et al. [90] explored the rheology of suspension of puller swimmers (*Chlamydomonas reinhardtii*) for bacterial concentrations ranging from 0-25% using a Taylor–Couette rheometer. In contrast to previous findings, they reported an increase in effective viscosity for this bacterial suspension. Similar findings were reported by Mussler and co-workers [137], who used both a Taylor Couette device and a cone plate device to measure the effective viscosity of the suspension. Furthermore, they compared the effective viscosity of dead cells with live cells and showed that the increase in effective viscosity is larger for living cells. They showed that the rheology of dead cell suspension followed the Einstien equation (Eq. (1.1)). This shows that dead cells behave as passive particles, and the increase in effective viscosity is related to the swimmers' swimming mechanism. The experimental results seem to suggest that pusher swimmers (such as *E.coli*) reduces the effective viscosity [14] while puller swimmers (such as *algae*) increase suspensions' viscosity [90, 137]. To understand this behaviour we discuss this and the mathematical models used to describe the rheological behaviour of bacterial suspension discussed in the next subsection.

1.3.2 Physical mechanism and mathematical model

From the experimental results discussed in the previous section, it is clear that the rheological behaviour of a bacterial suspension depends on the swimming mechanism adopted by the swimmer and its shape. A suspension of a pusher-type swimmer is seen to show viscosity reduction in contrast to increasing effective viscosity for a suspension of a puller-type swimmer. The physical mechanism for this viscosity reduction can be understood by i) noting that most bacteria are usually elongated in shape and ii) microswimmers exert active stress on the suspending fluid, which results in an in-

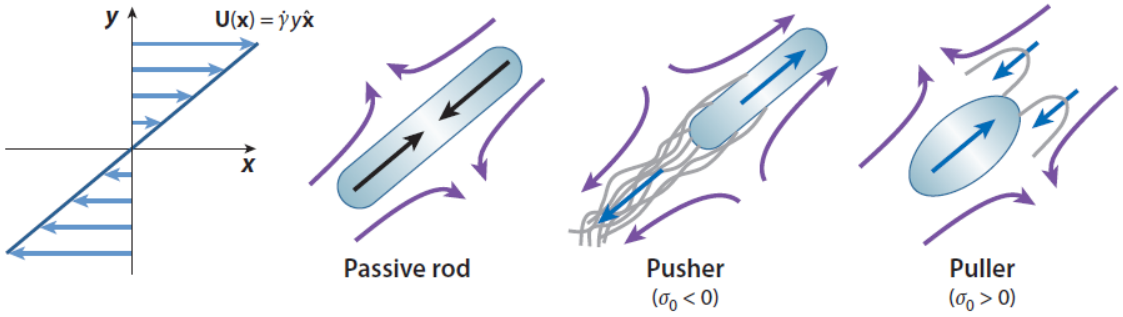

Figure 1.12: Schematic illustrating the basic mechanism for effective viscosity modification for passive rods and pusher and puller swimmers in a simple shear flow. The purple arrows illustrate the induced flow corresponding to each particle, which is responsible for modifying the suspension's effective viscosity. The elongated particles are aligned along the direction of shear flow. Image adapted from ref. [15]

duced flow which can modify the effective viscosity of the suspension [138]. Owing to its elongated shape, the orientation dynamics of an isolated microswimmer follow Jeffrey's orbit [139] in simple shear flows. As a result, the microswimmer spends more time oriented along the flow direction and consequently has an average orientation along this direction. With this average orientation, the force dipole corresponding to a pusher (puller) swimmer acts to reduce (enhance) the perturbed flow for a passive particle, as shown in Fig. 1.12. Consequently, the effective viscosity for a pusher (such as *E.coli*) suspension is expected to be lower than the suspending fluid if the active stress exerted by the particle dominates the passive stress due to rigidity. Meanwhile, for a puller suspension, the effective viscosity will always be greater than that of the suspended fluid.

To obtain quantitative results, Saintillan [140, 141] proposed a kinetic model which extends the classical theory for rodlike particles to include the additional active stress for microswimmer suspensions. Inter-particle interactions are neglected for a dilute suspension; thus, the suspension configuration is determined by just orientation distribution $\Psi(\boldsymbol{p})$ where Ψ is the probability of finding the particle oriented along director $\boldsymbol{p}$. Then, using the orientation distribution of the particle, orientation average active stress is evaluated as

$$\langle \boldsymbol{S}_{i,j} \rangle = \int_{\boldsymbol{p}} \boldsymbol{S}_{i,j} \Psi d\boldsymbol{p} \tag{1.2}$$

where $\boldsymbol{S}_{i,j}$ is the force dipole stress the microswimmer exerts as it self-propels. Similarly, average flow-induced and Brownian stress can be obtained following the works of Batchelor [142]. Including these stresses, the effective viscosity can be evaluated as [140, 141]

$$\mu_r = \frac{\mu}{\mu_0} = \frac{\sigma_{xy} + \Sigma_{xy}}{\mu_0 \dot{\gamma}} = 1 + \frac{\pi n l^3}{6\ln(2a_r)} \langle p_x^2 p_y^2 \rangle + \frac{3nk_BT + n\sigma_0}{\mu_0 \dot{\gamma}} \langle p_x p_y \rangle \tag{1.3}$$

where $\boldsymbol{\sigma}$ denotes the hydrodynamic stress tensor, $\boldsymbol{\Sigma}$ is the net stress tensor composed of active, flow-induced and Brownian components, a_r is the aspect ratio of the swimmer, n is the number density of the swimmer, l is the characteristic lengthscale of the suspension, k_B is Boltzmann's constant, T is the temperature σ_0 is the magnitude of the active stress, $\dot{\gamma}$ is the shear rate and μ_0 is the viscosity of the suspending fluid. This expression can be simplified for non-tumbling particles in the limit of weak shear rate as [140]

$$\mu_r^0 = \lim_{\dot{\gamma} \to 0} \mu_r = 1 + \frac{\pi n l^3}{30\ln(2a_r)} \left[\left(\beta + \frac{1}{3} \right) + \beta \frac{\sigma_0}{k_B T} \right] \tag{1.4}$$

where β is the Bretherton's constant. The first term on the above equation's right-hand side represents the effective viscosity's Newtonian component. In contrast, the second term reflects the

modification due to additional stresses. The two terms inside the square brackets are the passive and active contribution of the swimmer to the effective rheology. Notice that for pusher swimmers $\sigma_0 < 0$ and therefore, the modification to the Newtonian viscosity can be negative for $|\sigma_0| > k_b T(1 + 1/(3\beta))$. In contrast, a puller microswimmer increases the effective viscosity. While this captures the rheological behaviour at low shear rates, at higher shear rates, the orientation distribution must be solved numerically [141, 143]. As the shear rate increases, both $\langle p_x^2 p_y^2 \rangle$ and $\langle p_x p_y \rangle$ decreases as the orientation distribution peaks along the flow direction. As a result, the modification to the effective viscosity reduces with increasing shear rate which explains the shear thinning behaviour reported for a suspension of puller swimmers.

The limitation of kinetic modelling is that it works well only for dilute suspensions as the direct inter-particle interactions are neglected. The inter-particle interactions become important for dense suspension and therefore other modelling techniques must be applied. Ishikawa and Pedley [144] provided one of the earlier studies on dense bottom heavy microswimmer suspension using *Stokesian* dynamics. The non-bottom heavy swimmers merely tumble in the presence of shear flow resulting in a net-zero average active stress, and therefore bottom-heavy condition is necessary to introduce the orientation bias and consequently non-zero active stress. They modelled the self-propulsion of the microswimmer using a *squirmer* model and showed the decrease (increase) in apparent viscosity for pusher (puller) suspension when the gravity acts in the $-\boldsymbol{x}$ direction while the shear flow is applied in the $\boldsymbol{x} - \boldsymbol{y}$ plane. Interestingly, they showed that changing the direction of gravity from $-\boldsymbol{x}$ to $-\boldsymbol{y}$ results in opposite effect as changing the direction of gravity induces opposite stresses [144]. In a concentrated regime of planar monolayered swimmers, the effective viscosity increases more rapidly (upon increasing suspension density) compared to the inert spheres [145]. In contrast, for bottom-heavy pusher swimmers the effective viscosity can have negative values in certain conditions. This is due to aligned structure of the microswimmer suspension which helps the background shear flow.

This model predicts that microswimmers must be elongated to have any effect on the suspension's effective viscosity. This suggests that a suspension of spherical phoretic particles will show Newtonian behaviour as they tumble, leading to an average of zero active stress. However, in the presence of boundaries, phoretic particles are aligned along the boundary due to impenetrable boundaries, which in the presence of shear results in particles facing upstream [25]. In such cases, the phoretic particles may influence the effective viscosity of the suspension. However, in such cases, the distribution is more complicated and depends on spatial coordinates, making it difficult to obtain analytical results similar to Eq. (1.4). Consequently, numericla methods must be applied in order to obtain solution of the probability density function Ψ. In such cases, effective viscosity must be defined depending on the system. For instance, Traverso and Michelin [25] used a Poiseullie law to obtain an effective viscosity of the suspension. Using a kinetic model, they reported a significant reduction in the effective viscosity of a suspension of phoretic particles. In this case, they showed that the rheological behaviour directly depends on the self-organisation of the suspension driven by autochemotaxis.

1.4 Conclusion and structure of thesis

In this work, we focus on understanding self-organisation of a suspension of artificial phoretic microswimmers. This system falls under the category of wet active matter, where hydrodynamic interactions play a crucial role in self-organisation. With the help of various examples, we showed how the self-organisation of microswimmer suspension is affected by external cues such as strength of confinement, background flow and external gradients. For instance, confining a bacterial suspension results in transitioning from a complex turbulent-likes state to a 1D state. This suggests that the self-organisation of a microswimmer suspensions can be manipulated using external forcings.

As discussed using various examples in Sec. 1.3, the rheological properties of a microswimmer suspension shows non-Newtonian behaviour due to the active stresses that a microswimmer exerts on the fluid. The swimming mechanism decides the nature of stress (extensile/contractile) exerted

by an individual swimmer, whereas the distribution of active stress exerted to the surrounding fluid critically depends on the particle distribution. This suggests that the distribution of active stress and consequently the rheological properties of the fluid can be manipulated by controlling the self-organisation of the suspension.

Motivated by the link between the self-organisation and the rheology of the suspension, the central aim of this thesis is to first understand how does a suspension of phoretic particles self-organise under the influence of confinement and background shear. Then, based on the physical insights the next step is to propose control strategies to manipulate the rheological properties of the suspension by controlling the particle distribution. Keeping in mind these objectives, using a kinetic model, we study the collective response of a phoretic suspension confined between two flat wall boundaries. The wall boundaries move in the opposite direction to sustain a simple shear flow in the absence of particles. We study the collective response of the phoretic particles based on two control parameters namely i) strength of confinement and ii) shear rate. To understand the link between the rheological properties and suspensions' self-organisation, we analyze the induced flow structures and the effective viscosity of the suspension. We show that under strongly confined conditions, the modification to the effective viscosity is negligible due to its self-organisation behaviour. Here we identify that self-organisation must be manipulated to modify the effective viscosity of the suspension and propose a simple wall activity (consumption/production of solute) based strategy to manipulate suspensions' self-organisation and consequently its rheology. Using this strategy, we show that the suspension' effective viscosity can decrease even under strongly confined conditions, however the effect of confinement eventually dominates as confinement strength increases.

The structure of this manuscript is as follows: chapter 2 aims to introduce the reader to the modelling techniques adopted for describing the dynamics of a microswimmer suspension. This chapter introduces fluid dynamics fundamentals in the viscous-dominated regime observed for microswimmer suspension in Sec. 2.1. This is followed by a discussion on modelling self-propulsion for biological and artificial microswimmers in Sec. 2.2.1 and Sec. 2.2.3. A transition from modelling single swimmers to modelling suspension of swimmers is explored in the following section (Sec. 2.3), where we shed light on the fundamentals of kinetic theory for describing the collective dynamics of microswimmers. Finally, this chapter ends with a comprehensive review of kinetic theory-based models for describing microswimmer suspension in Sec. 2.4.

In chapter 3, using a kinetic model, we study the effect of dual forcings of strength of confinement and shear rate on the self-organisation of microswimmer suspensions. We begin this chapter by describing the physical model and summarizing the governing equations, characteristic scalings in Sec. 3.2. This is followed by a detailed discussion on the pseudo spectral method that we employ for solving the coupled partial differential equations in Sec. 3.3. Using Fourier transform, we convert the partial differential equations in physical space to a set of 1D Helmholtz equations and solve it in spectral space and we adopt a modified Cranck-Nicholson scheme for marching in time. Next, we analyse the self-organisation behaviour of the suspension, where three different long-term regimes are identified based on the two control parameters of the problem in Sec. 3.4.3. We show that the self-organisation behaviour can be captured by a reduced model based on the moment equations. This is followed by an overview of the resulting effective viscosity of the suspension, focusing specifically on the different flow patterns induced by the particle distribution and forcing in the different dynamical regimes previously discussed in Sec. 3.5. Finally, we analyse the suspension rheology, which discusses the different induced flows observed in different regimes.

Chapter 4 focuses on developing control strategies for the phoretic suspensions using external chemical based forcings. We identify the lack of viscosity modification under strongly confined conditions due to suspensions' self-organisation behaviour. To reduce viscosity under strongly confined state, we propose exploiting wall activity to trigger the chemotactic instability and explore the case of uniform activity in Sec. 4.3. We show that a uniform wall activity distribution cannot perturb the horizontal chemical gradient and, therefore, cannot trigger the chemotactic instability, which shows a non-uniform activity is required to trigger the instability. Subsequently, in Sec. 4.4, we explore a step like activity distribution and show that this activity distribution triggers instability, which leads to aggregates on each wall. The aggregates induce vortical flows, which resulted in reducing the

effective viscosity of the suspension even for stronger confinements. However, this scheme fails at moderate strength of background shear due to higher solute advection, preventing chemotactic instability from growing throughout the domain. We follow this by proposing a more robust strategy for higher viscosity reduction in Sec. 4.5. We show that this strategy is robust with respect to various parameters such as shear rate, strength of wall activity and wall activity distribution etc. Following this improved strategy, we show that the region of viscosity reduction on a phase diagram between shear rate and strength of confinement can be extended to higher confinement region.

Finally, in chapter 5 we conclude with summarising the major results presented in this thesis. This is followed by a discussion on future perspectives, where we explore potential future research problems in Sec. 5.2 based on the physical insights drawn from the thesis.

Chapter 2

Modeling dynamics of microswimmers and active suspensions

Contents

2.1 Fundamentals of Microhydrodynamics 36
2.1.1 Stokes Flow and its properties 36
2.1.2 Fundamental solutions of Stokes flow 38
2.2 Modeling Biological and artificial self-propulsion 39
2.2.1 Mathematical modelling for biological locomotion 39
2.2.2 Externally driven phoretic motion 41
2.2.3 Self-propulsion via- self-diffusiophoresis 43
2.2.4 Chemotaxis of phoretic swimmers 45
2.3 Fundamentals of Kinetic Modelling 46
2.3.1 Continuous description of a suspension 46
2.3.2 Deriving the Focker-Planck equation 47
2.3.3 Reduced distribution and correlation functions 49
2.4 Kinetic modelling of microswimmer suspensions: A review 51
2.4.1 Hydrodynamic instability 51
2.4.2 Chemotactic Instability 53
2.5 Conclusion 57

Overview

This chapter will familiarize readers with the modelling techniques employed to model wet active systems. As mentioned in the previous chapter, this thesis focuses on "wet" active matter; therefore, understanding the basic principles of fluid flow at small scales is paramount. Therefore, the first section of the chapter (Sec. 2.1) discusses the fundamentals of microhydrodynamics. With the help of scaling arguments, the general Navier-Stokes equation is simplified to the Stokes equation, followed by a discussion on fundamental flow singularities in this limit. The following section (Sec. 2.2) is dedicated to modelling the motion of tiny particles (typically smaller than $\sim 10^{-3}$m) in a fluid using the singularities discussed in the previous section. This section begins by discussing the swimming dynamics of biological swimmers and then explores the mathematical modelling techniques employed to describe their motion. Gaining insights from the mathematical model, the next two subsections (Sec. 2.2.3 and Sec. 2.2.4) focus on self-propulsion strategies for artificial particles using a phoretic mechanism. Moving towards modelling collective dynamics, the next section (Sec. 2.3) introduces the readers to the fundamentals of kinetic modelling. Finally, this is followed by a comprehensive literature review of studies which employ kinetic modelling techniques for active suspensions.

2.1 Fundamentals of Microhydrodynamics

2.1.1 Stokes Flow and its properties

The fluid flow dynamics are mathematically modelled using continuous fields of velocity and stresses. This *continuum* approximation is typically employed when the lengthscales in the system are much larger than the molecular lengthscales such that the fluctuations at the molecular level can be averaged to describe an average flow of quantities [128]. The governing equations are obtained by using the conservation principles applied to the mass and momentum of a fluid with density $\hat{\rho}$ and dynamic viscosity $\hat{\mu}$ (here hat symbol $\hat{(.)}$ denotes dimensional quantities) [128, 139]. As a result, we obtain

$$\frac{\partial \hat{\rho}}{\partial \hat{t}} + \hat{\nabla} \cdot (\hat{\rho}\hat{\mathbf{u}}) = 0. \tag{2.1}$$

and,

$$\hat{\rho}\left(\frac{\partial \hat{\boldsymbol{u}}}{\partial \hat{t}} + \boldsymbol{u} \cdot \hat{\nabla}\hat{\boldsymbol{u}}\right) = \hat{\nabla} \cdot \hat{\boldsymbol{\sigma}} + \hat{\boldsymbol{f}} \tag{2.2}$$

where $\hat{\mathbf{u}}$ is the velocity field, $\hat{\boldsymbol{\sigma}}$ is the Cauchy stress tensor and $\hat{\mathbf{f}}$ is the external force is applied in the fluid domain. The Cauchy stress tensor must be related with fluid properties to close the system of equations (2.1-2.2). For a *Newtonian fluid*, the stress tensor is linearly related to the rate of strain tensor [128] as

$$\hat{\boldsymbol{\sigma}} = -\hat{p}\mathbf{I} + 2\hat{\mu}\hat{\boldsymbol{E}} \tag{2.3}$$

where $\hat{p}$ is the pressure, $\hat{\mu}$ is the dynamic viscosity of the fluid, $\boldsymbol{I}$ is the identity tensor and $\hat{\boldsymbol{E}}$ is the rate of strain tensors defined as,

$$\hat{\boldsymbol{E}} = \frac{1}{2}\left(\hat{\nabla}\hat{\boldsymbol{u}} + (\hat{\nabla}\hat{\boldsymbol{u}})^T\right). \tag{2.4}$$

For an incompressible and homogeneous fluid, spatial and temporal density changes can be neglected simplifying Eq. 2.1 to

$$\hat{\nabla} \cdot \hat{\boldsymbol{u}} = 0 \tag{2.5}$$

whereas, substituting $\hat{\boldsymbol{\sigma}}$ from Eq. (2.3) to Eq. (2.2) we obtain the *Navier Stokes* Equations given by

$$\hat{\rho}\left(\frac{\partial \hat{\boldsymbol{u}}}{\partial \hat{t}} + \hat{\boldsymbol{u}} \cdot \hat{\nabla}\hat{\boldsymbol{u}}\right) = -\hat{\nabla}\hat{p} + \mu\hat{\nabla}^2\hat{\boldsymbol{u}} + \hat{\boldsymbol{f}}. \tag{2.6}$$

Eq. (2.5) and Eq. (2.6) govern the fluid transport for incompressible Newtonian fluids at all scales.

Identifying the relevant characteristic scales can help obtain important physical insights from Eq. (2.6) without solving the equations. If the characteristic length, time and velocity scales are $\hat{l}_0, \hat{t}_0, \hat{u}_0$ respectively, Eq. (2.6) can be written in a dimensionless form as

$$Re\left(St\frac{\partial \boldsymbol{u}}{\partial t} + \boldsymbol{u} \cdot \nabla\boldsymbol{u}\right) = -\nabla p + \nabla^2\boldsymbol{u} + \boldsymbol{f} \tag{2.7}$$

where, $\boldsymbol{u} = \hat{\boldsymbol{u}}/\hat{u}_0$, $\boldsymbol{f} = \hat{\boldsymbol{f}}/(\hat{\mu}\hat{u}_0/\hat{l}_0^2)$ and $p = \hat{p}/(\hat{\mu}\hat{u}_0/\hat{l}_0)$ are the dimensionless variables. Rendering the Navier-Stokes equation dimensionless. As a result the dynamics is completely described by two dimensionless numbers

$$\begin{aligned} Re &\sim \frac{|\hat{\boldsymbol{u}} \cdot \hat{\nabla}\hat{\boldsymbol{u}}|}{|\hat{\mu}\hat{\nabla}^2\hat{\boldsymbol{u}}|} = \frac{\hat{\rho}\hat{u}_0\hat{l}_0}{\hat{\mu}} = \frac{\text{Inertial Forces}}{\text{Viscous Forces}} \\ St &= \frac{\hat{t}_0}{\hat{l}_0/\hat{u}_0} = \frac{\text{Intrinsic timescale}}{\text{Advective timescale}}. \end{aligned} \tag{2.8}$$

The *Reynolds* number (Re) is the ratio of inertial to viscous forces, quantifying the relative strength of inertial effects to viscous effects. Whereas the *Strouhal* number (St) is the ratio of the intrinsic

timescale to the advective timescale and signifies the strength of local acceleration. If there are no other characteristic scales present in the system, these two dimensionless numbers completely describe the dynamics. Without an inherent timescale, St becomes one, which means that we chose an advective timescale as the characteristic timescale.

Notice that as the lengthscale of the system is reduced (while keeping all other parameters fixed), viscous forces play more important roles than inertial forces. For instance, the Reynolds number for swimming of a microorganism ($\hat{l}_0 \sim 10^{-5}$m) in water is about 10^{-4}, which suggests that viscous forces dominate in the swimming of a microorganism. In contrast, the Reynolds number associated with the swimming of a goldfish ($\hat{l}_0 \sim 0.1$ m) is about 10^4 and thus, inertial effects dominate its swimming. As a result, the Navier-Stokes equation can be simplified based on the specific system. For instance, for $Re \gg 1$, the inertial terms dominate, and the viscous term can be neglected. This approximation is often made for high Reynolds number dynamics and is known as the *inviscid* fluid approximation [128]. In this thesis, we focus on the other limit $Re \ll 1$ and thus neglect the inertial terms. As a result, we obtain

$$\nabla^2 \boldsymbol{u} - \nabla p + \boldsymbol{f} = 0. \tag{2.9}$$

This equation is called the *Stokes* Equation. It is important to note that by neglecting the inertial terms in Eq. (2.6), we also eliminated the non-linear terms. As a result, Eq. (2.9) is a linear partial differential equation. Consequently, some essential properties of Stokes flow are [132]

- Linearity: As the system of equations is linear, the general solution to the Stokes equations can be built with the help of linear superposition. Furthermore, a change in driving force by a factor k reflects linearly in the solution without changing the streamlines or the flow pattern. A mathematical consequence of the linearity is that the principle of superposition can be utilized to build the general solution to the Stokes equations that satisfy the same boundary conditions.

- Instantaneity: The consequence of neglecting the local acceleration term means that the motion in Stokes limit is quasi-static. In other words, the fluid flow has no dependence on the driving force's history, and the only required information to obtain flow field at a given instant is about the instantaneous driving force. Consequently, the changes in driving force are "communicated" in the entire field instantaneously.

- Reversibility: Another consequence of linearity is that if the driving force is precisely reversed from $\boldsymbol{f}$ to $-\boldsymbol{f}$, the solution also changes exactly from $\boldsymbol{u}$ to $-\boldsymbol{u}$ and as a result, the changes due to driving force $\boldsymbol{f}$ can be exactly reversed. This is illustrated beautifully in an experiment initially by G.I. Taylor in 1966, which can be found in ref. [146]. This is critical when choosing the swimming technique in a viscous-dominated regime, as discussed later in Sec.2.2.1.

Another consequence of the linearity is that the Lorentz *reciprocal* theorem [147] can be exploited to obtain integral quantities (such as net force, torque, etc.) without fully solving the Stokes equations. These quantities are evaluated by considering an auxiliary simpler problem with identical geometry whose solution is already known ($\boldsymbol{u}^*$), then we can show that

$$\int_S \boldsymbol{n} \cdot \boldsymbol{\sigma} \cdot \boldsymbol{u}^* = \int_S \boldsymbol{n} \cdot \boldsymbol{\sigma}^* \cdot \boldsymbol{u} \tag{2.10}$$

where $\boldsymbol{n}$ is a unit surface normal directed into the fluid. This is particularly helpful for swimming problems where the quantity of interest is usually the swimming velocity of a microswimmer for a given distribution of slip velocities at the surface [147]. For swimming problems, the swimming velocity of the swimmer is evaluated by considering a parallel problem where the particle with same geometry as the swimmer is considered to translate with the same velocity ($\boldsymbol{U}_0$) driven by a body force $\boldsymbol{F}^*$. Consequently, Eq. (2.10) simplifies to

$$\boldsymbol{F}^* \cdot \boldsymbol{U}_0 = -\int_S \boldsymbol{n} \cdot \boldsymbol{\sigma}^* \cdot \boldsymbol{u}_s \tag{2.11}$$

The next subsection explores the solution $\boldsymbol{u}_k$ for some simple cases.

2.1.2 Fundamental solutions of Stokes flow

To build the solution of Stokes equations Eq. (2.9), we first notice that taking the divergence of Eq. (2.9) and using the continuity equation (2.5) we obtain

$$\nabla^2 p = 0. \tag{2.12}$$

This implies that both the pressure and velocity fields consists of harmonic functions satisfying Laplace's equation. The general solutions to these Laplace equations are constructed using superimposing the linearly independent vector harmonic functions to obtain a general solution of Stokes equations [128] . This representation of the solution as a linear superposition of decaying and growing harmonics is known as the Lamb's solution [139].

Furthermore, the solution can also be constructed using Green's function due to the linearity of the Stokes equations. The general solution for driving force $\boldsymbol{f}(\boldsymbol{r})$ can be constructed using the Oseen tensor $\boldsymbol{T}$ and pressure vector $\boldsymbol{v}$ as,

$$\boldsymbol{u}(r) = \int \boldsymbol{T}(\boldsymbol{r}-\boldsymbol{r'}) \cdot \boldsymbol{f}(\boldsymbol{r'}) dV \tag{2.13}$$

$$p(r) = \int \boldsymbol{v}(\boldsymbol{r}-\boldsymbol{r'}) \cdot \boldsymbol{f}(\boldsymbol{r'}) dV \tag{2.14}$$

where

$$\boldsymbol{T}(\boldsymbol{r}) = \frac{1}{8\pi}\left(\frac{\boldsymbol{I}}{r} + \frac{\boldsymbol{rr}}{r^3}\right) \tag{2.15}$$

$$\boldsymbol{v}(\boldsymbol{r}) = \frac{1}{4\pi}\frac{\boldsymbol{r}}{r^3}. \tag{2.16}$$

The simplest case is of the force monopole, where the driving force is $\boldsymbol{f} = f_0 \boldsymbol{e_p} \delta(\boldsymbol{r}-\boldsymbol{r'})$ is located at point $\boldsymbol{r'}$ and directed along $\boldsymbol{e_p}$. This solution is evaluated using Eq. (2.13) as

$$\boldsymbol{u}_{pf}(\boldsymbol{r_0}) = \frac{f_0}{8\pi r_0}\left(\boldsymbol{I} + \frac{\boldsymbol{r_0 r_0}}{r_0^2}\right) \cdot \boldsymbol{p} \tag{2.17}$$

where $\boldsymbol{r_0} = \boldsymbol{r} - \boldsymbol{r'}$ and $r_0 = |\boldsymbol{r} - \boldsymbol{r'}|$. This solution is called the *Stokeslet* [148] and corresponds to the far-field solution of a particle moving due to external force, for example, sedimentation of a sphere in a viscous fluid. The solution decays as (1/r) and corresponds to the monopole contribution.

As the governing equation is a set of Laplace equations, a gradient of any solution also forms a solution, as a result the next fundamental solution is obtained by taking the gradient of Eq. (2.17). Physically, this corresponds to a pair of opposite point force driving the flow. Subsequently, the general force dipole can further be decomposed into symmetric and antisymmetric parts. Physically, these components induce strain (symmetric) and rotation (antisymmetric) effects on the particle. The corresponding flow fields are evaluated as

$$\boldsymbol{u}_{fd}(\boldsymbol{r_0}) = \frac{f_d}{8\pi r_0^2}\left(\frac{-\boldsymbol{r_0 I}}{r_0} + \frac{3\boldsymbol{r_0 r_0 r_0}}{r_0^3}\right) : \left(\boldsymbol{pp} - \frac{\boldsymbol{I}}{3}\right) \tag{2.18}$$

and

$$\boldsymbol{u}_{rot}(\boldsymbol{r_0}) = -\frac{T_e \times \boldsymbol{r_0}}{8\pi r_0^3}. \tag{2.19}$$

Here, f_d and T_e are the strengths of symmetric part of the force dipole and torque on the particle given. These solutions are known as *Stresslet* and *Rotlet*, where the induced flow decays slowly (r^{-2}) compared to the stokeslet. This solution is of particular importance for microswimmers as far field signature of a microswimmer has been experimentally observed to be a stresslet [18] as discussed in Sec. 2.2.1.

Linearity of Eq. (3.19) allows us to construct a general solution made up of superposition of force monopole, force dipole, force quadrupole (source dipole) and so on [132, 139]. For example,

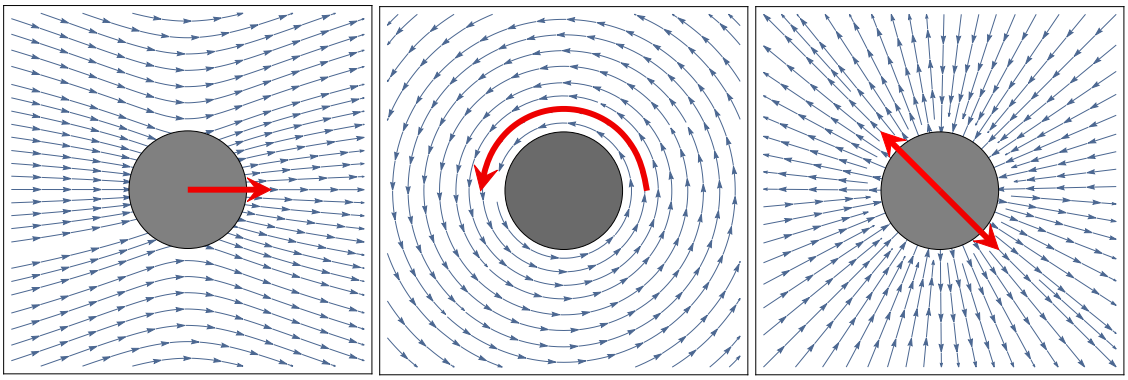

Figure 2.1: Fundamental singularities of the Stokes flow. (Left) Stokeslet : Flow field around a spherical particle settling under external force. (Center) Rotlet : Flow field around a particle rotating with an angular velocity. (Right) Stresslet: Flow field around a particle under extensional flow.

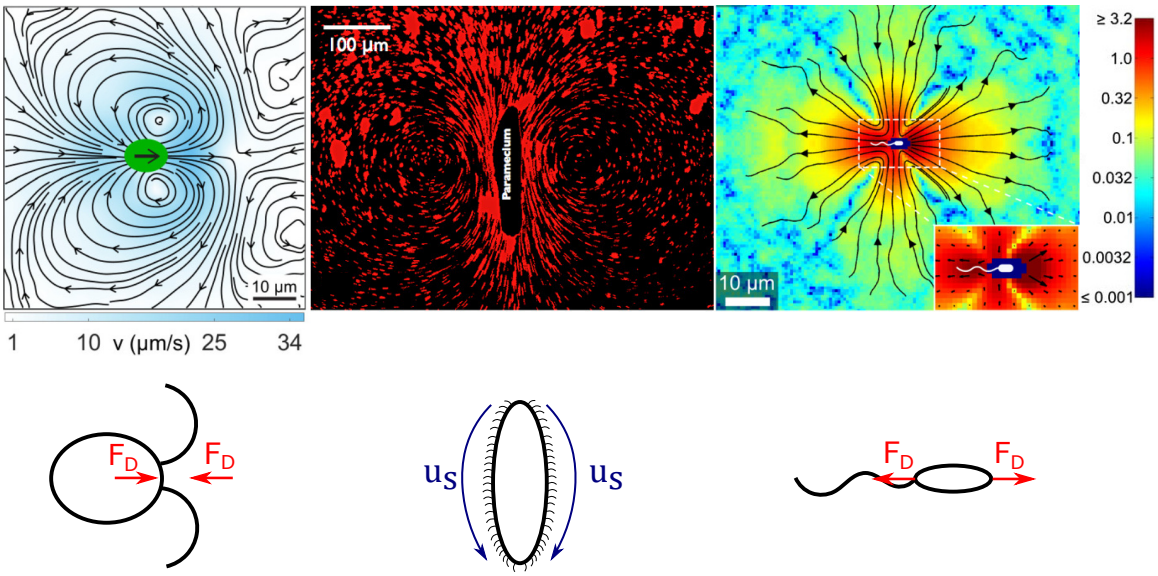

Figure 2.2: (Top panel) Experimental flow field of swimming (Left) *Chlamydomonas*(image adapted from Ref. [16]) (center) *Paramecium* [image adapted from Ref. [17]] and *E.coli* (image adapted from ref. [18]) [Drescher et.al 2010]. (Bottom panel) Schematic of the mathematical model of the corresponding swimmer.

the exact flow field around a sedimenting sphere is composed of two terms, i) the monopole that we discussed earlier and ii) a source dipole which appears due to the no slip condition on the particle surface. However, the source dipole term $(1/r^3)$ decays much quicker than the monopole term $(1/r)$. As a result, the settling particles interact through this slowly decaying monopole disturbance. In a general multipole expansion, the velocity field decays more rapidly for each higher pole compared to the previous pole. For instance, for a force dipole, the velocity field decays as $1/r^2$, which is one order quicker than a force dipole. Similarly, the velocity field for a force quadrupole decays as $1/r^3$ and so on.

2.2 Modeling Biological and artificial self-propulsion

2.2.1 Mathematical modelling for biological locomotion

Swimming at a small scale requires different strategies than swimming at a larger scale due to change in hydrodynamics. For example, consider the swimming strategy adopted by a scallop (typical size $\sim 10^{-2} - 10^{-1}$ m). A scallop closes its shell quickly to propel forward and then opens

it slowly to return to its initial configuration. It repeats this cycle to self-propel in water. However, this simple strategy fails at small scales due to the linearity and reversibility property of Stokes flows. The distance a microswimmer covers in the first half (closing the shell) cancels out exactly during the second half of the cycle (opening the shell) due to the reversibility property discussed in the previous section. This example, known as the scallop theorem, was discussed by Purcell in his famous article in 1977 [50]. This example also demonstrates that some simple successful strategies on large scales do not work on small scales. Thus, new strategies must be designed to achieve self-propulsion at the microscale.

Breaking spatial/temporal symmetry is necessary to self-propel at small scales due to the linearity property of the Stokes flow [50, 149]. Natural microorganisms break this temporal symmetry by continuous distortions of single or multiple appendages called cilia/flagella [150]. For some natural microswimmers such as *E.coli*, the appendages may be stiff helix structures which rotate with the help of embedded motors inside the cell [151]. In contrast, the flagella may also move like a whip to generate the propulsion force, as in the case of *spermatozoa* of different species [152].

The drag on a slender body is anisotropic; that is, the drag depends on the orientation of the slender body. For instance, the drag on a rod moving parallel to its axis is almost half compared to its motion perpendicular to its axis [128]. Consequently, the motion of a rod in any direction other than parallel and perpendicular to its length results in a component of drag force perpendicular to its motion. Microorganisms exploit this anisotropic nature of the drag on their appendages to generate thrust force and this mechanism is known as drag-based thrust [52]. The net drag generated due to flagella rotation can thus be evaluated by considering sections of rods along the local tangential direction moving with a specific velocity such that the overall motion reflects the solid body helical motion [150, 153]. The hydrodynamic drag on the cell body balances the drag on the flagella such that the net force on the microorganism is still zero.

Due to Newton's third law, the hydrodynamic drag experienced by the microorganism's 'head' and 'tail' is applied back to the fluid. Therefore, the associated flow in the far field can be modelled by representing a force dipole (directed away from the swimmer) singularity in the fluid. This simple representation correctly captures the far field signature of a swimming *E.coli* as demonstrated by Drescher and co-workers [18] as shown in Fig.2.2 (right). This type of microswimmer is called a *pusher* type swimmer, which *push* the fluid from the front and back while drawing fluid from the sides as shown in Fig. 2.3 (top right). On the other hand, for a microswimmer such as *Chlamydomonas reinhardtii*, the appendages are located towards the front and move like a breaststroke. As a result, such swimmers draw fluid from the front and back while pushing it from the sides as shown in Fig. 2.3(top left). This is represented by a force dipole directed towards the swimmer, and such swimmers are called *puller* type swimmers. The flow field is shown in Fig. 2.2(left). The force dipole representation is sufficient to capture the hydrodynamic interactions between such swimmers for dilute suspensions where interactions occur over larger lengthscales [150].

Another category of self-propelling microorganisms is that of cilliated microorganism, such as a *paramecium*. For such microswimmers, smaller appendages called cilia are distributed over their outer surface which synchronously beat to create a flow close to the surface around the bacteria [154], as shown in Fig. 2.2. The cilium exerts a force on the fluid and exploits the reaction force by the fluid to self-propel. Neglecting the complex collective motion of the cilia, a reduced order model based on pre-defined slip velocity at the particle surface is often employed to capture their swimming hydrodynamics. Other models have also been implemented where a shear stress [155] or torque [156] is applied at a finite but small distance from the swimmer surface instead of a slip velocity at the surface. However, here, we focus on the slip-driven *squirmer* model, which was first introduced by Lighthill [157] to model the swimming dynamics of microorganisms.

The consequence of the complex dynamics of the cilia movement is modelled by considering a distribution of slip velocity at the surface of a spherical particle. To simplify the model, we consider an axisymmetric slip distribution and express the slip velocity in the associated Legendre Polynomial basis as [158]

$$\boldsymbol{u}_s = \sum_{n=0}^{n=\infty} B_n V_n(\cos\theta) \tag{2.20}$$

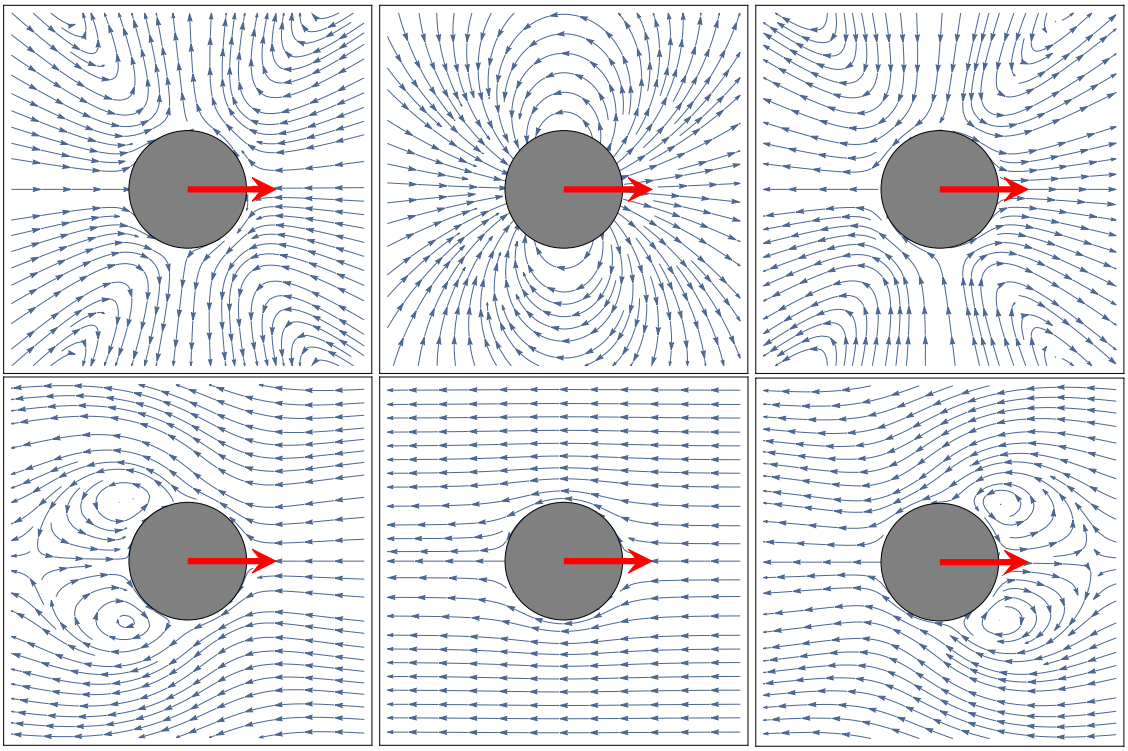

Figure 2.3: Flow field around a puller, neutral and pusher squirmer in (top panel) Lab frame and (bottom panel) Particle's frame.

where

$$V_n(\cos\theta) = \frac{-2}{n(n+1)} \frac{dP_n(\cos\theta)}{d\theta} \tag{2.21}$$

with $P_n(\cos\theta)$ being the n^{th} order Legendre polynomial. In response to this slip velocity at the particle surface, the particle may self-propel with a velocity U_0 along the axis of symmetry. Using the Lorentz reciprocal theorem, the swimming velocity is evaluated as $U_0 = 2B_1/3$. The far field signature of the squirmer is captured by taking into account the first two modes as they decay slower compared to higher order coefficients. Therefore, higher order coefficients are often neglected. Physically, the B_1 coefficient represents the strength of the source dipole decaying as r^{-3}, whereas the B_2 coefficient is related to the source dipole decaying as r^{-2}.

A squirmer parameter is defined as the ratio of the first two coefficients ($\beta = B_2/B_1$). The flow field distinctly differs for i) $\beta < 0$, ii) $\beta = 0$ and iii) $\beta > 0$ as shown in Fig. 2.3. This parameter reflects the force dipole's relative strength to the source dipole contribution. For $\beta < 0$, the slip distribution is dominant towards the rear end, and the flow field resembles the *pusher* swimmer as shown in Fig. 2.3. In contrast, for $\beta > 0$, the slip distribution dominates in the front, and the flow field resembles the *puller* swimmer as shown in Fig. 2.3. Finally, for $\beta = 0$, the force dipole component disappears, and the flow field is that of a source dipole, as shown in Fig. 2.3. Such a swimmer is called a *neutral* swimmer. Paramecium is an example of such a swimmer, and the associated flow field is shown in Fig. 2.2 (center). The squirmer model has been employed to understand hydrodynamic interactions between i) swimmers [159, 160], ii) walls [161, 162], iii) background flow [163, 164] and to study the collective behaviour of microorganisms [144, 165].

2.2.2 Externally driven phoretic motion

Synthetic particles can also move with the help of external driving force, the simplest example of this motion is the sedimentation of particles due to gravity. In sedimentation, the particle's motion is driven by external body force which acts at the center of mass and thus the flow field of a sedimenting particle corresponds to a *Stokeslet* in the far field as discussed in earlier subsection

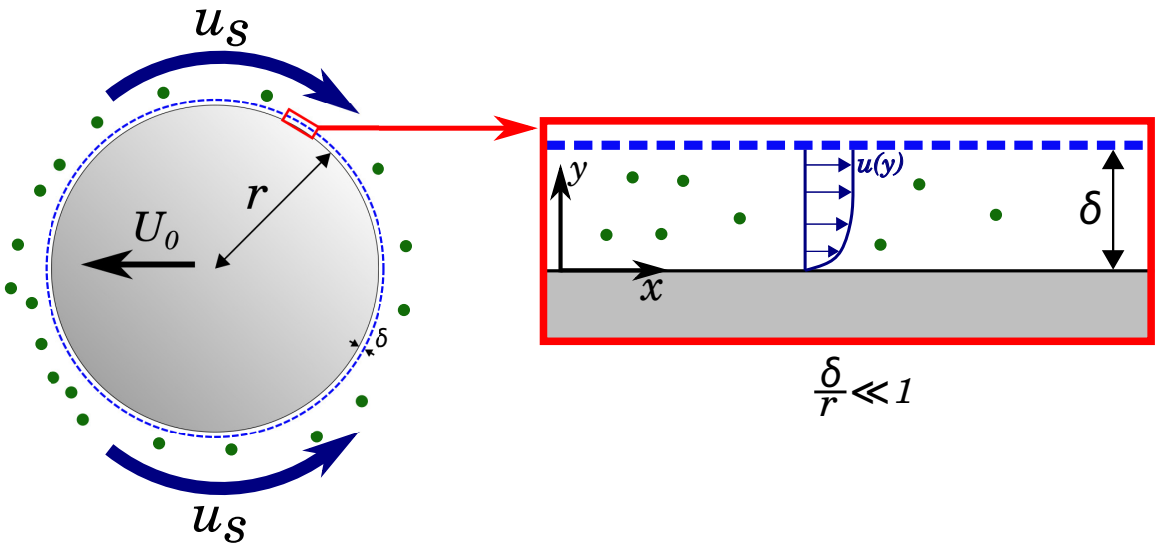

Figure 2.4: Schematic of Diffusiophoretic propulsion driven by external solute gradient. Solute interaction over a small thickness results in a flow close to the particle surface.

(Sec. 2.1.2).

In addition to a body force, a particle can also propel with the help of interfacial forces (which can be externally driven or self-driven) which give rise to fluid flow close to the particle surface. In practice, this is observed when a passive phoretic particle is placed in an external solute gradient, the particles moves up (down) the gradient depending on the interaction between the solute molecules and particle's surface [166, 167]. This migration of passive particles under external solute gradients is called as *diffusiophoresis*. There are other similar ways for a particle to propel using gradients of temperature [78] (*thermophoresis*), electric potential [168] (*electrophoresis*) etc.

We now discuss the model introduced by Anderson [169] to study this phoretic motion. Consider a particle of radius r placed in an external solute gradient as shown in Fig. 2.4. Generally, the solute particles can interact differently compared to the surrounding solvent (fluid) with the particle surface through various interactions such as van der Waals. The net effect of these interactions can be expressed as an interaction potential (Φ'). Consequently, the net force on a solute particle can be expressed as $-\nabla\Phi'$. With the solute concentration expressed as C', the solute, in turn, applies a volume force $-C'\nabla\Phi'$ on the fluid.

The interactions occur over a lengthscale δ with $\delta \ll r$, implying that the particle's surface can *locally* be approximated as a flat surface as illustrated in Fig. 2.4. Assuming thermal equilibrium inside the boundary layer results in obtaining the solute distribution as [169]

$$C' = C_\infty e^{-\Phi'/kT} \tag{2.22}$$

where C_∞ is the solute concentration at the particle scale, k is the boltzmann's constant and T is the temperature. The fluid flow (dimensional) inside the boundary layer is driven by the chemical potential, which results in a parallel flow given by

$$u = \left[\frac{-kT}{\mu}\int_0^y y'(e^{-\frac{\Phi(y')}{kT}} - 1)dy'\right]\frac{\partial C'}{\partial x} \tag{2.23}$$

where μ is the dynamic viscosity of the fluid. The term inside the square brackets on the right-hand side of Eq. (2.23) is defined as the difussiophoretic mobility of the particle, M. Note that M is defined based on local quantities and thus can vary along the surface. The diffusiophoretic mobility captures the interaction of the solute particles with the particle surface and can be either positive or negative. Consequently, the direction of the fluid flow inside the boundary layer depends on the mobility.

At the particle scale, the flow inside the boundary layer appears as a "slip" given by $u_s = M\nabla_{||}C'$, where $\nabla_{||}C'$ is the tangential solute gradient at the particle surface. As a result, the slip

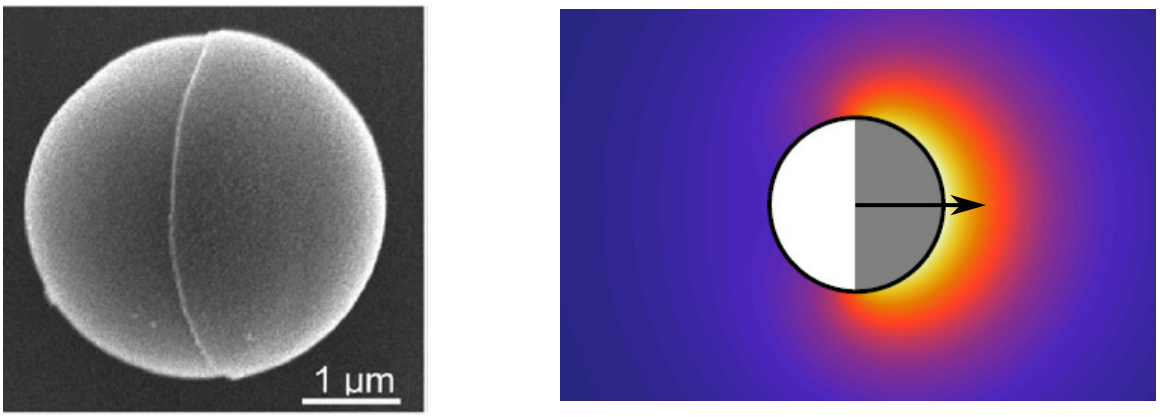

Figure 2.5: (Left) SEM image of a Silica-based Janus Particle adapted from ref. [19]. (Right) The solute field around the Janus particle, with a black arrow indicating self-propulsion direction. Image adapted from ref. [20]

velocity at any point can be evaluated using the solute distribution evaluated at the particle scale. For a spherical particle placed in a uniform external solute gradient, the solute distribution can be obtained by considering solute diffusion to be dominant and neglecting the solute advection due to particles' small size. Note that this formulation remains valid only when the particle size is also much smaller than the solute variation lengthscale. Under these conditions the solute distribution is governed by,

$$\nabla^2 C' = 0 \tag{2.24}$$

with the boundary conditions

$$\frac{dC'}{dr} = 0 \quad \text{at } r = 1 \tag{2.25}$$

$$C' \to G\boldsymbol{x} \quad \text{as } r \to \infty \tag{2.26}$$

The solution for Eq. (2.24)-(2.26) can be readily obtained using spherical harmonics as

$$C' = C_\infty + \frac{1}{2}\frac{G\boldsymbol{x}}{r^3} \tag{2.27}$$

The slip velocity can now be evaluated by Eq. (2.23) as $\boldsymbol{u}_s = -(3/2)M(\theta)|\nabla C_\infty| \sin\theta \boldsymbol{e}_\theta$, where $M(\theta)$ is the surface mobility of the particle and θ is the polar angle. For uniform surface mobility, the slip velocity simplifies to $\boldsymbol{u}_s = -(3/2)M|\nabla C_\infty| \sin\theta \boldsymbol{e}_\theta$. As a result, the swimming velocity is evaluated using the Lorentz reciprocal theorem [170] as

$$\boldsymbol{U}_0 = \frac{1}{4\pi}\int_S \boldsymbol{u}_s dS = M\nabla C_\infty \tag{2.28}$$

Comparing the slip velocity with the squirmer model, we find that the β parameter for this case is 0, which suggests that this particle motion is similar to a neutral squirmer with the velocity field of a source dipole decaying as $1/r^3$ instead of a stokeslet decaying as $1/r$ for a sedimenting particle. Consequently, the interaction between a phoretically propelling particle and a wall differs significantly from that between a sedimenting particle and a wall as observed experimentally in ref. [169, 171, 172].

2.2.3 Self-propulsion via- self-diffusiophoresis

In the previous subsection, we looked at how an apparent slip velocity at the particle surface can be realized using external gradients. We now explore the case when the solute gradient is self-generated due to non-uniform catalyst coverage. The presence of a catalyst results in consuming/producing solute species in the domain; this ability to consume/produce solute at the surface through a chemical reaction is called *surface activity*. Note that this is different from the general definition of

activity for *active matter*, which refers to mechanical actuation resulting in motion [27, 173]. This non-uniform surface activity generates a tangential solute gradient, which drives the "slip" at the particle surface, resulting in the particles' self-propulsion. In contrast to the squirmers, the apparent slip velocity for self-diffusiophoretic particles is not imposed; instead, it needs to be evaluated by solving the solute transport.

Here, we focus on the simplest case of a spherical particle with different surface activity in each hemisphere denoted as A_f and A_b for front and back face respectively. These types of colloidal particles are often termed as *Janus* particles owing to the two "faces" as shown in Fig. 2.5 (left). Generally, surface activity can lead to multiple solute species in the domain; however, we will simplify by assuming the transport of just a single species. Furthermore, we assume that the chemical reaction at the surface follows a zeroth order kinetics, i.e., a constant rate of production/consumption occurs at the surface. This type of chemical kinetics is physically realized when the chemical reaction follows Michaelis–Menten kinetics in the limit of high solute concentration [174]. Finally, owing to the small size of the colloidal particles, the associated *Peclet* number (relative strength of advection to diffusion of solute) defined as $U_0 a/D_c$ (a is the particles' size) is typically of the order $10^{-3} - 10^{-1}$ [8, 175]. As a result, the advective effect in the solute transport can be neglected. Various studies have relaxed these simplifications to explore their effect in refs. [20, 114, 176, 177].

With all the simplifications in place, following ref. [175], the solute transport is governed by,

$$\nabla^2 C = 0 \tag{2.29}$$

with the boundary condition obtained by balancing the flux at the particle surface due to a chemical reaction

$$-D_c \boldsymbol{n} \cdot \nabla C = A(\theta). \tag{2.30}$$

Here D_c is the solute diffusivity, θ is the polar angle and $A(\theta)$ surface activity. Following ref. [175], the solute field for a step activity is given by

$$C = C_\infty + \frac{a}{D_c} \sum_{l=0}^{\infty} \frac{A_l}{l+1} \left(\frac{a}{r}\right)^{l+1} P_l(\cos\theta) \tag{2.31}$$

where C_∞ is the uniform background solute concentration, $P_l(\cos\theta)$ is the Legendre Polynomials of order l and A_l are the corresponding coefficient of activity expanded in Legendre Polynomials ($A(\theta) = \Sigma_{l=0}^{\infty} A_l P_l(\cos\theta)$). For a step activity transitioning at the equatorial plane, the solute field is given by

$$C(r,\theta) = C_\infty + \left(\frac{2\pi a^2 A^+}{D_c}\right)\frac{1}{4\pi r} - \left(\frac{3\pi a^3 A^-}{2D_c}\right)\frac{\cos\theta}{4\pi r^2} + \frac{a}{D_c}\sum_{l=2}^{\infty}\frac{A_l}{l+1}\left(\frac{a}{r}\right)^{l+1} P_l(\cos\theta) \tag{2.32}$$

where $A^+ = A_f + A_b$ and $A^- = A_f - A_b$ are the two hemispheres' net surface activity and difference in activity with A_f, A_b being the activity of the front and back face respectively. Eq. (2.32) implies that in the far field, at leading order, this particle behaves as a source with the net production (consumption) rate proportional to net activity (A^+), while at next order, it behaves as a source dipole proportional A^-. The complete solute field is shown in Fig. 2.5 adapted from ref. [20].

Using, Eq.(2.32), the slip velocity is evaluated as

$$\boldsymbol{u}_s = \frac{M(\theta)}{D_c}\left(-\frac{3}{8}A^- + \sum_{l=2}^{\infty}\frac{A_l}{l+1}\frac{dP_l(\cos\theta)}{d\theta}\right)\boldsymbol{e}_\theta \tag{2.33}$$

Finally, the self-propulsion velocity is evaluated using the Lorentz reciprocal theorem as [175]

$$\boldsymbol{U}_0 = \frac{A^- M^+}{8D_c}\boldsymbol{p} \tag{2.34}$$

where $\boldsymbol{p}$ is the unit vector along the axis of symmetry, and M^+ is the net surface mobility. Eq. (2.34) implies i) symmetry breaking in surface activity($A^- \neq 0$) and ii) net non-zero mobility is essential for self-propulsion ($M^+ \neq 0$).

The axisymmetry results in no particle rotation. Whereas the induced stresslet can be evaluated with the help of Lorentz reciprocal theorem as [178]

$$\boldsymbol{\sigma}_s = \sigma_s\left(\boldsymbol{pp} - \frac{\boldsymbol{I}}{3}\right), \quad \text{where } \sigma_s = \frac{-10\pi\mu a^2 \kappa M^- A^-}{D_c} \tag{2.35}$$

where κ is a numerical constant expressed as

$$\kappa = \frac{3}{4}\sum_{l=1}^{\infty}\frac{2l+1}{l+1}\left(\int_0^{\pi/2} P_l(\cos\theta)(-\sin\theta)d\theta\right)\left(\int_0^{\pi/2}\cos\theta\sin^2\theta\frac{P_l(\cos\theta)}{d\theta}d\theta\right) \approx 0.0872 \tag{2.36}$$

Note that as $\kappa > 0$, the particle has a pusher far field signature for $M^- A^- > 0$ and a puller far field signature for $M^- A^- < 0$. Additionally, for a uniform surface mobility, the particle behaves as a neutral swimmer with zero stress intensity.

2.2.4 Chemotaxis of phoretic swimmers

In the previous section, we explored the swimming dynamics of an isolated Janus particle and neglected the presence of other particles which may disturb the chemical and hydrodynamical field. An isolated Janus particle acts as a source in the far field (see Eq. (2.32)); thus, other particles perturb the background solute field. Before we proceed to understand how Janus particles respond to chemical field perturbed by their neighbours it is important to first understand the effect of external solute gradient on a Janus particle's motion. In dilute suspensions, the background solute field varies slowly around each particle. Consequently, we can expand the solute field as a Taylor series at the particle centroid, that is, $C_{ext} \approx C_\infty + \nabla C_{ext} \cdot \boldsymbol{x}$ [179]. Note that this is a linear approximation and accurate up to $O(a/l_c)$ (where l_c is the lengthscale of the suspension). As a result, higher-order corrections for dilute suspensions $(a/l_c \ll 1)$ can be neglected.

In the diffusion-dominated regime, the solute transport for this problem can thus be seen as a linear superposition of i) isolated Janus problem and ii) Passive ($A(\theta) = 0$) particle in an external solute gradient [115]. The solute transport for both these problems has been discussed in the previous two subsections, and the solute field is given by Eq. (2.32) and Eq. (2.27). Thus we obtain the solute field as [115]

$$C = C_\infty + \frac{1}{2}\frac{\boldsymbol{G}\cdot\boldsymbol{x}}{r^3} + \left(\frac{2\pi a^2 A^+}{D_c}\right)\frac{1}{4\pi r} - \left(\frac{3\pi a^3 A^-}{2D_c}\right)\frac{\cos\theta}{4\pi r^2} + \frac{a}{D_c}\sum_{l=2}^{\infty}\frac{A_l}{l+1}\left(\frac{a}{r}\right)^{l+1} P_l(\cos\theta) \tag{2.37}$$

where $\boldsymbol{G} = \nabla C_{ext}$. The slip velocity can be evaluated as

$$\boldsymbol{u}_s^e = \frac{3}{2}M(\theta)(\boldsymbol{I} - \boldsymbol{nn})\cdot\boldsymbol{G} + \boldsymbol{u}_s \tag{2.38}$$

where $\boldsymbol{u}_s$ is the slip velocity for the case of isolated Janus particle (Eq. (2.33)). The additional slip velocity due to external gradient results in *chemotactic reorientation* and *phoretic drift* given by [178]

$$\boldsymbol{U}_{PD} = \chi_t \boldsymbol{G} \quad \text{and } \boldsymbol{\Omega}_c = \chi_r \boldsymbol{p}\times\boldsymbol{G} \tag{2.39}$$

where $\boldsymbol{p}$ is a unit vector along the symmetry axis, and χ_t, χ_r are related to mobility coefficient as [178]

$$\chi_t = -\frac{M^+}{2} \quad \text{and } \chi_r = \frac{9M^-}{16a}. \tag{2.40}$$

Note that the reorientation of the particle depends on the mobility contrast; therefore, a particle with uniform mobility will not reorient along the external chemical gradient. Whereas, the particles reorients along (against) the chemical gradient for $M^- < 0$ ($M^- > 0$). This suggests that particle

reorients such that the more repulsive half of the particle is directed towards less solute concentration. The corresponding additional stresslet can be obtained using the reciprocal theorem given by [178]

$$\boldsymbol{\sigma}_e = \sigma_e[\boldsymbol{G}\boldsymbol{p} + \boldsymbol{p}\boldsymbol{G} + \boldsymbol{G}\cdot\boldsymbol{p}(\boldsymbol{p}\boldsymbol{p} - \boldsymbol{I})] \tag{2.41}$$

where $\sigma_e = (15/8)\mu a^2 \pi M^-$ is the strength of the associated stesslet. It is important to note that such stresslet is absent in natural microorganisms as the reorientation mechanism for microorganisms is very different from a phoretic particle.

2.3 Fundamentals of Kinetic Modelling

The previous subsection explored the modelling swimming mechanism of a Janus particle. As Janus particle disturbs both the chemical and hydrodynamic field, it has the ability to interact with other Janus particles using both the hydrodynamic and chemical field. These complex hydro-chemical interactions results in the complex collective dynamics observed at the suspension scale. Therefore, we now focus our attention on modelling these inter-particle interactions.

To obtain exact solutions, a bi-spherical coordinate system must be adopted to conveniently impose the boundary condition on the surface of each particle. The solution is then expressed in terms of an infinite sum of associated Legendre polynomials [180]. However, for dilute suspensions when the distance between the two particles is larger than their size, these interactions can be captured using the analytical technique known as the method of reflection. In this technique, the hydrodynamic and solute field are evaluated as a correction to the isolated field based on the presence of the other particle. Using the method of reflection, Varma and Michelin [181] developed a systematic framework to model the dynamics of a couple of Janus particles for arbitrary level of accuracy based on size to separation ratio. Extending it to more number of particles, they showed rich collective dynamics.

However, we must turn to computational methods to model collective dynamics at the suspension scale. Some computational techniques that have been employed to model the suspension dynamics include Stokesian Dynamic Simulation [182, 183], Boundary Element Method [159, 184], Immersed Boundary Methods [185, 186] etc. However, modelling collective dynamics becomes computationally expensive when dealing with a large number of particles. Turning to a *kinetic modelling* technique is often more helpful, where a probability density function is used to model suspension dynamics.

The change of approach is also necessary, as the questions of interest at the suspension level are often very different from those at the particle level. This approach is often used to model transport processes in different systems with large number of particles. For instance, consider a simple fluid dynamic experiment where the quantity of interest is the flow rate for a certain pressure drop. This experiment is perfectly reproducible, and we obtained the same flow rate for a given pressure drop in the same fluid. However, if we look at the microscopic scale, the motion of individual fluid particles (molecules) will be different each time. This shows that the fluctuations at the microscopic level have practically no effect on macroscopic quantities. Therefore, focusing on the motion of each fluid particle may not be relevant; instead, the quantity of interest is some *average* of the particles' motion. We introduce the basic principles of this modelling technique in the context of the current study on the suspension of autophoretic particles.

2.3.1 Continuous description of a suspension

In a suspension of N particles, if a set of k coordinates defines each particle, then the number of degrees of freedom for this system N_f is equal to kN (in the context of Janus particles, $k = 5$ with three spatial and two angular coordinates). To move from a discrete description to a continuous description, we must define a consistent map which connects the continuous fields with the associated discrete quantity. In other words, for a discrete quantity $b(\boldsymbol{z}, \boldsymbol{r}, t)$ (with $\boldsymbol{z} = \{\boldsymbol{x}, \boldsymbol{p}\}$) a

corresponding continuous filed $B(\boldsymbol{r},t)$ must be defined

$$b(\boldsymbol{z},\boldsymbol{r},t) \rightarrow B(\boldsymbol{r},t). \tag{2.42}$$

For example, in the context of autophoretic suspension, the information of particle distribution must be mapped to a continuous particle density distribution. A common mapping which is often used based on a phase space function $F(\boldsymbol{z})$ is given by [187]

$$B(\boldsymbol{r},t) = \langle b \rangle = \int d\boldsymbol{z} b(dz,\boldsymbol{r},t)F(\boldsymbol{z}). \tag{2.43}$$

Note that the integral in Eq. (2.43) is over the complete phase space, i.e., $d\boldsymbol{z} = d\boldsymbol{x}_1 d\boldsymbol{x}_2..d\boldsymbol{x}_N d\boldsymbol{p}_1..d\boldsymbol{p}_N$ where $\boldsymbol{x}$ extends over the complete domain and $\boldsymbol{p}$ sweeps all possible orientations on a unit sphere. A normalized form of the function $F(\boldsymbol{z})$ is called as *phase space distribution function* [187] and plays the same role as the probability function. This function reflects the probability of finding the system (information about all the particles) in a particular state. Specifically, $F(\boldsymbol{z})d\boldsymbol{z}$ is the probability of finding the system in a state within an infinitesimal domain $d\boldsymbol{z}$. The dynamical field $B(\boldsymbol{r},t)$ defined in Eq. (2.43) is an average of the discrete quantity b and called as the *phase space average of the dynamical quantity* of $b(\boldsymbol{z},\boldsymbol{r},t)$. Note that in this framework, the state of the system is represented by the distribution function ($F(\boldsymbol{z})$), which acts as a weight for all possible states instead of a single point in phase space. This is referred to as *statistical ensemble*.

The time evolution of the dynamical quantities (such as particle distribution in a suspension) is expressed using the Hamiltonian operator H as,

$$b(\boldsymbol{z}(t),\boldsymbol{r}) = e^{Ht} b(\boldsymbol{z}(t=0),\boldsymbol{r}) \tag{2.44}$$

As a result, the equivalent continuous macroscopic field B evolves in time according to

$$B(\boldsymbol{r},t) = \int d\boldsymbol{z} e^{Ht} b(\boldsymbol{z}(0),r)F(\boldsymbol{z}). \tag{2.45}$$

Using self-adjoint property of Hamiltonian operator H, the Hamiltonian operator is shifted from the dynamical quantity b to distribution function $F(\boldsymbol{z})$ [188]. As a result, we obtain,

$$B(\boldsymbol{r},t) = \int d\boldsymbol{z} b(\boldsymbol{z}(0),r)e^{-Ht}F(\boldsymbol{z}) \tag{2.46}$$

The time-dependence can be clubbed with the distribution function to obtain the *time dependent distribution function* as

$$F(\boldsymbol{z},t) = e^{-Ht}F(\boldsymbol{z}). \tag{2.47}$$

Consequently, solving the time evolution of the time-dependent distribution function is necessary for describing the evolution of all the particles. The Eq. (2.46) is still a complicated equation as the number of degrees of freedom is still large. Therefore, to make any progress, a few simplifying approximations are made. In the next subsections, we will show the derivation of the Focker-Planck equation, which describes the evolution of $F(\boldsymbol{z},t)$ and later focus on simplifying the distribution and correlated functions.

2.3.2 Deriving the Focker-Planck equation

We begin by considering that the variables associated with the particles (for example, position $\boldsymbol{x}$ or orientation $\boldsymbol{p}$) follow Langevin dynamics consisting of a deterministic term and a noise term. The only constraint on the deterministic part is that it is Markovian, i.e., the deterministic part does not have a memory effect. As a result, the equations of motion for each particle are given as

$$\frac{d\boldsymbol{z}}{dt} = \boldsymbol{v}(\boldsymbol{z}) + \boldsymbol{N}(t). \tag{2.48}$$

In the context of phoretic particles, $\boldsymbol{z} = \{\boldsymbol{x},\boldsymbol{p}\}$, $\boldsymbol{v}$ is the velocity (both translation and angular, $\boldsymbol{v} = \{\dot{\boldsymbol{x}},\dot{\boldsymbol{p}}\}$), $\boldsymbol{N}(t)$ is the thermal noise present in the system (for microorganisms, this is due to

their reorientation mechanism). The constraints imposed on the noise are i) it is Gaussian noise, ii) its mean is zero, and iii) its second moment is delta correlated, i.e $\langle \boldsymbol{N}(t)\boldsymbol{N}(t')\rangle = 2\boldsymbol{K}\delta(t-t')$. The angle bracket here denotes the time average of the quantity. As a result, the tensor $\boldsymbol{K}$ is symmetric and reflects the strength of noise in the system.

As discussed earlier, instead of solving Eq. (2.48) for each particle, we focus on probability $F(\boldsymbol{z},t)$ of finding the particle at a particular point $\boldsymbol{z}$ at time t. We are more interested in determining the average of this probability distribution over the noise. To proceed further, we first note that the probability density $F(\boldsymbol{z},t)$ is a conserved quantity. Therefore, we can write a conservation law similar to the mass/momentum conservation laws. As a result, we obtain [188]

$$\frac{\partial F}{\partial t} + \frac{\partial}{\partial \boldsymbol{z}} \cdot \left(\frac{\partial \boldsymbol{z}}{\partial t} F \right) = 0 \tag{2.49}$$

On substituting the temporal derivative from Eq. (2.48),

$$\frac{\partial F}{\partial t} = -\frac{\partial}{\partial \boldsymbol{z}} \cdot (\boldsymbol{v}(\boldsymbol{z})F + \boldsymbol{N}(t)F) = 0. \tag{2.50}$$

Following ref. [188], the deterministic part of the Eq. 2.50 is written as an operator L acting on the probability density function F, such that

$$LF \equiv -\frac{\partial}{\partial \boldsymbol{z}} \cdot (\boldsymbol{v}(\boldsymbol{z})F) \tag{2.51}$$

as a result, Eq. (2.50) transforms as

$$\frac{\partial F}{\partial t} = -LF - \frac{\partial}{\partial \boldsymbol{z}} \cdot \boldsymbol{N}(t)F \tag{2.52}$$

Upon integrating in time once, we obtain the following operator equation

$$F(\boldsymbol{z},t) = e^{-tL}F(\boldsymbol{z},0) - \int_0^t ds e^{-(t-s)L} \frac{\partial}{\partial \boldsymbol{z}} \cdot \boldsymbol{N}(s)F(\boldsymbol{z},s). \tag{2.53}$$

Note that the probability density function F depends on the noise $\boldsymbol{N}(s)$ only for $s < t$. Now the idea is to obtain a series expansion for F in terms of powers of noise, therefore this is substituted back in the stochastic term of Eq. (2.52) to obtain

$$\frac{\partial F}{\partial t} = -LF - \frac{\partial}{\partial \boldsymbol{z}} \cdot (\boldsymbol{N}(t)e^{-tL}F(\boldsymbol{z},0)) + \frac{\partial}{\partial \boldsymbol{z}} \cdot \boldsymbol{N}(t) \int_0^t ds e^{-(t-s)L} \frac{\partial}{\partial \boldsymbol{z}} \cdot \boldsymbol{N}(s)F(\boldsymbol{z},s) \tag{2.54}$$

Following ref. [188], the Focker Planck equations are obtained by taking the noise average of Eq. (2.54). As a result, we obtain

$$\frac{\partial \langle F\rangle}{\partial t} = -\frac{\partial}{\partial \boldsymbol{z}} \cdot (\boldsymbol{v}(\boldsymbol{z})\langle F\rangle) + \frac{\partial}{\partial \boldsymbol{z}} \cdot \boldsymbol{K} \cdot \frac{\partial}{\partial \boldsymbol{z}} \langle F\rangle \tag{2.55}$$

where the angle brackets denote the averaged quantity and $\boldsymbol{K}$ may be any function of $\boldsymbol{z}$. However taking it as a constant with respect to $\boldsymbol{z}$ simplifies Eq. (2.55) to

$$\frac{\partial F}{\partial t} = -\frac{\partial}{\partial \boldsymbol{z}} \cdot (\boldsymbol{v}(\boldsymbol{z})F) + \boldsymbol{K}\frac{\partial^2}{\partial \boldsymbol{z}^2} F. \tag{2.56}$$

Here, F denotes the average over noise, and the angled brackets have been dropped for convenience. In Eq. (2.56), the noise term acts like a diffusion term on the probability function with an equivalent diffusion coefficient related to $\boldsymbol{K}$.

2.3.3 Reduced distribution and correlation functions

In the next step, we now simplify the dynamic and distribution functions. Consider the Hamiltonian of the system expressed as

$$H(z_1, z_2, ..., z_n) = \sum_{j=1}^{N} H_0(z_j) + \sum_{j<}\sum_{k=1}^{N} V(z_j, z_k). \tag{2.57}$$

In Eq. (2.57), the first term H_0 represents the non-interaction Hamiltonian component, which has the identical functional form (as all the particles are identical) for all particles depending on its location in phase space. For the current scope of this thesis, an example for the first term is the particle density, which only depends on the particles' spatial location

$$\Phi(\boldsymbol{r}, t) = \sum_{j=1}^{N} \delta(\boldsymbol{r}(t)_j - \boldsymbol{r}) \tag{2.58}$$

In contrast, a general dynamical function $b(z_1, z_2.., z_N)$ is expressed as [187]

$$b = b_0 + \sum_{j=1}^{N} b_1(z_j) + \sum_{j<k}\sum_{k=1}^{N} b_2(z_j, z_k) + \sum_{j<k}\sum_{k<l}\sum_{l=1}^{N} b_3(z_j, z_k, z_l). \tag{2.59}$$

Here, the function has been decomposed into different contributions depending on the type of interactions, and the constraints on the sum are due to the symmetric property. The terms b_s for $s \geq 3$ represent the many-body interaction effects and are usually negligible compared to the first three terms, especially in dilute suspensions [187]. As a result, the approximation $b_s = 0$ for $s \geq 3$ is often made, further simplifying the equations.

The continuous function $B(\boldsymbol{r}, t)$ can be evaluated at each order of b_s. For instance, at zeroth order, it will simply be b_0 as it is independent of $\boldsymbol{z}$. The contribution of single particle function b_1 is given by substituting $\sum_{j=1}^{N} b_1(\boldsymbol{z_j})$ in Eq. (2.46). As a result, we obtain

$$\int dz_1..dz_N \sum_{j=1}^{N} b_1(\boldsymbol{z_j}) F(z_1, ...z_N) = N \int dz_1..dz_N b_1(\boldsymbol{z_j}) F(z_1, ...z_N). \tag{2.60}$$

Indeed, the distribution function is symmetric; therefore, the sum equals N times the integral over phase space of one particle (here, we have taken $j = 1$). Note that by expressing in such a form, we can now define a *reduced one-particle distribution function* which reflects the probability of finding a particle at $\boldsymbol{z}_1$ as

$$f_1(z_1) = N \int dz_2..dz_N F(z_1, z_2, ..z_N) \tag{2.61}$$

Using this one particle distribution function, the average of b_1 can be evaluated directly by $f_1(z_1)$ instead of using the complete distribution function $F(z_1, z_2, ..z_N)$.

$$N \int dz_1..dz_N b_1(\boldsymbol{z_j}) F(z_1, ...z_N) = \int dz_1 b_1(z_1) f_1(z_1) \tag{2.62}$$

Similarly, the reduced s particle function can be evaluated as [187]

$$f_s(z_1, z_2, ..z_s) = \frac{N!}{(N-s)!} \int dz_{s+1}..dz_N F(z_1, .., z_N) \tag{2.63}$$

where the prefactor exists due to the symmetry of f_s. The reduced distribution function f_s is interpreted physically as the probability of finding s particles simultaneously at $z_1, z_2, .., z_s$. The continuous function at suspension scale $B(\boldsymbol{r}, t)$ is expressed as

$$B(\boldsymbol{r}, t) = \sum_{s=0}^{N} \frac{1}{s!} \int dz_1 dz_2..dz_s b_s(z_1, dz_2..dz_s) f_s(dz_1, dz_2..dz_s). \tag{2.64}$$

As a result, we have represented the observable function B completely in terms of a reduced set of reduced distribution functions. Consequently, knowledge of two (sometimes three) reduced distribution functions is sufficient to evaluate the macroscopic quantity of interests as $b_s \equiv 0$ for $s \geq 3$ of most dynamic functions. However, this advantage is unclear as the reduced distribution functions are composed of the complex distribution function F. Additionally, evaluation of f_s requires the knowledge of f_{s+1} which results in formation of a hierarchy. Consequently, the system of equations is open, and some approximations must be made to close the system of equations and make further progress.

In most cases, the complex hierarchy can be simplified by ignoring higher-order reduced correlation functions and expressing the lower-order correlation functions in a single particle reduced distribution function [189]. Cases for which these simplifications can be made are called to be in the *kinetic regime*, and the governing equations are called the *kinetic equations*. To derive closure schemes, the distribution function is expressed as

$$f_s(\boldsymbol{z}_1, .., \boldsymbol{z}_s) = \prod_{j=1}^{s} f_j(\boldsymbol{z}_j) + f_{gs}(\boldsymbol{z}_1, \boldsymbol{z}_2, ..\boldsymbol{z}_s). \tag{2.65}$$

The first term accounts for the probability of finding particles at some point independent of the presence of other particles and thus expresses as a product of N probabilities. On the other hand, the second term accounts for the correlation between the particles. The primary aim in the current context is to obtain the closure scheme for f_2 as we assume $f_s = 0$ for $s \geq 3$, and therefore we write

$$f_2(\boldsymbol{z}_1, \boldsymbol{z}_2) = f_1(\boldsymbol{z}_1) f_1(\boldsymbol{z}_2) + f_{g2}(\boldsymbol{z}_1, \boldsymbol{z}_2) \tag{2.66}$$

here f_{g2} is the irreducible correlation function. The most simplified approximation from the mathematical point of view is to ignore the correlated function completely. This simplification seems drastic but often works well for systems with uniformly small interacting potential. Such approximations are often made [190] when studying the physics of fully ionized plasma as they interact with long-ranged Coulomb forces. The phoretic particles interact via long-ranged hydrodynamic and chemical fields in dilute suspensions. Consequently, we also make this approximation for our case of phoretic particles, i.e. we approximate $f_{g2} = 0$. This approximation is called the *mean field* approximation as it physically translates to modelling the collective behaviour based on the dynamics of a single particle in the mean field.

As a result, the continuum field at the suspension scale $B(\boldsymbol{r})$ at any instant of time is obtained by $\int d\boldsymbol{x}' d\boldsymbol{p}' b(\boldsymbol{x} - \boldsymbol{x}') f_1(\boldsymbol{x}', \boldsymbol{p}')$. For instance, the hydrodynamic mean field is evaluated as

$$\boldsymbol{u}(\boldsymbol{r}, t) = \int d\boldsymbol{x}' d\boldsymbol{p}' u_d(\boldsymbol{x} - \boldsymbol{x}') f_1(\boldsymbol{x}', \boldsymbol{p}') \tag{2.67}$$

where u_d is the induced flow field by a single microswimmer. Note that in this formulation, the particles interact only through the mean field of other particles, which acts as an external field. The mean field is, in turn, evaluated by the particle distribution function through Eq. (2.67) at each instant. Consequently, this couples the particle dynamics with the mean fields, resulting in a non-linear yet closed system of equations. This approximation is only valid when the number of particles in the system is sufficiently large such that the average quantities can be properly defined. More precisely, this assumption is valid when the number of particles N_p and the system volume V tend to infinity, but the ratio N_p/V remains constant.

Finally, the dynamics of the N particle system can be described using a reduced single-particle distribution function given by

$$\frac{\partial f_1}{\partial t} = -\frac{\partial}{\partial \boldsymbol{z}} \cdot (\boldsymbol{v}(\boldsymbol{z}) f_1) + \boldsymbol{K} \frac{\partial^2}{\partial \boldsymbol{z}^2} f_1. \tag{2.68}$$

In the next section, we explore this model in the context of microswimmer suspensions.

2.4 Kinetic modelling of microswimmer suspensions: A review

We now explore the application of the kinetic model discussed in the previous section for suspension of microswimmers. Therefore, this sections aims to familiarize readers with recent progress in kinetic modelling of microswimmer suspensions.

As discussed in Sec. 2.2.1, the perturbed hydrodynamic field of a swimming microorganism behaves as a force dipole which decays as $O(1/r^2)$. In a dilute microswimmer suspension, the microswimmers interact via this long ranged hydrodynamic field, and the mean flow is forced through this active stress as discussed later in Sec. 2.4.1. The induced flow in turn modfies the swimmer dynamics through *Faxen* laws [139]. This feedback mechanism may result in complex dynamics on the suspension scale [53, 56]. Kinetic theory has been employed extensively to study the dynamics of suspension of natural microswimmers and here we first review some of these studies and then discuss how kinetic theory can be implemented for our system of interest, i.e. phoretic particles.

2.4.1 Hydrodynamic instability

The initial studies on modelling dynamics of a microswimmer suspension were motivated by experimental observations of coherent spatio-temporal fluctuations on lenthscales much larger than individual unit. For instance, Mendelsen et.al [56] reported vortical patterns and Dombrowski et al. [60] reported high speed jets in a suspension of neutrally buoyant *Bacillus subtilis* bacterium. Such coherent dynamics results in enhanced diffusion for both the bacterium [191] and passive tracers as well [192, 193]. These observations suggest that the collective swimming modes have long ranged spatio-temporal correlations.

Simha & Ramaswamy [194] were among the first to make an attempt at modelling suspension of self-propelling particles. They employed a continuum model describing the hydrodynamics of polar suspension of microswimmers. Using physical arguments (such symmetry and conservation laws), they built up a governing equation for the director field (polarisation) in the suspension and via a linear instability analysis showed that a polar suspension of microswimmers is inherently unstable to long wavelength fluctuations. More importantly, they reported that the instability is independent of the type of the swimmers (pusher and puller). However, as swimming bacteria undergoes a run and tumble mechanism for self-propulsion, the orientation distribution in dilute suspensions is expected to be closer to isotropic in contrast to polar order considered in this study. Therefore, stability of a near isotropic distribution is more important for bacterial suspension than a polar state.

Saintillan and Shelly [195, 196] provided the study on the stability of isotropic distribution of bacteria using a kinetic theory which is briefly discussed here. The dynamics of bacterial suspension is modelled using a continuous function $\Psi(\boldsymbol{x}, \boldsymbol{p}, t)$ as discussed in Sec. 2.3. This function physically represents the probability of finding a bacterium at $\boldsymbol{x}$ oriented along $\boldsymbol{p}$ at time t. This function evolves in time according to

$$\frac{\partial \Psi}{\partial t} = -\nabla_{\boldsymbol{x}} \cdot (\dot{\boldsymbol{x}}\Psi) - \nabla_{\boldsymbol{p}} \cdot (\dot{\boldsymbol{p}}\Psi). \tag{2.69}$$

Here, $\dot{\boldsymbol{x}}$ and $\dot{\boldsymbol{p}}$ are the translation and orientation velocities of the bacteria and $\nabla_{\boldsymbol{x}}, \nabla_{\boldsymbol{p}}$ are the gradient operators in physical space and particle orientation respectively. Due to its elongated shape, the bacteria is modelled as a rodlike particle. Thus, its translation and rotation velocities are given by

$$\dot{\boldsymbol{x}} = U_0\boldsymbol{p} + \boldsymbol{u} - D\nabla_{\boldsymbol{x}}\ln\Psi \tag{2.70}$$

and

$$\dot{\boldsymbol{p}} = (\boldsymbol{I} - \boldsymbol{pp}) \cdot [(\boldsymbol{E} + \boldsymbol{\omega}) \cdot \boldsymbol{p} - d_r\nabla_{\boldsymbol{p}}(\ln\Psi)]. \tag{2.71}$$

The translation velocity in Eq. (2.70) is composed of i) swimming velocity of the bacteria ($U_0\boldsymbol{p}$) ii) advection along the local fluid velocity ($\boldsymbol{u}$) and iii) a diffusive term ($D\nabla_{\boldsymbol{x}}\ln\Psi$). Similarly, the orientation dynamics is governed by Jefferey's equation in terms of rate of strain ($\boldsymbol{E}$) and rotation ($\boldsymbol{\omega}$) tensor along with orientation diffusion ($d_r\nabla_{\boldsymbol{p}}(\ln\Psi)$). Next, we must solve the fluid flow equations

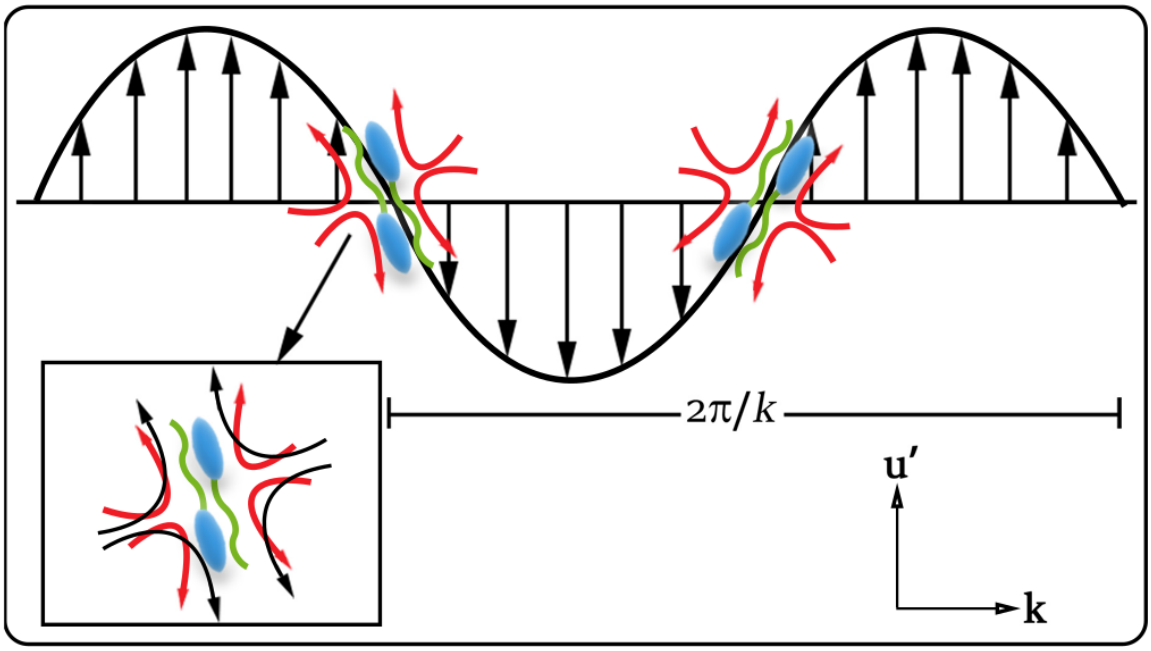

Figure 2.6: Schematic of the hydrodynamic instability mechanism for a suspension of pusher swimmers. The elongated microswimmer aligns along the extensional component of the perturbed flow (shown by black arrows) which results in enhancing the velocity perturbation due to the induced flow of the bacteria (illustrated by red arrows). This results in the growth of the instability.Image adapted from ref [21].

(mean field) to close the system. The flow equations are forced by mean bacterial stress $\boldsymbol{\sigma}_p$ given by

$$\boldsymbol{\sigma}_p = \sigma_0 \int \Psi(\boldsymbol{x}, \boldsymbol{p}, t) \left(\boldsymbol{pp} - \frac{\boldsymbol{I}}{3} \right) \tag{2.72}$$

where σ_0 is the intensity of the force dipole. Note that for a pusher type swimmer $\sigma_0 < 0$ and for a puller type swimmer $\sigma_0 > 0$. The fluid flow is modelled as an incompressible Stokes flow governed by

$$\begin{aligned} \nabla_{\boldsymbol{x}} \cdot \boldsymbol{u} &= 0 \\ -\nabla_{\boldsymbol{x}}^2 \boldsymbol{u} + \nabla_{\boldsymbol{x}} &= \nabla_{\boldsymbol{x}} \cdot \boldsymbol{\sigma}_p. \end{aligned} \tag{2.73}$$

The isotropic distribution of microswimmers is one of the solutions to this coupled system of equations, and therefore, a linear stability analysis of this isotropic state can be performed. Saintillan and Shelly reported that the isotropic is linearly unstable *only* for $\sigma_0 < 0$, i.e. for pusher swimmers. This is an important finding, suggesting that the suspension's collective behaviour depends directly on an individual swimmer's self-propulsion mechanism. This was confirmed both by experiments [54, 197] and simulations [198]. Furthermore, Saintillan and Shelly also recovered the unstable modes reported by Simha and Ramaswamy [194] for the polar state.

The physical mechanism for the onset of the hydrodynamic instability can be understood using i) the induced flow that pusher swimmers create and ii) due to their elongated shape. Due to its elongated shape, the bacteria orients along the extensional axis of the perturbed velocity field. The induced flow of the swimmers then reinforces the extensional component of the long wave perturbation. This is illustrated in Fig. 2.6 where the red coloured arrows indicate the induced flow and the black arrows in the inset show the extensional component of the perturbed flow. Consequently, the amplitude of the perturbation grows for a pusher suspension. As a result, the isotropic suspension becomes linearly unstable. In contrast, for a suspension of pullers (and for passive rods), induced flow is exactly the opposite of the pushers, which dampens the long wave velocity perturbations. As a result, an isotropic distribution of puller swimmers is linearly stable.

These studies, however, did not account for the "tumbling" dynamics of the bacteria's swimming motion. As a result, this predicts that a suspension of pusher swimmers will remain unstable for any concentration of swimmers. This contradicts the experimental observation of Wu and coworkers [191] where they reported enhanced diffusivity of tracer particles only above a certain threshold of bacterial concentration. Subramanian and Koch [53] accounted for the tumbling dynamics by modelling it a Poisson process with a timescale τ. As a result, an additional term appears in Eq. (2.69) given by

$$\frac{\partial \Psi}{\partial t} = -\nabla_{\boldsymbol{x}} \cdot (\dot{\boldsymbol{x}}\Psi) - \nabla_{\boldsymbol{p}} \cdot (\dot{\boldsymbol{p}}\Psi) - \frac{1}{\tau}\Big(\Psi - \frac{1}{4\pi}\int \Psi d\boldsymbol{p}'\Big). \tag{2.74}$$

The expression for translation and rotation velocity and the hydrodynamic equations are identical to Saintillan and Shelley's formulation and given by equations Eq. (2.70), (2.71) and (2.73). Using the linear stability analysis of the isotropic state, they showed the existence of a threshold bacterial concentration which is a function of swimming parameters of an individual bacterium. The threshold is given by [199],

$$(nL^3)_{crit} = \frac{1}{\sigma_0}\left[\frac{5L}{U_0\tau} + \frac{30Ld_r}{U_0}\right] \tag{2.75}$$

where L is the typical size of the system, n is the number density,U_0 is the self-propulsion velocity, d_r is the diffusion coefficient of the bacteria and σ_0 is the active stress exerted by the bacteria. This suggests that the critical strength of bacterial concentration depends solely on the self-propulsion mechanism adopted by the swimmer. This is an important result as this suggests that the self-propulsion mechanism of an individual swimmer directly affects the collective dynamics of the suspension.

2.4.2 Chemotactic Instability

In addition to the hydrodynamic interactions, it is also well established that microorganisms respond to environmental chemical cues to complete complex tasks. As discussed in chapter 1 this is called chemotaxis [83], resulting in complex spatio-temporal patterns in bacterial colonies [83, 200]. Due to this additional coupling, the complexity of collective dynamics in these systems thus increases significantly. In this subsection, we focus on modelling this added chemical coupling in the system.

The chemical interactions between microorganisms can occur between different distinct species, for instance spermatozoa detects the chemical signals produced by mammalian eggs which plays crucial role during fertilization [111]. In contrast, when the same species secrete the chemical cues, it is called auto-chemotaxis and is observed in certain microorganisms, resulting in complex spatio-temporal patterns [200, 201]. Here, we focus on the case of autochemotaxis.

As discussed in chapter 1, a microorganism controls its tumbling frequency to preferably move towards higher/lower solute concentration as illustrated in Fig. 2.7. Based on this mechanism, Lushi et.al [202] modified the tumbling term in the kinetic equation proposed by Subramanian and Koch [53] in Eq. (2.74) based on Alt's formulation [203]. In this formulation, the tumbling rate depends on the temporal rate of change of solute concentration expressed as $\lambda(D_tC)$. When the rate of change of solute concentration is zero or negative along the swimming direction, the tumbling frequency remains constant. On the other hand, if the rate of change of concentration along the swimming direction is positive, the tumbling frequency reduces. Chen et al. [204] previously utilised this type of biphasic tumbling frequency to model bacterial chemotaxis. As a result, we obtain the following equation for the single-particle probability function

$$\frac{\partial \Psi}{\partial t} = -\nabla_{\boldsymbol{x}} \cdot (\dot{\boldsymbol{x}}\Psi) - \nabla_{\boldsymbol{p}} \cdot (\dot{\boldsymbol{p}}\Psi) - \Big(\Psi\lambda(D_tC) - \frac{1}{4\pi}\int \Psi\lambda(D_tC) d\boldsymbol{p}'\Big). \tag{2.76}$$

where the function λ is given by

$$\lambda(D_tC) = \begin{cases} \lambda_0(1-\chi_t D_tC), & \text{if } 0 < D_tC < 1/\chi_t \\ 0, & \text{if } 1/\chi_t < D_tC \\ \lambda_0, & \text{otherwise} \end{cases} \tag{2.77}$$

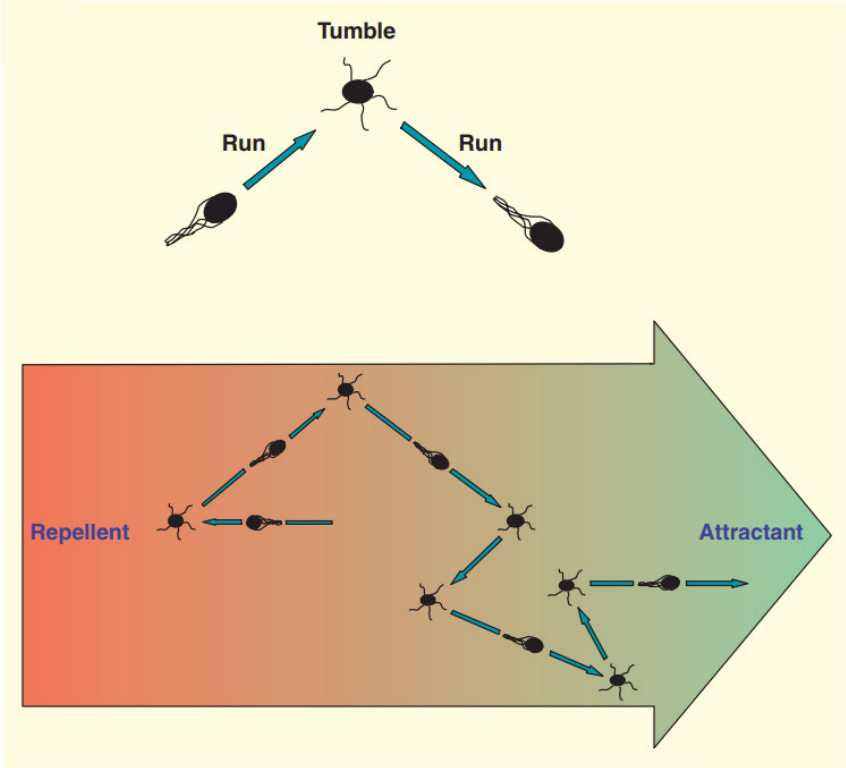

Figure 2.7: (Top) Run and tumble mechanism for self-propulsion of a bacteria (bottom) Chemotactic behaviour of bacteria undergoing the run and tumble swimming. Image adapted from ref. [22]

where λ_0 is the tumbling frequency in the absence of chemical gradient (equivalent to $1/\tau$ in Eq. (2.74)), χ_t is the strength of bacteria's chemotactic ability, and $D_t C$ is the rate of change of solute concentration along the swimming direction given by,

$$D_t C = \frac{\partial C}{\partial t} + (\boldsymbol{u} + U_0 \boldsymbol{p}) \cdot \nabla_{\boldsymbol{x}} C, \tag{2.78}$$

and the hydrodynamics is governed by the same equation as Eq. (2.73). However, due to chemical coupling, we must also solve the mean-field solute transport to close the system of equations. The advection-diffusion equation with additional terms corresponding to solute production proportional to local bacterial density (Φ) and solute degradation following first-order kinetics governs the mean field solute transport. Consequently, the governing equation for the solute transport is given by

$$\frac{\partial C}{\partial t} + \boldsymbol{u} \cdot \nabla_{\boldsymbol{x}} C = D_c \nabla^2_{\boldsymbol{x}} C - \beta_1 C + \beta_2 \Phi \tag{2.79}$$

where $\Phi(\boldsymbol{x}, \boldsymbol{t}) = \int \Psi d\boldsymbol{p}$ is the local bacterial concentration.

They evaluated two distinct dispersion relations via a linear stability analysis of the isotropic state corresponding to the two kinds of instability in such systems: hydrodynamic instability (previously shown by Subramanian and Koch) and a new chemotactic instability [205]. Interestingly, the dispersion relation corresponding to chemotactic instability is independent of σ_0 and depends only on the solute transport. This suggests that this instability is independent of the swimming mode adopted by the swimmer. In other words this chemotactic instability is independent of the far field signature of the swimmer. Furthermore, they also showed that a "turning particle" model where the chemotaxis is modelled by a rotational velocity on the swimmer $(\chi_t(\boldsymbol{p} \times \nabla_{\boldsymbol{x}}) \times \boldsymbol{p})$ results in qualitatively similar results.

The physical mechanism of this chemotactic instability can be understood as follows. A small perturbation to the isotropic state results in regions with higher bacterial concentration than its neighbourhood. The higher number of bacteria in these locations produces more solute, inviting

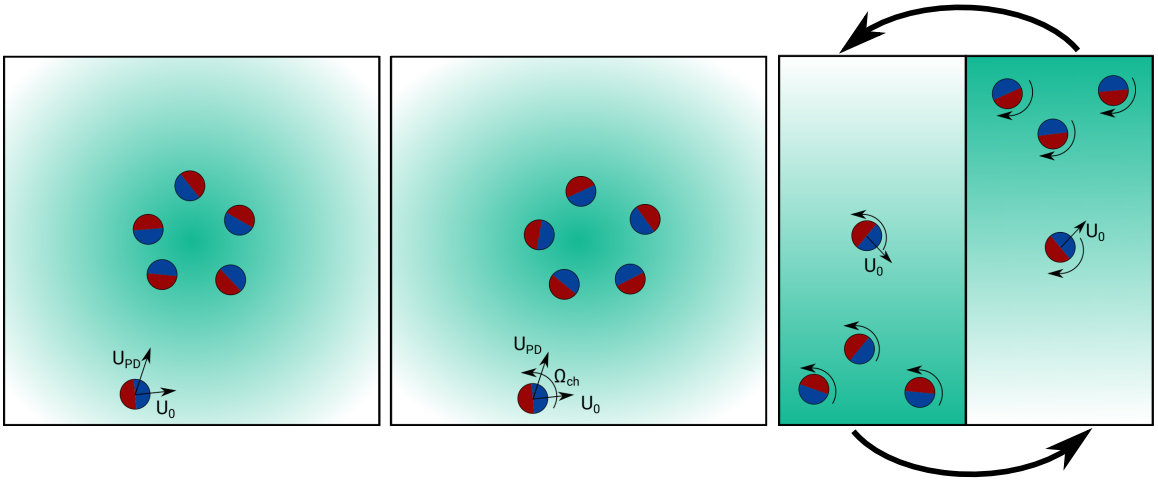

Figure 2.8: Schematic of final state of the suspension for different limits.(left) In the phoretic limit, the particles are drifted towards the higher solute regions (formed due to higher particle density as the particles act as sources) in addition to its self-propulsion resulting in aggregation without polarisation. (center) In the chemotactic limit, the particles have the ability to reorient along the local solute gradient resulting in formation of asters. (right) In contrast in the anti-chemotactic limit, the system undergoes fixed oscillation with the aggregates oscillating in the physical domain. The two arrows point the transition between the two extremes in one cycle.

more bacteria to these locations. As more bacteria arrive, they produce even more solute and this positive feedback loop results in bacterial aggregates throughout the domain.

Suspension of phoretic particles

After exploring the application of the kinetic model for bacterial suspensions, We now turn towards our specific system of interest, which is a suspension of phoretic particles. The first point of difference between bacteria and a phoretic swimmer comes from their different shapes. As discussed earlier, most bacteria have elongated bodies and are modelled using the slender body theory. As a result, the bacteria reorients along the extensional axis. On the other hand, phoretic particles are usually spherical [206].

Consequently, the particles are not expected to orient along the extensional axis of the perturbed flow. As a result, the hydrodynamic instability discussed in the previous section (Sec. 2.4.1) will not be triggered for phoretic suspensions. However, a chemotactic instability can still be triggered as external concentration gradients drive the orientation mechanism. Similar to the bacterial suspension discussed so far, Traverso and Michelin [178] employed kinetic theory to study and understand the dynamics of the phoretic (Janus type) suspensions quantitatively. Here, we briefly explore the model and discuss the important insights from the study.

The difference in motion between a bacterial run and tumble and a phoretic particle must be accounted for. Thus, we replace the tumbling term from the kinetic equation and include chemotactic reorientation term for a phoretic swimmer. More precisely, the translation velocity of an individual phoretic particle in an external concentration gradient is composed of i)self-propulsion component, ii) advective component iii) phoretic drift discussed in Sec. 2.2.4 and iv) thermal diffusion due to its small size. Similarly, the orientation dynamics of an individual phoretic swimmer is composed of rotation due to i)background vorticity, ii) chemotactic reorientation discussed in Sec. 2.2.4 and orientation diffusion. Consequently, the evolution of the single-particle density function (Ψ) obeys the following equation

$$\frac{\partial \Psi}{\partial t} = -\nabla_{\boldsymbol{x}} \cdot (\Psi \dot{\boldsymbol{x}}) - \nabla_{\boldsymbol{p}} \cdot (\Psi \dot{\boldsymbol{p}}) \tag{2.80}$$

where the translation and rotation velocity of the phoretic particle is given by

$$\dot{\boldsymbol{x}} = U_0\boldsymbol{p} + \boldsymbol{u} + \chi_t \nabla_{\boldsymbol{x}} C - D_x \nabla_{\boldsymbol{x}}[\ln\Psi] \tag{2.81}$$

and

$$\dot{\boldsymbol{p}} = \frac{1}{2}\omega \times \boldsymbol{p} + \chi_r(\boldsymbol{p} \times \nabla_x C) \times \boldsymbol{p} - D_p \nabla_p[\ln(\Psi)]. \tag{2.82}$$

Here, χ_r and χ_t are the phoretic and chemotactic mobilities which relate to the surface mobility by Eq. (2.40) in Sec. 2.2.4. The particle-induced stress drives the mean fluid flow governed by Stokes equations similar to Eq. (2.73). However, the active stress in phoretic suspensions is composed of a linear superposition of two components given by Eq. (2.35) and Eq.(2.41). While the mean field solute transport is governed by an advection-diffusion equation similar to Eq. 2.79. Using a linear stability analysis, they identified three distinct limits for different instabilities, namely i) Phoretic limit, ii) chemotactic limit and iii) anti-chemotactic limit. Here, we discuss the physical mechanism of the instabilities,

- **Phoretic limit**: For a phoretic suspension of particles with $\chi_r = 0$, the particles cannot reorient along the local concentration gradient as they swim. However, since the particles also experience a phoretic drift, particle aggregates can form attractive phoretic interactions ($\chi_t > 0$). Increasing solute production at regions of relatively high particle concentration results in a chemical gradient that invites more particles. More particles produce more solute and a positive feedback loop is set up, similar to the case of auto-chemotactic bacteria, which results in the growth of the initial perturbation as illustrated in Fig. 2.8 (left). Note that in this mechanism, the particle orientation in the aggregate is still near isotropic as the particle orientation is unaffected by the solute gradient, however the particles still tumble based on the background vorticity. In this case, the particle motion is directed towards the vector sum of phoretic drift and its self-propulsion; therefore, if the self-propulsion velocity is sufficiently stronger than the phoretic drift, the particle has insufficient time to respond to the gradient and the perturbation dampens stabilizing the isotropic state. Thus, the particles' self-propulsion has a stabilizing effect on the suspension dynamics. In contrast, if the particle does not self-propel, the system remains linearly unstable for all wavenumbers [178].

- **Chemotactic limit**: In this case, the physicochemical properties of the swimmers are such that $\chi_r > 0$ and $\chi_t < 0$. In other words, the particle, in this case, reorients along the chemical gradient, but the phoretic drift is repulsive. This is illustrated in Fig. 2.8 (center). This limit is similar to the case explored by Lushi et al. [202] for bacterial suspensions with additional phoretic drift. The instability mechanism in this limit also relies on the positive feedback loop due to incoming particles and solute production. In this limit, the particles have an orientation towards the aggregate center, and this type of aggregate is known as *asters*. Still, in this case, the instability mechanism relies on self-propulsion velocity compared to the phoretic limit. Therefore, the limit of no self-propulsion is stable in this case. Although at sufficiently large self-propulsion velocity, when the swimming timescale is much shorter than the reorientation timescale, it has a stabilizing effect similar to the phoretic limit.

- **Anti-chemotactic limit** Finally, in this limit, the particle shows anti-chemotactic behaviour, i.e., the particle reorients against the solute gradient and the phoretic drift drives the particle towards low concentration regions. Due to anti-chemotactic behaviour, the particles move towards regions of low solute concentration. However, as more particles arrive, the low solute concentration region transitions to the high solute concentration region. Consequently, the particles are driven away from this region, and the cycle repeats as illustrated in Fig. 2.8 (right).

Furthermore, this kinetic model has also been used to study the effect of confinement and background flow on the dynamics of microswimmer suspensions [25, 207]. The presence of the wall imposes a no flux boundary condition at the wall, which results in wall accumulation of the swimmers. The accumulation at the walls requires just two ingredients, first self-propulsion velocity and

second no penetration condition at the walls; with these ingredients the accumulation can be explained as follows, the swimmers propel in different directions, but as soon as they encounter the wall, they get trapped until their orientation changes due to orientation diffusion. As a result, the swimmers are trapped at solid boundaries. Traverso and Michelin [25] showed that the suspension dynamics in pressure-driven flow show complex dynamics with two timescales depending upon the strength of the background flow. In the short term, they report wall accumulation. In their study, the particles act as chemical sources resulting in generating a solute gradient towards the walls leading to more particles travelling towards the walls and enhancing the particle trapping. However, they report that this state is unstable to small perturbations resulting in complex pattern formation depending on the strnegth of pressure driven flow. Furthermore, they define an effective viscosity of the suspension based on the Poisuelle law for Newtonian fluids. Using the definition of the effective viscosity, they report a non-Newtonian rheological behaviour of the suspension.

2.5 Conclusion

In this chapter, we explored the different modelling techniques required to model the dynamics in wet active matter properly. Starting with hydrodynamics, we showed how the physics of fluid motion at a small significantly differs from that at a macro scale. This poses a unique challenge for designing swimming strategies at small scales. Taking inspiration from nature, we then discussed the swimming mechanism of natural microorganisms and its mathematical model, including via i)flow singularities and ii) slip velocity. This slip velocity is realized in physical systems using phoretic mechanisms. We showed how phoretic particles exploit this slip velocity to self-propel and discussed the effect of external solute gradient on individual particle motion. Moving from individual dynamics to collective dynamics requires tools from statistical mechanics, which were then formally introduced. Finally, we provided an extensive review of the application of the kinetic model for various microswimmer suspensions.

Chapter 3

Self-organization of phoretic suspension in confined shear flows

This chapter is a modified version of a scientific article published in Physical Review Fluids [208].

Contents

3.1 Introduction 60
3.2 Modeling dilute suspensions of sheared phoretic particles 61
3.2.1 Physical model 61
3.2.2 Dimensionless equations 64
3.3 Numerical Framework 65
3.3.1 Stokes Solver 65
3.3.2 Time marching scheme 67
3.3.3 Selection of the physical parameter values 69
3.4 Self-organisation dynamics 70
3.4.1 Overview of the suspension dynamics 71
3.4.2 Short term dynamics 71
3.4.3 Long term dynamics 72
3.4.4 Linear Stability of the 1D equilibrium: a minimal model 77
3.5 Rheology of phoretic suspensions 80
3.5.1 Defining an effective viscosity 80
3.5.2 Induced Flow 81
3.5.3 A simplified model for the induced flows 83
3.5.4 Time evolution of the effective viscosity 85
3.6 Conclusions 87

Overview

After discussing the modelling techniques in the last chapter, we implement kinetic modelling to study the dynamics of a phoretic suspension in confined shear flows. We begin with a physical description of our problem before proceeding towards implementing the kinetic model discussed in the previous chapter in Sec. 3.2. This is followed by a detailed discussion of the numerical approach that we implement to solve the set of governing equations in Sec. 3.3. Then, we analyze the self-organisation behaviour in detail and identify three different long-term responses to the external mechanical forcing (shear and confinement) in Sec. 3.4.3. Subsequently in Sec. 3.4.4, we provide a minimalistic model based on moment equations to gain further insights by identifying the key ingredients required for such complex collective dynamics. Next, using the induced flow fields, we analyze the rheological response of the suspension corresponding to the control parameters (shear and confinement strength) in Sec. 3.5.1. This leads to developing a simple model for the flow forcing based on physical properties such particle concentration, solute concentration gradient and local polarization in Sec. 3.5.3. This model provides physical insights for the induced flow discussed in Sec. 3.5.2. Finally, we summarize the major findings from this study in Sec. 3.6.

3.1 Introduction

A large part of the early work on active suspensions has focused on their spontaneous organisation in unbounded and quiescent flows, thus neglecting any potential environmental forcing or coupling, and focusing specifically on the intrinsic suspensions dynamics [53, 195, 196]. Yet, to achieve targeted applications (e.g. in biomedicine [209–211]), control strategies must be obtained in realistic environments that feature confinement (i.e. the presence of bounding walls) and/or non-uniform background flows, reflecting an external mechanical actuation of the system. Motivated by this observation, this work focuses on the response of a suspension of Janus particles under the dual influence of varying strength of confinement and externally-applied shear. Response to shear further provides some insight into the effective rheology of the suspension [14, 90, 212]. Focusing specifically on Janus phoretic swimmers, Ref. [25] considered the dynamic response and effective rheology of a dilute suspension in pressure-driven Poiseuille flow between two rigid walls, identifying five different regimes depending on the relative strength of the flow-inducing pressure drop.

Microswimmers are able to interact with confining boundaries through their stirring of the surrounding fluid. The constraint of a no-slip boundary condition at finite distance introduces an additional flow perturbation that modifies their dynamics and results in non-trivial behaviour, even at an individual scale. Among other effects, previous studies report attraction and reorientation towards a wall [213], scattering of biflagellate microswimmers from circular surfaces [214, 215], microswimmer trapping using a stationary obstacle [216], or the observation of different states depending on catalyst coverage for Janus particles [217, 218] and wall accumulation at suspension scale [98].

Wall accumulation of swimmers is well documented [96–98]: accumulating spermatozoa at the rigid walls [98] play an important role in mammalian reproduction [219]. Interestingly, in contrast with short-term dynamics of individual swimmers, at time scales much larger than the typical reorientation or run-and-tumble rate of the swimmers, hydrodynamics is not even necessary to explain such wall accumulation, which can then be seen as a result of the coupling of self-propulsion and confinement [207, 220]. The characteristic length-scale of the confining boundaries further plays an important role in controlling the collective dynamics of microswimmer suspensions [105, 106]: in the experimental results of Wioland.*et.al* [10], the distribution of bacteria suspended in a fluid transitions from a complex 2D structure to a streamwise independent 1D distribution as the confinement strength is increased. This points to the critical role of the confinement strength, whose effect on the suspension's self-organisation is a central motivation for the present work.

The presence of a background flow also results in a distinct swimmer behavior, such as the directional bias of *E.coli* in pressure-driven flows [221]. Such rheotaxis can be understood from the dual effect of steric interactions and background shear, which aligns the bacteria against the flow due to their elongated shape [222]. Similar results were also reported for sperm cells in shear

flows [223]. Synthetic swimmers such as Janus phoretic particles also display rheotactic behavior, which was reported for spherical and rod-shaped catalytic colloids in confined shear flows [127, 224]. More recently, Traverso and Michelin [25] showed that Janus particles also polarize against the flow, like *E.coli*, under strong background Poiseuille flow. For spherical particles, such rheotaxis can be understood from the competition of wall normal polarization and background vorticity. For elongated particles, for which steric effects play an important role, Ref. [224] showed that rheotaxis can also be tuned using the detailed activity and actuation patterns of the active particles.

Understanding the behaviour and response of chemotactic suspensions in shear flows is critical for their applications as fluids of non-trivial or even tunable effective viscosity [14, 225]. It is now well established that elongated pusher-type swimmers tend to decrease the effective viscosity of the suspension [14, 197], while spherical puller-type swimmers (e.g. algae) tend to increase it [90] , thanks to the microscopic stresses they exert on the surrounding fluid and the shear alignment of the swimmers. The rheological response is qualitatively captured by theoretical models proposed by Saintillan [141] and Hatwalne *et al.* [138] for unconfined suspensions. These models are furthermore not applicable to a suspension of spherical Janus particles which do not experience geometric shear alignment. The rheology of such suspensions in Poiseuille flows was therefore recently analysed by Ref. [25], that reported a net reduction in the global effective viscosity at low shear rates, consistently with the observations on other microswimmer suspensions [197].

The primary goal of this work is to understand the dual effect of background shear flow and confinement. While previous studies have explored the effect of shear on self-organisation of active suspensions, most of them focused on pressure-driven flows [25, 207] with non-uniform shear profile. As a result, the regions where background shear is most significant overlaps with the regions where the wall influence dominates, leading to complex dynamics [25] and making it harder to decipher the role of each effect. To avoid this, we focus in this work on a simple shear profile (Couette), such that the effect of shear is similar in the entire domain, whether close or far from the boundaries. In contrast, the effect of confinement is profoundly non-uniform across the channel, affecting mostly the regions away from the centerline. Additionally, in this configuration, the asymmetric shear flow results in a differential advection of the particles on both sides of the channel and in horizontal interactions between the aggregates which has not been reported earlier. So far existing studies have either explored fixed confinement effect [25, 207], or varying confinement for non-chemotactic suspensions [226]; by varying the confinement strength, we obtain here a better insight into the role of confinement on the suspension dynamics with respect to the intrinsic chemotactic behaviour and report that the confinement strength stabilizes the 1D regime observed at short times, due to strong transverse gradients. Finally, the flow induced by the particles' self-organisation and the suspension's rheology is discussed and a minimalistic model is proposed.

3.2 Modeling dilute suspensions of sheared phoretic particles

3.2.1 Physical model

Description

In this chapter, we consider self-organisation and rheological response to shear of a suspension of self-propelling Janus particles of radius $\hat{R}$ in a Newtonian fluid (viscosity $\hat{\eta}$) confined between two flat walls separated by a distance $2\hat{H}$; both walls move in opposite directions at a speed of $\hat{u}_w$: in the absence of any particle, this would establish a steady Couette shear flow with uniform shear rate $\hat{\gamma} = \hat{u}_w/\hat{H}$ as illustrated in Fig. 3.1, a quantity referred to in the following as background shear rate. All dimensional quantities are represented with a 'hat($\hat{}$)' in order to distinguish them later on from their dimensionless counterparts. Particles interact with a chemical solute of concentration $\hat{C}(\hat{\mathbf{x}}, \hat{t})$ through two fundamental physico-chemical properties: a chemical *activity* $\hat{A}(\hat{\mathbf{x}})$ (namely the ability to produce or consume solute) and a mobility $\hat{M}(\hat{\mathbf{x}})$ that converts surface tangential gradients of solute into slip flows along their boundaries, the combination of which enables the particle to set up local chemical gradients through which it can self-propel [6, 175]. The particles

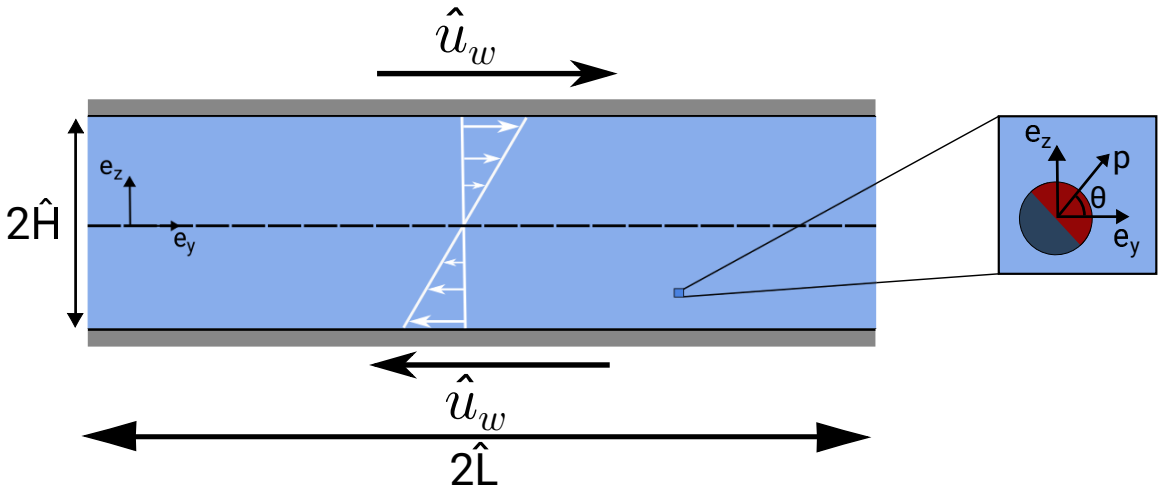

Figure 3.1: Problem Schematic. A dilute suspension of Janus particle placed between two flat walls. The walls move opposite to each other to establish a simple shear flow

considered in this chapter consist of two chemically-homogeneous hemispheres, and $\boldsymbol{p}$ is thus the particle orientation while $\hat{A}^{\pm}$ and $\hat{M}^{\pm}$ denote the sum $(+)$ and front-back difference $(-)$ in activity and mobility of the two hemispheres.

Kinetic model of dilute suspensions

Sec. 2.4 of chapter 2 introduced the kinetic model adopted previously [15, 202] to model collective dynamics of dilute suspension of microswimmers. Here, we adapt a similar model for current system and forcings. As discussed earlier, the kinetic model based on a probability density function $\hat{\Psi}(\hat{\boldsymbol{x}}, \boldsymbol{p}, \hat{t})$ is employed for sufficiently dilute suspensions (when the interparticle distance and the channel width is much larger than individual size of the particles). As the probability density function is a function of six coordinates (3 spatial, 2 angular and time), using this model in 3D is usually computationally intensive. To gain some physical insight on the suspension dynamics while keeping computational costs manageable, we restrict ourselves to the analysis of the two-dimensional problem, where $\hat{\Psi}$ only depends on two spatial and a single angular coordinate $(\hat{y}, \hat{z}, \theta)$ (Fig. 3.1) and time $\hat{t}$. Such two dimensional reduction has been made in previous studies and showed qualitatively accurate with respect to experiments [106, 195, 205].

Following previous studies [25, 178], the local particle density $\hat{\Phi}(\boldsymbol{x}, t)$ and polarisation $\boldsymbol{n}(\hat{\boldsymbol{x}}, \hat{t})$ are defined as,

$$\hat{\Phi} = \int_{\Omega} \hat{\Psi}(\hat{\boldsymbol{x}}, \boldsymbol{p}, \hat{t}) d\boldsymbol{p}, \qquad \boldsymbol{n} = \frac{1}{\hat{\Phi}} \int_{\Omega} \hat{\Psi}(\hat{\boldsymbol{x}}, \boldsymbol{p}, \hat{t}) \boldsymbol{p} d\boldsymbol{p} \tag{3.1}$$

where Ω spans all possible orientations (unit circle in $2D$); the mean particle density in the suspension is then given by

$$\hat{N} = \frac{1}{\hat{S}} \int_{\hat{\mathcal{S}}} \hat{\Phi} d\hat{S} = \frac{1}{\hat{S}} \int_{\hat{\mathcal{S}}} \int_{\Omega} \hat{\Psi}(\hat{\boldsymbol{x}}, \boldsymbol{p}, \hat{t}) d\boldsymbol{p} d\hat{S}. \tag{3.2}$$

The conservation of particles writes locally as a Smoluchowski equation for $\hat{\Psi}$ as discussed in Sec. 2.4,

$$\frac{\partial \hat{\Psi}}{\partial t} = -\hat{\nabla}_x \cdot (\dot{\hat{\boldsymbol{x}}} \hat{\Psi}) - \hat{\nabla}_p \cdot (\dot{\boldsymbol{p}} \hat{\Psi}) \tag{3.3}$$

with $\hat{\nabla}_x$ and $\hat{\nabla}_p$, the differential operators in space and orientation.

The translation and rotation fluxes on the right-hand side of Eq. (3.3) are obtained from the translation $\dot{\hat{\boldsymbol{x}}}$ and rotation velocity $\dot{\boldsymbol{p}}$ of an isolated particle placed in the hydrodynamic and chemical mean-fields $\hat{\boldsymbol{u}}(\hat{\boldsymbol{x}})$ and $\hat{C}(\hat{\boldsymbol{x}})$, corrected for the diffusion contribution [25]

$$\dot{\hat{\boldsymbol{x}}} = \hat{U}_0 \boldsymbol{p} + \hat{\boldsymbol{u}} + \hat{\chi}_t \hat{\nabla}_x \hat{C} - \hat{D}_x \nabla_x [\ln(\hat{\Psi})], \tag{3.4}$$

$$\dot{\boldsymbol{p}} = \frac{1}{2}\hat{\omega} \times \boldsymbol{p} + \hat{\chi}_r(\boldsymbol{p} \times \hat{\nabla}_x \hat{C}) \times \boldsymbol{p} - \hat{D}_p \hat{\nabla}_p[\ln(\hat{\Psi})]. \tag{3.5}$$

Here, $\hat{U}_0$ is the self-propulsion velocity of the Janus particle, $\hat{\chi}_t$ and $\hat{\chi}_r$ its translation and rotation phoretic mobilities, $\hat{\omega} = \hat{\nabla}_x \times \hat{\boldsymbol{u}}$ the local vorticity, and $\hat{D}_x, \hat{D}_p$ are translation and orientation particle diffusivities.

The specific values of $\hat{U}_0, \hat{\chi}_t, \hat{\chi}_r$ depend on detailed physico-chemical properties (surface activity and surface mobility) and coating patterns. For the hemispherical particles considered here, $\hat{U}_0, \hat{\chi}_t, \hat{\chi}_r$ are given by [25, 178]

$$\hat{U}_0 = \frac{\hat{A}^- \hat{M}^+}{8\hat{D}_c}, \; \hat{\chi}_t = -\frac{\hat{M}^+}{2}, \; \hat{\chi}_r = \frac{9\hat{M}^-}{16\hat{R}}. \tag{3.6}$$

The suspension is bounded at the top and bottom by impermeable walls, so that the wall-normal component of the probability flux $\hat{\Psi}\dot{\hat{\boldsymbol{x}}}$ must vanish there

$$\left(\hat{U}_0 \sin\theta + \chi_t \frac{\partial \hat{C}}{\partial \hat{z}}\right)\hat{\Psi} = \hat{D}_x \frac{\partial \hat{\Psi}}{\partial \hat{z}} \qquad \text{at } \hat{z} = \pm\hat{H}. \tag{3.7}$$

Hydrodynamic problem

Finding $\hat{\Psi}$ also requires solving for the chemical and hydrodynamic fields $\hat{C}$ and $\hat{\boldsymbol{u}}$. The small lengthscales of typical experiments ($\hat{H} \sim 10^{-4} - 10^{-3} m$) [12, 14, 105] guarantee that inertial effects on the flow are negligible (Re $\sim O(10^{-2})$). The flow velocity $\hat{\boldsymbol{u}}(\boldsymbol{x})$ and pressure $\hat{q}(\boldsymbol{x})$ therefore satisfy Stokes equations forced by the moving boundaries and the individual hydrodynamic active stresses $\hat{\boldsymbol{S}}(\hat{\boldsymbol{x}}, \hat{t})$ exerted by the particles (see Sec. 2.4):

$$\hat{\nabla}_x \cdot \hat{\boldsymbol{u}} = 0, \qquad -\hat{\eta}\hat{\nabla}_x^2 \hat{\boldsymbol{u}} + \hat{\nabla}_x \hat{q} = \hat{\nabla}_x \cdot \hat{\boldsymbol{S}}. \tag{3.8}$$

The no-slip boundary condition at the walls imposes

$$\hat{\boldsymbol{u}} = \pm \hat{u}_w \boldsymbol{e}_y \;\; \text{at} \;\; \hat{z} = \pm\hat{H}. \tag{3.9}$$

Here, $\hat{\boldsymbol{S}}$ is the local stress induced by the Janus particles which is evaluated by taking orientation average of the stresslet produced by a single swimmer oriented along $\boldsymbol{p}$ as [25, 195]

$$\hat{\boldsymbol{S}}(\hat{\boldsymbol{x}}, \hat{t}) = \int_\Omega \hat{\boldsymbol{S}}_{\boldsymbol{p}}(\hat{\boldsymbol{x}}, \boldsymbol{p}, \hat{t})\hat{\Psi} d\boldsymbol{p}. \tag{3.10}$$

The stresslet $\hat{\boldsymbol{S}}_{\boldsymbol{p}}$ produced by the slip forcing at the surface of a single Janus particle consists of two parts: (i) the response $\hat{\boldsymbol{S}}_{\boldsymbol{s}}$ to self-induced chemical gradients (i.e. the particle's own activity) and (ii) the response $\hat{\boldsymbol{S}}_{\boldsymbol{e}}$ to chemical gradients induced at the particle position by its surroundings and neighbors. The strength of both parts depend on physico-chemical properties and are given for the present two-dimensional problem by [25, 178],

$$\hat{\boldsymbol{S}}_{\boldsymbol{s}} = \hat{\alpha}_s \left(\boldsymbol{pp} - \frac{\boldsymbol{I}}{\boldsymbol{2}}\right) \quad \text{with } \hat{\alpha}_s = -\frac{10\pi\kappa\hat{\eta}\hat{R}^2\hat{M}^-\hat{A}^-}{\hat{D}_c} \tag{3.11}$$

$$\hat{\boldsymbol{S}}_{\boldsymbol{e}} = \hat{\alpha}_e \left[\hat{\boldsymbol{G}}\boldsymbol{p} + \boldsymbol{p}\hat{\boldsymbol{G}} + (\hat{\boldsymbol{G}} \cdot \boldsymbol{p})\left(\boldsymbol{pp} - \frac{3\boldsymbol{I}}{2}\right)\right] \quad \text{with } \hat{\alpha}_e = \frac{15}{8}\pi\hat{\eta}\hat{R}^2\hat{M}^- \tag{3.12}$$

with $\kappa \approx 0.0872$ and $\hat{\boldsymbol{G}}$ the local external solute gradient.

Chemical problem

Each particle's activity perturbs the solute field, and at the scale of a single particle, the disturbance field is classically obtained in terms of spherical harmonics [175]. However, at the suspension scale, we retain the most slowly decaying term (i.e. the monopole term) which corresponds to the net consumption/production by the particle with a rate $2\pi\hat{R}^2\hat{A}^+$. In the following, and without any loss of generality, the considered particles are net solute producers ($\hat{A}^+ > 0$). As discussed in Sec. 2.4, the solute concentration $\hat{C}(\hat{\boldsymbol{x}},\hat{t})$ satisfies an advection diffusion equation forced by the particles' individual solute production and a relaxation towards a background equilibrium, namely

$$\frac{\partial \hat{C}}{\partial \hat{t}} + \hat{\boldsymbol{u}}\cdot\hat{\nabla}_x\hat{C} = \hat{D}_c\hat{\nabla}_x^2\hat{C} - \hat{\beta}\hat{C} + 2\pi\hat{R}^2\hat{A}^+\Phi \tag{3.13}$$

The walls are chemically inert: $\hat{C}$ must also satisfy a no-flux boundary condition,

$$\frac{\partial \hat{C}}{\partial \hat{z}} = 0 \text{ at } \hat{z} = \pm\hat{H} \tag{3.14}$$

3.2.2 Dimensionless equations

In the following, the channel half-width ($\hat{H}$) and corresponding solute diffusion time ($\hat{H}^2/\hat{D}_c$) are chosen as characteristic length- and timescales, and $\hat{D}_c/\hat{H}$ and $\hat{\eta}\hat{D}_c/\hat{H}^2$ are the corresponding velocity and pressure scales, respectively. The characteristic concentration scale $\hat{C}_{ch} = \hat{H}\hat{A}^+/\hat{D}_c\zeta$ is obtained by balancing the solute production ($\hat{N}\hat{R}^2\hat{A}^+$) with solute diffusion ($\hat{D}_c\hat{C}_{ch}/\hat{H}^2$) where $\zeta = (\hat{H}\hat{N}\hat{R}^2)^{-1}$ is the ratio of the characteristic suspension scale $(\hat{N}\hat{R}^2)^{-1}$ [195,196] to the channel half-width $\hat{H}$. The parameter ζ is a relative measure of the suspension's length scale to the channel width and thus defines the degree of confinement. The probability density is normalized by the mean number density $\hat{N}$. Equation (3.3) remains unchanged with dimensionless translation and rotation fluxes now given by

$$\dot{\boldsymbol{x}} = u_0\boldsymbol{p} + \boldsymbol{u} + \frac{\xi_t}{\zeta}\nabla_x C - d_x\nabla_x[\ln\Psi], \tag{3.15}$$

$$\dot{\boldsymbol{p}} = \frac{1}{2}\omega\times\boldsymbol{p} + \frac{\xi_r}{\rho\zeta}(\boldsymbol{p}\times\nabla_x C)\times\boldsymbol{p} - d_p\nabla_p[\ln(\Psi)] \tag{3.16}$$

where $\rho = \hat{R}/\hat{H}$ is the relative particle size, and $d_x = \hat{D}_x/\hat{D}_c$ and $d_p = \hat{D}_p\hat{H}^2/\hat{D}_c$, the ratios of particle translation or rotation diffusion to solute diffusion, respectively. Meanwhile, the dimensionless self-propulsion speed u_0, phoretic drift coefficient ξ_t and chemotactic reorientation coefficient ξ_r are

$$u_0 = \frac{\hat{A}^-\hat{M}^+\hat{H}}{8\hat{D}_c^2},\ \xi_t = -\frac{\hat{M}^+\hat{A}^+\hat{H}}{2\hat{D}_c^2},\ \xi_r = \frac{9\hat{M}^-\hat{A}^+\hat{H}}{16\hat{D}_c^2} \tag{3.17}$$

Using Eq. (3.14), the boundary condition for Ψ can be written as

$$u_0\sin\theta\Psi = d_x\frac{\partial\Psi}{\partial z}. \tag{3.18}$$

Stokes equation are written in non-dimensional form as

$$\nabla_x\cdot\boldsymbol{u} = 0, \qquad -\nabla_x^2\boldsymbol{u} + \nabla_x q = \nabla_x\cdot\boldsymbol{S} \tag{3.19}$$

with boundary conditions

$$\boldsymbol{u} = \pm\gamma\boldsymbol{e_y} \text{ at } z = \pm 1, \tag{3.20}$$

and the strength of the dimensionless stresslets are now given by

$$\alpha_s = \frac{640\pi\kappa}{9}\frac{\xi_r u_0}{\xi_t\zeta},\ \alpha_e = \frac{10\pi}{3}\frac{\xi_r}{\zeta^2}. \tag{3.21}$$

Note here that the dimensionless ratio γ/u_0 determines the relative strength of the externally-imposed shear flow to the particles' self-propulsion: for $\gamma \ll u_0$ (weak shear), the background forcing is not sufficiently strong to influence significantly the particle transport; in contrast, for strong shear forcing ($\gamma \gg u_0$), the particles behave as if they were passive.

Finally, the advection-diffusion equation becomes in dimensionless form

$$\frac{\partial C}{\partial t} + \boldsymbol{u} \cdot \nabla_x C = \nabla_x^2 C - \beta C + 2\pi\Phi \tag{3.22}$$

where $\beta^{-1/2} = \hat{l}_c/\hat{H}$ with $\hat{l}_c = \sqrt{\hat{D}_c}/\hat{\beta}$ the dimensionless screening length introduced by the relaxation of the concentration (essentially the range of chemical influence of individual particles). The no flux boundary condition for the solute remains unchanged in dimensionless form.

3.3 Numerical Framework

In this section we provide the details of the numerical method and time marching scheme adopted for solving Eqs. (3.3),(3.19) and (3.22) with respective boundary conditions. We adapt the numerical framework of ref. [25] to the present work's configuration and forcing. Sec. 3.3.1 discusses the implementation of the *influence matrix* method employed to solve the Stokes equation. Note that the Stokes equations are independent of time and therefore time-marching is not necessary. Subsequently, in Sec. 3.3.2, we discuss the time discretization adopted for solving the temporal dependent transport equations for Ψ (Eq. (3.3))and C (Eq. (3.22)).

We expand the field variables in the Fourier basis along the periodic directions (y, θ directions with N_y and N_θ number of modes respectively) and Chebyshev polynomial basis (for non-periodic z direction with N_z number of modes) and solve the system of equations in spectral space which provides a better convergence for the transport equations. Consequently, any generalized field variable f is written as

$$f(y,z,\theta) = \sum_{k=0}^{N_z} \sum_{l=0}^{N_y-1} \sum_{m=0}^{N_\theta-1} \tilde{f}_{k,l,m} T_n(z) e^{ik_{y_l} y + ik_{\theta_m}\theta} \tag{3.23}$$

where $T_n(z)$ is the n^{th} order Chebyshev polynomial.

The central idea in both methods is to obtain a set of 1 dimensional Helmholtz equations which are solved using *tau-method* which is discussed in detail in the appendix A. The set of Helmholtz equations are obtained after expanding the field variables in Fourier basis along y, θ direction. The advantages of using tau-method is twofold; first, the Helmholtz equations are expressed as quasi-tridiagonal matrix operator in contrast to the full differential matrix operator for the case of collocation method which reduces the computational costs. Secondly, the odd and even Chebyshev modes are decoupled for uniform boundary conditions which results in solving two system of equations of half the original size which also reduces the computational costs. This is discussed in more detail in Sec. 3.3.2.

A resolution of $N_y = N_z = 64$ and $N_\theta = 32$ is chosen for the results presented here, for which a relative error of 10^{-3} on the effective viscosity (i.e. integrated force on the top plate) is measured with respect to a refined discretization with $N_y = N_z = 128$ and $N_\theta = 64$. For $\zeta = 1$, the computational box chosen for the results reported here has dimensions $L_y = 2\hat{L}/\hat{H} = 6\pi$ in the streamwise direction and $L_z = 2$ in the vertical direction. We observe that doubling L_y does not change the self-organisation results reported in Sec.3.4 which suggests that the box size does not affect the system dynamics, at least provided $L_z \ll L_y$. We now discuss the numerical method adopted in this work in more detail.

3.3.1 Stokes Solver

As the Stokes equations are instantaneous, time marching is not necessary and we must solve them at each time instant for a given solute and particle distribution. In this subsection we discuss the

numerical scheme adapted for solving the fluid flow equations governed by Eq. (3.19) along with the corresponding boundary condition given by Eq. (3.20). As mentioned earlier, the field variable (here pressure and velocity field) are expressed in Fourier basis along the periodic y-direction as,

$$\boldsymbol{u}(y,z) = \sum_{-N_y/2}^{N_y/2} \tilde{\boldsymbol{u}}_l(z) e^{2\pi i l y/L_y} \tag{3.24}$$

and

$$q(y,z) = \sum_{-N_y/2}^{N_y/2} \tilde{q}_l(z) e^{2\pi i l y/L_y}. \tag{3.25}$$

As a result, the Stokes equations are expressed as a set of 1D ordinary equations in the Fourier space for each Fourier mode associated with the wavenumber $k_l = 2\pi l/L_y$ as

$$-\tilde{\boldsymbol{u}}_l'' + k_l^2 \tilde{\boldsymbol{u}}_l = \tilde{\boldsymbol{f}}_l - \widetilde{\nabla}_l \tilde{q}_l \tag{3.26}$$

with the continuity equations for each Fourier mode given by

$$\widetilde{\nabla}_l \cdot \tilde{\boldsymbol{u}}_l = 0 \tag{3.27}$$

and the boundary conditions for each l mode as

$$\begin{aligned} &\tilde{\boldsymbol{u}}_l(\pm 1) = 0 \quad \forall\, l \neq 0 \\ &\tilde{\boldsymbol{u}}_0(\pm 1) = \pm N_y \gamma \quad \text{for } l = 0. \end{aligned} \tag{3.28}$$

Here, an apostrophe ($'$) denotes continuous derivative in the z direction and the gradient operator in Fourier space is expressed as

$$\widetilde{\nabla}_l = \left(ik_l, \frac{d}{dz} \right) \tag{3.29}$$

As a result, the Stokes equation is represented as N_y ordinary differential equations. In the remainder of the subsection, we drop the subscript 'l' from the field variables for convenience. Before proceeding further, we notice that taking the divergence of Eq. (3.26) and using the incompressibility condition results in

$$-\tilde{q}'' + k_l^2 \tilde{q} = -\tilde{\nabla} \cdot \tilde{\boldsymbol{f}} \tag{3.30}$$

the corresponding boundary conditions are given as

$$ik_l \tilde{u} + \tilde{v}' = 0 \quad \text{at } z = \pm 1. \tag{3.31}$$

Note that with this semi-discrete gradient operator, the divergence may vanish in general for any discretization along z. To overcome this problem, we implement *tau-correction* method proposed by Kleiser and Schumann (See [227] for more details).

As $\tilde{u}_l = 0$ for $l \neq 0$ and $k_l = 0$ for $l = 0$ the first term in Eq. 3.31 is always zero. Consequently, the boundary condition is expressed as

$$\tilde{v}' = 0 \tag{3.32}$$

On the other hand, the Stokes equation for the vertical component of the flow is given as

$$-\tilde{v}'' + k_l^2 \tilde{v} - \tilde{f}_z - \tilde{q}' = 0 \tag{3.33}$$

with boundary conditions

$$\tilde{v}(\pm 1) = 0. \tag{3.34}$$

Now, Eq. (3.30)-(3.34) forms a closed system of 1 dimensional Helmholtz equations and can be solved independently of $\tilde{u}$. We follow Klessier and Schuman algorithm to solve this set of equations (*A-problem*). As the system of equations (Eq. (3.30)-(3.34)) is linear, the solution is expressed

as a linear superposition of three auxiliary problems (*B-problems*) [227] forced with a single inhomogeneity for each auxilliary problem. The first auxilliary problem is forced by the active stresses with homogenous boundary conditions for both vertical velocity and pressure. This is given as

$$-\tilde{q}''_{B1} + k_l^2 \tilde{q}_{B1} = -(ik_l \tilde{f}_y + \tilde{f}'_z) \text{ with } \tilde{q}_{B1}(\pm 1) = 0 \tag{3.35}$$

$$-\tilde{v}''_{B1} + k_l^2 \tilde{v}_{B1} = -\tilde{q}'_{B1} + \tilde{f}_z \text{ with } \tilde{v}_{B1}(\pm 1) = 0 \tag{3.36}$$

The second and third auxiliary problems are homogenous differential equations forced by unit pressure conditions at the top and bottom plates. As a result, we obtain

$$-\tilde{q}''_{B2} + k_l^2 \tilde{q}_{B2} = 0 \text{ with } \tilde{q}_{B2}(1) = 1, \text{ and } \tilde{q}_{B2}(-1) = 0 \tag{3.37}$$

$$-\tilde{v}''_{B2} + k_l^2 \tilde{v}_{B2} = -\tilde{q}'_{B2} \text{ with } \tilde{v}_{B2}(\pm 1) = 0 \tag{3.38}$$

and

$$-\tilde{q}''_{B3} + k_l^2 \tilde{q}_{B3} = 0 \text{ with } \tilde{q}_{B3}(1) = 0, \text{ and } \tilde{q}_{B3}(-1) = 1 \tag{3.39}$$

$$-\tilde{v}''_{B3} + k_l^2 \tilde{v}_{B3} = -\tilde{q}'_{B3} \text{ with } \tilde{v}_{B3}(\pm 1) = 0. \tag{3.40}$$

Using linear superposition, the solution for $\tilde{v}$ and $\tilde{q}$ is expressed as the linear superposition with unknown coefficients R_{B2}, R_{B3} as

$$\begin{bmatrix} \tilde{q} \\ \tilde{v} \end{bmatrix} = \begin{bmatrix} \tilde{q}_{B1} \\ \tilde{v}_{B1} \end{bmatrix} + R_{B2} \begin{bmatrix} \tilde{q}_{B2} \\ \tilde{v}_{B2} \end{bmatrix} + R_{B3} \begin{bmatrix} \tilde{q}_{B3} \\ \tilde{v}_{B3} \end{bmatrix} \tag{3.41}$$

The unknown coefficients are determined by solving a 2×2 system of equations obtained by imposing the no penetration boundary condition on $\tilde{v}$ given by

$$\begin{bmatrix} \tilde{v}'_{B2}(1) & \tilde{v}'_{B3}(1) \\ \tilde{v}'_{B2}(-1) & \tilde{v}'_{B3}(-1) \end{bmatrix} \begin{bmatrix} R_{B2} \\ R_{B3} \end{bmatrix} = - \begin{bmatrix} \tilde{v}'_{B1}(1) \\ \tilde{v}'_{B1}(-1) \end{bmatrix} \tag{3.42}$$

The above matrix on the left-hand side of Eq. (3.42) is called as the influence matrix and this method is called the *influence matrix* method. It is important to note that the homogenous B problems driven by unit pressure at the walls can be solved once for the complete simulation as they are independent of the active stresses. As a result, these solutions are required to be calculated only once. In contrast the inhomogenous B problem is driven by the active stress and therefore depends on the particle distribution. As the particle distribution evolves in time, this sub-problem must be solved at each time. After evaluating $\tilde{v}$ and $\tilde{q}$, $\tilde{u}$ is evaluated by solving the Stokes equation (Eq. (3.26)) in the y-direction taking care of the non-zero boundary condition for the $l = 0$ mode.

3.3.2 Time marching scheme

We now turn to the time marching scheme for the probability density function governed by Eq. (3.3) with the boundary condition Eq. (3.18). Exploiting the periodic conditions along the y and θ direction, the probability density function is expressed in the Fourier basis as

$$\Psi(y, z, \theta, t) = \sum_{l=0}^{N_y - 1} \sum_{m=0}^{N_\theta - 1} \tilde{\Psi}_{l,m}(z, t) e^{ik_{y_l} y + ik_{\theta_m} \theta} \tag{3.43}$$

where $k_{y_l} = 2\pi l / Ly$ and $k_{\theta_m} = 2\pi m / L_\theta$ are the wavenumbers for for corresponding l, m modes. We modify the Cranck-Nicholson time marching scheme by treating the linear diffusive terms ($d_x \nabla_x^2 \Psi, d_p \nabla_p^2 \Psi$ in Eq. (3.3) and $\nabla_x^2 C$ in Eq. (3.22)) semi-implicitly while treating the non-linear terms explicitly. As a result, we obtain

$$\begin{aligned} \tilde{\Psi}^{n+1}_{l,m} =& \tilde{\Psi}^n_{l,m} - \Delta t \left[\widetilde{\nabla}_x \cdot (\widetilde{\Psi \dot{X}})^n_{l,m} + \widetilde{\nabla}_p \cdot (\widetilde{\Psi \dot{P}})^n_{l,m} \right] \\ &+ \frac{\Delta t}{2} \left[d_x \left(\frac{d^2 \tilde{\Psi}^n_{l,m}}{dz^2} - k_{y_l}^2 \tilde{\Psi}^n_{l,m} \right) - d_p k_{\theta_m}^2 \tilde{\Psi}^n_{l,m} \right] \\ &+ \frac{\Delta t}{2} \left[d_x \left(\frac{d^2 \tilde{\Psi}^{n+1}_{l,m}}{dz^2} - k_{y_l}^2 \tilde{\Psi}^{n+1}_{l,m} \right) - d_p k_{\theta_m}^2 \tilde{\Psi}^{n+1}_{l,m} \right] \end{aligned} \tag{3.44}$$

where the superscript denotes the time step and the subscripts denote the Fourier mode in y, θ direction and $\dot{X}$ and $\dot{P}$ are the translation and rotation velocity of the swimmer after accounting for diffusive terms separately given by

$$\dot{X} = u_0 \boldsymbol{p} + \boldsymbol{u} + \frac{\xi_t}{\zeta} \nabla_x C \tag{3.45}$$

and

$$\dot{P} = \frac{1}{2} \boldsymbol{\omega} \times \boldsymbol{p} + \frac{\xi_r}{\rho \zeta} (\boldsymbol{p} \times \nabla_x C) \times \boldsymbol{p}. \tag{3.46}$$

The gradient operators in Eq. (3.44) are continuous in z direction and discrete in y, θ directions given by

$$\widetilde{\nabla}_x = \left(ik_{y_l}, \frac{d}{dz} \right) \quad \text{and} \quad \widetilde{\nabla}_p = ik_{\theta_m}. \tag{3.47}$$

Grouping terms at the same time step in Eq. (3.44) results in obtaining a set of 1D Helmholtz equations of given by

$$-\frac{d^2 \tilde{\Psi}^{n+1}_{l,m}}{dz^2} + \lambda_{l,m} \tilde{\Psi}^{n+1}_{l,m} = \tilde{h}^n_{l,m}. \tag{3.48}$$

where $\lambda_{l,m}$ and $\tilde{h}^n_{l,m}$ are given by

$$\lambda_{l,m} = \frac{2}{d_x \Delta t} + k^2_{y_l} + \frac{d_p}{d_x} k^2_{\theta_m} \tag{3.49}$$

and

$$\begin{aligned} \tilde{h}^n_{l,m} = \frac{2}{d_x \Delta t} \tilde{\Psi}^n_{l,m} - \frac{2}{d_x} \Big[\underbrace{\widetilde{\nabla}_x \cdot (\widetilde{\Psi \dot{X}})^n_{l,m} + \widetilde{\nabla}_p \cdot (\widetilde{\Psi \dot{P}})^n_{l,m}}_{\tilde{A}^n_{l,m}} \Big] \\ \Big[\underbrace{\frac{d^2 \tilde{\Psi}^n_{l,m}}{dz^2} - k^2_{y_l} \tilde{\Psi}^n_{l,m} - \frac{d_p}{d_x} l^2_{\theta_m} \tilde{\Psi}^n_{l,m}}_{\tilde{B}^n_{l,m}} \Big]. \end{aligned} \tag{3.50}$$

It is important to note that the non-linear products that appear in the explicit terms produce aliasing errors which must be corrected. We employ $3/2$ de-aliasing technique [228] to correctly evaluate the non-linear products. Eq. (3.48) is a 1 dimensional Helmholtz equation for each Fourier mode which is forced by the explicit terms evaluate at the previous time step. Thus, at each time step we must solve a set of $N_y N_\theta$ Helmholtz equations. This can be reduced to solving $N_y N_\theta / 4$ number of equations as the probability density function is real and thus the Fourier coefficients at negative wavenumbers can be directly evaluated from the complex conjugate of its positive counter part. The Helmholtz equation is solved using a tau method discussed in detail in the appendix A.

The non-linear nature of the boundary condition (Eq. (3.18)) due to the term $u_0 \Psi \sin\theta$ complicates the implementation as it appears as a convolution sum in Fourier space which couples the θ modes to the y modes. This coupling leads to higher computing costs reducing the efficiency of this method significantly. Therefore, here, we treat the non-linearity explicitly, and iterate upon the solution until the solution converges. Treating the non-linear term explicitly renders the boundary condition to a linear Neumann condition given by

$$d_x \frac{d \tilde{\Psi}^{it+1,n+1}_{l,m}}{dz} = u_0 \sum_{j=0}^{N_\theta - 1} \tilde{f}_j \tilde{\Psi}^{it,n}_{l,m-j} \tag{3.51}$$

where $\tilde{f}_j$ represents the sinusoidal function in Fourier space and the superscript denotes the iteration it at the same time step $n+1$. To define the convergence criteria, a Euclidean norm is defined as

$$Nm = \left[\sum_{i,j,k} \left(\frac{\Psi^{it+1,n+1} - \Psi^{it,n+1}}{\Psi^{it,n+1}} \right)^2 \right]^{1/2} \tag{3.52}$$

Symbol	Physical Parameter	Magnitude estimate
$\hat{R}$	Particle Radius [8, 229]	$10^{-6}m$
$\hat{H}$	Channel Width [14]	$10^{-4}m$
$\hat{U}_0$	Swimming Speed [68]	$10^{-6}ms^{-1}$
$\hat{D}_p$	Rotational Diffusion coefficient [230]	$10^{-1}s^{-1}$
$\hat{D}_c$	Solute Diffusion coefficient [231]	$10^{-9}m^2s^{-1}$
$\hat{D}_x$	Particle Diffusion coefficient [8]	$10^{-11}m^2s^{-1}$

Table 3.1: Dimensional parameters of the system together with their typical order of magnitude in experiments and references where such an estimate can be drawn from.

for $i = 0, 1..N_z$, $j = 0, 1, ...N_y$ and $k = 0, 1, ..N_\theta$. The solution is considered converged when the value of the norm Nm becomes smaller than 10^{-4}. At the first iteration for a particular time step, the initial guess is taken from the previous time step, and since at a particular timestep, the iterations modify the fields variables this is reflect by modifying the forcing term $\tilde{h}^n_{l,m}$ as

$$\tilde{h}^n_{l,m} = \frac{2}{d_x \Delta t}\tilde{\Psi}^{it+1,n}_{l,m} - \frac{1}{d_x}\left(\tilde{A}^{it,n}_{l,m} + \tilde{A}^{it+1,n}_{l,m}\right) + \tilde{B}^{it+1,n}_{l,m} \tag{3.53}$$

after the first iteration. This improves the numerical stability of the iterative scheme while ensuring a second order accuracy convergence. While this scheme has a clear advantage of reducing the computation cost compared to solving the coupled system of equations, this semi-implicit representation imposes a limitation on the size of time step which may result in large computation time.

With the numerical scheme is place, the simulations are initiated starting from a nearly uniform and isotropic state given by $\Psi(\boldsymbol{x}, \boldsymbol{p}, t = 0) = \frac{1}{2\pi} + \epsilon\tilde{\Psi}(\boldsymbol{x}, \boldsymbol{p})$ with $\epsilon \ll 1$, and the corresponding purely diffusive solution for C is approximated as the intial solute distribution. The full governing equations are then marched in time as described in this subsection where we solve a set of 1D Helmholtz equations at each time step for each iteration. A similar scheme is used to solve the solute transport (Eq. (3.22)) at each time step with no flux condition at the walls (Eq. (3.14)). Next we discuss the reasoning for the parameter selection for the full simulations.

3.3.3 Selection of the physical parameter values

The problem is described by various non-dimensional parameters $(\xi_r, \xi_t, u_0, \rho, d_p, d_x, \beta, \zeta, \gamma)$, and in the following, we specifically focus on the role of confinement ζ and shear γ. To estimate these, dimensional parameter values are chosen so as to be relevant to existing experiments (see Table. 3.1). Janus particles are typically micron-sized [8, 229] ($\hat{R} \sim 10^{-6}$m) and swim at a speed of a few bodylengths/sec [68] ($\hat{U}_0 \sim 10^{-6}$m/s). Typical microfluidic channels feature sub-millimeter widths ($\hat{H} \sim 10^{-4} - 10^{-3}$ m) [12, 14] and the solute diffusion coefficient for small molecules such as dissolved oxygen gas is $\hat{D}_c \sim 10^{-9}$ m^2/s [231]. As a result, the non-dimensional swimming velocity of the particles $u_0 \sim O(1)$, therefore setting $u_0 = 0.5$ in the simulation ensures physical relevancy. We consider chemotactic particles (i.e. that reorient along local chemical gradients), and fix $\xi_r/\rho = 1.25$ and $\xi_t = -0.5$; we note that such particles leave a pusher-like hydrodynamic footprint on the surrounding fluid, Eq. (3.21). With these values, the effects of phoretic drift, chemotactic reorientation and self-propulsion are of similar magnitude resulting in complex dynamics. A stronger self-propulsion velocity would prevent the particles to form aggregates while a lower u_0 would delay the aggregates' formation [178]. The rotational diffusion coefficient for the particles can be estimated based on temperature ($\hat{T}$), radius ($\hat{R}$) and viscosity ($\hat{\eta}$) by Einstein's relation as $\hat{D}_p = \hat{k}_B\hat{T}/(8\pi\hat{\eta}\hat{R}^3) \sim 10^{-1}$m^{2}s^{-1} [230] which results in dimensionless diffusion coefficient as $d_p = \hat{D}_p\hat{H}^2/\hat{D}_c = 0.25$. Similarly, the effective translational diffusion coefficient for the particles can be estimated as $\hat{D}_x = \hat{k}_B\hat{T}/(8\pi\hat{\eta}\hat{R}) + \hat{U}_0^2\hat{D}_p^{-1}/2 \sim 10^{-11}$m^{2}s^{-1} [8], so that $d_x = D_x/D_c = 0.025$. Finally, setting $\beta = \pi/2$ results in a $O(1)$ dimensionless screening length thus ensuring that particles interact throughout the channel.

3.4 Self-organisation dynamics

The suspension's self-organisation results from different intrinsic effects (the particles' self-propulsion, their phoretic attraction/repulsion and chemotactic reorientation) and their competition with shear-induced rotation. In addition, the particles evolve in a confined setting and are transported by the flow. To shed a better light on the results presented in the rest of the paper, and understand how the dynamics of the present system arise from their interaction, we first describe how chemotaxis, flow forcing and confinement independently act on the suspension's organisation.

Self-organisation of unbounded phoretic suspensions in quiescent flows is dominated by autochemotaxis, i.e the particles' ability to sense, reorient and migrate toward or away from a specific chemical signal, here generated by the chemical signatures of their neighbours. Such chemically-driven interactions are also known to play an important role in the self organisation of biological suspensions [83,232], where the microswimmers typically change their tumbling rate depending on a specific chemical cue to create an orientation bias towards the chemical source [233]. Such chemotactic self-organisation results in a variety of complex behaviour such as pattern formation [233], swarms [234, 235], bacterial turbulence [1], etc. Janus phoretic swimmers instead exploit a front-back asymmetric coating and the resulting polarity in their interaction with suspended solutes, in order to reorient along chemical gradients [115,179]. Particle aggregation and cluster formation may result from such chemotactic interactions. For net solute producers ($\hat{A}^+ > 0$, as in the present configuration), any infinitesimal inhomogeneity in the spatial distribution of phoretic colloids triggers more solute production and local solute accumulation in specific regions [178,236]. The associated long-ranged chemical gradients generate an orientation bias towards those regions among the particles nearby, which cause their own swimming and accumulation in the regions of already-higher particle concentration (for positively-chemotactic particles). More solute is then generated there which results in a positive feedback loop and extension of the process throughout the domain [178].

The characteristic timescale for such chemotactic clustering is $\tau_c \sim (\tau_\chi/\tau_\beta)\tau_s^\lambda$ [178], where $\tau_s^\lambda \sim 1/(kU_0)$ is the characteristic time scale of self-propulsion over a perturbation wavelength $\lambda = 2\pi/k$, $\tau_\chi \sim (kC_{\text{ref}}\chi_r)^{-1}$ is the typical scale for the chemical reorientation in the concentration gradient associated with the perturbation's spatial inhomogeneity, and $\tau_\beta \sim 1/\beta$ the characteristic relaxation time of the solute concentration in the bulk. Here $C_{\text{ref}} = HA^+/\zeta D_c$ is the characteristic concentration scale obtained by balancing solute production of the particles and the diffusive flux. The definition of τ_c with respect to the three time scales can be physically understood as follows: chemical reorientation polarises the suspension towards regions of excess solute toward which a majority of the (polar) particles swim. Clustering of the self-propelled particles take a time τ_s for fully-polarized particles. Polarisation, i.e. chemical reorientation however takes a finite amount of time and τ_χ/τ_β can be seen as a measure of how much polarized the suspension is able to get before the concentration perturbation triggering the reorientation relaxes under the effect of chemical decay. This instability eventually saturates when the chemotactic flux is balanced by other processes such as diffusion and any potential repulsive phoretic drift within the chemical gradient, thus leading to the formation of high-density particle aggregates.

The suspension dynamics and self organisation are also influenced by the presence of background (i.e. externally-imposed) flows; these not only advect particles differentially in non-uniform flows, but flow gradients also introduce a local reorientation/rotation of the particles (Faxen Laws). For the anti-symmetric background flow imposed here (a simple shear flow), particles in the top half are advected in the opposite direction with respect to particles present in the bottom half, and the vorticity (and the clockwise induced rotation) is uniform throughout the channel (see Sec. 3.4.3).

Lastly, the presence of walls impermeable to both particles and chemical solutes, result in their confinement and accumulation near the boundaries, a well-known feature of any (biological or synthetic) suspension of microswimmers [12, 97, 105, 237].

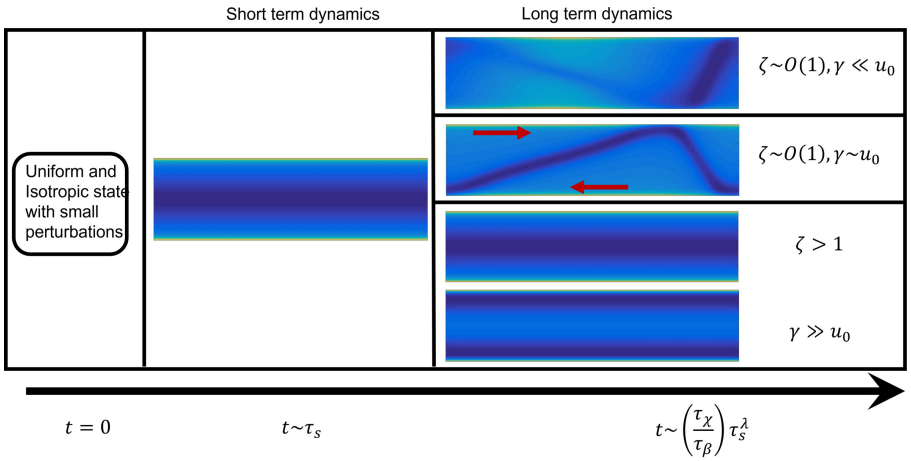

Figure 3.2: Figure depicting the overview of self-organisation of the current system. Identification of three different regimes based on shear rate and confinement. Strong shear or strong confinement tends to stabilise the 1D state.

Control parameters		Long term response	
Background Shear	Confinement	Temporal	Spatial
Strong/Weak	Strong	Steady	1D
Weak	Weak	Steady	2D
Strong	Weak	Unsteady	2D

Table 3.2: Distinctive characteristics of the long-term dynamics of the chemotactic suspension for different level of confinement and background shear forcing.

3.4.1 Overview of the suspension dynamics

Starting from an initial perturbation of the isotropic initial condition, the dynamics of the suspension can be decomposed into two successive phases occuring over two different and well-separated timescales: a short time scale associated with self-propulsion across the channel width, and a long time scale associated with self-organisation due to chemotactic instability (Fig. 3.2). Its main features are outlined here before being discussed in more details in the next subsections.

At short times, as a result of the particles' self-propulsion and of their lateral confinement, the suspension quickly develops a transient 1D state (i.e. spatially invariant in the streamwise direction). This phase and the transient state it converges to, do not depend on the shear rate or confinement ratio for the range of confinement and shear rates explored in this work(Fig. 3.2). However, the clustering timescale suggests that the clustering time reduces with decreasing confinement. As a result, in the limit of unconfined suspensions, $\zeta \to 0$, the aggregation timescale becomes shortest resulting in clustering in the short-term itself.

On the other hand, the long term solution results from the competition of chemotaxis, imposed shear and confinement; as such the long term dynamics and three regimes are obtained, as shown in table 3.2, depending on the strength of confinement and shear. These regimes can be distinguished by their spatial distribution (1D or 2D) and temporal nature (steady/unsteady). The "steady" nature of the converged state was checked for such situations by a doubling of the simulation time to ensure proper convergence.

3.4.2 Short term dynamics

Starting from the initial nearly-uniform and isotropic distribution, the suspension quickly relaxes to the 1D transient state shown in Fig. 3.3. Out of the three different effects driving the self-organisation of the suspension, namely the external shear, the chemotactic instability and self-propulsion across the channel width, the latter is associated with the shortest time scale $\tau_s^H \sim$

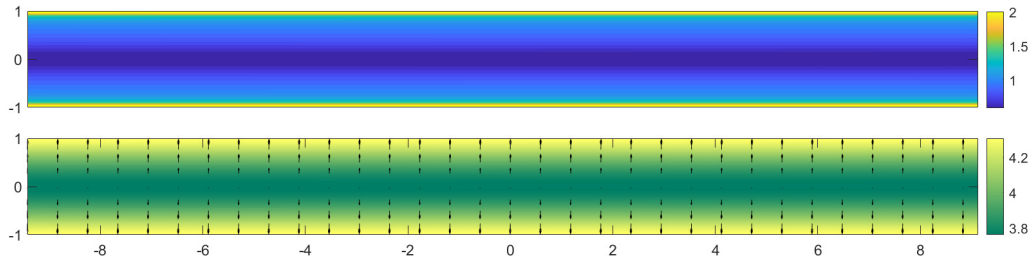

Figure 3.3: Short-term particle (top) and solute distribution (bottom) obtained for $\zeta = 1, \gamma = 0.25$. The black arrows(bottom) represent the local polarisation direction and magnitude of the particles.

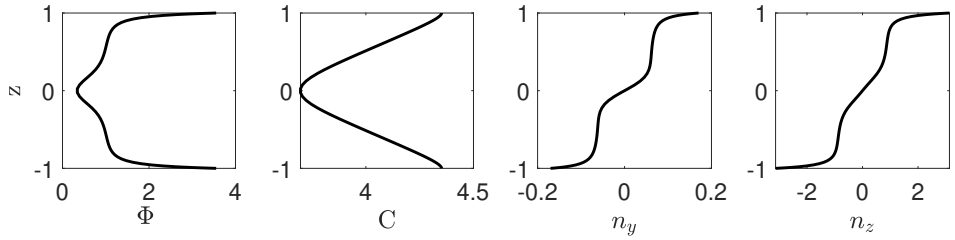

Figure 3.4: 1D profiles of the solute and particle concentrations, and streamwise and wall-normal components of the particle polarisation in the transient regime. The 1D profiles are for $\zeta = 1, \gamma = 0.25$.

H/U_0, and thus drives the dynamics of this early phase.

This 1D state is characterised by high particle densities near the boundaries (Fig.3.4), a rather intuitive behaviour that is also well-established for suspensions of biological microswimmers [97, 237]: particles located in the vicinity of an impermeable boundary and oriented towards it are trapped there as they can only escape thanks to translational and rotational diffusion; instead particles oriented away from the boundary quickly swim away from this region. This results in a strong wall polarisation $\boldsymbol{n}$, Eq. (3.3), within a thin boundary layer of particles near the channel walls (Fig.3.4), whose thickness is proportional to rotational and translational diffusion and inversely proportional to self propulsion velocity [207].

The particles are net solute producers ($A^+ > 0$), and their accumulation near the wall leads to a locally-increased solute production near the impermeable walls, resulting in an accumulation of solute in the walls' vicinity. Consequently, the solute distribution across the channel width is characterised by a V-shaped profile (Fig.3.4) associated with strong chemical gradients pointing toward the boundaries. This results in the formation of a strong solute gradient toward the boundary, which polarises the suspension toward the nearest wall under the effect of chemical reorientation ($\xi_r > 0$ here). This reorientation combined with self-propulsion reinforces the particles' polarisation, accumulation and trapping near the boundary. The chemotactic behavior of the particles and their response to rapid spatial changes in the local solute gradient direction results in a divergent chemotactic flux and an additional local dip in the particle concentration profile near the channel center line, as seen on Fig. 3.4.

3.4.3 Long term dynamics

Depending on the background shear and confinement levels, the transient 1D state described in the previous section may be unstable with respect to (slower) streamwise perturbations under the effect of chemotactic clustering. In that case, the evolution of the system toward its long-term dynamics is driven by the chemotactic instability and the typical duration of this evolution thus scales as $\tau_c \sim \chi_r C_{\text{ref}}/U_0\beta$ (see section 3.4.1). The relevant characteristic scale for solute concentration remains the one used for non-dimensionalisation $C_{\text{ref}} = HA^+/\zeta D_c$.

The long term dynamics broadly divides into two different types of regimes, depending on

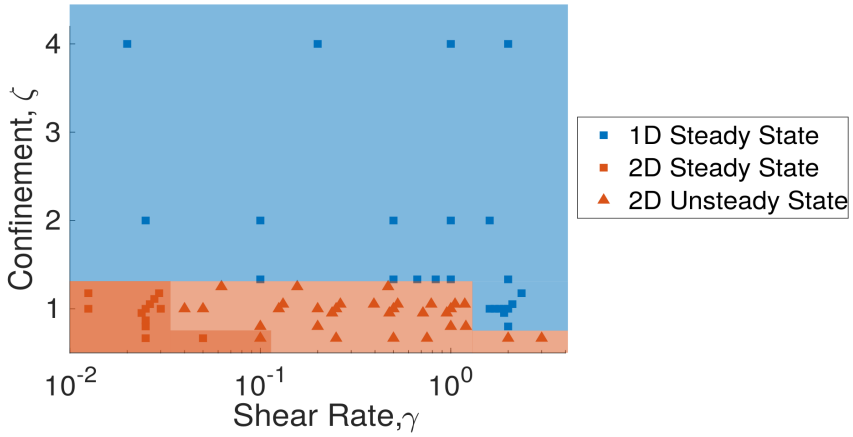

Figure 3.5: Long-term dynamics of the chemotactic suspension for varying relative shear rate γ and degree of confinement $\zeta = (\hat{H}\hat{N}\hat{R}^2)^{-1}$. Colours indicate the nature of the particle distribution: 1D (blue) and 2D (orange). Different symbols are used for steady (square) and unsteady (triangle) regimes.

Figure 3.6: 1D boundary layer chemotactic destabilisation: a small disturbance in the particle distribution along the wall and the particles' activity introduce a local increase in solute concentration (green colour) and a small horizontal bias of the orientation of neighboring particles that start swimming toward and accumulating in this solute-rich region.

the confinement level as summarized on the phase map of Fig. 3.5. For strong confinement (small channel width, $\zeta < 1$), the behaviour of the system remains that observed in the transient dynamics, namely the confinement-induced particle accumulation near the wall . In that case, the particle and solute distributions are independent of both y and t (steady 1D regime).

In contrast, when the channel width is large enough (i.e. low confinement, $\zeta > 1$), the long term solution is characterised by the formation of aggregates along each wall, breaking the y-invariance of the solution, as a result of the chemotactic instability. In such regimes, the influence of the walls is weaker and the dynamics is thus more prominently driven by the intrinsic behaviour of the chemotactic suspension, as for unconfined suspensions [205, 238]. The particle and solute distributions are now fully two-dimensional and can be steady or unsteady depending on the shear rate forcing.

These different regimes are presented and discussed in more detail in the following.

Weak confinement

For weak confinement (or in the absence of any confinement, $\zeta < 1$), the 1D transient state observed at short time becomes unstable with respect to two-dimensional (i.e. y-dependent) perturbations and evolves into the formation of 2D particles' aggregates. For confined suspensions, the 1D state is characterised by much higher density of particles near the walls and a strong polarisation of these particles towards the wall, as discussed in the previous section. This has two important consequences. First, the chemotactic instability and clustering develop preferentially within and along this concentration boundary layer. Additionnally, given the strong vertical chemical gradient of the 1D state, small disturbances in the solute concentration only significantly impact the horizontal con-

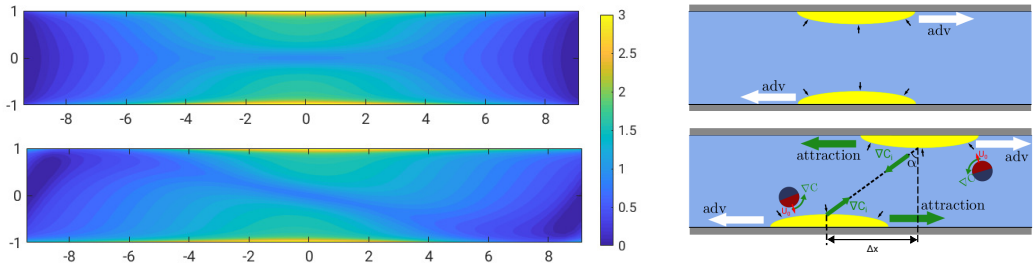

Figure 3.7: (Left) Long term particle distribution for $\zeta = 1$ and in the absence of external flow (top) and for $\gamma = 0.025$ (bottom) . (Right) Schematic representation of the opposite-walls aggregates in the absence of background flow (top) and for weak shear flow (bottom). The black arrows represent the local polarisation of the particles, white arrows show the direction of background advection and green arrow indicate the direction of chemotactic bias (reorientation).

centration gradient and particle polarisation. These two effects result in the 1D version of the more general chemotactic instability reported for unconfined suspensions [178] as shown schematically in Fig. 3.6.

In the absence of external flows, the particles form aggregates at regularly-spaced positions along each wall, determined by the dominant wavelength of the chemotactic instability. Inside each aggregate, particles remain mostly oriented toward the wall with a slight horizontal tilt to wards the center of the aggregate they belong to. For sufficiently wide channels (weak confinement), aggregates along each wall only weakly influence each other, yet, they introduce a small bias in the horizontal solute gradient seen by an aggregate located close to the opposite wall.

This cross-channel chemotactic influence is unable to overcome the strong wall polarisation and strong vertical solute gradients seen by the particles, but any offset of the aggregagtes on opposite walls introduces a (very weak) horizontal bias given by $|\nabla_x C_i| \sin\alpha$ where α is the relative position angle of the particle aggregates (Fig. 3.7). The horizontal bias coupled with self propulsion results in horizontal particle migration (Fig.3.7, bottom right) along the walls, until the aggregates are placed symmetrically. This arrangement is an equilibrium position of the system in the long term in the absence of external flows.

Externally-imposed flows (and their gradient) transport both particles and solute in the streamwise direction. For a symmetric flow such as Poiseullie flow, the particle aggregates on each wall are advected in the same direction resulting in a travelling wave solution at long times [25]. For the present Couette flow configuration (homogeneous external shear), the aggregates on either walls are transported in opposite directions, and this anti-symmetric transport competes with the chemotactic clustering described above. For relatively-weak flow forcing ($\gamma \ll u_0$), chemotaxis is strong enough to maintain a steady offset equillibrium of the aggregates (Fig. 3.7): as the background forcing is weaker than self propulsion, the particles' positions remain trapped until diffusion enables them to escape. Consequently, aggregates are slightly offset horizontally, Fig. 3.7, with an horizontal offset Δx increasing linearly with the shear intensity (Fig. 3.9) : the perturbation of the solute gradient magnitude seen by a given aggregate due to the counterpart on the opposite wall is negligible, and $\sin\alpha \approx \frac{\Delta x}{2H}$, resulting in a linear relationship between the chemotactic attraction and Δx, and thus with the convective transport by the background shear (Fig. 3.7).

When the shear rate becomes large enough, the horizontal offset of the aggregates becomes significant and the magnitude of the perturbed concentration gradient($\nabla_x C_i$) responsible of their attraction decays as $O\left(\frac{1}{d^2}\right)$ (aggregates are net solute sources) where $d = \Delta x / \sin\alpha$ is the total distance between the two aggregates. Beyond a critical horizontal separation (Fig. 3.9), the chemotactic attractive effect is not sufficient to balance the convective forcing, resulting in a continuous relative transport of the aggregates by the flow in the streamwise direction, and an unsteady but periodic dynamics (Fig. 3.8).

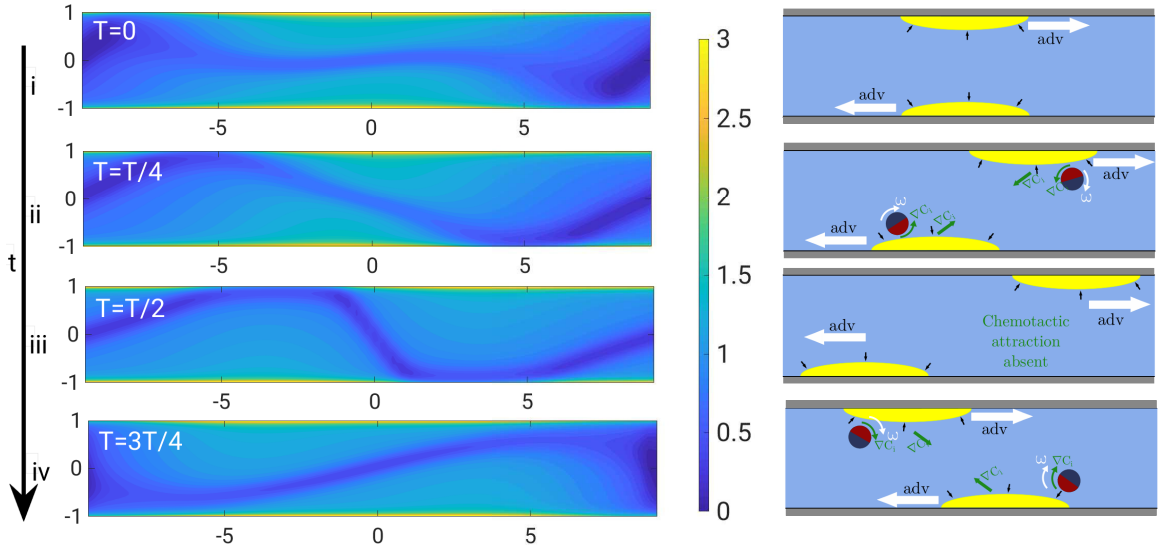

Figure 3.8: (Left) Evolution of the particle density in time over a period of the relative motion of aggregates on opposite walls for $\gamma = 0.125$ and $\zeta = 1$. (Right) Corresponding schematic representation of the position of the particles' aggregates.

This periodic regime is however characterised by an asymmetric evolution of Δx over one period (Fig. 3.9, centre), which can be understood by considering the relative direction of the chemotactic and convective forcings seen by the different moving aggregates, over a given period starting when aggregates from opposite walls are at their minimum distance ($\Delta x \approx 0$, Fig. 3.8i). During the first half-period, cross-channel chemotactic effects compete with particle and solute transport by the shear flow until they are perfectly offset from each other (i.e. maximum Δx, Fig. 3.8iii): this results, at least at first, in a slower relative motion of the aggregates in comparison with a purely convective transport. In contrast, during the second half of the cycle, chemotactic attraction by the closest opposite-wall aggregate takes some time to build up (due to the large distance of the walls) and can not significantly enhance the transport velocity, even though it is acting now in the same direction as the convective forcing. This suggests, that once the chemotactic attraction is reversed (Figure 3.8ii), the aggregates are merely advected in opposite directions by the background shear flow, and the time taken to complete this second half of the period is identical to that for two non-chemotactic aggregates. Overall, the total period of the oscillation is greater than for non chemotactic aggregates as the chemotactic attraction resists advection in the first half reducing the separation velocity (Fig. 3.9). This increase is most significant for low shear rate, as expected as chemotactic coupling is able to act longer (Fig. 3.9, right).

Strong confinement

For stronger confinement, i.e. when the channel width is comparable to or smaller than the characteristic wave length of the chemotactic instability, the influence of the confining boundary on the distribution of particles and solutes tends to suppress the onset of the chemotactic instability of the 1D state observed at short times (Sec. 3.4.2).

This was already reported on other microswimmer systems in previous experimental [10, 63] and numerical studies [226, 239] – and even in macroscopic systems [240]. Its main origin is the relative weakening of horizontal gradients of solute in comparison with the strong vertical gradients. Consequently, the particles maintain a strong vertical polarisation and horizontal reorientation and polarisation is more difficult and unlikely : the net relative horizontal displacement of the particles is then negligible. As a result, for strong confinement, the long term dynamics is invariant in y (1D) and t (steady), as in the short term. The exact particle distribution of this 1D state depends on the specific value of shear rate considered, and may be significantly different from the transient

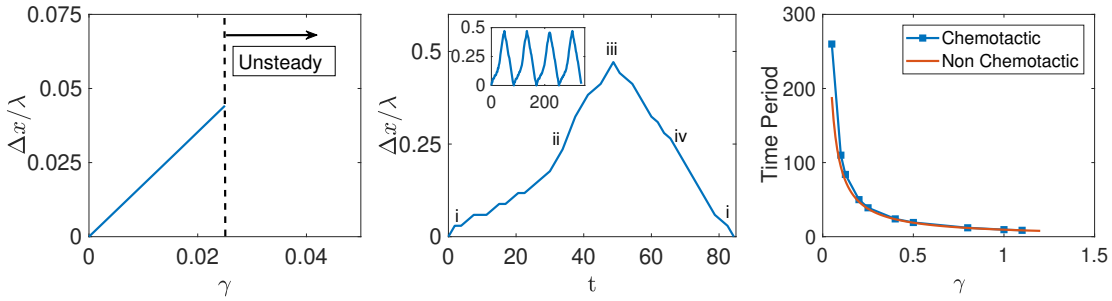

Figure 3.9: (Left) Evolution of the steady minimum offset between aggregates on opposite walls($\Delta/\lambda x$) with the shear intensity(with λ representing the wavelength of the most unstable mode), in the limit of weak shear and $\zeta = 1$. (Centre) Time evolution of $\Delta x(t)/\lambda$ for the unsteady regime at $\zeta = 1$ and sufficiently large shear forcing($\gamma = 0.125$) with λ representing the wavelength of the most unstable mode. (Right) Evolution with the shear rate intensity of the time period of the oscillations in the relative positioning of aggregates on the opposite walls for $\zeta = 1$.

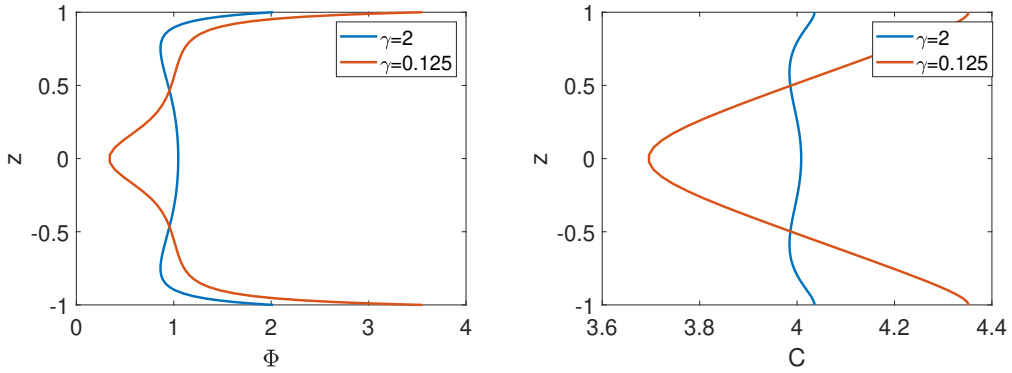

Figure 3.10: Particle distribution (left) and solute concentration (right) observed in the strongly confined regime ($\zeta = 2$) for low and high shear rates.

regime characteristics; yet, all long-term regimes share common features regardless of the shear rate intensity, including the strong polarisation and accumulation of both solute and particles near the wall. The main characteristics of these 1D regimes are illustrated on Fig. 3.10 for weak and strong shear, respectively.

For low shear rates, the long term solution is in fact essentially identical to the transient solution, being characterised by high particle density at the walls and a strong reduction of the particle density near the channel centerline (see Sec. 3.4.2). This should be no surprise: for weak shear, the flow forcing is negligible and the dominant mechanisms leading to the self-organisation of the suspension are those intervening in the short-term (namely the impermeable wall boundaries), since the 2D chemotactic instability and clustering are suppressed.

In contrast, for strong shear rates, background vorticity dominates the orientation dynamics resulting in the tumbling of particles (the particles are spherical) in the bulk of the channel where wall polarisation effects are weaker. This reduces or prevents the reorientation of particles present in the bulk in the direction of the closest wall under chemotactic effects, and maintains a larger concentration of the particles in the channel's bulk (Fig. 3.10). As a direct consequence, and due to the presence of this increased number of solute-producing particles, the chemical concentration is also higher further reducing the influence of chemotaxis toward the channel walls, flattening the solute distribution profile at high shear rates in comparison to the V-shaped profile observed at low shear values.

3.4.4 Linear Stability of the 1D equilibrium: a minimal model

In order to gain insights into the emergence of the different regimes described above as a result of the competition of confinement and shear with the chemotactic instability, we focus in this section on a minimalistic model based on a moment expansion of the probability density function. This model includes qualitatively the main physical features of the problem and we show that it is able to capture at least qualitatively some of the complex suspension dynamics, such as the long-term state for various shear rate and degree of confinement. It follows in that regard an approach already used in existing works on active suspensions [25, 207].

Its central idea is to reduce the description of the probability distribution to its first orientational moments [238], namely the particle density Φ(zeroth moment) and its local orientation $\boldsymbol{n}$(first moment). We refer the readers to appendix B for more details on the governing equation and its derivation. Such models are often applied to non-chemotactic elongated swimmers, whose interactions depend critically on the second moment of Ψ [195, 238]. In contrast, interactions among spherical Janus particles and with the background flow can already be included in a model involving only the zeroth (concentration) and first moments (orientation).

We noted that a full simulation of the system systematically predicted the emergence (at least transiently) of a 1D y-invariant state for all the simulations performed for the range of degree of confinement(ζ) and shear rate(γ) considered in this work. Depending on the relative importance of confinement, shear and chemotaxis, this invariance along the horizontal was either maintained at long times or evolved toward steady/unsteady 2D regimes. We interpret this long term evolution of the system as the result of the stability/instability of the system's steady 1D solution of the problem. Formulation of the regime selection as a simple eigenvalue problem is one of the main goal of the present reduced model for which the stability analysis can be carried out more easily.

With that objective in mind, we first seek a 1D equilibrium solution by marching a 1D version of the reduced equations Eqs. (B.3)–(B.5) and (3.22) [25]. The existence of such a symmetric 1D solution (Fig. 3.11) and its qualitative similarity with the 1D transient state of the full simulations (Fig. 3.4) is a clear indication that the present reduced model is able to qualitatively capture strong wall polarisation and high particle density near the wall.

In a second step, the full (2D) reduced equations are linearised around that 1D steady state:

$$\begin{aligned} \Phi &= \Phi_0(z) + \epsilon\Phi_1(y,z,t), \\ \boldsymbol{n} &= \boldsymbol{n}_0(z) + \epsilon\boldsymbol{n}_1(y,z,t), \\ C &= C_0(z) + \epsilon C_1(y,z,t), \end{aligned} \tag{3.54}$$

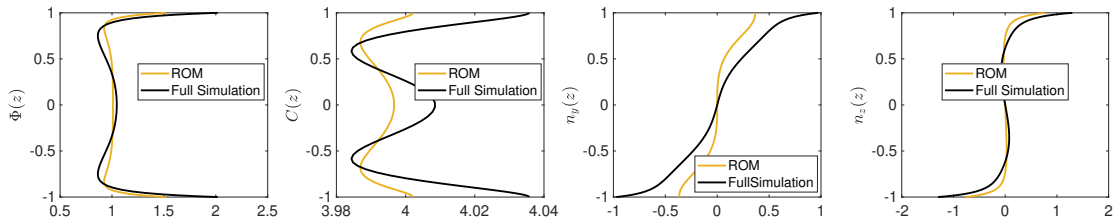

Figure 3.11: Comparisson between the 1D steady states obtained by solving 1D version of the reduced order equations to the full simulation for $\zeta = 1$ and $\gamma = 1.5$.

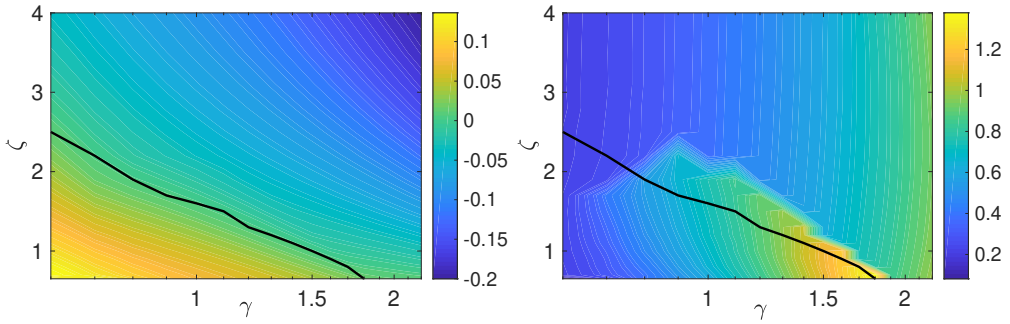

Figure 3.12: (Left) Linear growth rate($Re(\sigma)$) as a function of background shear and degree of confinement. (Right) Frequency($Im(\sigma)$) of the most unstable mode as a function of background shear and degree of confinement. The black curve is the neutral stability curve separating the stable region from the unstable region.

where 0 and 1 subscripts refer to the steady 1D state and unsteady 2D perturbation, respectively. Linearising the governing equations at $O(\varepsilon)$, and assuming a normal mode decomposition in (y,t) for the perturbation fields $\Phi_1, \boldsymbol{n}_1$ and C_1:

$$\Phi_1(y,z,t) = \tilde{\Phi}(z,k)e^{iky+\sigma t},\ \boldsymbol{n}(y,z,t) = \tilde{\boldsymbol{n}}(z,k)e^{iky+\sigma t},\ C_1(y,z,t) = \tilde{C}(z,k)e^{iky+\sigma t}. \quad (3.55)$$

The linearised set of equations can be recast into an eigenvalue problem of the form

$$\mathcal{G}[\boldsymbol{x}_0]\cdot\tilde{\boldsymbol{x}} = \sigma\tilde{\boldsymbol{x}} \quad (3.56)$$

where $\tilde{\boldsymbol{x}}$ is a column vector containing the perturbation amplitudes, $(\tilde{\Phi}, \tilde{n}_y, \tilde{n}_z, \tilde{C})$ with $\mathcal{G}[\boldsymbol{x}_0]$ a linear operator that depends on the 1D base state. The real and imaginary parts of the eigenvalue σ, namely $\mathrm{Re}(\sigma)$ and $\mathrm{Im}(\sigma)$ are respectively the growth rate and frequency of the perturbation.

This eigenvalue problem is discretized using a Gauss-Lobatto grid with $N+1$ points $(z^{(i)})_{1\le i\le N+1}$ across the channel width. The eigenvector $\tilde{\boldsymbol{x}}$ is now

$$\tilde{\boldsymbol{x}} = \left[\tilde{\Phi}(z^{(1)}),...,\tilde{\Phi}^{(N+1)},\tilde{n}_y^{(1)},...,\tilde{n}_y^{(N+1)},\tilde{n}_z^{(1)},...,\tilde{n}_z^{(N+1)},\tilde{C}^{(1)},...,\tilde{C}^{(N+1)}\right] \quad (3.57)$$

and the discretised linear operator $\mathcal{G}$ is now obtained from pseudo-spectral differential operators with modifications to include the boundary conditions corresponding to Eqs.(B.3)–(B.4). Following Ref. [25], this eigenvalue problem, Eq. (3.56) is solved numerically using MATLAB's algorithm based on the principle of minimized iterations [241]. Eq. (3.56) is solved for discrete values of $0 \le k \le 2$ with a discrete step size of 0.01; the maximum value of $Re(\sigma)$ is reported in Fig. 3.12.

Figure 3.12 (left) shows the variation of the growth rate of the least stable or most unstable mode (i.e. that with largest growth rate, $\mathrm{Re}(\sigma)$), as a function of shear rate (γ) and confinement (ζ). The growth rate reduces with an increase of either background shear or degree of confinement demonstrating the stabilising effect of both mechanisms, already observed on the full simulation. Above the neutral curve, which corresponds to the parameters where the least stable mode is neutral ($\mathrm{Re}(\sigma) = 0$), the 1D fixed point is therefore stable (all eigenmodes have negative growth rate) with

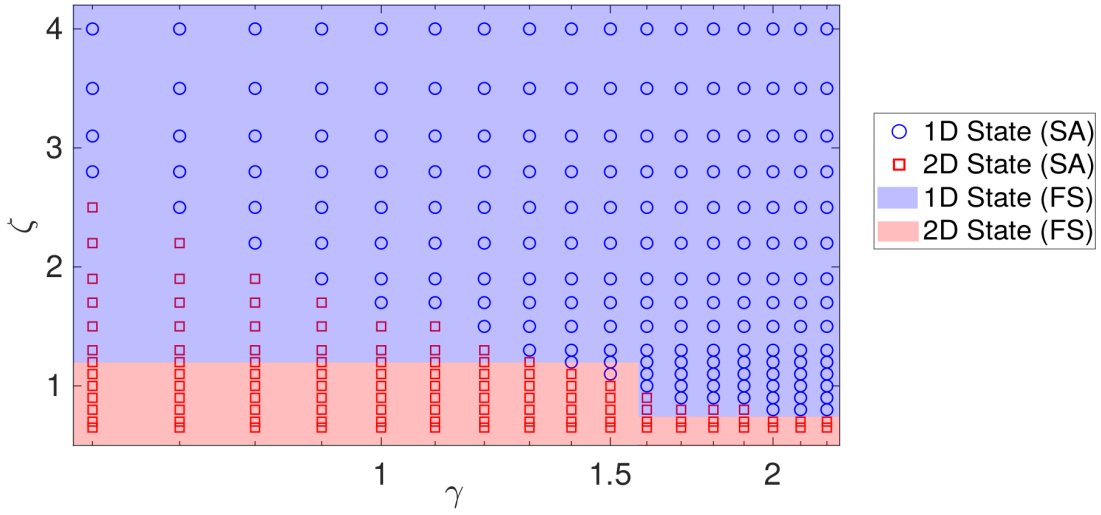

Figure 3.13: Comparison of the phase plot obtained via the linear stability analysis (referred to as SA in the legend) with the phase plot obtained using the full simulation (referred to as FS in the legend)Red squares represent unstable 1D state while the blue circles represent the stable 1D state.

respect to 2D perturbations, an observation that is also consistent with the results of the full model that predict a $1D$ steady long-term dynamics for the larger values of γ, ζ (strong confinement or shear).

For lower shear and/or confinement, there exists at least one unstable mode whose frequency $\mathrm{Im}(\sigma)$ indicates the temporal nature of the dominant mode (oscillatory or monotoneous). Fig. 3.12 (right) shows that (i) $\mathrm{Im}(\sigma)$ is non zero, so that the dominant mode is oscillatory in nature. Furthermore, $\mathrm{Im}(\sigma)$ is positive and increases with shear, for the range of shear rate and confinement considered here. This observation is consistent with the results of the full simulations (Sec. 3.4.3) which noted the oscillatory effect introduced by an increasing shear, introduced by the periodic interaction of chemotactic aggregates located along each boundary as they are advected in opposite directions by the background shear. Indeed, the present minimalistic model includes such background advection ($\boldsymbol{u} \cdot \nabla_x \Phi$ in Eq.B.3). Note however, that the full simulations predicted a *steady* 2D regime at low shear rates, when the background shear is sufficiently weak for chemotaxis to be able to compensate the advection of opposite-wall aggregates. This discrepancy is somewhat not surprising, as it occurs in the low shear rate regime which we do not expect the present model to be able to reproduce/predict properly as one of the model's key assumption lies in its neglecting of all other contribution to the flow field than the background shear flow itself (see Appendix B).

Finally, based on $\mathrm{Re}(\sigma)$ and $\mathrm{Im}(\sigma)$ we plot a phase diagram similar to Fig. 3.5 as shown in Fig. 3.13. In Fig. 3.13 data points shown by red squares have a positive growth rate for the most unstable eigen mode with non-zero frequency. The most unstable eigen mode corresponds to asymmetric wall aggregates as shown in Fig. 3.14, and therefore this region corresponds to 2D ($\mathrm{Re}(\sigma) > 0$) and unsteady($\mathrm{Im}(\sigma) > 0$) long term dynamics. Whereas, for data points marked with blue circles, the 1D fixed point is stable and the long-term solution is 1D steady state (despite $\mathrm{Im}(\sigma) > 0$ as the 1D fixed point is stable). This phase diagram qualitatively resembles with the phase diagram corresponding to the full simulations (Fig. 3.5). As expected, the match is particularly good in the strong shear region($\gamma \sim 2$) where the reduced order model correctly predicts the transition from the 2D unsteady state and 1D steady state at $\zeta \sim 0.8$.

To summarise, the reduced order equations show existence of a y-independent equillibrium

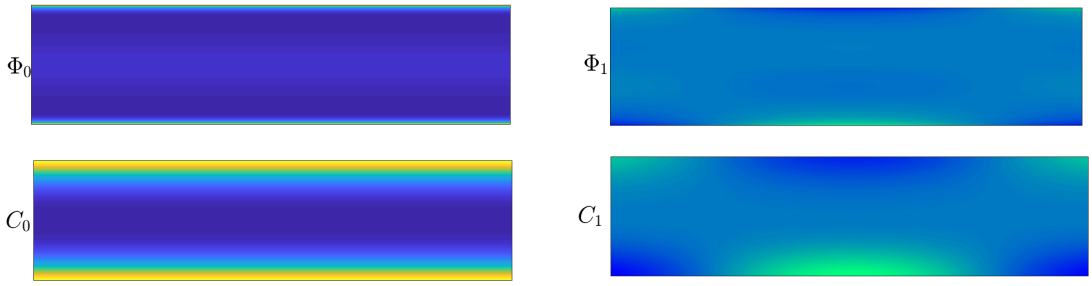

Figure 3.14: (Left) The steady state particle distribution and (right) real part of the eigenmodes of the particle density and solute distribution corresponding to the most unstable mode.

state with strong particle and solute concentration at the walls. Streamwise perturbation of this 1D fixed point shows that asymmetric eigenmodes with aggregate formation on either wall exist for weak confinement. The imaginary part(representing the oscillation frequency) corresponding to the unstable eigen mode is non zero leading to 2D unsteady dynamics in the long term below the neutral stability curve(Fig.3.12). The linear perturbation analysis reveals that the 1D fixed point is stable for strong bakground shear and strong confinement resulting in a 1D steady state solution in the long term in agreement with full simulation results. Thus, this simple model is able to qualitatively capture complex self-organisation dynamics with sufficient accuracy.

3.5 Rheology of phoretic suspensions

In this section, we analyze the rheological behaviour of the phoretic suspension as a result of the previously-discussed self-organisation. It is now well established that microswimmer suspensions, through the microscopic mechanical forcing they exert on their surroundings, can profoundly modify the macroscopic behaviour of the fluid and in particular its rheology [13, 14, 137]. We begin the analysis by defining an 'effective' viscosity of the suspension, based on the tangential stress exerted by the fluid and particles on the plate. The particles indeed modify the velocity field from a pure Couette flow and we thus analyze the flow patterns induced by the particles for the different states discussed in Sec. 3.4.3. The flow organization results from multiple tightly linked factors, and in order to gain a better physical insight, a simplified model retaining the dominant phenomena is discussed in detail in Sec. 3.5.3. Finally, the temporal variation of the effective viscosity for different states and the effect and shear and strength of confinement on effective viscosity is presented.

3.5.1 Defining an effective viscosity

Viscosity is classically introduced as the ratio of the local stress and strain rate in Newtonian fluids, however when the fluid or suspension shows a non-Newtonian behaviour, as for active suspensions, such an approach can become more difficult as the relative magnitude of stress and strain rate is expected to strongly depend upon the location considered.

Alternatively, the viscosity can also be defined based on classical *global* results on parallel flows. This approach is commonly employed in effective viscosity measurements in Taylor-Couette devices for passive and active suspensions alike [14, 90, 132]. This is also the point of view adopted for dilute phoretic suspensions in pressure-driven flows in Ref. [25], where the definition of an effective viscosity is based on the classical Poiseuille law relating the imposed pressure drop and flow rate within the channel. The advantage of such an approach is the particular relevance of pressure-driven pipe flows for different industrial, microfluidic or biomedical applications, but it overlooks the intrinsic non-uniformity of the imposed shear rate in such parabolic flow configuration.

A similar approach is followed here on the simpler Couette-like flow configuration, where an anti-symmetric translation of the top and bottom boundaries results in a uniform shear stress dis-

tribution for Newtonian fluids. The effective viscosity can then be defined as the ratio of the force per unit area required to maintain the imposed translation of the boundaries, and compared to the Newtonian viscosity of the solvent obtained in the absence of the particles. More precisely, in the absence of particles, the force to apply on the plate is measured as $\hat{F} = \hat{\eta}\hat{\gamma}\hat{A}_s$, where $\hat{\eta}$ is the viscosity of the Newtonian fluid, $\hat{\gamma} = \hat{u}_w/\hat{H}$ is the imposed shear rate and $\hat{A}_s$ is the surface area considered. For a microswimmer suspension, we extend this definition by defining the suspension's effective viscosity $\hat{\eta}_e$ as $\hat{\eta}_e = \hat{F}/\hat{\gamma}\hat{A}_s$, with $\hat{F}$ now computed in the presence of the phoretic particles in terms of the total fluid stress tensor $\hat{\boldsymbol{\Sigma}}$ as

$$\hat{F} = \int_{\hat{A}_s} \hat{\boldsymbol{n}}_{\boldsymbol{n}} \cdot \hat{\boldsymbol{\Sigma}} \cdot \hat{\boldsymbol{t}}_{\boldsymbol{n}} d\hat{A}_s \qquad \text{with } \hat{\boldsymbol{\Sigma}} = -\hat{q}\boldsymbol{I} + \hat{\eta}\left[\hat{\nabla}_x \hat{\boldsymbol{u}} + (\hat{\nabla}_x \hat{\boldsymbol{u}})^T\right] + \hat{\boldsymbol{S}} \tag{3.58}$$

where $\hat{\boldsymbol{n}}_{\boldsymbol{n}} = -\boldsymbol{e}_z$ and $\hat{\boldsymbol{t}}_{\boldsymbol{n}} = \boldsymbol{e}_y$ are the normal and tangential vectors to the upper plate. It should be noted here that the phoretic particles modify $\hat{F}$ (and $\hat{\eta}_e$) both directly via their active stresses, and indirectly via the viscous stresses exerted by the modified flow fields resulting from their self-organisation and cumulated forcing. The relative viscosity can then be defined as $\eta_r = \hat{\eta}_e/\hat{\eta}$.

Substituting the total stress field in Eq. (3.58) and using the no penetration boundary condition at the plate results in

$$\hat{F} = \int_{A_s} \hat{\boldsymbol{n}}_{\boldsymbol{n}} \cdot \hat{\boldsymbol{\Sigma}} \cdot \hat{\boldsymbol{t}}_{\boldsymbol{n}} d\hat{A}_s = \int_{A_s} \left(\hat{\eta}\frac{\partial \hat{u}_y}{\partial \hat{z}} + \hat{\boldsymbol{n}}_{\boldsymbol{n}} \cdot \hat{\boldsymbol{S}} \cdot \hat{\boldsymbol{t}}_{\boldsymbol{n}}\right) d\hat{A}_s. \tag{3.59}$$

As a result, the relative effective viscosity is given by,

$$\eta_r = 1 + \frac{1}{A_s}\int_{A_s} \left(\frac{1}{\gamma}\frac{\partial u_{d,y}}{\partial y} + \frac{\boldsymbol{n}_{\boldsymbol{n}} \cdot \boldsymbol{S} \cdot \boldsymbol{t}_{\boldsymbol{n}}}{\gamma}\right) dA_s. \tag{3.60}$$

where u_d and γ are the disturbance velocity field and the shear rate respectively. It is important to note that in this formulation, the effect of the finite size of the particles and the influence of the resulting non-deformation stress are neglected. As a result, the effective viscosity of a passive suspension is equal to that of the pure solvent, i.e. thereby neglecting the Einstein's viscosity contribution to the suspension stress in this dilute limit [242].

It is also noteworthy yet expected that the modification of the relative viscosity tends to zero in the limit where the imposed shear rate is large (in comparison with the diffusion of solute): as the externally imposed shear rate increases, the relative influence of the particles' active stress becomes negligible, and the particles behave similarly to passive particles as confirmed experimentally [12, 14, 90].

Its definition in Eq. (1.1) identifies clearly two contributions to the effective viscosity, namely the Newtonian solvent stress resulting from the flow induced by the particles and the active stress exerted by the particles directly on the wall. In an effort to elucidate more precisely the effect of the former, we first discuss the induced flow field generated for different shear forcing and confinement in Sec. 3.4.3 before considering to the global evolution of the effective viscosity in Sec. 3.5.4.

3.5.2 Induced Flow

The particle-driven disturbance flow is significantly influenced by the particles' self-organisation and we discuss here the characteristics of these induced flows for the different types of suspension dynamics observed at long times when varying confining and forcing conditions, as discussed in Sec. 3.4.3. Stokes' equations are instantaneous; furthermore, the solute's relaxation is much faster than that of the particles: as a result, the induced flow at a given time essentially depends on the particles' distribution at that specific time only. In the following, we therefore discuss the induced flow field instantaneously, i.e. without considering the steady/unsteady nature of the self-organisation dynamics: in an unsteady regime, one expects to observe successively the different induced flows generated by the successive particles' organisation in time.

For weak confinement, and depending on the flow forcing, the active suspension self-organizes into regularly distributed wall aggregates along each wall either moving or stationary as discussed in

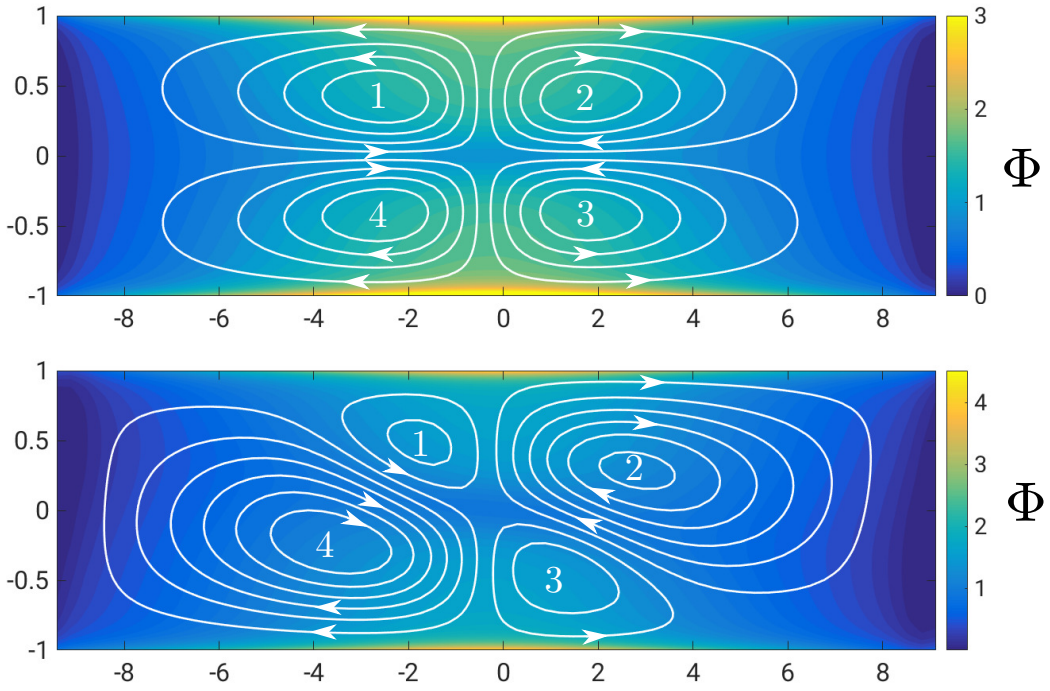

Figure 3.15: Streamlines of the induced flow for 2D steady state for $\gamma = 0$(top) and $\gamma = 0.0167$(bottom).

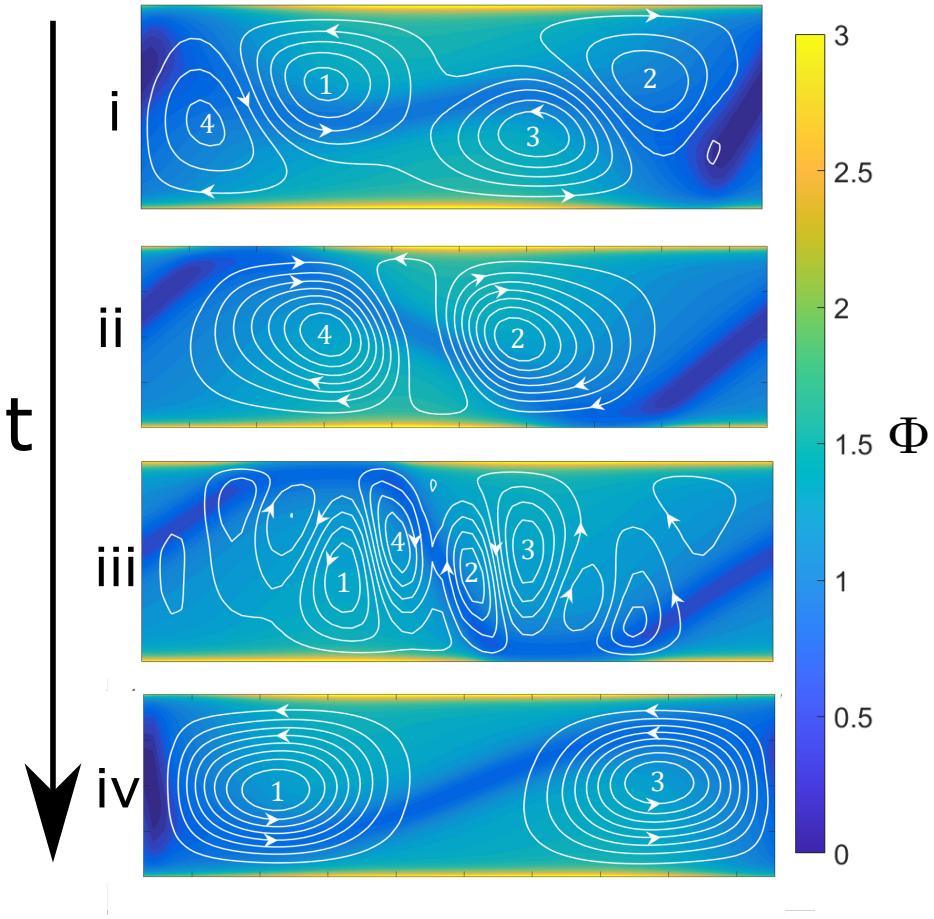

Figure 3.16: Evolution in time of particle density distribution and induced flow streamlines over a period of the unsteady regime, (i) $t = 0$, (ii) $t \sim T/4$, (iii) $t \sim T/2$ and (iv) $t \sim 3T/4$ with $\gamma = 0.125, \zeta = 1$.

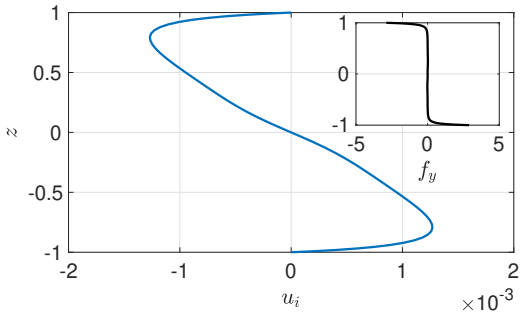

Figure 3.17: (Left) Induced Flow field for the 1D symmetric flow for 1D steady state regime with $\gamma = 0.125, \zeta = 1.33$, inset shows the driving force due to active stress exerted by the particles.

Sec. 3.4.3. In the absence of a background flow, the aggregates are placed symmetrically with particles oriented mainly toward the closest wall in response to the confinement-induced solute gradient (Fig. 3.7). As a result the induced flow is also top-down and left-right symmetric and is characterized by two pairs of counter-rotating vortices (Fig. 3.15), driven by the particles' aggregates with a dominant stagnation point flow toward the wall driven by the aggregates.

The introduction of a background shear breaks the symmetry in the particle organisation and transport (see Sec. 3.4.3). Consequently, the induced flow also loses such top-down and left-right symmetries: for weak shear, the induced flow still consists of four vortices with one of the two pairs of co-rotating vortices becoming dominant over the other one which gradually disappears as shear is further increased Fig. 3.15. The rotation direction of the dominant and surviving vortex pair strongly depends on the relative arrangement of the staggered vortices (Fig. 3.16). For instance, if the top aggregate is displaced towards the right of the bottom aggregate, the counter-clockwise vortices in the first and third quadrant (1,3) are brought closer to and counteract each other thus forming a weaker pair, leaving the clockwise rotating vortices of the second and fourth quadrant (2,4) dominant. The reverse configuration is observed when the top aggregate is located slightly to the left of the bottom one (Fig. 3.16). As shear is further increased and the suspension's organisation becomes unsteady and periodic, the vortex arrangement can be understood similarly in terms of the successive aggregates' relative positions during a period, by exploiting the instantaneous nature of the Stokes problem. Such vortex flows are reminiscent of flows observed for bacterial suspensions [10, 243, 244] and in other active systems [245]. A more detailed explanation of the induced flow is discussed in the next subsection, in particular the link between local polarization, the direction of the concentration gradient and the induced flow.

Strong confinement stabilizes the chemotactic instability resulting in 1D particle distribution with high particle density near the channel walls as discussed in Sec. 3.4.3. The particles are strongly polarised toward the wall but can be slightly tilted by the imposed shear, resulting in a net horizontal fluid forcing near the wall regions. Such 1D induced flow closely resembles induced flow already reported in experimental and numerical studies on microswimmer suspensions as well [10,106,226].

3.5.3 A simplified model for the induced flows

In an effort to provide a more intuitive insight into the role of particle distribution, local polarisation and solute concentration gradient in the establishment of the induced flows, a qualitative form of the fluid forcing induced by the particles is presented in this section. To this end, qualitative observations are made on the numerical results for the parameter values and ranges considered here.

While the magnitude of the self-induced stresslet $\boldsymbol{S_s}$ is intrinsic and fixed for each particle, that of the stresslet $\boldsymbol{S_e}$ induced by external concentration gradients depends on the local concentration gradient,Eq. (3.12). Therefore depending on the local solute distribution arrangement, each particle will either behave as a net pusher or a net puller. The no-flux condition at the wall for the solute concentration together with solute diffusion ensures that $|\nabla_x C| \sim O(1)$ everywhere and at all times (see Fig. C.1 and appendix C). For the specific values chosen here for ξ_t, ξ_r and u_0, the strength

of the pusher contribution is therefore almost twice that of the puller contribution, which is further confirmed by noting the similarity in flow patterns (see Fig. C.2 and appendix C)) obtained for the full forcing or using solely the pusher contribution (i.e. ignoring the externally-induced stresslet). Note that such similarity is also observed throughout the simulation. This suggests that the phoretic particles considered here behave as net pushers with modified stress intensities $\sigma_m \sim \alpha_s + \alpha_e$ ($\sigma_m < 0$).

Furthermore, as a result of the relatively strong concentration gradients and chemotactic behaviour of the particles, the suspension is strongly polarised (i.e. $|\boldsymbol{n}|$ roughly close to 1, see Fig. C.1) in particular close to the wall where solute and particles accumulate: locally, most particles share the same orientation which is close to that of the local solute concentration gradient. As a first approximation, it is therefore possible to consider that $\Psi(\boldsymbol{x},\mathbf{p},t) \sim \Phi(\boldsymbol{x},t)\delta(\boldsymbol{p}-\boldsymbol{n}(\boldsymbol{x},t))$ with $\boldsymbol{n} \approx \nabla_x C/|\nabla_x C|$, which significantly simplifies the description of the suspension. In particular, the average active stress field is now simply given by

$$\langle \boldsymbol{S} \rangle = \int_\Omega \Psi(\boldsymbol{x},\boldsymbol{p})\boldsymbol{S}(\boldsymbol{p})d\boldsymbol{p} \approx \boldsymbol{S}(\boldsymbol{n}) \int_\Omega \Psi(\boldsymbol{x},\boldsymbol{p})d\boldsymbol{p} = \sigma_m \Phi(\boldsymbol{x}) \left(\boldsymbol{nn} - \frac{\boldsymbol{I}}{2} \right). \tag{3.61}$$

The fluid forcing is then

$$\boldsymbol{f} = \nabla_x \cdot \langle \boldsymbol{S} \rangle = \boldsymbol{S}(\boldsymbol{n}) \cdot \nabla_x \Phi + \Phi(\nabla_x \cdot \boldsymbol{S}(\boldsymbol{n})). \tag{3.62}$$

Both terms of Eq. (3.62) in fact roughly provide similar forcing throughout the domain (with different magnitudes) as seen in Fig. C.3. As a result, retaining one of the two terms of Eq. (3.62) with a corrected amplitude ($\nu > 0$ in this case based on Fig. C.3 in Appendix. C). Thus,

$$\boldsymbol{f} = \nu \boldsymbol{S} \cdot \nabla_x \Phi \tag{3.63}$$

further simplifies the problem's description and treatment without qualitatively changing the effect of active forcing. The exact value of ν can be determined by taking the ratio of the two components; we however note that the precise chosen value does not modify the conclusion qualitatively.

We now employ the relation to quantitatively understand the induced flow for 1D and 2D regimes.

1D regime

As the particle density varies only in the vertical direction, the fluid forcing simplifies to

$$\boldsymbol{f} = \nu \sigma_m \left(\boldsymbol{nn} - \frac{\boldsymbol{I}}{2} \right) \cdot \frac{d\Phi}{dz} \boldsymbol{e_z} \tag{3.64}$$

Here, we are interested in the horizontal component of this forcing, namely $f_y = \nu \sigma_m n_z n_y \frac{\mathrm{d}\Phi}{\mathrm{d}z}$, as it is responsible for the emergence of the induced flow observed in Fig. 3.17 – the y-independent vertical forcing simply modifies the pressure distribution across the channel. Here $\nu > 0$ (see Fig. C.3) and $\sigma_m < 0$ and emergence of horizontal forcing is therefore tightly linked to horizontal polarization, away from the local (mostly vertical) solute gradient. Such a tilt of the particles is caused by the background shear flow which rotates the spherical particles in the clockwise direction throughout the channel. In a steady regime, this hydrodynamic torque is balanced by the chemotactic one that tends to bring the particles back to a vertical orientation; the particles thus maintain a slight clockwise tilt, i.e. $n_y > 0$ ($n_y < 0$) in the upper (resp. lower) half of the channel. In that region, the concentration gradient and particles' vertical polarisation are directed toward the upper (resp. lower) wall, $\mathrm{d}\Phi/\mathrm{d}z, n_z > 0$ (resp. $\mathrm{d}\Phi/\mathrm{d}z, n_z < 0$) and $\sigma_m < 0$ so that $f_y < 0$ (resp. $f_y > 0$) and the induced forcing acts against the background flow.

The flow forcing by the particles is maximum at the walls where a no-slip condition is enforced, and thus results in a maximum magnitude of the induced flow field slightly away from the no-slip walls (Fig.3.17).

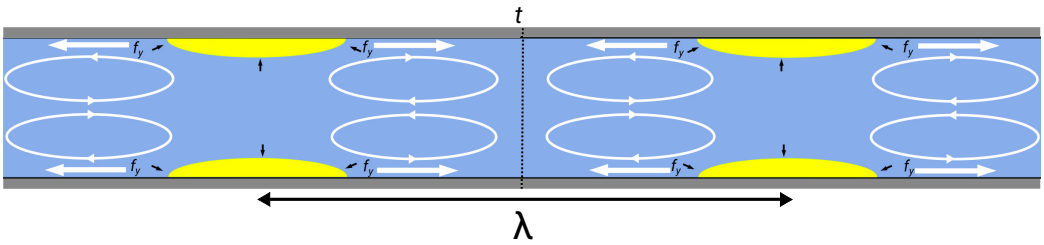

Figure 3.18: Illustration of the fluid flow for 2D symmetric case. The white arrows show the direction of horizontal fluid forcing, and the black arrow shows particle polarization. The fluid forcing changes direction at a point t equidistant from the aggregates in the same wall due to a change in horizontal polarization.

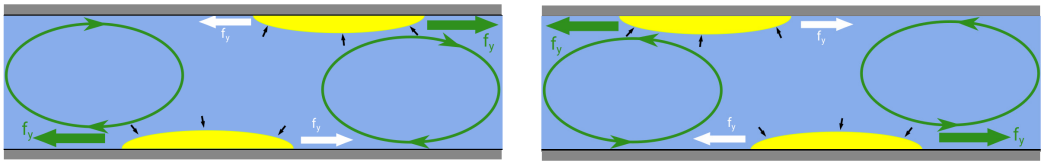

Figure 3.19: Schematic showing asymmetrical horizontal forcing which leads to two vortices with the same direction of rotation. Green arrows show the relative dominant flow forcing resulting in the two vortex flows shown in green. The relative increase in the flow forcing is due to the orientation bias created to due to the presence of aggregate on the opposite wall.

2D regimes

We now turn to the 2D suspension dynamics and first consider the symmetric and steady flow induced in the absence of any background flow as discussed in Sec. 3.4.3. The particles are positively aligned along the solute gradient which roughly follows the gradient $\nabla_x \Phi$ in particle density. The particles are net pushers and exert an extensile forcing along their direction, i.e. toward and away from the aggregates. As the particle concentration increases toward the aggregates, the forcing by each particle toward the accumulation region is counteracted by a stronger forcing in the opposite direction by the particles located in front of it. As a result, the net flow forcing by the particles is oriented against their polarisation and away from the chemotactic aggregates. Consequently, particles present on the right (left) of aggregate induce a flow in positive (negative) y-direction, leading to a pair of counter-rotating vortices oriented as illustrated on Fig. 3.18, and by mass conservation, a vertical flow pumping toward each aggregate and recirculation into the four-cell structure described in Sec. 3.5.2.

The same arguments remain applicable for non-symmetric chemotactic aggregates. The top-down symmetry is now broken resulting in an asymmetry of the horizontal forcing (Fig. 3.19). Considering for example the configuration where the top aggregate is positioned on the right of its bottom counterpart, particle horizontal polarisation around the top aggregates is now weaker on the left, where it is perturbed by the closer presence of the bottom aggregate, than on the right side, resulting in a stronger forcing by the latter that drives the dominant clockwise vortex below. Similar arguments can be followed to rationalise the dominance of a pair of counter-clockwise vortices when the top aggregate is located on the left of the bottom one.

3.5.4 Time evolution of the effective viscosity

Having understood the flow field forced by the particles in the different regimes, it is now possible to consider the modified force exerted by the suspension on the moving plate and compute the effective viscosity of the suspension in this Couette geometry as defined in Sec. 3.5.1. The time evolution of viscosity is directly related to the suspension's self-organisation and its steady/unsteady evolution is a clear reflection of the steady/unsteady nature of the particle distribution.

In all simulations, $\eta_r = 1$ initially in all cases (there is no net induced flow for an isotropic and

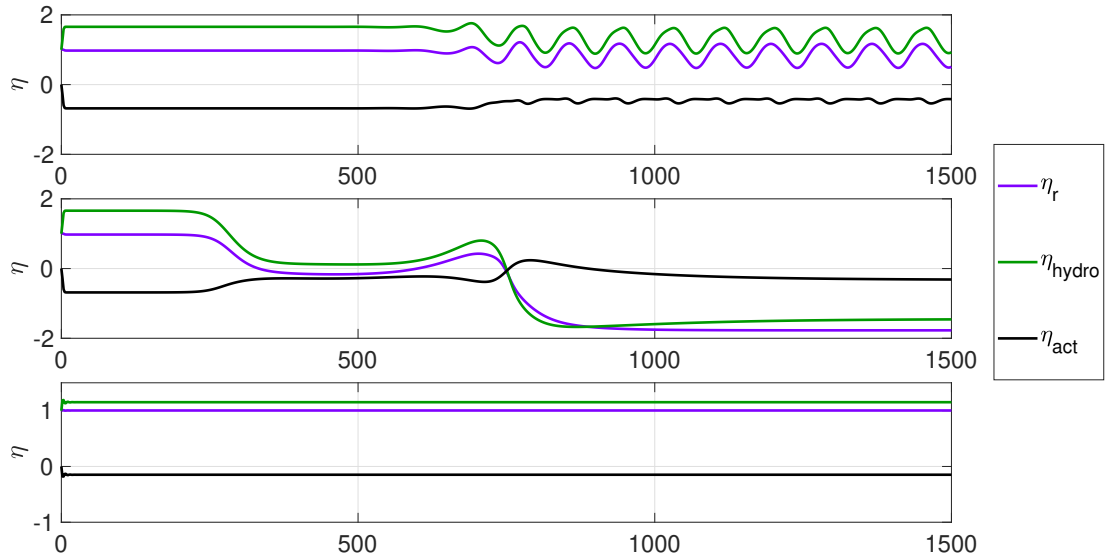

Figure 3.20: Time evolution of effective viscosity($\eta_r = \eta_{hydro} + \eta_{act}$) for 2D unsteady (top) state and 2D steady state(centre) and 1D steady state (bottom) for parametric values $\gamma = 0.125, \zeta = 1$(top), $\gamma = 0.025, \zeta = 1$(centre) and $\gamma = 2, \zeta = 1$.

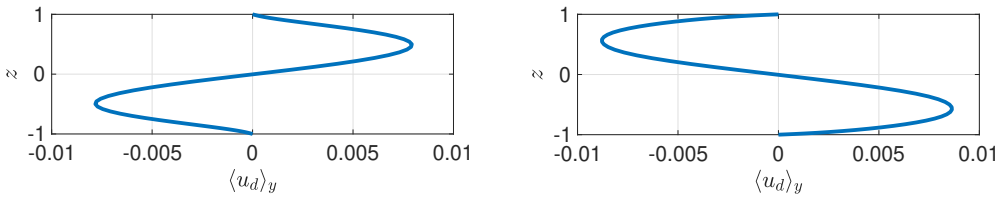

Figure 3.21: $\langle u_d \rangle_y$ (average disturbance velocity profile) for the 2D particle distribution with top aggregate displaced right (left) of bottom aggregate and (right) top aggregate displaced to the left of bottom aggregate for $\gamma = 0.125, \zeta = 1$ (Unsteady regime).

uniform suspension). A weak reduction of the effective viscosity is observed during the transient 1D state, but the decomposition of the suspension forcing on the plate into a hydrodynamic part (the shear force resulting from both the imposed and induced flows) and an active part (stress exerted directly by the particles on the plate) shows that both effects are of appreciable amplitude and act in opposite directions, with the hydrodynamic and active contributions respectively enhancing and reducing the total force to apply on the plate and the effective viscosity. The former is the result of the induced flow counteracting the background shear flow resulting from the rightward motion of the plate, thus enhancing the velocity gradient at the wall and resulting shear force. The direct active force exerted by the particles on the top wall can be written as $f_w = \boldsymbol{n_n} \cdot \boldsymbol{S} \cdot \boldsymbol{t_n} \approx -\sigma_m n_y n_z \Phi$, with $\boldsymbol{n_n} = -\boldsymbol{e}_z$ and $\boldsymbol{t_n} = \boldsymbol{e}_y$ the unit normal and tangent vectors at the wall. Here, $\sigma_m < 0$ and $n_y n_z > 0$ at both the walls as discussed previously, resulting in a net force pushing the plate in the flow direction, thus reducing the effective viscosity. As the 1D transition state is stable for strong confinement, the viscosity remains at a constant value throughout the simulation (Fig. 3.20). This corresponds to the region marked with yellow boundaries in Fig. 3.23 (right) and the plateau region in Fig. 3.23 (left) which correspond to high shear.

For weak confinement and strong shear forcing, the long-term suspension's response and effective viscosity are unsteady but periodic (Fig. 3.20). The oscillation of viscosity can be understood as the result of the changing directions of rotation of the vortex cells identified in the unsteady 2D regime (see Sec. 3.4.3). When the top aggregate is located to the right of the bottom one, a system of clockwise vortices is generated that tends to entrain the top plate in its direction of motion, thus reducing the velocity gradient and shear stress at the wall, or reducing the effective viscosity. Instead, the emergence of a counter-rotating vortex system entrains the plate in the opposite direction,

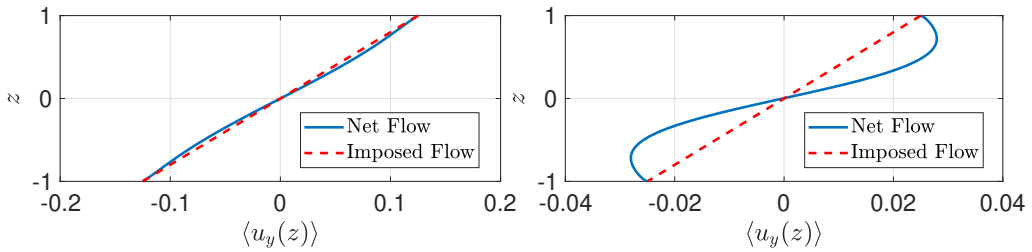

Figure 3.22: Net flow(averaged along the flow direction) compared to the imposed flow for (left) shear rates 0.125 (unsteady regime) and (right) 0.025 (steady regime) and $\zeta = 1$ at viscosity minima for the 2D unsteady state.

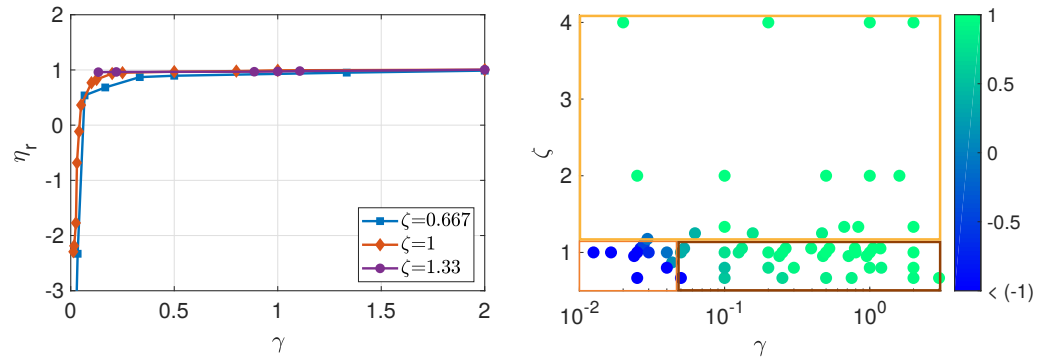

Figure 3.23: (Left)Variation of effective viscosity with respect to background shear rate for different degrees of confinement(ζ). (Right) Long term effective viscosity(η_r) on shear rate(γ) - confinement space(ζ). The range of the colour axis is modified such that the effective viscosity below -1 is all coloured identically as the data points are highly skewed for weak shear rates and weak confinement. Rough boundaries are drawn for the different long term regimes for respective shear rate and strength of confinement. Golden boundary indicates long term 1D steady state, orange boundary indicate long term 2D steady state and brown boundary indicate long term 2D unsteady state.

thus enhancing the viscous shear stress and effective viscosity at the wall.

For weak shear rates ($\gamma \ll u_0$), the suspension's dynamics is steady, with chemotactic aggregates on the top wall shifted to the right (see Sec. 3.4.3), resulting in a clockwise dominant vortex system is observed which reduces the shear gradient at the walls. Consequently, reduction, in fact reversal, of the hydrodynamic forcing on the plate, leads to a net negative viscosity (Fig. 3.20). This regime corresponds to maximum viscosity reduction due to i) clockwise rotating vortices and ii) low shear which enhances the relative contribution of active stress. This regime is represented with orange boundary in Fig. 3.23.

3.6 Conclusions

Based on a kinetic model, this work analysed numerically and theoretically the self-organisation dynamics of a two-dimensional dilute suspension of auto-phoretic particles under the dual forcing of confinement and of a background shear (Couette flow). In comparison with earlier studies [25], this setup allows a more precise investigation of the relative and coupled effects of shear and confinement by releasing the correlation of strong shear and strong confinement present in pressure-driven flows. The results presented here further investigate the whole range of confinement intensities to bridge the gap between confinement-driven dynamics and the spontaneous bulk one. The dynamic response of the suspension provides some important qualitative and quantitative insights on the rheological behaviour of such chemotactic active suspensions.

Starting from a perturbed uniform and isotropic distribution of Janus phoretic particles within the channel, a rapid development of a one-dimensional (cross-channel) distribution is a common feature for the range of confinement and shear rate intensities considered in this work, and results from the swimming particles' accumulation in the immediate vicinity of the bounding walls. At longer times, its persistence depends on the competition of this effective wall attraction with chemotaxis. For sufficiently strong confinement, this 1D steady state remains stable to streamwise perturbations and thus observed at large times for small channel widths. However, when the bounding walls are too far apart, streamwise perturbations destabilize this 1D regime as a result of the chemotactic instability [178], which results in the formation of particle aggregates on the walls. These aggregates are transported by the background flow in opposite directions along each wall. When the shear rate is low enough, the chemotactic attraction of opposite-wall aggregates is sufficient to maintain a steady two-dimensional regime with offset positions of the particle clusters across the channel. Beyond a critical shear rate, chemotaxis attraction cannot compete with particle and solute transport by the flow resulting in a periodic two-dimensional dynamics of the system, which is asymmetric in time as a result of the retarded chemotaxis response. A simple reduced model based on the particle density and polarization is proposed and shown to be sufficient to capture the flow forcing and the induced flow qualitatively.

In a second step, the hydrodynamic forcing exerted by the particles on the surrounding flow is computed to analyse the dynamical response and resistance exerted by the suspension on the moving walls, providing insight into the effective viscosity (i.e. force response to a given shear rate). The modification from the solvent viscosity is two-fold, resulting both from the active stresses exerted by the particles which modify the velocity gradients (and shear force) at the walls, and from the direct forcing exerted by the particles on the walls.

In agreement with now-classical rheological behaviour of bacterial suspensions [14, 90], this work shows that the modification in effective viscosity is largest for weak background shear: active stresses are then relatively stronger. In contrast for large imposed shear rates, the background forcing dominates the flow dynamics and forces, and particle dynamics are essentially similar to that of passive colloids. Consequently, the suspension maintains a Newtonian behaviour at larger shear rates (Fig. 3.23, left).

For low shear rates, the self-organisation of the confined suspension is directly responsible of the complex non-Newtonian behaviour of the suspension, and is characterised by significant reduction in the effective viscosity as a result of the active forcing of the particle. This forcing results from the competing surface-driven flows generated by the particles in response to their chemical activity and the phoretic forcing of the suspension's solute distribution.

However, under strong confinements, the chemotactic instability is suppressed which results in this 1D particle distribution. In this 1D state, the change in effective viscosity is negligible as the additional hydrodynamic stress is balanced by the active stress. One potential way to decrease the effective viscosity of the suspension at stronger rates is to introduce a perturbation using external forcing which onsets the chemotactic instability in the domain. Once the chemotactic instability is initiated, it induces self-sufficient chemotactic forcing which is expected to result in particle aggregates on the walls. With the formation of particle aggregates, we may expect a decrease in effective viscosity. We explore such a strategy using activity distribution at the walls in the chapter 4. Indeed similar external forcings have been used in other systems for example magnetic [246], electric [247], chemical [248], or optical [11, 249] forcing to precisely control suspensions' behaviour.

Chapter 4

Control of collective dynamics and rheology of phoretic suspensions using chemically active walls

Contents

4.1 Introduction 90

4.2 Kinetic model for externally forced phoretic suspension 92

4.2.1 Dimensionless Equations 92

4.2.2 Numerical Scheme 93

4.3 Case of spatially constant distribution of wall activity 94

4.4 Triggering chemotactic instability using spatially varying wall activity 97

4.4.1 Suspension dynamics in the presence of step-like activity distribution at a wall 97

4.4.2 Effect of magnitude and coverage of wall activity on suspension dynamics 100

4.4.3 Limitations to this strategy 101

4.5 An improved pre-conditioned strategy 103

4.5.1 Self-organisation and rheology of phoretic suspensions for improved control strategy 105

4.5.2 Phase diagrams for collective and rheological behaviour following S2 strategy 107

4.6 Conclusion 109

Overview

Chapter 3 explored the collective and rheological response of a phoretic suspension under dual forcing of shear rate and confinement. For strongly confined suspensions, the initial isotropic state relaxes into a 1D state with insignificant modification to the effective viscosity. This chapter proposes different control strategies based on chemical activity of the wall. In Sec. 4.3 we begin by discussing the simplest wall driven chemical control via uniform chemical activity. Subsequently, in Sec. 4.4 we identify the link between the 2D particle distribution and the decreasing effective viscosity. Therefore, in this section, we propose design strategies based on solute production/consumption at the wall boundaries to transform 1D state into a 2D state. An improved strategy is then proposed in the following section (Sec. 4.5), where we propose a pre-conditioning which substantially reduces the effective viscosity at moderate shear rates. Finally, based on this strategy, we illustrate the phase diagrams of the suspension behaviour as a function of shear rate and strength of confinement and compare it with the phase diagrams obtained in Chapter 3.

4.1 Introduction

In the previous chapter, we explored the response of the phoretic suspension to mechanical forcings by imposing background shear at different confinement strengths. One of the chapter's major findings was that at higher confinements, the suspension relaxes into a 1D state where the induced flow resists the shear forcing. This resistance is balanced by the active stress the particles exert on the fluid, resulting in negligible changes in effective viscosity. On the other hand, the shear forcing dominates the active stresses at high shear rates, leading to the suspension's Newtonian behaviour at higher shear rates. Consequently, the region of significant change of effective viscosity on a phase diagram ($\gamma - \zeta$) is a small region where both the shear rate and the confinement are relatively weak (see Fig. 3.23 (right) in chapter 3). The central objective of this work is to explore whether this region can be extended using external chemical forcings produced at the wall.

The idea of exploiting external fields to control individual trajectory, suspension dynamics or suspension rheology has been implemented in both active and passive systems. For instance, Li and Xuan [23] experimentally demonstrated that particles can be sorted using an electric field parallel to the channel flow as shown in Fig. 4.1 (a). Depending on the direction of the electric field and particles' material properties, the electrophoretic particles migrate either towards the channel centerline or the walls. The cross-stream motion of the particle is explained using the modification in the inertial lift force due to electrophoretic slip at the particle surface [250, 251]. As the slip depends on the particles' material properties this setup can be used in particle separation processes. Additionally, external electric fields have also been exploited to control the self-assembly of colloidal particles due to the induced long-ranged dipole interactions [252, 253].

Similarly, active systems respond to external gradients as well. For instance, Garcia and coworkers [11] elegantly showed that using an external light source can control the dynamics of an algae suspension as shown in Fig. 4.1 (b). Depending on the relative direction of pressure-driven flow and the external light source, the microswimmers either focus at the channel centerline or migrate towards the channel walls. The cross-stream migration for algae is due to the balance between the torque exerted by the background flow and the phototactic reorienting torque on the microswimmer. This balance results in stable orientation for the swimmer towards the walls or the channel centerline which results in cross stream migration due to their self-propulsion.

Magnetotactic bacteria also tend to form jets in the presence of external magnetic fields along the channel axis similar to the phototactic bacteria as experimentally demonstrated by Waisbord and co-workers [24]. The focused jet of microswimmers evolves into aggregates (called as *pearling instability*) at stronger magnetic field strengths as shown in Fig. 4.1 (c). Using numerical simulations, Jibuti and co-workers [254] showed that the self-focused jet is unstable due to hydrodynamic interactions between the microswimmers. This instability leads to fragmentation of the jet to form aggregates, which was also reported by Ishikawa and co-workers [183] who implemented Stokesian dynamics simulations and by Lauga and Nadal who implemented both continuum and discrete simulations. However, such instability has not yet been reported experimentally for phototactic microswimmers as the experiments are usually performed at low concentrations where the hydrodynamic interactions between the microswimmers are expected to be weak.

Recently, Koessel and Jabbari-Firouji [255] employed a kinetic model similar to the model discussed in the current thesis to study the collective response of magnetic swimmers to a uniform external magnetic field. They showed that a uniform polar state is unstable for moderate magnetic fields and sufficiently high activity for both puller and pusher type swimmers. The hydrodynamic instability is due to external alignment of the magnetic swimmers which leads to enhancing the hydrodynamic interactions resulting in four distinct dynamical patterns of collective behaviour.

In addition to controlling the collective behaviour of the suspensions or particles, previous studies have also demonstrated that the rheological properties of suspensions can be controlled using external fields such as magnetic and electric fields [256]. For passive systems, this has been studied extensively, McTaugue [257] was among the first to demonstrate experimentally an increase in effective viscosity of ferromagnetic fluids in the presence of constant magnetic field. This effect in passive suspensions is explained by a constant magnetic torque experienced by the particles, which

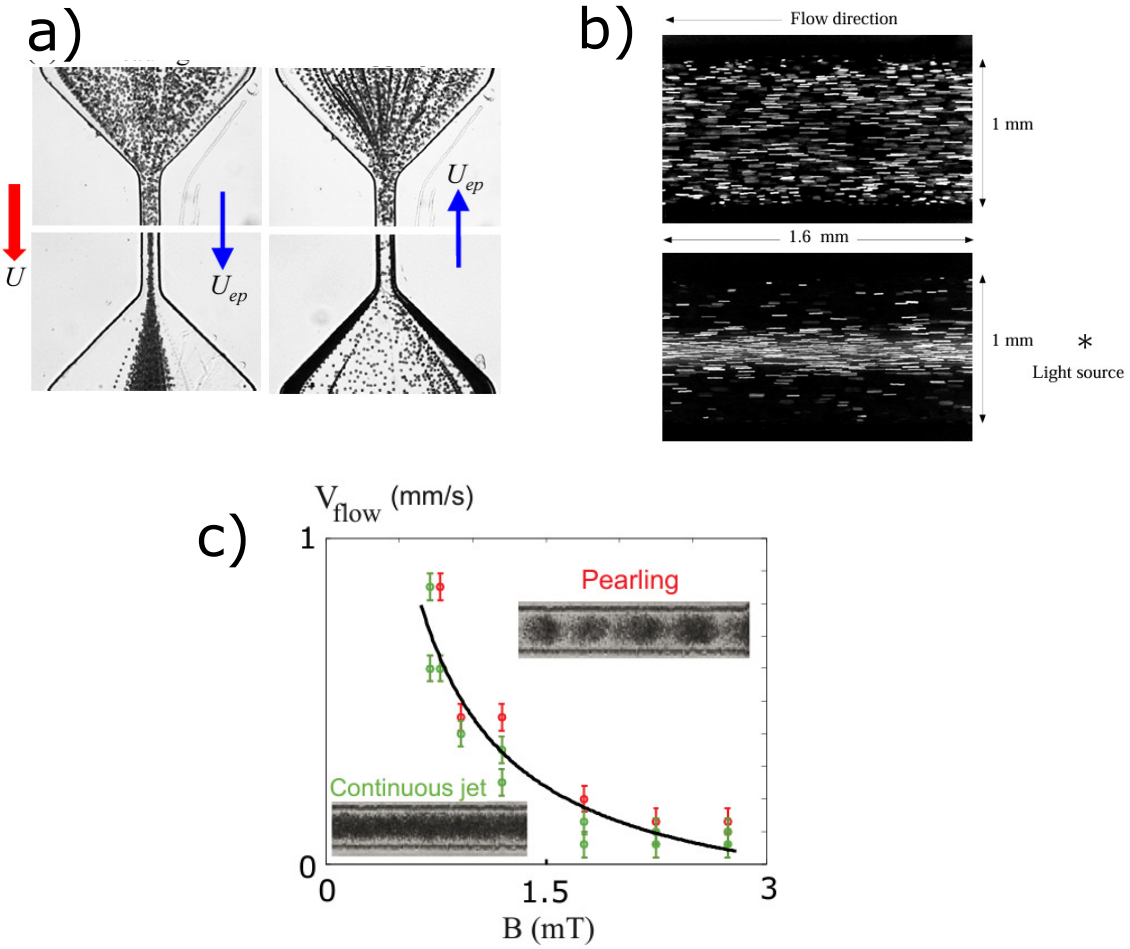

Figure 4.1: (a) Control of migration of electrophoretic particles based on the direction of electric field which controls the direction of the slip velocity shown by blue arrow and the red arrow represents the direction of fluid flow (Image adapted from ref. [23]). (b) (Top panel) uniform distribution of photactic bacteria in pressure driven flow. (bottom panel) focussed stream of phototactic bacteria in the presence of a light source (image adapted from ref. [11]). (c) Phase diagram showing distinct behaviour (pearling and continuous jet) of magnetotactic bacteria (image adapted from ref. [24]).

resists the torque due to background shear [258,259]. As a result, the particles exert additional stress on the fluid, resulting in increasing the effective viscosity of the suspension [260].

Extending it to active systems, using kinetic theory Matilla and Saintillan [261] explored the rheological response of a magnetotactic suspension (ability of the microswimmers to orient along magnetic fields) to external magnetic fields. They characterized the effective viscosity of the suspension based on the flow rate for both Couette and Poiseuelle flows and showed that the effective viscosity of the suspension can be manipulated using external magnetic field. Furthermore, they showed that a confined magnetotactic suspension can act as a ferromagnetic pump where the orientation and strength of the external magnetic field decides the direction and flow rate of the induced flow.

Most control strategies in active suspensions have focused on using either light or magnetic signals to control the collective dynamics. However, similar studies on chemotactic microswimmers is scarce, which forms the first motivation for this work. Additionally, motivated by the lack of spontaneous modification of the viscosity of strongly confined phoretic suspensions as discussed in chapter 3, the central aim of this study is to design control strategies to achieve spontaneous viscosity reduction using wall activity (consuming/producing solute at the walls). Here it is important to realize the connection between the particle distribution and its rheological response as discussed in chapter 3. The negligible modification of effective viscosity at strong confinements ($\zeta > 1.2$) is due to the 1D particle distribution where the induced flow resists the external forcing. In contrast, for a 2D state, the induced flow assists the external forcing resulting in reduced effective viscosity. One possible route to reduce effective viscosity at stronger confinements ($\zeta > 1.2$) is therefore by introducing a specific chemical perturbation to trigger the self-organisation of the system into a 2D state. This forms the central objective of the current work.

The chapter is organized as follows: We begin by revisiting the model adopted in the previous chapter to model the suspension dynamics of Janus swimmers in Sec. 4.2. Subsequently, we explore the case of uniform wall activity and show that non-uniform wall activity is essential to break the systems' symmetry in along the y-direction. Next, we discuss the suspension dynamics for a step-like wall activity on one of the walls. Here we show that using a step-like wall activity, the 1D state can be triggered to a 2D state. However, we show that this strategy has limitations at moderate shear strengths. Therefore, we propose a more robust technique where the wall activity and the background shear are applied step wise. Here, we show that using this technique, the region of viscosity reduction can be extended for stronger confinements strengths and weak background shear. Finally, we conclude the major findings of this study in the last section.

4.2 Kinetic model for externally forced phoretic suspension

Here, we revisit the mathematical model adopted in the previous chapter and discuss the required changes to account for wall activity. Kinetic model along with transport equations for mass and momentum are employed to capture the suspension dynamics similarly to chapter 3. Here we present the dimensionless equations and the numerical method.

4.2.1 Dimensionless Equations

Similar to the previous chapter, the suspension dynamics is modeled using a kinetic model coupled with the solute transport and the Stokes equations. The characteristic scales remain identical with channel half-width ($\hat{H}$) as the length scale, and corresponding diffusion time ($t_{ch} = H^2/D_c$) as the timescale. Using the length and timescales, the velocity scale is obtained as $u_{ch} = l_{ch}/t_{ch} = \hat{D}_c/\hat{H}$ whereas the pressure scale is obtained by balancing the pressure gradient with the viscous term in the Stokes equation as $\hat{\eta}\hat{D}_c/\hat{H}^2$. Finally, balancing the solute production from the particles ($\hat{N}\hat{R}^2\hat{A}^+$) with the solute diffusion ($\hat{D}_c\hat{C}_{ch}/\hat{H}^2$) we obtain the characteristic solute concentration scale as $\hat{C}_{ch} = \hat{H}\hat{A}^+/\hat{D}_c\zeta$ where $\zeta = (\hat{H}\hat{N}\hat{R}^2)^{-1}$ reflects the strength of confinement (higher ζ corresponds to stronger confinements) as it is the ratio of suspension length scale to the channel half-width [195, 196]. The probability density is normalized by the mean number density $\hat{N}$.

As the basic system remains unchanged with the external forcings changing only at the boundaries, the kinetic equations (Eq. (3.3), (3.15) and (3.16)) and the transport equations remain identical. As the walls are impermeable, we impose a no flux condition at the walls given by,

$$\left(u_0 \sin\theta + \xi_t \frac{\partial C}{\partial z}\right)\Psi = d_x \frac{\partial \Psi}{\partial z}. \tag{4.1}$$

Note that an additional term appears at the boundary condition as the solute flux at the walls may not be zero. This additional term increases (decreases) the trapping behavior of the particles when the solute gradient is towards the channel center-line (walls). The hydrodynamic problem is identical to chapter 3, described by Eq. (3.19), (3.20). Finally, the solute transport is governed by Eq.(3.22), with the modified boundary condition to account for the wall activity as,

$$\begin{aligned} \frac{dC}{dz} &= f_1(C,y) \quad \text{at z=1} \\ \frac{dC}{dz} &= f_2(C,y) \quad \text{at z=-1} \end{aligned} \tag{4.2}$$

.

Eq. (4.2) represents the general form of wall activity by introducing solute flux at the wall as a function of y-cordinate and local solute concentration. In this work, we explore three different categories of the boundary condition namely, i) fixed flux condition, ii) fixed concentration condition and iii) first order decomposition/production at the walls. Experimentally, these conditions are realized based on the nature of the chemical reaction at the boundary. For instance, the fixed flux condition is usually implemented [174] for a reaction following Michaelis-Menten kinetics in the limit of high solute concentration. Whereas, in the other limit of low solute concentration, the Michaelis–Menten reduces to a first order kinetics (case iii). Finally, the fixed solute concentration condition (case ii) is imposed when the walls are permeable and in contact with a solution with fixed solute concentration.

4.2.2 Numerical Scheme

We retain the numerical scheme adopted in the previous chapter with modifications to account for non-zero solute flux at the walls. For a uniformly distributed fixed flux case, the Neumann condition is of the form

$$\frac{dC}{dz} = f_n \quad \text{at z=}\pm 1 \tag{4.3}$$

In Fourier space, this transforms as

$$\begin{aligned} \frac{d\tilde{C}_l}{dz} &= N_y f_n \quad \text{at z=}\pm 1\text{, for } k_y = 0 \text{ mode} \\ \frac{d\tilde{C}_l}{dz} &= 0 \qquad \text{at z=}\pm 1\text{, for } k_y \neq 0 \text{ modes .} \end{aligned} \tag{4.4}$$

As the wall activity is uniformly distributed, just the zeroth mode of the Fourier mode is modified in Eq. 4.4. Similarly, the uniform distribution of fixed solute concentration (case ii) in Fourier space is transformed as

$$\begin{aligned} \tilde{C}_l &= N_y f_n \quad \text{at z=}\pm 1\text{, for } k_y = 0 \text{ mode} \\ \tilde{C}_l &= 0 \qquad \text{at z=}\pm 1\text{, for } k_y \neq 0 \text{ modes .} \end{aligned} \tag{4.5}$$

The Dirichlet condition in this case for each y mode is represented in Chebyshev space as

$$\begin{aligned} \sum_{k=0}^{N} \tilde{C}_{k,l} &= N_y f_n \qquad \text{at z=1} \\ \sum_{k=0}^{N} (-1)^k \tilde{C}_{k,l} &= N_y f_n \quad \text{at z=-1} \end{aligned} \tag{4.6}$$

Whereas, for a uniformly distributed wall activity with first order decomposition condition is represented as a robin boundary condition expressed as,

$$\frac{dC}{dz} = f_n C \quad \text{at z=}\pm\ 1. \tag{4.7}$$

The corresponding Fourier transformed condition is given by

$$\frac{d\tilde{C}_l}{dz} - f_n \tilde{C}_l = 0, \tag{4.8}$$

and implemented for each y Fourier mode as

$$\begin{aligned} &\sum_{k=0}^{N} k^2 \tilde{C}_{k,l} - f_n \tilde{C}_{k,l} = 0 \qquad \text{at z=1} \\ &\sum_{k=0}^{N} (-1)^k \tilde{C}_{k,l} - (-1)^k \tilde{C}_{k,l} = 0 \quad \text{at z=-1} \end{aligned} \tag{4.9}$$

.

For a non-uniform wall activity, the fixed flux condition is slightly modified as

$$\frac{dC}{dz} = f_n(y) \quad \text{at z=}\pm\ 1 \tag{4.10}$$

where $f_n(y)$ captures the non-uniform distribution. In this case, the Fourier transformed boundary condition is represented as

$$\frac{d\tilde{C}_l}{dz} = \tilde{f}_{n_l} \quad \text{at z=}\pm\ 1\text{, for } k_y = 0 \text{ mode .} \tag{4.11}$$

Implementing robin type non-uniform condition becomes difficult due to the coupling between the y dependent function $f_n(y)$ and the solute concentration C. However, this difficulty can be resolved by treating this boundary condition explicitly and iterating until the solution converges similar to the way non-linearity is treated in Eq. (3.18). We follow the time marching scheme described in Sec. 3.3, and the initial state is considered as the isotropic for results in Sec. 4.3 and 4.4. Whereas for the results reported in Sec. 4.5, we march in time from a 2D particle distribution.

4.3 Case of spatially constant distribution of wall activity

We begin by exploring the effect of spatially constant distribution of wall activity on the evolution of the suspension dynamics. As discussed earlier, we explore three different types of wall activity, namely i) fixed flux ii) fixed solute concentration and iii) first order reaction.

Fixed flux activity

$$\frac{dC}{dz} = \pm A_1 \quad \text{at } \pm \text{ z=1} \tag{4.12}$$

Here, we report the results for two cases, namely i) net outward flux case that is fixed rate consumption and ii) net inward flux case (that is fixed rate production). For fixed consumption at the walls, we fix $A_1 = -0.1$ which results in a local dip in solute concentration at the walls as the solute is consumed at the walls as illustrated in Fig. 4.2(right bottom). AS a result, close to the wall, the solute gradient changes its direction (compared to the inert wall case) and is now directed away from the wall. This reversal in direction of solute gradient at the walls has negligible affect on the chemotactic trapping as the particles at the walls are nonetheless trapped due to solid boundaries. On the contrary, the phoretic repulsion reduces ($\xi_t > 0$) leading to more particles getting trapped at

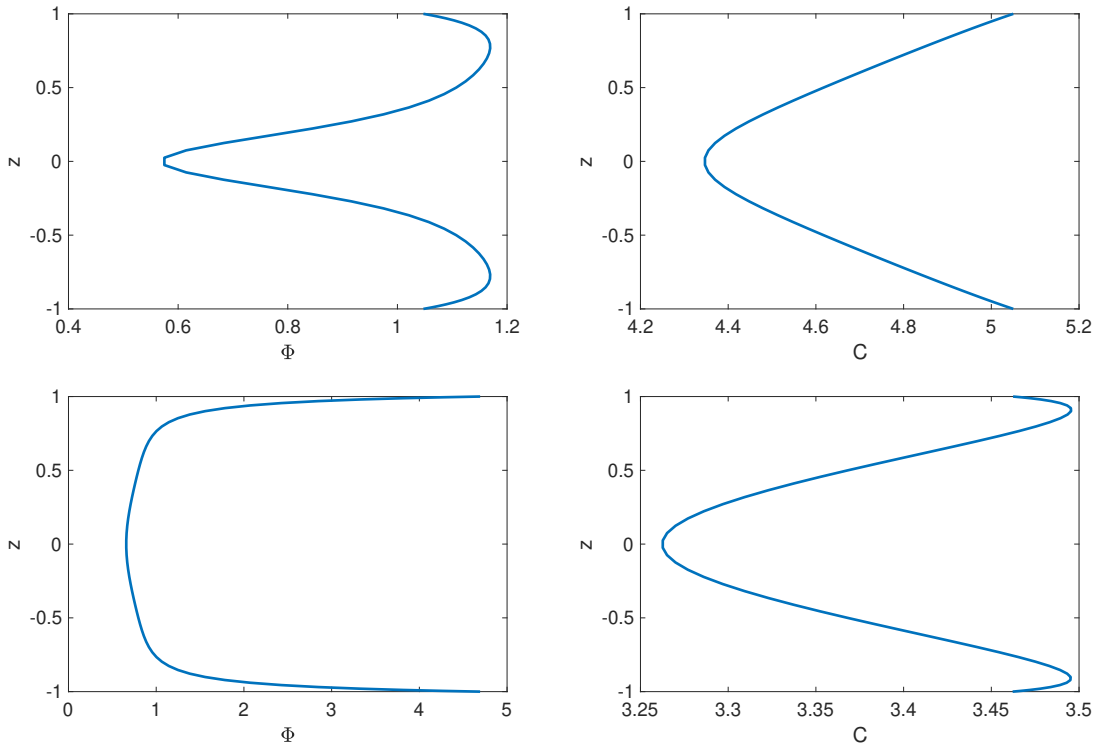

Figure 4.2: (Top left) Particle distribution across the channel width for $\zeta = 1.33, \gamma = 0$ for $A_1 = 0.1$. (Top right) The corresponding solute distribution across the channel width.(Bottom left) Particle distribution across the channel width for $\zeta = 1.33, \gamma = 0$ for $A_1 = -0.1$. (Bottom right) The corresponding solute distribution across the channel width.

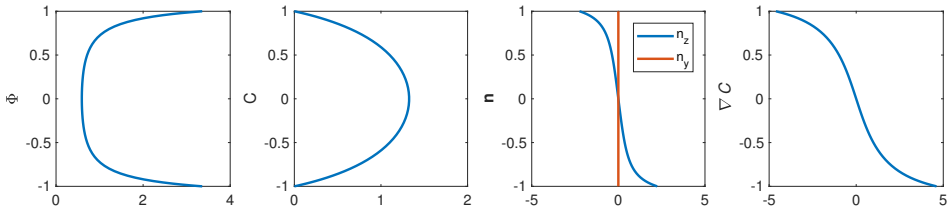

Figure 4.3: Distribution of (Left to right) particle, solute, polarization and vertical solute gradient across the channel width for Dirichlet condition $C = 0$ at the walls for $\zeta = 1.33, \gamma = 0$.

the walls. As a result of this reduction of phoretic repulsion, the thickness of the "boundary layer" of particles near the walls is modified as shown in Fig. 4.2 (bottom left).

In contrast, the solute concentration rises near the boundary when the solute is produced at the walls. This results in enhancing the solute gradient which attracts more particles from the bulk resulting in a sharp decrease in particle density at the channel centerline as shown in Fig. 4.2 (top left). Increasing the strength of solute gradient increases, i) the particle polarization and ii) the phoretic repulsion. These effects counteract and the strength of solute gradient decides which of these two effect dominate. For $\nabla_x C > u_0/\xi_t$, the phoretic repulsion dominates, and the particle shows antichemotactic behaviour (motion against solute gradient). The dip at near the wall for particle density observed in Fig. 4.2 is explained by increased phoretic repulsion near the walls. As a result, the particle density peaks at a finite distance from the walls. However, independent of solute production or consumption, the respective 1D states are observed in long term for stronger confinements ($\zeta > 1.2$). This shows that for both solute production and consumption at the walls, the effect of wall activity is restricted to modifying the thickness of the boundary layer of particle density for strong confinements ($\zeta > 1.2$).

Fixed concentration

The suspension dynamics can also be influenced using a fixed solute concentration condition which is often encountered when the walls are permeable and the system is placed in a bath of uniform concentration to maintain an equilibrium with the outer reservoir. For such cases, the appropriate boundary condition for the relative solute transport is then given by

$$C = 0 \text{ at } z = \pm 1. \tag{4.13}$$

It is important to point out here that the solute concentration can be different at the two boundaries thus creating a vertical solute concentration gradient in the domain. While we did not explore this condition, it is expected that the particles will be attracted to wall featuring the highest solute concentration and accumulate uniformly on this wall.

Due to permeable walls, the solute produced by the particles escapes through the boundaries such that the boundary condition $C = 0$ is satisfied. Consequently, this condition at the walls ensures that the solute concentration peaks at the channel centerline as shown in Fig. 4.3. As a result, the vertical solute gradient reverses its direction compared to the inert walls as shown in Fig. 4.3. The reversal in the direction of solute gradient results in a reversal in particle polarization; that is, the particles are oriented towards the channel centerline in contrast to the case of inert walls. Interestingly, despite this vertical orientation towards the channel centerline, the particles are trapped at the walls as shown in Fig. 4.3. This trapping behaviour is a result of the competition between the phoretic repulsion (acting towards the walls) and the self-propulsion acting towards the channel centerline. The magnitude of phoretic repulsion can be evaluated based on the strength of local solute gradient. The average solute gradient strength is evaluated as 2.5, therefore an average phoretic repulsion can be evaluated as ($\xi_t \nabla C|_z \sim 0.5 \times 2.5 = 1.25$). In contrast the self-propulsion velocity of the swimmer is $u_0 = 0.5$. As a result, the phoretic repulsion wins, and the particles move towards the walls (Fig. 4.3).

Due to the absence of any forcing in the horizontal direction, the horizontal polarization is negligible while the particles are strongly polarized vertically (Fig. 4.3. A much stronger vertical polarisation compared to the inert wall case, requires a stronger horizontal chemical gradient to trigger the chemotactic instability. However, the uniform Dirichlet condition at the wall boundaries ensures that the horizontal solute gradient is extremely weak which results in this 1D state to persist in the long term as well.

First order reaction at the walls

Finally, the reaction at the wall may follow a first order kinetics (with rate constant $\hat{k}$) in which case, balancing the solute flux at the boundaries, we obtain,

$$\frac{\partial C}{\partial z} + \lambda_p C = 0 \text{ at } z = \pm 1 \tag{4.14}$$

where $\lambda_p = \hat{k}\hat{H}^2/\hat{D}_c$ is the ratio of the diffusive timescale to the reaction timescale reflecting the competition between reaction and solute diffusion. The effect of the dimensionless parameter λ_p can be understood by considering the two extreme limits of $\lambda_p \to 0$ and $\lambda_p \to \infty$. The limit $\lambda_p \to 0$ corresponds to diffusion dominated regime where the rate of reaction is extremely slow compared to rate of diffusion transport, resulting in the no flux condition at the walls whose dynamics has been discussed extensively in the previous chapter (chapter 3). In contrast, the other limit, $\lambda_p \to \infty$, corresponds to fast chemical reaction where the diffusion is not sufficiently strong to transport the solute from the bulk to the boundaries. As a result, complete reaction occurs at the boundaries resulting in a constant solute concentration at the boundaries. This results in solute accumulation at the channel centerline as discussed previously. Thus, in both limits, the uniform surface activity prevents formation of stronger horizontal solute gradients which may trigger the chemotactic instability. Thus, for each of three cases, the suspension shows a 1D distribution in the long term under strong confinement ($\zeta > 1.2$). In contrast, for intermediate values of λ_c,

the chemotactic instability sets up for weakly confined suspensions similar to the inert wall case and the suspension viscosity is expected to drop similarly. However, for strong confinements, the chemotactic instability is not triggered as the time required for chemotactic orientation exceeds the time taken for solute diffusion. As a result, the suspension remains in the 1D state in the long term.

4.4 Triggering chemotactic instability using spatially varying wall activity

In the previous section, we showed that a uniform wall activity favors the 1D state regardless of the boundary conditions for stronger confinements ($\zeta > 1.2$). This is due to the uniform distribution of the wall activity which does not induce additional horizontal solute gradient responsible for the onset of chemotactic instability. Consequently, the effect of induced flow is balanced by that of active stress resulting in insignificant modification of the effective viscosity. Based on the results from chapter 3, where the drop in effective viscosity is linked with a 2D particle distribution, one potential way could be to perturb the 1D state which leads to formation of particle aggregates. Once the 2D state is obtained, the viscosity drop is expected as the particle distribution drives a pair of co-rotating vortices which drag the wall boundaries resulting in decreasing the effective viscosity as discussed in Sec. 3.5.4. We term this strategy of imposing wall activity and background shear together as S1

For strong confinements, the suspension remains in the 1D state in the long term as confinements stabilizes the chemotactic instability as discussed in Sec. 3.4.3. To understand why strength of confinement stabilizes the 1D state, we compare the timescales of solute diffusion (t_{diff}) and chemotactic reorientation (t_{chem}). As a result we obtain this ratio as

$$\frac{t_{chem}}{t_{diff}} = \frac{\hat{H}^2}{\hat{\chi}_r \hat{\nabla}\hat{C}\hat{D}_c} = \frac{\zeta}{\xi_r} \tag{4.15}$$

Eq. (4.15), suggests that as confinement strength increases, this ratio of the two timescales increases; in other words, it takes longer for the particle to reorient compared to the time it takes for solute to diffuse over the channel width. As a result, initial small disturbance introduced at $t = 0$ relax to uniform solute distribution at the walls.

A non-uniform distribution of wall activity can induce sufficiently strong horizontal solute gradient which may induce the onset of the chemotactic instability. Therefore, in this section, we impose a non-uniform activity distribution at the walls. We impose a step-like distribution for the wall activity as it may be tested experimentally by incorporating a catalytic patch on one of the walls. We anticipate that the non-uniform distribution of the wall activity will be able to trigger the onset of the chemotactic instability, after which we anticipate it to grow into eventual aggregates at the walls. Note that we now consider the wall activity distribution only on one wall in contrast to the previous section as we intend to perturb the 1D state minimally.

Before we discuss the evolution of the suspension dynamics, it is important to characterise the wall activity to understand the relative strengths of wall activity compared to particles' activity. We define a dimensionless parameter A_w to characterise the wall activity. This dimensionless number is the ratio of the mean wall activity and particles' net activity, that is, $A_w = \frac{|\hat{A}_w|\zeta}{\hat{A}^+}$. Large values of A_w corresponds to higher wall activity compared to particles' activity where the particles organistaion is expected to be directly affected by the wall activity. As the purpose of the current work is just to perturb the particle distribution which leads to favorable self-organisation, we focus on the case $A_w < 1$. In the next section, we discuss the self-organisation of the suspension in the presence of step-like wall activity distribution.

4.4.1 Suspension dynamics in the presence of step-like activity distribution at a wall

We now describe the time evolution of the suspension dynamics after introducing step-like activity distribution at the wall. We consider the bottom wall inert and the top wall active with a fixed flux

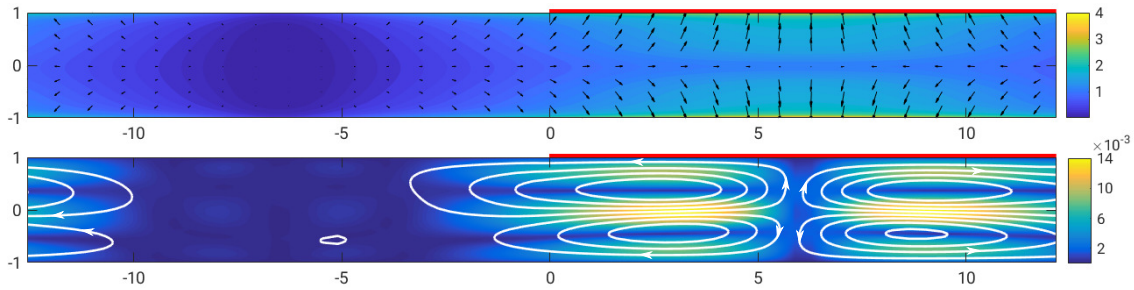

Figure 4.4: (Top) Particle distribution in the long term in the presence of active wall (shown by red strip) producing solute at fixed rate with black arrows illustrating the local average orientation of the particles for $\gamma = 0, \zeta = 1.33$. (Bottom) Streamlines of the induced flow with the background color representing the strength of the induced flow.

and step-like activity distribution. Note that in this formulation, we consider wall activity to be fixed while the boundary moves with a constant velocity. This is reflected in the boundary condition of the solute transport equations as,

$$\frac{dC}{dz} = f_1(y) = \begin{cases} 0 & y < 0 \\ A_w & y > 0 \end{cases} \text{ at } z = 1 \tag{4.16}$$

and

$$\frac{dC}{dz} = f_2(y) = 0 \text{ at } z = -1 \tag{4.17}$$

For the results presented in this subsection, we fix $A_w = |0.1|$. This suggests, that the solute consumption at the wall per unit area is 10% of the solute production by the particle per unit area and the negative sign represents solute consumption at the walls.

We begin by first describing the suspension dynamics in the absence of background shear, $\gamma = 0$. The non-uniform consumption at the wall sets up a horizontal chemical gradient that is strongest at the edge of the catalytic patch. The horizontal solute gradient induces the chemotactic torque on the particles nearby resulting in the onset of particle aggregation near the edges. As the aggregates at the transition points grow, they merge into a single aggregate due to chemotactic attractive effect between the aggregates. As the aggregate formation begins, it also acts as a source for solute production. The non-uniform solute production at the active wall then induces non-uniform solute distribution at the inert walls due to no penetration condition. This triggers the chemotactic instability on the inert wall as well. As a result, symmetric aggregates are formed on each wall as shown in Fig. 4.4 (top). Note that this 2D state resembles the 2D state obtained for inert walls under weak confinements ($\zeta < 1.2$) as the suspension dynamics still self-organises after the onset of the chemotactic instability. Moreover, the location of aggregate depends on the type of activity applied on the wall; for solute production, the top aggregate forms near the active patch as the increased solute production attracts particles. Contrastingly, for solute consumption, the particle aggregate forms on the inert half.

The fluid forcing induced by this 2D particle distribution is identical to the 2D fluid forcing discussed in Sec. 3.5.2. The fluid forcing is stronger near the walls (than the bulk) and directed against the local polarisation as the microswimmers have a pusher signature (see Fig. 3.18). As a result, the 2D state is accompanied by the induced flow of 2 pair of vortices with the diagonal vortices rotating in the same direction as shown in Fig. 4.4. The no slip condition at the walls results in weak induced flow near the walls. In contrast, the induced fluid flow is strongest at the channel centerline on each side of the aggregates as both the top and bottom vortices reinforce the flow at the channel centerline (see Fig. 4.4).

In the presence of background shear, particle distribution evolves similarly as shown in Fig. 4.5, where the aggregates start forming at the edge of the active patch leading to particle aggregates on each wall (Fig. 4.5 (bottom)). In contrast to the symmetric particle distribution for $\gamma = 0$,

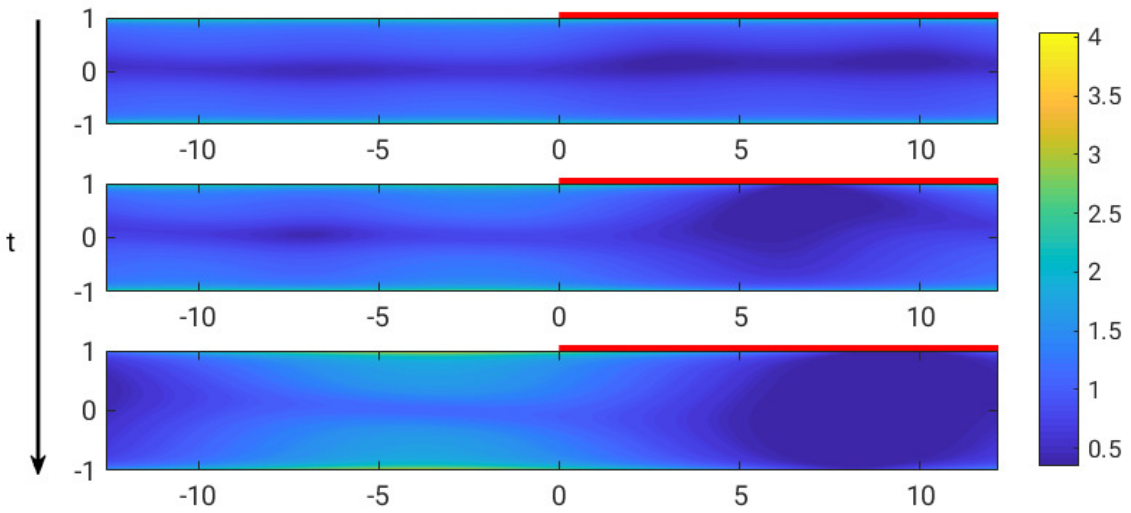

Figure 4.5: Temporal evolution of the particle density distribution in the channel for $\zeta = 1.33, \gamma = 0.015$. The red strip shows the location of wall activity (externally driven solute consumption). The presence of wall activity triggers the particle aggregation at the transition (visible in the center panel). The chemotactic instability is triggered on both the walls and results in a 2D like state.

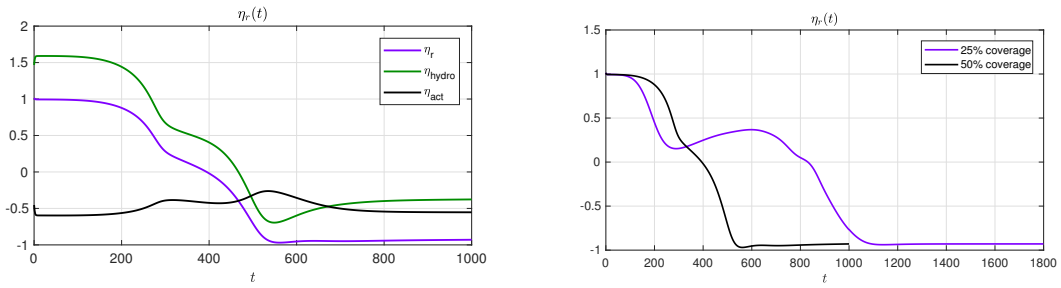

Figure 4.6: (Left) Temporal evolution of the net effective viscosity (η_r) and the two components (η_{hydro}, η_{act}) for half active wall and $\zeta = 1.33, \gamma = 0.015$. (Right) Comparison between the temporal evolution of the effective viscosity for half active wall (black) and quarter active wall (magenta).

the presence of background shear displaces the aggregates to off-symmetric positions as shown in Fig. 4.5. The weak background advection is balanced by the chemotactic attraction between the aggregates resulting in an equilibrium state.

The effective viscosity of the suspension is defined based on the force required to move the wall boundaries with constant speed similar to the previous chapter. The force at the wall is evaluated using the modified fluid stress and can thus be expressed as a linear sum of two components, i) hydrodynamic stress and ii) active stress. This is expressed as,

$$\eta_r = \int_{A_s} \left(\underbrace{\frac{1}{A_s} + \frac{1}{A_s}\frac{1}{\gamma}\frac{\partial u_{dy}}{\partial y}}_{\eta_{hydro}} + \underbrace{\frac{1}{A_s}\frac{\boldsymbol{n_n}\cdot\boldsymbol{S}\cdot\boldsymbol{t_n}}{\gamma}}_{\eta_{act}} \right) dA \tag{4.18}$$

where A_s is the surface area of the walls, $\boldsymbol{n_n}, \boldsymbol{t_n}$ are normal and tangential unit vectors to the walls respectivle, u_d is the disturbance velocity, and γ is the shear rate.

The time evolution of the effective viscosity of the suspension for $\gamma = 0.015$ is shown in Fig 4.6. As anticipated, in this case, the effective viscosity of the suspension drops (Fig. 4.6) significantly due to the formation of a pair of clockwise rotating vortices which drag the top and bottom plates in the direction of external shear forcing. Alternatively, as the direction of rotation of the induced flow

is in the same direction as the external vorticity, the velocity gradient in Eq. (4.18) is negative. As a result, the effect of the induced flow is to reduce the effective viscosity. Fig. 4.6 (left) also illustrates the temporal evolution of the rheological behaviour of the suspension with the two components. Starting from an effective viscosity of 1, where the active stress component balances the viscous stresses (η_{hydro}), the effective viscosity drops as the particle aggregate forms on the active wall, beginning at $t \sim 200$. Finally, at the steady state, the viscous stress aids the active stresses to reduce the effective viscosity of the suspension drastically. This shows that wall activity can be exploited to modify the effective viscosity from $\eta_r \sim 1$ to $\eta_r \sim -0.97$ by modifying the particle distribution.

4.4.2 Effect of magnitude and coverage of wall activity on suspension dynamics

In the previous subsection, we fixed the magnitude of the surface activity (A_w) such that the solute production/consumption at the wall per unit area is 10% of that produced by the particles per unit area and the fraction of active area (defined as f_A from here on) while describing the temporal evolution of the suspension. However, both parameters can influence the temporal evolution and consequently the final state of the system. To characterize the effect of both these parameters, we now vary these parameters, starting with varying the magnitude of the wall activity.

Fig. 4.7 (left) illustrates the long term effective viscosity of the suspension for different wall activity strengths for $\gamma = 0.015, \zeta = 1.33, f_A = 0.5$, with the inset showing the particle distribution in the two regions. The figure clearly shows that below a critical strength the wall activity does not influence the 1D state favorable at strong confinements. Below the threshold wall activity, the chemotactic reorientation time for the particle exceeds the orientation diffusion timescale of the particle. In other words, the orientation diffusion prevents particle reorientation which results in suppressing the chemotactic instability. As a result, at strong confinements, the effective viscosity is identical to the surrounding fluid. In contrast, above a threshold, the chemotactic instability is triggered in the system resulting in a sharp drop in effective viscosity due to the corresponding induced flow discussed in the previous chapter. It is important to note that the rheological response of the suspension is directly related to the particle distribution. Therefore, below the critical strength of wall activity, the suspension continues to be in the 1D state with the corresponding viscosity ~ 1. In contrast, when the strength of wall activity is above the critical value, the suspension relaxes into a 2D state with a significant drop in effective viscosity. This explains the discontinuity of the effective viscosity with respect to strength of wall activity.

Fig. 4.7 (right) shows an increasing behaviour of the maximum horizontal solute gradient induced as a result of imposing step like distribution of wall activity for a given mean value (x-axis). Consequently, as the strength of wall activity reduces, the horizontal chemical gradient decreases almost linearly (as the solute transport is diffusion dominated at low shear rates) which results in increasing the time required for chemotactic reorientation. Below this threshold, the chemotactic reorientation time exceeds the orientation diffusion timescale and thus the chemotactic instability cannot be triggered. The critical value of the wall activity is independent to the nature (consuming/producing) of the active patch. The only difference that occurs is the relative position of the aggregates, for the case of production, the aggregate is positioned at the active half instead of the inert half. This change in position can be understood based on the chemotactic response of the particles; when the active patch produces solute, this invites particles towards the active side whereas when it consumes solute, the particles are reoriented away from the active patch.

Furthermore, the active wall fraction (f_A) also plays an important role in both the evolution and final states of the system. Fig. 4.8 shows the final particle distribution for $\gamma = 0.015, \zeta = 1.33$ and $A_w = -0.1$ (solute consumption at the active patch) for two different coverage of wall activity ($f_A = 0.25, 0.5$) with the black arrows represents the particle orientation in the domain. The particle aggregate at the top wall seems to be pinned with the transition which is not surprising as the horizontal solute gradient is strongest at the junction between the active and passive patch. As a result, the aggregate starts growing at the junction. Varying f_A, changes the location of the edge of the catalytic patch. This explains the relative shift of the aggregate for the two cases shown in Fig. 4.8. The shift however, has negligible effect on the effective viscosity of the suspension as

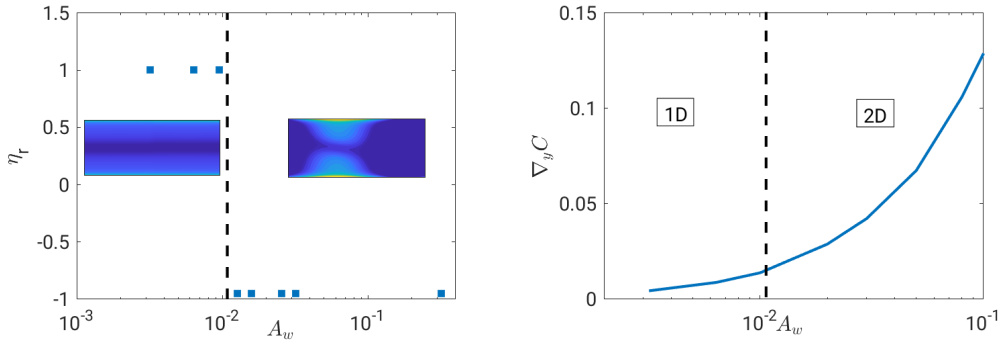

Figure 4.7: (Left) Effective viscosity dependence on the magnitude of wall activity. Inset shows the particle distribution for respective regions. (Right) Maximum horizontal solute gradient induced as a function of magnitude of wall activity.

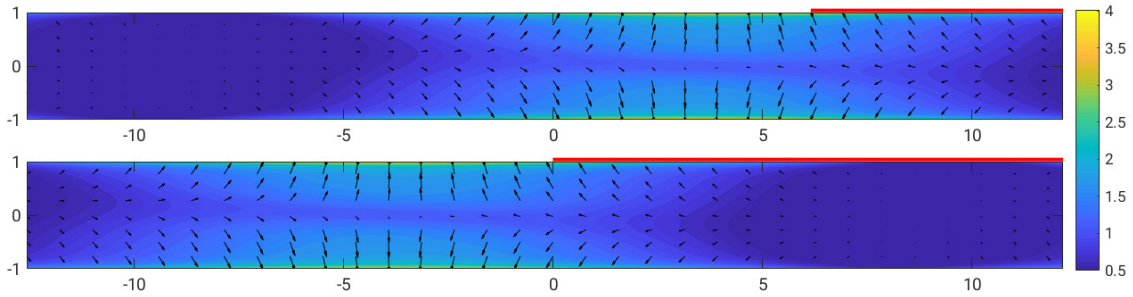

Figure 4.8: Comparison between the particle distribution for $A_w = 0.5$ and $A_w = 0.25$ for $\zeta = 1.33, \gamma = 0.015$. The black arrows represent the local average orientation of the particles.

shown in Fig. 4.6, as the flow structure for both are similar. In contrast, the temporal evolution is indeed different for both cases; it takes longer to reach the steady state for smaller area coverage. This can be explained based on different distances the particles have to cover for different f_A. For $f_A = 0.5$ the particles that are furthest from the junction are at a distance of $\sim L_y/4$ in contrast to a distance of $L_y/2$ for $f_A = 0.25$. As a result, the strength of solute horizontal gradient experienced by the particles located the furthest from the patch decreases, thus increasing the time it takes to reorient. Furthermore, the particles must travel longer distances to form the aggregate. These two factors lead to higher time requirement to reach the steady state as the active area fraction is reduced. The distance between the catalytic edge and the particles that are farthest from the junction is minimum for $f_A = 0.5$ due to periodic domain, as a result the least amount of time required for reaching the steady state is expected to be at $f_A = 0.5$.

4.4.3 Limitations to this strategy

The wall activity triggers the chemotactic instability in two steps: i) the horizontal solute gradient first triggers the instability on the active wall, and ii) Once the aggregate is formed on the active wall, it acts as a solute source, resulting in the onset of the instability on the inert wall. Increasing background shear directly affects the second step, as increasing background shear increases solute advection. With our choice of characteristic timescale as the solute diffusion time across the channel, γ plays the same role as the *Peclet* number for solute transport.

For shear rates $\gamma \geq 0.05$, the evolution of the suspension dynamics differs greatly compared to those under low shear rates. The time evolution of the collective behaviour follows similar dynamics until the aggregate forms on the active wall; the wall activity introduces horizontal chemical gradients which triggers the chemotactic instability at the active wall. However, once the aggregate is formed at the active wall, it is unable to trigger chemotactic instability on the inert wall for stronger ($\gamma > 0.05$) background shear for two reasons: i) Increased background shear rate increases solute

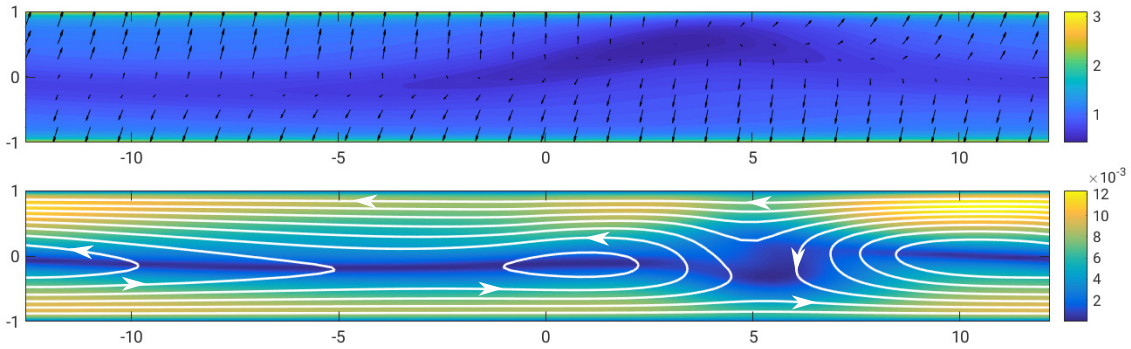

Figure 4.9: (Top) Instantaneous particle distribution across the channel for half active wall and $\zeta = 1.33, \gamma = 0.1$. The black arrows depict the local particle polarization. (Bottom)The induced flow in the channel with the background color reflecting the strength of the flow.

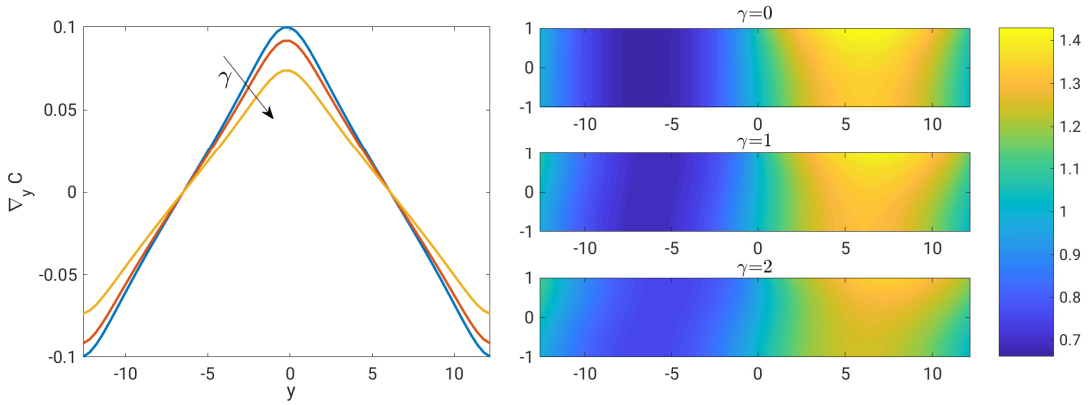

Figure 4.10: (Left) Horizontal solute gradient at the inert wall and (right) Solute distribution in the channel for different strength of solute advection.

advection, and ii) the aggregate spends less time at any point due to stronger background advection.

Due to increased solute advection, the amount of solute produced by the aggregate that reaches the inert wall substantially reduces. Consequently, the solute distribution at the inert wall remains nearly uniform. As a result, the chemotactic instability is not triggered on the inert wall, resulting in a uniform particle distribution. Additionally, as the aggregate on the active wall is advected with the background flow velocity, it does not spend sufficient time at any location which also prevents solute accumulation on the inert wall.

To gain further insights, we considered a much simpler problem, focusing only on the solute transport with different background shear rates (equivalently, different *Peclet* numbers) in the absence of particles and their induced flow. Considering a stationary source which produces solute at a fixed rate at the top wall, we solve the solute transport with bulk destruction similar to the original problem. In this simplified problem, we replace the particle aggregate which acts as a source in the complete problem, with a stationary source. Additionally, we also neglect the induced flow generated by the particles and the bulk production of solute by the particles. The solute transport is governed by the advection-diffusion equation given as

$$\frac{\partial C}{\partial t} + Pe(\boldsymbol{u} \cdot \nabla C) = \nabla^2 C - \beta C \tag{4.19}$$

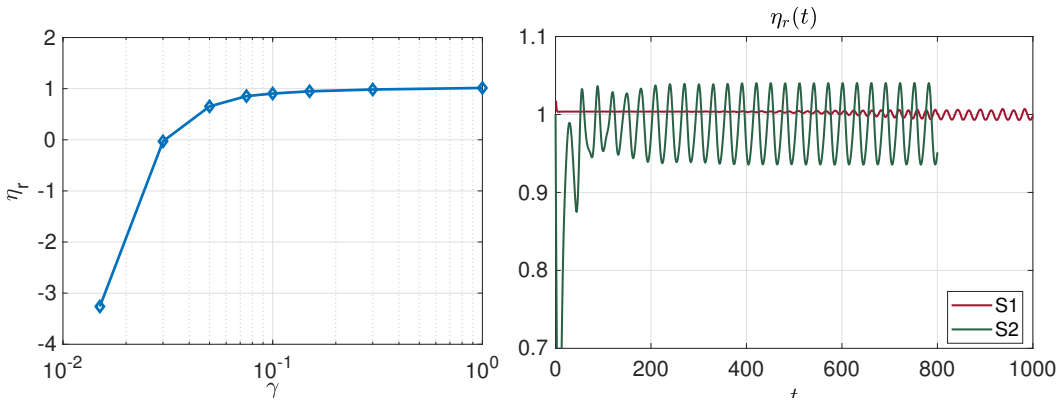

Figure 4.11: (Left) Effective viscosity for the fixed flux step-like distribution of the wall activity for $\zeta = 1.33$ following the S2 strategy. (Right) Time evolution of the effective viscosity for the two schemes for $\zeta = 1.33, \gamma = 0.3$. S1 represents the scheme where both activity and background shear imposed at the same time and throughout the run. S2 represents the second scheme where first the wall activity is introduced, and then shear is introduced after removing the activity.

with the boundary conditions as

$$\begin{aligned} \frac{\partial C}{\partial z} &= F(y) \text{ at } z = 1 \\ \frac{\partial C}{\partial z} &= 0 \text{ at } z = -1 \end{aligned} \tag{4.20}$$

with $F(y) = 0.1$ for right half of the wall and $F(y) = 0$ for left half of the top wall.

Fig. 4.10 (right) shows the steady state solute distribution for different Peclet numbers (γ_w) illustrating that the background advection inhibits vertical transport of the solute produced at the wall. More precisely, Fig. 4.10 (left) shows that increasing the shear rate decreases the horizontal solute gradient induced on the opposite wall. This reduction in horizontal solute gradient is responsible for suppressing the chemotactic instability on the inert wall resulting in a uniform particle distribution on the inert wall.

As a result, the particle distribution shows a different 2D state where the aggregate is formed only on the active wall while the particle distribution is uniform on the inert wall, as shown in Fig. 4.9 (top). Consequently, the induced flow lacks the coherent vortices (Fig.4.9) required for stronger modification in effective viscosity. The viscous stresses induced corresponding to the induced flow are balanced by the active stresses exerted by the particles, resulting in insignificant viscosity reduction as shown later in Fig. 4.11.

In addition to the above disadvantage, this strategy introduces various parameters (for example, strength of wall activity, area coverage, etc.), making it more difficult to characterise the systems' response. Moreover, in this strategy, we consider the catalytic patch to be fixed while the walls move with constant speed which may be difficult to realize in experiments. Furthermore, this strategy requires a high amount of wall activity as the wall activity is switched on throughout the run. Due to these various limitations, we propose a more robust (with respect to parameters such as background shear, strength and fraction of activity etc.) strategy discussed in the next subsection.

4.5 An improved pre-conditioned strategy

Due to the limitations outlined in Sec. 4.4, the previous strategy (S1) is unfavorable as the chemotactic instability is suppressed at moderate shear rates. Therefore, it is important to ensure the growth of the chemotactic instability throughout the domain to reduce suspensions' effective viscosity. Here we propose an improved strategy and revisit the S1 strategy proposed in Sec. 4.4 to clearly distinguish the two

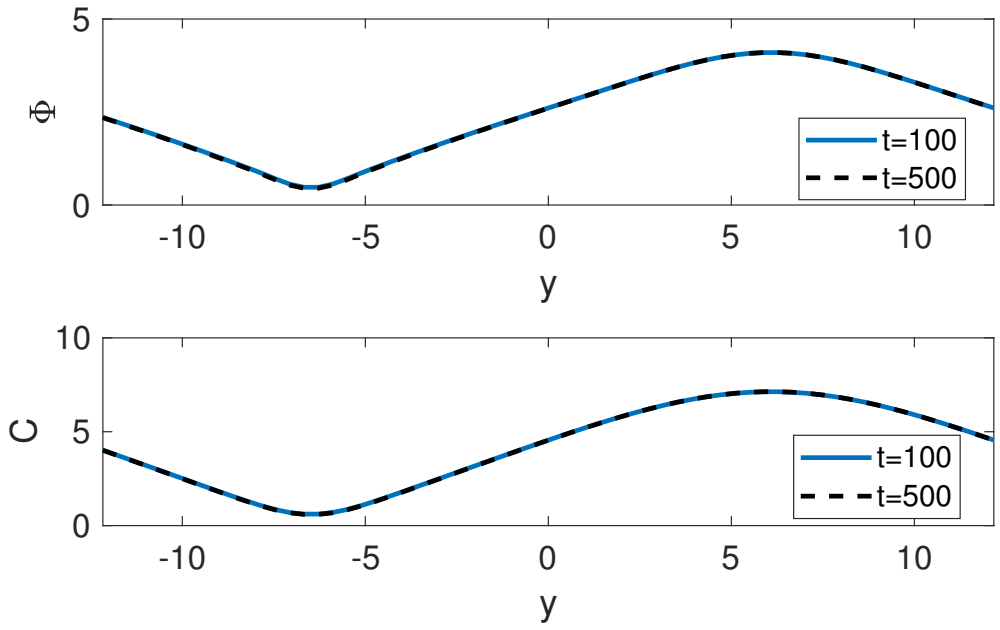

Figure 4.12: Particle and solute distribution on the active wall for a preconditioned suspension with $\gamma = 0, \zeta = 1.33$ at t=100 and 500. The overlap between the two curves show that the 2D particle distribution is a steady state.

- S1 : Step-like wall activity distribution and the background shear is introduced simultaneously to the 1D state until the suspension dynamics converges to its final state.

- S2 : First, step-like activity distribution is introduced to the 1D state in the absence of shear to trigger the onset of chemotactic instability. The first step acts like a preconditioned step where, the suspension is essentially prepared before applying background shear. Once the system transforms into a 2D state, the activity is switched off and the required shear rate is applied.

The improved strategy is based on two central observations, i) formation of particle aggregates at the walls result in decreasing the effective viscosity of the suspension in the presence of background shear and ii) once the wall activity is switched off, the suspension relaxes into a 2D state closely resembling the 2D state discussed in chapter 3. Fig. 4.12 shows the particle density and solute concentration distribution at $z = 1$ after removing the wall activity. Once the wall activity is switched off, it takes about $t \sim 100$ to relax into the 2D steady state which persists in the long term (four times longer than it took to relax into this state). In other words, the system shows a bi-stable behaviour with both 1D and 2D states as solutions to the governing equations. Indeed, an isotropic initial state relaxes into a 1D state in the absence of external perturbations for $\zeta > 1.2$. However, using the perturbation provided by the wall activity, the 1D particle distribution can transition to a 2D state.

The chemotactic instability grows without competing with the background shear in its absence. As a result, the chemotactic instability grows unhindered resulting in formation of particle aggregates on both walls. Once the aggregates are formed, they induce self-sufficient chemotactic forcing resulting in sustaining this state in the long term even in the absence of wall activity as shown in Fig. 4.12. As a result, the induced flow patterns are expected to decrease the suspensions' effective viscosity.

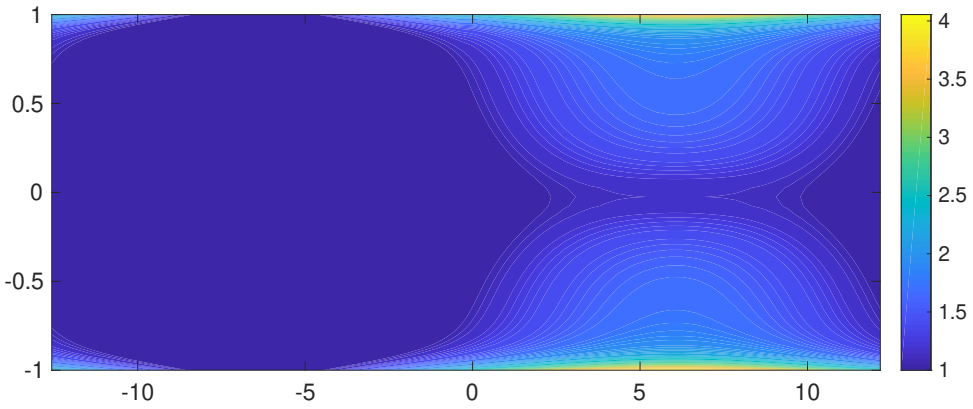

Figure 4.13: The 2D particle distribution after switching off the wall activity for $\zeta = 1.33, \gamma = 0$ following the S2 strategy. The suspension remains in this 2D state even after switching off the wall activity.

4.5.1 Self-organisation and rheology of phoretic suspensions for improved control strategy

During the preconditioning stage (introducing wall activity in the absence of background shear), the evolution of the suspension dynamics from the 1D state to the 2D state follows a similar relaxation as discussed in Sec. 4.4. The presence of step-like activity distribution creates horizontal solute gradients near the active wall at the step-transition. It is important to point out here that the vertical solute gradient introduced by the wall activity is negligible compared to the vertical solute gradient established due to the particle distribution and therefore does not affect the self-organization directly. In addition, the wall activity introduces a horizontal gradient which triggers the chemotactic instability first at the active wall and then on the inert wall too. The aggregates are placed symmetrically (top-bottom) as the aggregates experience a chemotactic attraction discussed in chapter 3. Thus, a symmetric 2D state is formed as a result of introducing activity at the walls. This completes the first step of the proposed strategy

Following S2 strategy, the wall activity is now switched off and background shear rate is applied. For weaker shear rates ($\gamma < 0.05$), the suspension behaviour is practically identical for both S1 and S2 strategies. We now present the results for the suspensions' behaviour under weak shear following S2 strategy for the sake of completeness.

In the absence of background shear, the particle aggregates are formed symmetrically as discussed earlier. The fluid forcing induced by this symmetric state is directed away from the aggregates in the transverse direction similar to the flow forcing discussed in Sec. 3.5.3. The fluid forcing is strongest at the walls due to high particle density and strong polarization. As a result, the induced flow consists of two pairs of vortices with identical direction of rotation for diagonal vortices as illustrated in Fig. 4.4.

Introducing weak background shear ($\gamma < 0.05$ for $\zeta = 1.33$) displaces the aggregates in the flow direction which is balanced by the attractive chemotactic effect between the aggregates. Consequently, the aggregates are placed in an off-symmetric positions resulting in inducing a pair of clockwise rotating vortices which assist the external shear forcing resulting in decreasing effective viscosity (Fig. 4.6). In addition, the active stress exerted by the particles on the boundaries also reduces the effective viscosity due to pusher nature of these microswimmers.

As the strength of external shear increases, it overcomes the chemotactic attraction between the aggregates. This results in advection of the aggregates along the flow direction, which results in an unsteady yet periodic state. The aggregates induce a 2D chemotactic forcing responsible for sustaining the aggregates in the long term even in the presence of moderate shear rates ($\gamma > 0.05$). In contrast, following the S1 strategy for $\gamma > 0.05$ resulted in uniform particle concentration at the inert wall. This shows the vastly different suspension behaviour following the two strategies.

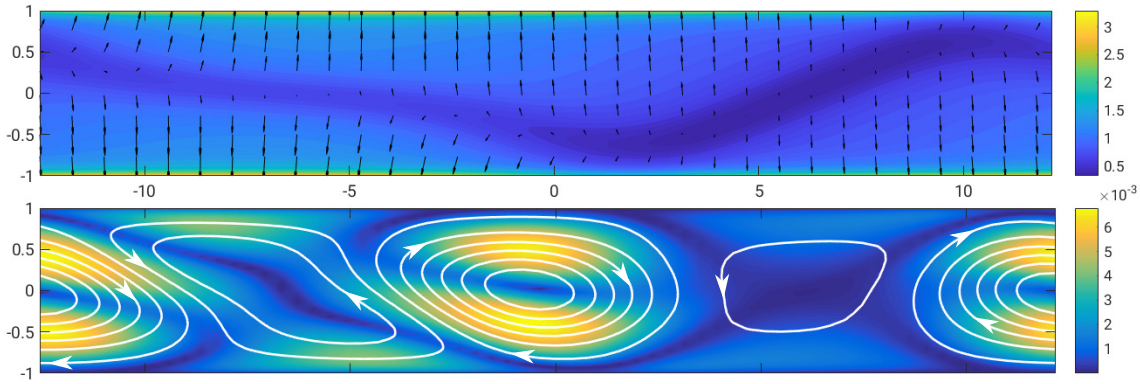

Figure 4.14: (Top) Particle distribution with the particle polarization shown by black arrows for $\zeta = 1.33, \gamma = 0.1$ after switching off the wall activity and imposing background shear. (Bottom) Induced flow with the background contour showing the strength of induced flow after switching off the wall activity and imposing background shear.

The periodic nature of the 2D state is also reflected in the time evolution of the effective viscosity as shown in Fig. 4.11. The minimum viscosity is observed when the top aggregate lies to the right on bottom aggregate which induces a clockwise rotating (see Fig. 4.14) flow which assists the external shear forcing, thus reducing the effective viscosity. In contrast, the maximum viscosity is observed when the top aggregate lies to the left of bottom aggregate inducing a pair of counter-clockwise rotating vortices. As a result, the induced flow resists the shear forcing resulting in increasing effective viscosity. Additionally, between these two extreme configurations, viscosity increases when the separation between the aggregates decreases while the viscosity decreases during the increase in aggregate separation. However, as the aggregates spend more time while the separation between the aggregates increases compared to the time spent while the aggregate separation is decreasing due to chemotactic attraction between the aggregates, the time average of the effective viscosity in one period shows a net reduction in effective viscosity (see Fig. 4.11). Furthermore, the pusher nature of the microswimmers exert extensile stress at the boundaries resulting in further drop in effective viscosity.

The 2D state is maintained *after* switching off the wall activity which suggests that both the 1D state and the 2D state are the solutions of the unforced system of equations, and the suspension preferentially chooses the 1D state for $\zeta > 1.2$ when the suspension evolves from an uniform isotropic distribution. However, with the help of external forcings via wall activity, the 1D particle distribution can be converted into a more favorable (with respect to rheology) 2D particle distribution. However, this improved strategy also has limitations; beyond a critical strength of confinement, the 2D chemotactic forcing induced by the aggregate is not sufficiently strong relative to the confinement effect to self-sustain the aggregates. As a result, for $\zeta > 2$ the 2D symmetric state relaxes back to the 1D state after the wall activity is switched off as illustrated in Fig. 4.15. This suggests that beyond $\zeta = 2$, the 2D state is no longer a solution to the unforced system of equations.

Before we attempt to understand the reason behind this relaxation from a 2D state to a 1D state, we must realize that the 2D state was an equilibrium state where the number of particles arriving towards the aggregate (due to chemotaxis) balances the number of particles leaving the aggregates due to orientation diffusion. The transition from the 2D state to the 1D state suggests that beyond a critical strength of confinement, the number of particles arriving towards the aggregate decreases compared to the number of particles leaving the aggregate. The particles that are arriving towards the aggregate have two possible choices, i) to reorient and swim towards the aggregate due to chemotaxis or ii) to swim towards the wall using the velocity component directed towards the boundaries. Note that the particles away from the aggregates are weakly polarized (see Fig. 4.9 (top)), and therefore the particles will have a velocity component towards the walls. Now as the strength of confinement increases, it is more likely that the particle encounters the wall before it can reorient towards the aggregate. Once the particle reaches the wall boundaries, it is trapped at the

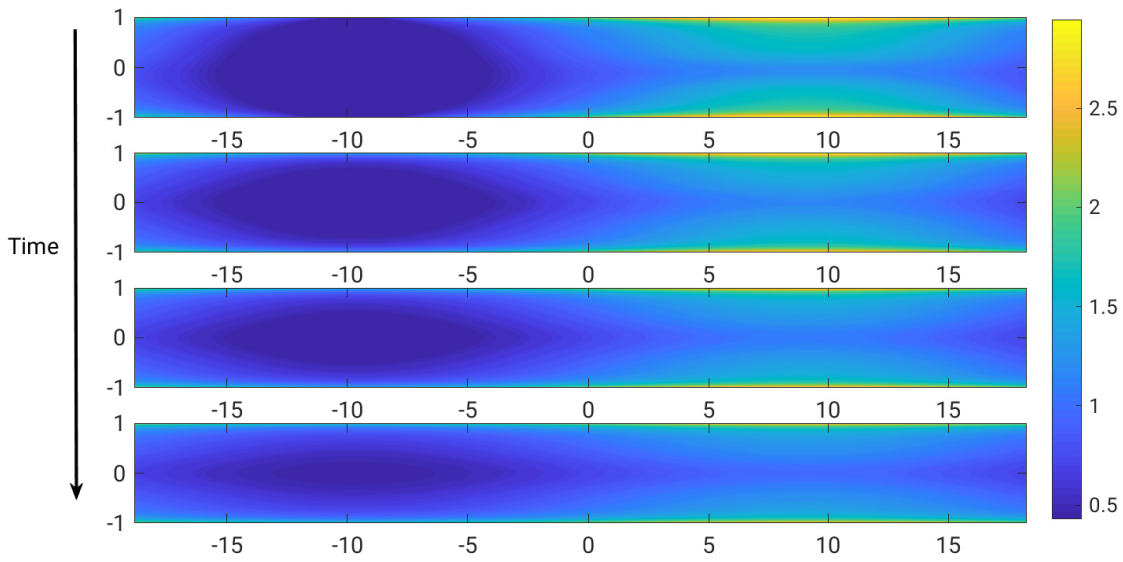

Figure 4.15: Progression of the particle distribution for strongly confined condition ($\zeta = 2, \gamma = 0$). The 2D state slowly relaxes into the 1D state as the particle flux towards the aggregate is unable to balance the outward flux due to orientation diffusion.

walls and the 2D state slowly relaxes into a 1D state. To quantitatively understand this, we compare timescales associated with swimming across the width (t_{swim}) and chemotactic reorientation (t_{chem}),

$$\frac{t_{chem}}{t_{swim}} = \frac{\zeta u_0 \rho}{\xi_r}. \tag{4.21}$$

Eq. (4.21) shows that the ratio between the two timescales is directly proportional to confinement ζ and therefore as confinement increases, the time taken by the particle to reorient towards the aggregate becomes larger than the time it takes to swim towards the wall. As a result the particles swim towards the wall instead of swimming towards the aggregate. Once the particles reach the wall, they are trapped until orientation diffusion can help them escape. The transition between the 2D and the 1D state is expected to occur when the ratio in Eq. (4.21) becomes $O(1)$. As a result we obtain the threshold strength of confinement as,

$$\zeta \sim \frac{\xi_r}{\rho u_0}. \tag{4.22}$$

Substituting the parameters used in the simulations ($\xi_r/\rho = 1.25, u_0 = 0.5$), we obtain the critical confinement as $\zeta \sim 2.5$. The critical strength of confinement based on the results from full simulation ($\zeta = 2$) is of the same order of magnitude. Furthermore, to understand this transition to 1D state let us look at the orientation dynamics of the particle given by (Eq. (3.16))

$$\dot{\boldsymbol{p}} = \frac{1}{2}\omega \times \boldsymbol{p} + \frac{\xi_r}{\rho\zeta}(\boldsymbol{p} \times \nabla_x C) \times \boldsymbol{p} - d_p \nabla_p [\ln(\Psi)]. \tag{4.23}$$

The strength of the chemotactic term weakens as the confinement strength increases as the strength of solute gradient (dimensional) weakens. This suggests that the particles behave as non-chemotactic swimmers when the strength of confinement increases. Therefore, it is natural that the particle distribution relaxes to a 1D state for strong confinements as the strength of chemotactic reorientation decreases.

4.5.2 Phase diagrams for collective and rheological behaviour following S2 strategy

We now explore the parametric space for the shear rate and strength of confinement (ζ, γ) to obtain a phase diagram illustrated in Fig. 4.16. Fig. 4.16 (left) shows that the region where two-dimensional

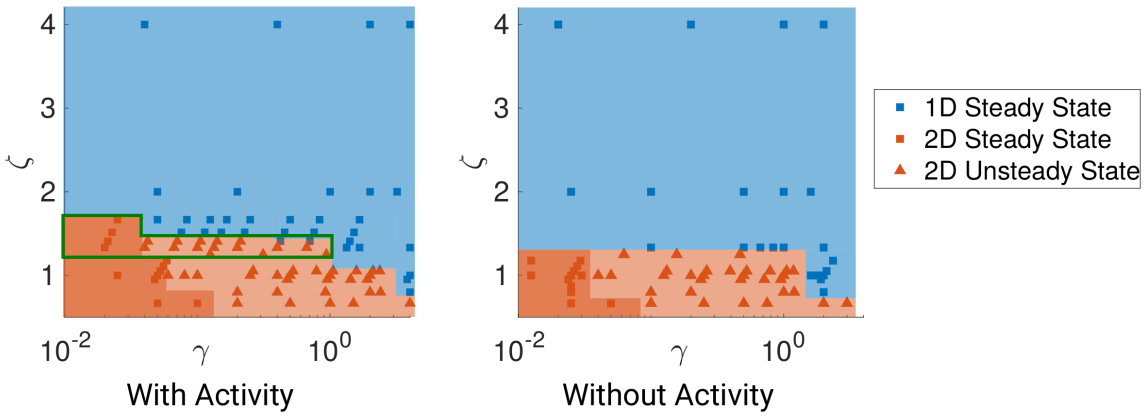

Figure 4.16: Comparison of the phase map between the wall active case (left) with the original phase map obtained for inert walls (right). The region marked with green border corresponds to the 2D state achieved with the help of wall activity.

states are observed is extended to higher confinement strengths highlighted using green boundaries. As the external forcing is absent for both the cases, this suggests that both the 1D and 2D state are solutions to the governing equations in this green region, and they can be obtained based on the initial conditions. Indeed, as the confinement strength increases beyond a critical value, the initial 2D state relaxes into a 1D state.

Increasing shear rate also results in transitioning from the long term 2D state to a long term 1D state. However, in this case, it is the stronger background vorticity which is responsible for the 1D particle distribution in the long term. To obtain the boundary of transition between a longterm 2D and 1D state can be estimated by comparing the timescales associated with chemotactic reorientation ($t_{chem} \sim \zeta\rho/\xi_r$) and the shear rate ($1/\gamma$). The persistence of the 2D state depends critically on the particles responding to the chemical gradient as the particle incoming flux must be balanced by the outgoing flux due to orientation diffusion. Increasing the shear rate decreases the associated timescale and therefore particle takes longer to reorient compared to its tumbling dynamics due to shear. As a result, the boundary which separates the 1D and 2D states can be estimated when the two timescales are of similar order of magnitude. That is,

$$\frac{1}{\gamma} \sim \frac{\zeta\rho}{\xi_r}. \tag{4.24}$$

As a result, we obtain,

$$\gamma \sim \frac{\xi_r}{\rho\zeta}. \tag{4.25}$$

This suggests that the critical shear rate where the transition between the 2D and 1D state occurs decreases with increasing strength of confinement. This is qualitatively observed in Fig. 4.16 where the boundary shifts to lower shear rates at strong confinements while at higher shear rates, the transition occurs at lower confinement strength.

As discussed in chapter 3, the rheological response of the suspension strongly depends on the collective dynamics. By triggering the onset of chemotactic instability to the 1D state under strongly confined conditions, we show that significant decrease in effective viscosity is possible especially at low shear rates (Fig. 4.17 (left)). Note that this reduction takes place in a region (on γ-ζ space) where the suspension originally (with inert walls) had the same viscosity as the fluid. To quantitatively compare the change between the inert wall case and the active wall case, we can define a relative change in effective viscosity as,

$$\Delta\eta/\eta = \frac{\eta_{active} - \eta_{inert}}{\eta_{inert}} \tag{4.26}$$

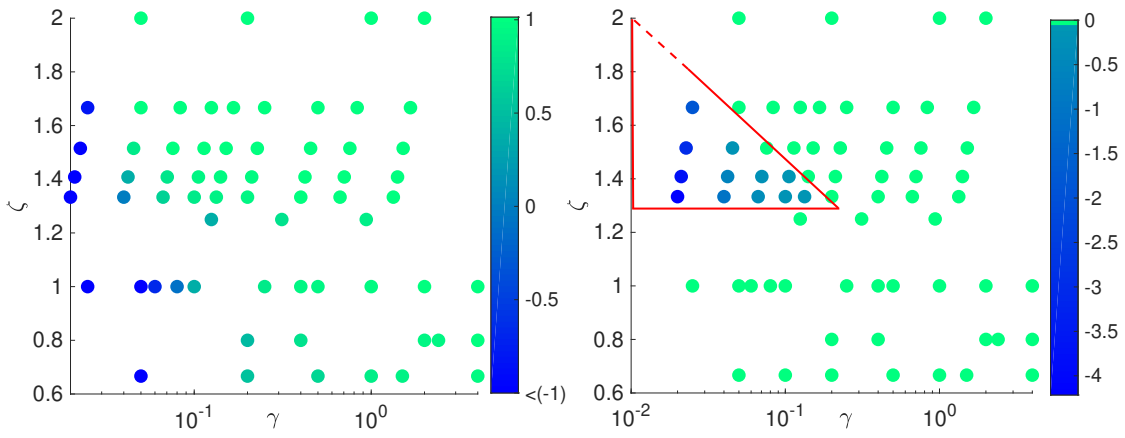

Figure 4.17: (Left) The effective viscosity on the ζ-γ space with wall activity. (Right) Relative fractional change in effective viscosity after introduction of activity.

where η_{active} and η_{inert} is the effective viscosity with and without wall activity respectively. This quantity is shown in Fig. 4.17 (right), the maximum change in effective viscosity at low shear rates is not surprising as the relative strength of induced flow is comparable to externally driven shear flow at weak shear rates. This region is identified and shown by a rough red boundary in Fig. 4.17 (right) where the dotted line represents the expected transition boundary. Note that the rheological response of the suspension changes exclusively in the region where the suspensions' self-organisation is modified from 1D state to a 2D state. This shows that using the wall activity, the region of interest (where viscosity reduction is significant) can be extended from low shear low confinement (Fig. 3.23 in chapter 3) for the case of inert walls to low shear moderate confinements using this strategy. As the strength of background shear rate increases, the relative strength of the active stresses decreases resulting in weak modification to suspensions' effective viscosity despite the 2D state of the suspension.

4.6 Conclusion

Based on a kinetic model in this work, we explore the control of collective dynamics and rheology of a phoretic suspension using chemically active wall. Controlling suspension dynamics using external forcing has been explored in other active and passive systems using optical [11], electrical [23], magnetic [255] forcings, however similar studies on chemotactic swimmers is scarce. This forms as the first motivation for the current work.

Our results show that wall activity can indeed be exploited to control the collective behaviour of the phoretic suspensions, as it perturbs the solute field which affects the particles' response. The results presented in this chapter show that using a uniform distribution of wall activity, the thickness of the "boundary layer" can be controlled as introducing the solute gradient via wall activity modifies the balance between phoretic repulsion and self-propulsion. Additionally, we explore different conditions for the solute flux at the wall corresponding to different limits of the catalytic reaction occurring at the walls. However, our results suggest that the distribution remains in a 1D state for uniform distribution of wall activity regardless of the flux condition at the wall.

In order to trigger the chemotactic instability under stronger confinements, our results suggests that a non-uniform wall activity is essential to induce a stronger horizontal gradient. As a result, using the wall activity, the effective viscosity can be modified significantly by triggering the onset of the chemotactic instability. However, imposing both wall activity and shear rate fails to trigger chemotactic instability at moderate shear rates as the solute advection suppresses the growth of chemotactic instability. To overcome this problem, we propose an improved strategy where the suspension is pre-conditioned before introducing background shear. The wall activity is first introduced in the absence of shear, to ensure growth of chemotactic instability throughout the channel.

This results in aggregate formation on each wall; the aggregates in-turn exert chemotactic forcing to sustain themselves. As a result, introducing the background shear to this 2D state ensures that the aggregates are present for higher background shear. As a result, a higher decrease in effective viscosity compared to the previous strategy is reported.

This work shows that the wall activity can indeed modify the effective viscosity of the suspension. The leads to whether an optimum wall activity distribution exists such that the effective viscosity is minimum. One of the possible ways to obtain this optimum distribution is to apply some optimization technique (for instance the gradient descent method).

Reducing the effective viscosity of the suspension has direct implications in reducing the external driving force. This can be beneficial specially for strongly confined suspensions where the viscous drag is substantial. In fact our results suggest, that we can potentially harvest energy at low shear rates.

Chapter 5

Conclusions and perspectives

Contents

5.1 Summary and general remarks 111
5.2 Ongoing work and future perspectives 112

5.1 Summary and general remarks

This thesis aims to understand the collective dynamics of dilute phoretic suspensions using continuum kinetic model and to propose control strategies for the same. As the phoretic particles perturb both the solute and the flow fields, they have the ability to interact through both the fields resulting in complex pattern formation. Building upon previous work from Traverso and Michelin [25, 178], the objectives of the first part of the work were i) to understand the self-organisation dynamics under dual influence of background shear and strength of confinement and ii) to understand and characterising the rheological response of such suspensions. Based on the physical insights, the central objective of the second part of the thesis was to propose control strategies based on external chemical forcings to reduce the effective viscosity of the suspension under stronger confinements. We employ a continuum kinetic model to mathematically describe the suspension dynamics of the phoretic suspension, where the inter-particle chemo-hydro interactions are captured using a mean field approach.

To understand the suspensions' response to background shear and strength of confinement, we start from a near isotropic state and march forward in time for different shear rates and confinement strengths. For all shear rates and confinement strength considered in this work, we find a common short term state where the particles accumulate at the boundaries (see Fig. 3.4) as the walls are impermeable for the particles. For strongly confined states, the short term state persists in the long term. In contrast, weakly confined suspensions tend to form particle aggregates at the walls due to the chemotactic instability. The aggregates are symmetrically placed in the absence of background shear as the aggregates are attracted towards each other due to chemotaxis as illustrated in Fig. 3.7. The aggregates are displaced off-symmetrically for weak shear rates as the chemotactic attraction balances the weak advection due to background flow. However, as the shear rate increases, the advective effect overcomes the chemotactic attraction resulting in advection of the aggregates. As a result, the suspension reaches an unsteady yet periodic final state as depicted in Fig. 3.8. Further increase in background shear results in suppressing the chemotactic instability as the particle tumble due to strong shear which prevents them to reorient along the local solute gradient. Furthermore, as the 1D state is a common feature for all confinement strengths and shear rates, we perform a linear stability analysis on the short term state using different moments of the kinetic equation which reveals that the 1D state is linearly unstable for weak confinements with the most unstable mode resembling with the particle aggregate state as discussed in Sec.3.4.4.

In the next step, we study the rheological response of these different states using a bulk effective viscosity. This effective viscosity is defined based on the drag exerted by the suspension on the plate

compared to a Newtonian fluid for the same shear rate. Using this definition, we show that the effective viscosity of the suspension has two contributions, the first coming from the hydrodynamic stress due to the induced flow and the second due to the active stress exerted by the particles at the wall boundaries. For the 1D state observed at strong confinements, the hydrodynamic contribution balances the active stress contribution resulting in insignificant modification to the effective viscosity of the suspension. In contrast, for weakly confined suspensions at low shear rates, the hydrodynamic component and active stress component assist the shear forcing which results in strong reduction in effective viscosity of the suspension (see Fig. 3.20). For moderate shear rates, the unsteady periodic state is reflected in the time evolution of the effective viscosity as well (Fig. 3.20). When the aggregates are being separated due to background shear, the effective viscosity drops. In contrast the effective viscosity rises when the aggregates approach each other. However, the average viscosity in one cycle is still lower than the Newtonian viscosity as the system spends more time during the separation phase than the other phase. The effective viscosity reduction however decreases with increase in background shear rate, resulting in effective viscosity approaching the viscosity of the suspension as shear rate increases (Fig. 3.23). Using a minimalistic model, we also obtain relations between the driving force for the fluid flow and physical properties such as, polarization, particle density and stresslet strength.

In the second part, we first realize that at stronger confinements, the system relaxes to a 1D state where the two components of the effective viscosity compete resulting in insignificant modification to the effective viscosity. As the suspensions' rheological response is directly related to its self-organisation, we propose a control strategy based on external chemical forcing via wall activity to manipulate the suspensions' self-organisation. In chapter 4, we show that while a uniform wall activity controls the thickness of the boundary layer at the walls, a non-uniform wall activity (consumption/production at the wall) is essential to trigger the chemotactic instability. However, imposing stationary wall activity and background shear is not only practically difficult to design experimentally, it also fails to trigger the chemotactic instability at larger shear rates as the increased solute advection suppresses the growth of the chemotactic instability, resulting in a lower reduction in effective viscosity. Therefore, we propose a more robust strategy where the wall activity and the background shear is introduced separately. Introducing wall activity without background shear ensures chemotactic instability grows throughout the domain. Next, we introduce the required background shear to the 2D state. As a result, a higher drop in effective viscosity is reported. However, this strategy has an upper threshold for confinement strength as the time taken to swim across the channel width reduces compared to chemotactic reorientation. Thus, above a critical threshold the 2D state cannot sustain itself and the suspension relaxes to a 1D state.

5.2 Ongoing work and future perspectives

Optimum wall activity distribution

While proposing the strategies to reduce the effective viscosity of the suspension under strong confinements, we explore the most simple wall activity distribution to test the idea of externally modifying the suspensions' rheology by modifying the collective dynamics in Chapter. 4. We explored only some simple wall activity distributions (uniform and step-like), however different distributions may result in complex and rich collective and rheological dynamics. This leads to the question "whether an optimum wall activity distribution exists for minimising the effective viscosity?". And more importantly, "what is the optimum activity distribution if it exists ?".

One of the potential ways to evaluate the optimum viscosity distribution is by employing a gradient descent optimization technique where the idea is to calculate the local gradient of the objective function (here the effective viscosity) with respect to the design variables (in this case, the shape of the activity distribution). Based on the local gradient, the wall activity distribution is updated by taking small steps along the gradient. However, the evaluation of the gradient requires full solution of the system of equations for each design variable to obtain the sensitivity derivatives. As a result, in our system, the system of equations must be solved N_y times at each step as the

design variables are the Fourier modes of the wall activity distribution. Therefore, such technique is computationally expensive for large number of design variables and a more efficient technique must be used.

Adjoint state method can be employed to reduce the computational power for evaluating the gradient of the objective function [262]. In this method, the gradient of the objective function is indirectly evaluated using the "adjoint fields". As a result, only two system of equations (original set of equations and the adjoint set of equations) must be solved to evaluate the gradient thus significantly reducing the computational cost. Such adjoint based optimization techniques are frequently used while designing the shape of aerodynamic bodies to reduce the drag force and have been found to accurately evaluate the gradient [263].

In the adjoint state method, we first consider a small perturbation in the design variable and therefore the system of equations are linearised corresponding to this perturbation (See Sec. D.1). We can now define an adjoint field corresponding to each physical field variable. For instance, if $R^{\delta\Psi}$ represents the governing equation for the perturbed probability field, then based on an inner product the adjoint field ($\tilde{\Psi}$) is defined such that,

$$\int_{V,\theta,t} \tilde{\Psi} R^{\delta\Psi} = \int_{V,\theta,t} R^{\tilde{\Psi}} \delta\Psi + \text{surface terms}. \tag{5.1}$$

Based on a similar definition, adjoint fields corresponding to the flow and solute concentration can be defined.

Now, the idea is to express the objective function $\delta\eta_r$ in terms of an augmented function $\delta\eta_{aug}$ as

$$\delta\eta_{aug} = \delta\eta_r + \int_{V,t} \tilde{\boldsymbol{u}} R^{\delta\boldsymbol{u}} + \int_{V,t} \tilde{q} R^{\delta q} + \int_{V,\theta,t} \tilde{\Psi} R^{\delta\Psi} + \int_{V,t} \tilde{C} R^{\delta C} + \lambda \int_{V,\theta,t} \delta\Psi + \mu \int_S \delta A \tag{5.2}$$

Note that the last two terms represent the constraints imposed on Ψ (conserved field) and wall activity (zero mean activity). The constraint on wall activity is imposed so that the mean wall activity remains unchanged, while changing only the distribution.

Now, using the definition of the adjoint fields, this can be expressed as (see Sec. D.2)

$$\begin{aligned} \delta\eta_{aug} =& \delta\eta_r + \int_{V,t} R^{\tilde{\boldsymbol{u}}} \delta\boldsymbol{u} + \int_{V,t} R^{\tilde{q}} \delta q + \int_{V,\theta,t} R^{\tilde{\Psi}} \delta\Psi + \int_{V,t} R^{\tilde{C}} \delta C + \mu \int_S \delta A \\ &+ \text{surface terms} \end{aligned} \tag{5.3}$$

Note that the above expression represents the sensitivity of the objective function with respect to all the field variables. The adjoint variables can now be chosen such that they satisfy $R^{\tilde{\boldsymbol{u}}} = R^{\tilde{q}} = R^{\tilde{\Psi}} = R^{\tilde{C}} = 0$. As a result, the adjoint variables are governed by

$$\left\langle \Psi \frac{\partial\tilde{\Psi}}{\partial z} - \frac{1}{2}\frac{\partial\Psi}{\partial y}\frac{\partial\tilde{\Psi}}{\partial\theta} - \frac{1}{2}\Psi\frac{\partial^2\tilde{\Psi}}{\partial y\partial\theta} \right\rangle_\theta + C\frac{\partial\tilde{C}}{\partial z} - \frac{\partial\tilde{q}}{\partial z} + \nabla_x^2 u_z = 0 \tag{5.4}$$

$$\left\langle \Psi \frac{\partial\tilde{\Psi}}{\partial y} + \frac{1}{2}\frac{\partial\Psi}{\partial z}\frac{\partial\tilde{\Psi}}{\partial\theta} + \frac{1}{2}\Psi\frac{\partial^2\tilde{\Psi}}{\partial z\partial\theta} \right\rangle_\theta + C\frac{\partial\tilde{C}}{\partial y} - \frac{\partial\tilde{q}}{\partial y} + \nabla_x^2 u_y = 0 \tag{5.5}$$

$$\nabla\cdot\tilde{\boldsymbol{u}} = 0 \tag{5.6}$$

$$\begin{aligned} &\frac{\partial\tilde{\Psi}}{\partial t} + u_s(\nabla_x\tilde{\Psi}\cdot\boldsymbol{p}) + \boldsymbol{u}\cdot\nabla_x\tilde{\Psi} + \xi_t(\nabla_x\tilde{\Psi}\cdot\nabla_x C) + d_x\nabla_x^2\tilde{\Psi} + \frac{1}{2}\omega\frac{\partial\tilde{\Psi}}{\partial\theta} \\ &+ \frac{\xi_r}{\rho}\frac{\partial\tilde{\Psi}}{\partial\theta}(\nabla_x C\cdot\boldsymbol{e}_\theta) + d_p\nabla_p^2\tilde{\Psi} + 2\pi\tilde{C} - \boldsymbol{S}_p : \nabla\tilde{\boldsymbol{u}} + \lambda = 0 \end{aligned} \tag{5.7}$$

$$\frac{\partial\tilde{C}}{\partial t} + \boldsymbol{u}\cdot\nabla_x\tilde{C} + \nabla_x^2\tilde{C} - \beta\tilde{C} - \left\langle \xi_t(\nabla_x\Psi\cdot\nabla_x\tilde{\Psi} + \Psi\nabla_x^2\tilde{\Psi}) - \frac{\xi_r}{\rho}\nabla_x\left(\Psi\frac{\partial\tilde{\Psi}}{\partial\theta}\right)\cdot\boldsymbol{e}_\theta \right\rangle_\theta = 0 \tag{5.8}$$

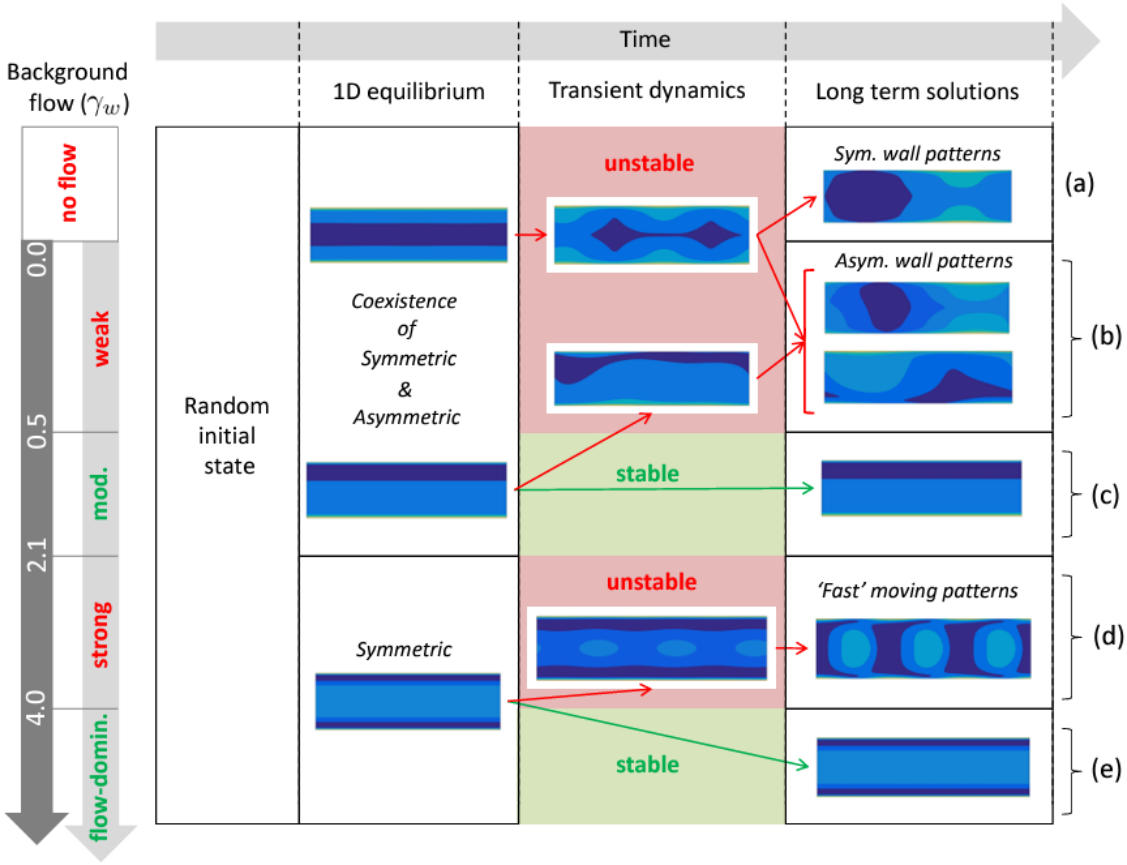

Figure 5.1: Summary of the suspension dynamics in pressure driven flow. Image adapted from [25]

where the angle brackets ($\langle . \rangle$) represent the average over subscript coordinate.

The boundary conditions for the adjoint set of equations can be imposed such that the surface terms in Eq. (5.3) simplify (See Sec. D.2 for more details). As a result, the corresponding boundary conditions are given by

$$\nabla \tilde{\Psi} \cdot \boldsymbol{e}_z = 0 \quad \text{at } z = \pm 1 \tag{5.9}$$

$$\frac{\partial \tilde{C}}{\partial z} = \left\langle \xi_t \frac{\partial \tilde{\Psi}}{\partial z} \Psi + \frac{\xi_r}{\rho} \Psi \frac{\partial \tilde{\Psi}}{\partial \theta} \sin\theta \right\rangle_\theta = 0 \quad z = \pm 1 \tag{5.10}$$

Finally the boundary condition for the adjoint flow field is given by

$$\begin{aligned} \tilde{\boldsymbol{u}} &= -\boldsymbol{e}_y \quad \text{at } z = 1 \\ \tilde{\boldsymbol{u}} &= 0 \quad \text{at } z = -1. \end{aligned} \tag{5.11}$$

As a result, the gradient of the objective function is now expressed as a surface integral of the adjoint solute field given as (Eq. (D.26))

$$\delta \eta_{aug} = \int_S \tilde{C} \delta A \tag{5.12}$$

Owing to the similarity between the adjoint equations and the governing equations in physical space, similar numerical schemes can be adopted to solve the equations. However, as the adjoint equations must be solved for each small change in wall activity, time marching scheme adopted to reach steady state for primal equations may not be efficient. Therefore, other numerical methods should be adopted to solve the adjoint equations to improve efficiency in terms of required time.

Other possible future directions

To verify our results, we propose a potential experimental set-up for a suspension of photocatalytic Janus particles in Fig. 5.2. Photocatalytic Janus particles have a catalytic coating of TiO_2 which acts

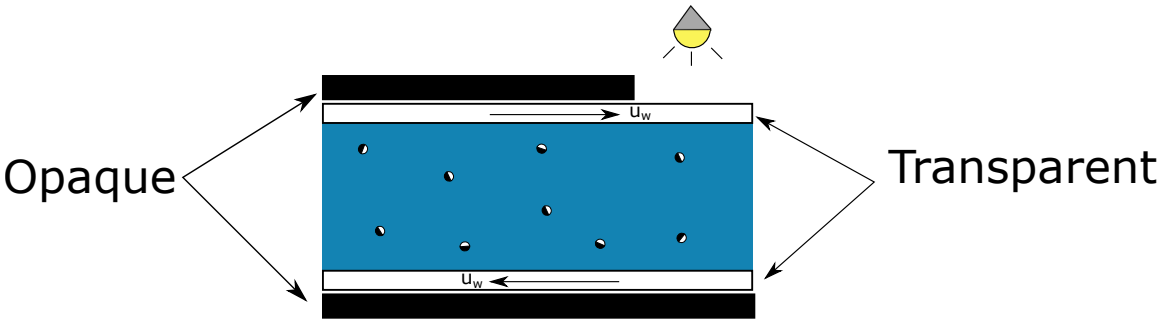

Figure 5.2: Schematic of experimental set-up to verify our results of chapter 4

as the active half in the presence of UV light [264]. As a result, in the presence of UV light, the H_2O_2 reacts on the TiO_2 and the particle self-propels due to diffusiophoresis. Due to photocatalytic nature of the swimmers, wall activity can be introduced using additional light source as shown in Fig. 5.2. Additionally, fixed opaque blinds can be used to alter the light intensity distribution to mimic the S1 scheme discussed in chapter 4. As the particle propels using the diffusiophoretic mechansim, the particles are expected to show chemotacti behaviour as reported [264]. Fig. 5.2 illustrates a possible experimental setup; the walls are made up of transparent material and move in the opposite direction to externally impose the background shear. Now opaque blinds can be introduced close to the transparent wall to control the amount of light passing through the transparent walls. Use of asymmetric blinds (as illustrated in Fig. 5.2) is expected to have similar effect of introducing wall activity on the suspension dynamics. Moreover, phototactic algae can also be used in a similar set-up, however as the phototactic algae do not undergo chemotactic instability, the results may differ.

In the current thesis, we focused on a simpler setting of confined uniform shear flow, however in certain applications, it might be the pressure driven flow that is of interest. Traverso and Michelin [25] worked on this problem with inert walls, where they studied the rheology of the suspension using the Poiseuille law. They reported rich and complex suspension dynamics which is summarised in Fig. 5.1. Their major finding was that the viscosity modification is significant only at weak background flow where the particle distribution looses the top-bottom symmetry ((b) in Fig. 5.1). The top-bottom symmetry in this case can be broken using a non-uniform activity distribution on one of the walls. The non-uniform activity distribution is expected to trigger the chemotactic instability on one of the walls resulting in the desired particle distribution. Finally, similar to the shear flow case, the optimum wall activity distribution can be evaluated using the gradient descent method for maximising the net flow rate.

Another interesting future direction for extending the current results maybe to work in a 3D setting. Kinetic models of bacterial suspension in three dimensions have been explored previously by Theillard and Saintillan [239] in terms of moment equations. They truncated the moment expansion of Ψ at nematic order tensor and used a level set method to solve the system of equations. Their results qualitatively matched with the 2D results however, the three-dimensional results provided a higher quantitative agreement with experimental results. The level-set method allowed them to explore more complex geometries, however for simpler setting such as flat walls, retaining pseudo spectral scheme is preferable due to quicker convergence compared to finite difference scheme.

Similar to Theillard and Saintillan [239], working with moment equations is preferred due to increased dimensionality of the probability function Ψ. However, in contrast the moment equations can be truncated at polarisation itself as the particles are spherical. In this case, the moment equations (1 for particle density and 3 for particle polarisation) will be coupled with the solute transport and the fluid flow problem. These coupled partial differential equation can then be solved following a pseudo spectral scheme similar to the current scheme.

Appendix A

Chebyshev tau method

The purpose of the appendix is to outline the Chebyshev Tau method to solve the Helhlholtz equations obtained for after spectral decomposition of governing equations. This section closely follows the method outlined in ref. [228].

All the field variables are expressed in Chebyshev basis, that is for any variable g, we can write

$$g(x) = \sum_{k=0}^{\infty} \tilde{g}_k T_k(x) \tag{A.1}$$

where T_k are Chebyshev polynomial of the first kind of degree k. For most practical applications, the above series (Eq. (A.1)) is truncated to finite number of terms. In other words, we approximate

$$g(x) = \sum_{k=0}^{N} \tilde{g}_k T_k(x) \tag{A.2}$$

for some finite but large N. After decomposing the governing equations, we end up with a set of 1D Helhmholtz equations of the form

$$-\frac{d^2u}{dx^2} + \lambda u = f \tag{A.3}$$

with boundary conditions

$$u(-1) = u(1) = 0. \tag{A.4}$$

Note that we use this system of equations as an example to illustrate the method. The boundary conditions for solute transport and kinetic equations have Neumann type boundary conditions while the y-component of the flow equations have non zero Dirichlet condiditon. Therefore, some changes must be made for the given set of equations which are mentioned in the text later. In Chebyshev basis, Eq. A.3, (A.4) transform as

$$-\tilde{u}_k^{(2)} + \lambda \tilde{u}_k = \tilde{f}_k \quad k = 0, 1, 2, ...N-2 \tag{A.5}$$

where $\tilde{u}_k^{(2)}$ is the k^{th} mode of the second derivative and

$$\sum_{k=0}^{N} \tilde{u}_k = 0, \quad \sum_{k=0}^{N} (-1)^k \tilde{u}_k = 0 \tag{A.6}$$

where the tilde ($\tilde{.}$) represents the same quantity in Chebyshev space. As a result, the boundary condition can be expressed as

$$\sum_{k=0,\text{even}}^{N} \tilde{u}_k = 0, \quad \sum_{k=1,\text{odd}}^{N} \tilde{u}_k = 0 \tag{A.7}$$

Note that this condition modifies for a non-zero Dirichlett condition. For a general case, with boundary condition given by

$$\begin{aligned} u(-1) &= b_1 \\ u(1) &= b_2 \end{aligned} \tag{A.8}$$

the corresponding boundary condition in Chebyshev space is written as

$$\sum_{k=0,\text{even}}^{N} \tilde{u}_k = \frac{b_{1_k} + b_{2_k}}{2}, \quad \sum_{k=1,\text{odd}}^{N} \tilde{u}_k = \frac{b_{1_k} - b_{2_k}}{2} \tag{A.9}$$

Using the property of Chebyshev Polynomials, Eq. A.5 is transformed as

$$-\frac{1}{c_k} \sum_{\substack{p=k+2 \\ p+k \text{ even}}}^{N} p(p^2 - k^2)\tilde{u}_p + \lambda \tilde{u}_k = \tilde{f}_k \;\; k = 0, 1, ..N-2 \tag{A.10}$$

where $c_k = 1$ for $k \geq 1$ and $c_0 = 0$.Thus we arrive at a linear system of equations which can be solved by inverting the upper traingualr operator. This inversion requires N^2 operations, and a more efficient method exists which exploits the decoupling between the odd and the even modes of the Chebyshev trasnformed variables. To decouple the odd and even modes, we explout the recurssive relation

$$2k\tilde{u}_k^{(1)} = c_{k-1}\tilde{u}_{k-1}^{(2)} - \tilde{u}_{k+1}^{(2)} \tag{A.11}$$

and using Eq. (A.5), we obtain

$$2k\tilde{u}_k^{(1)} = c_{k-1}(-\tilde{f}_{k-1} + \lambda\tilde{u}_{k-1}) - (-\tilde{f}_{k+1} + \lambda\tilde{u}_{k+1}) \tag{A.12}$$

Now using another recurssive relation given by

$$c_k\tilde{u}_k^{(1)} = \tilde{u}_{k+2}^{(1)} + 2(k+1)\tilde{u}_{k+1}, \;\; k = 0, 1, ...N-3 \tag{A.13}$$

Eq. (A.12) is finally written as

$$\begin{aligned} &-\frac{c_{k-2}\lambda}{4k(k-1)}\tilde{u}_{k-2} + \left[1 + \frac{\lambda\beta_k}{2(k^2-1)}\right]\tilde{u}_k - \frac{\lambda\beta_{k+2}}{4k(k+1)}\tilde{u}_{k+2} \\ &= -\frac{c_{k-2}}{4k(k-1)}\tilde{f}_{k-2} + \frac{\beta_k}{2(k^2-1)}\tilde{f}_k - \frac{\beta_{k+2}}{4k(k+1)}\tilde{f}_{k+2} \;\; k = 2, ...N \end{aligned} \tag{A.14}$$

where the β parameter is introduced to account for the four equations dropped in Eq. (A.13). β_k is defined as

$$\beta_k = \begin{cases} 1, & 0 \geq k \leq N-2 \\ 0, & k > N-2 \end{cases} \tag{A.15}$$

As a result, the odd and the even modes have been decoupled which reduces the size of the matrix by a factor of 2 thus reducing the computational power required for solving the 1D helmlholtz equation. Note that for Neumann condition, Eq. (A.6) is transformed as

$$\sum_{k=1}^{N} k^2\tilde{u}_k = 0 \quad \sum_{k=1}^{N}(-1)^k k^2\tilde{u}_k = 0 \tag{A.16}$$

and consequently, Eq. (A.7) transforms as

$$\sum_{k=0,\text{even}}^{N} k^2\tilde{u}_k = 0, \quad \sum_{k=1,\text{odd}}^{N} k^2\tilde{u}_k = 0 \tag{A.17}$$

We use this method to solve the 1D Helmholtz equation obtain for each mode as shown in Sec. 3.3 in chapter 3.

Appendix B

Reduced order equations

We outline here the derivation of the reduced order equations, which closely follows that in Ref. [25] to which the reader is referred to for more details.

The $\boldsymbol{p}$-dependance of the probability density function Ψ can be decomposed onto spherical harmonics of successive orders, thereby decomposing Ψ as an infinite sum of orientation moments [238]. Each moment corresponds to a physical quantity, and contributes to the characterisation of the variability in particle orientation. For instance, the zeroth order moment corresponds to the local particle density Φ, the first order moment to the local average orientation or polarisation of particles $\boldsymbol{n}$, the second moment correspond to the nematic order, and so on. This expansion is truncated here after the first two moments, resulting in

$$\Psi(\boldsymbol{x},\boldsymbol{p},t) = \frac{1}{2\pi}\Phi(\boldsymbol{x},t) + \frac{1}{\pi}\boldsymbol{p}\cdot\boldsymbol{n}(\boldsymbol{x},t). \tag{B.1}$$

Taking successive moments of the Smoluchowski equation, Eq. 3.3, with respect to $\boldsymbol{p}$ provides the equations of evolution for the particle concentration and polarisation. Note that classically, a closure relationship is needed as directional self-propulsion introduces a forcing of each moment by higher order ones; following, Ref. [25] the nematic ordering is thus represented as

$$\boldsymbol{Q}(\boldsymbol{x},t) = \langle \boldsymbol{pp} - \frac{\boldsymbol{I}}{2}\rangle \approx \frac{\Phi \boldsymbol{I}}{2}. \tag{B.2}$$

As the dynamics of the suspension can be qualitatively understood without including the effect of the induced flows on the particles' transport, we further disregard such contributions so that the flow field used in the evaluation of the particles' transport is simply the background shear flow. This essentially decouples the Stokes equations from the particle distribution dynamics and results in the following evolution equations for Φ and $\boldsymbol{n}$:

$$\frac{\partial\Phi}{\partial t} + \boldsymbol{u}\cdot\nabla_x\Phi = -u_0\nabla_x\cdot\boldsymbol{n} - \frac{\xi_t}{\zeta}\left[\nabla_x C\cdot\nabla_x\Phi + \Phi\nabla_x^2 C\right] + d_x\nabla_x^2\Phi \tag{B.3}$$

$$\begin{aligned}\frac{\partial\boldsymbol{n}}{\partial t} + \boldsymbol{u}\cdot\nabla_x\boldsymbol{n} = &-\frac{u_0}{2}\nabla_x\Phi - \frac{\xi_t}{\zeta}\left[\nabla_x C\cdot\left(\nabla_x\boldsymbol{n}\right)^T + \boldsymbol{n}\nabla_x^2 C\right] + \frac{\xi_r\Phi\nabla_x C}{2\rho\zeta} + d_x\nabla_x\cdot\left(\nabla_x\boldsymbol{n}\right)^T \\ &- d_p\boldsymbol{n} + \frac{\gamma}{2}\boldsymbol{n}\cdot\left(e_z e_y - e_y e_z\right)\end{aligned} \tag{B.4}$$

In Equation (B.3), the successive terms on the right hand side correspond respectively to self-propulsion, phoretic drift and translational diffusion of the particles, respectively, while in Eq. (B.4), the successive forcing terms can be identified as self-propulsion, phoretic drift, chemotaxis, translational and rotational diffusions, and reorientation by the background vorticity.

The boundary conditions are evaluated similarly from Eq. (3.18) as

$$u_0 n_z = d_x\frac{\partial\Phi}{\partial z}, \qquad \frac{\partial n_y}{\partial z} = 0, \qquad u_0\Phi = d_x\frac{\partial n_z}{\partial z} \qquad \text{at} \quad z = \pm 1. \tag{B.5}$$

The solute concentration evolution equation and corresponding boundary conditions remain unchanged, Eq. (3.22).

Appendix C

Simplification of the fluid forcing

In this appendix, we revisit and justify the assumptions made in Sec. 3.5.3 to simplify the flow forcing.

First, we approximate that the particles in the system are locally aligned completely. This assumption is supported by the observation that the spatial mean in particle polarization ($\langle|\boldsymbol{n}|\rangle$) is close to 1, as depicted in Fig. C.1. This suggests that the pusher ($\mathbf{S_s}$) and puller contribution ($\mathbf{S_e}$) directly compete, resulting in the particle behaving as a net pusher/puller. We approximate the net behaviour of the particles as pushers based on the maximum strength of the concentration gradient, which remains of $O(1)$ (as shown in Fig. C.1.), suggesting that the pusher contribution is the dominant contribution. As a result, the fluid forcing can be approximated as a product of local particle density and the pusher contribution $\mathbf{S_s}$ in Eq. (3.61).

The approximation of pusher behaviour for each particle is further validated by observing the close similarity in the induced flows by including both the contributions (top) and only the pusher contribution (bottom) in Fig. C.2. The background contour plot in Fig. C.2 shows the domain's particle density distribution (Φ).

The next simplification is based on the observation that the two contributions in Eq. (3.62) act in the same direction as shown in Fig. C.3. Consequently, only one term with corrected amplitude is retained in Eq. 3.62, which correctly describes the induced flow based on particle density (Φ), polarisation ($\boldsymbol{n}$) and the sign of stress intensity (σ_m). Fig. C.3 further illustrates that the forcing effect is negligible in the bulk region and predominantly influences the flow near the walls. To emphasize this behavior, the figure is presented in a Chebyshev-Fourier space instead of physical space, enabling a clearer visualization of the strong forcing in close proximity to the walls.

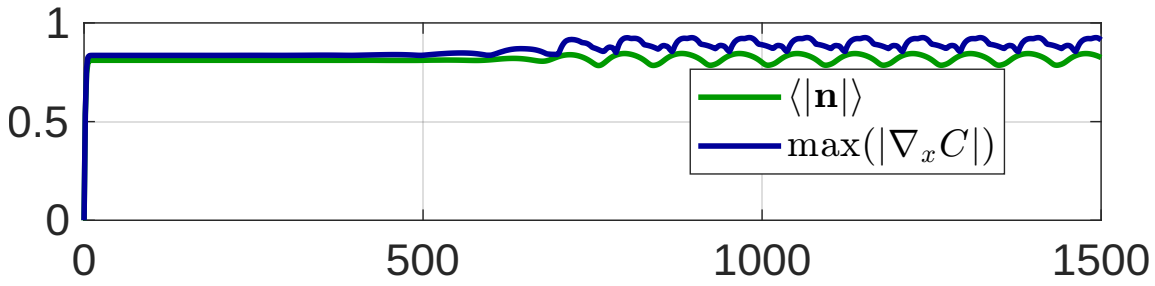

Figure C.1: Time evolution of spatial mean polarization magnitude and maximum $|\nabla_x C|$ for weak confinement case. The plateau region corresponds to the 1D transient state and the long-term periodic behaviour corresponds to the long-term unsteady 2D state. The plots are for $\gamma = 0.125$, $\zeta = 1$.

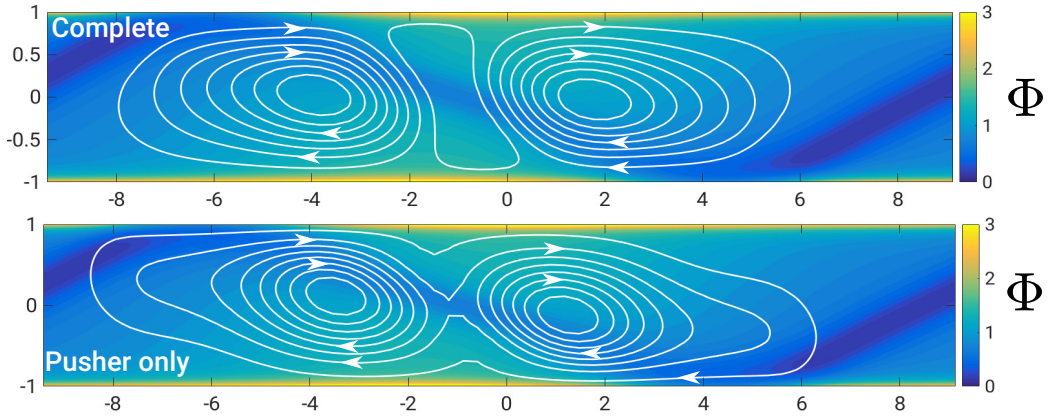

Figure C.2: Comparison between disturbance velocity field due (top)total active stress and (bottom)only the pusher signature of active stress for $\gamma = 0.125, \zeta = 1, t = 1325$. The colour bar represents the particle density in the domain.

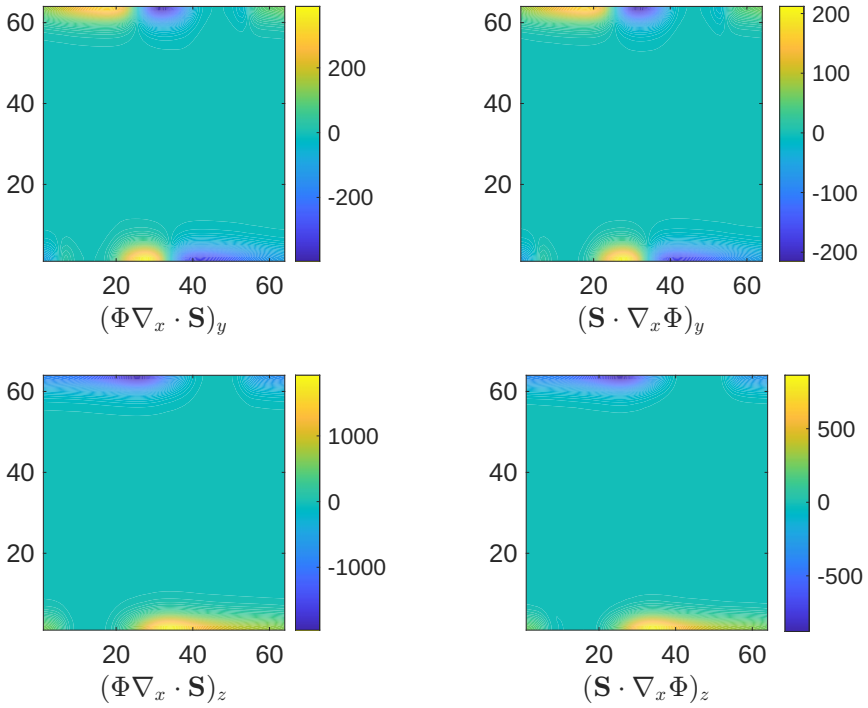

Figure C.3: Horizontal and vertical fluid forcing for the two terms of Eq. 3.62 for $\gamma = 0.125, \zeta = 1, t = 1500$. The forcing field is shown on equally spaced grid points instead of the Chebyshev-Fourier grid so that the regions of strong forcing (very close to the walls) are visible. Both effects have the same pattern of contribution to the driving force.

Appendix D

Adjoint state method

This appendix provides the derivation of the adjoint set of equations starting from the governing equations (Eq. (3.3),Eq. (3.19) and Eq. (3.22)). As we consider active walls with some arbritrary distribution, an extra term appears in the no-penetration boundary condition for the particles similar to Eq. (4.1) resulting in

$$\left(u_s \sin\theta + \xi_t \frac{\partial C}{\partial z}\right)\Psi = d_x \frac{\partial \Psi}{\partial z} \qquad \text{at } z = \pm 1. \tag{D.1}$$

Moreover, the solute flux at the wall is given by

$$\frac{\partial C}{\partial z} = A(y) \text{ at } z = +1 \tag{D.2}$$

$$\frac{\partial C}{\partial z} = 0 \text{ at } z = -1. \tag{D.3}$$

The objective of this exercise is to obtain the gradient of viscosity with respect to the activity distribution $\delta\eta/\delta A$. Therefore, we now introduce small perturbations to the system of equations which results in small change in effective viscosity.

D.1 Linearised equations

Introducing a perturbation in surface activity ($A \rightarrow A + \delta A$) results in perturbations in the probability density ($\Psi \rightarrow \Psi + \delta\Psi$), velocity field ($\boldsymbol{u} \rightarrow \boldsymbol{u} + \delta\boldsymbol{u}$), pressure field ($q \rightarrow q + \delta q$) and solute field ($C \rightarrow C + \delta C$). Consequently, the governing equations are perturbed for small changes in surface activity. The perturbed equations are as follows,

Kinetic equation

$$\begin{aligned}
&-\frac{\partial \delta\Psi}{\partial t} - \nabla_x \cdot (\delta\Psi u_s \mathbf{p}) - \nabla_x \cdot (\mathbf{u}\delta\Psi + \Psi\delta\mathbf{u}) - \nabla_x \cdot (\xi_t \delta\Psi \nabla_x C + \xi_t \Psi \nabla_x \delta C) \\
&+ \nabla_x \cdot (d_x \nabla_x \delta\Psi) + \nabla_p \cdot (d_p \nabla_p \delta\Psi) - \nabla_p \cdot (\frac{1}{2}(\boldsymbol{\omega} \times \mathbf{p})\delta\Psi + \frac{1}{2}(\delta\boldsymbol{\omega} \times \mathbf{p})\Psi) \\
&- \nabla_p \cdot (\frac{\xi_r}{\rho}(\delta\Psi(\mathbf{p} \times \nabla_x C) \times \mathbf{p} + \Psi(\mathbf{p} \times \nabla_x \delta C) \times \mathbf{p})) = 0
\end{aligned} \tag{D.4}$$

In (D.4) higher order terms are neglected and $O(1)$ terms exactly cancel out as it is the solution of the base state. Similarly, the boundary condition is linearised resulting in

$$\left(u_s \sin\theta + \xi_t \frac{\partial C}{\partial z}\right)\delta\Psi + \xi_t \frac{\partial \delta C}{\partial z}\Psi = d_x \frac{\partial \delta\Psi}{\partial z} \qquad \text{at } z = \pm 1. \tag{D.5}$$

Hydrodynamics

Linearised Stokes equations are given by

$$\nabla_x \cdot \delta \boldsymbol{u} = 0, \qquad \nabla_x \cdot (\delta \boldsymbol{\sigma}) = 0. \tag{D.6}$$

Here $\delta\boldsymbol{\sigma} = -q\boldsymbol{I} + (\nabla_x(\delta\boldsymbol{u}) + \nabla_x(\delta\boldsymbol{u})^T) + \delta\boldsymbol{S}$ is the Cauchy stress tensor while $\delta\boldsymbol{S} = \int \boldsymbol{S}_p \delta\Psi d\boldsymbol{p}$ is the active stress tensor with $\boldsymbol{S}_p$ representing the stresslet of individual swimmer (containing both contributions). The boundary condition is given by

$$\delta\boldsymbol{u} = \boldsymbol{0} \;\text{ at }\; z = \pm 1, \tag{D.7}$$

Solute equations

The linearised advection diffusion equations are given as

$$-\frac{\partial \delta C}{\partial t} - \boldsymbol{u} \cdot \nabla_x \delta C - \delta\boldsymbol{u} \cdot \nabla_x C + \nabla_x^2 \delta C - \beta \delta C + 2\pi \delta\Phi = 0 \tag{D.8}$$

with $\delta\Phi = \int \delta\Psi dp$. The corresponding boundary conditions are given by

$$\frac{\partial \delta C}{\partial z} = \delta A \text{ at } z = +1 \tag{D.9}$$

$$\frac{\partial \delta C}{\partial z} = 0 \text{ at } z = -1 \tag{D.10}$$

D.2 Adjoint fields and their governing equations

Based on the definition of the effective viscosity, finding minima in viscosity is identical to finding minima in drag force as the effective viscosity is proportional to the drag force. Therefore, we now define the drag force on the top wall as the objective function and the primary objective is to find the gradient $\delta F_D / \delta A$. The idea of gradient descent optimization is to introduce small changes in the direction of gradient and evaluate the gradient at each step. To reduce computational cost, we construct an augmented function to determine the gradient of the objective function. The augmented function is defined as

$$\delta F_{aug} = \delta F_D + \int_{V,t} \tilde{\boldsymbol{u}} R^{\delta \boldsymbol{u}} + \int_{V,t} \tilde{q} R^{\delta q} + \int_{V,\theta,t} \tilde{\Psi} R^{\delta \Psi} + \int_{V,t} \tilde{C} R^{\delta C} + \lambda \int_{V,\theta,t} \delta\Psi + \mu \int_S \delta A \tag{D.11}$$

where variables with a tilde ($\sim$) are the adjoint fields. The adjoint fields can also be seen as the Lagrange multipliers acting on the governing equations given by $R^{\delta\boldsymbol{u}} = 0, R^{\delta q} = 0, R^{\delta\Psi} = 0, R^{\delta C} = 0$. Note that the time integral acts only on the final state; that is if the final state is steady, the time integral can be neglected. Whereas, for periodic unsteady states, the time integral acts on the period. Furthermore, the term $\lambda \int_{V,\theta,t} \delta\Psi$ reflects the particle conservation constraint as $\int_{V,\theta,t} \delta\Psi$=0. The governing equations are given by,

$$R^{\delta q} \equiv \nabla_x \cdot \delta\boldsymbol{u} \tag{D.12}$$

$$R^{\delta \boldsymbol{u}} \equiv -\nabla_x \cdot (\delta\boldsymbol{\sigma}) \tag{D.13}$$

$$\begin{aligned} R^{\delta\Psi} \equiv & -\frac{\partial \delta\Psi}{\partial t} - \nabla_x \cdot (\delta\Psi u_s \mathbf{p}) - \nabla_x \cdot (\mathbf{u}\delta\Psi) - \nabla_x \cdot (\Psi \delta\mathbf{u}) - \nabla_x \cdot (\delta\Psi \xi_t \nabla_x C) \\ & - \nabla_x \cdot (\Psi \xi_t \nabla_x \delta C) + \nabla_x \cdot (d_x \nabla_x \delta\Psi) - \nabla_p \cdot (\frac{1}{2}(\boldsymbol{\omega} \times \mathbf{p})\delta\Psi) \\ & - \nabla_p \cdot (\frac{1}{2}(\delta\boldsymbol{\omega} \times \mathbf{p})\Psi) - \nabla_p \cdot (\frac{\xi_r}{\rho}\delta\Psi(\mathbf{p} \times \nabla_x C) \times \mathbf{p}) + \nabla_p \cdot (d_p \nabla_p \delta\Psi) \end{aligned} \tag{D.14}$$

and

$$R^{\delta C} \equiv -\frac{\partial \delta C}{\partial t} - \boldsymbol{u} \cdot \nabla_x \delta C - \delta\boldsymbol{u} \cdot \nabla_x C + \nabla_x^2 \delta C + \beta \delta C - 2\pi\delta\Phi. \tag{D.15}$$

The idea now is to express Eq. (D.11) in a form which reflects the sensitivity of the objective function with respect to $\delta\Psi$,$\delta\boldsymbol{u}$, δq and δC. That is, the objective is to express Eq. (D.11) as

$$\delta F_{aug} = \delta F_D + \int_{V,t} R^{\tilde{\boldsymbol{u}}}\delta\boldsymbol{u} + \int_{V,t} R^{\tilde{q}}\delta q + \int_{V,\theta,t} R^{\tilde{\Psi}}\delta\Psi + \int_{V,t} R^{\tilde{C}}\delta C + \mu\int_S \delta A + \text{surface terms} \tag{D.16}$$

By transforming the Eq. (D.11) in such a form, we can then impose constraints on the adjoint problem such that this sensitivity with respect to small changes in state variables disappears. We use integration by parts for this transformation. As a result, we obtain,

$$\begin{aligned}\delta F_{aug} =& \delta F_D + \int_V R^{\tilde{\boldsymbol{u}}}\delta\boldsymbol{u} + \int_V R^{\tilde{q}}\delta q + \int_{V,\theta} R^{\tilde{\Psi}}\delta\Psi + \int_V R^{\tilde{C}}\delta C \\ &+ \int_S BC_{\delta\boldsymbol{u}}\delta\boldsymbol{u} + \int_S BC_{\delta\Psi}\delta\Psi + \int_S BC_{\delta C}\delta C \\ &+ \int_S \tilde{C}\delta A + \mu\int_S \delta A + \int_S \tilde{\boldsymbol{u}}\cdot\delta\boldsymbol{\sigma}\cdot\boldsymbol{n}\end{aligned} \tag{D.17}$$

where $R^{\tilde{\boldsymbol{u}}}, R^{\tilde{q}}, R^{\tilde{\Psi}}, R^{\tilde{C}}$ are the adjoint equations given by,

$$R^{\tilde{u_z}} \equiv \left\langle \Psi\frac{\partial\tilde{\Psi}}{\partial z} - \frac{1}{2}\frac{\partial\Psi}{\partial y}\frac{\partial\tilde{\Psi}}{\partial\theta} - \frac{1}{2}\Psi\frac{\partial^2\tilde{\Psi}}{\partial y\partial\theta}\right\rangle_\theta + C\frac{\partial\tilde{C}}{\partial z} - \frac{\partial\tilde{q}}{\partial z} + \nabla_x^2 u_z = 0 \tag{D.18}$$

$$R^{\tilde{u_y}} \equiv \left\langle \Psi\frac{\partial\tilde{\Psi}}{\partial y} + \frac{1}{2}\frac{\partial\Psi}{\partial z}\frac{\partial\tilde{\Psi}}{\partial\theta} + \frac{1}{2}\Psi\frac{\partial^2\tilde{\Psi}}{\partial z\partial\theta}\right\rangle_\theta + C\frac{\partial\tilde{C}}{\partial y} - \frac{\partial\tilde{q}}{\partial y} + \nabla_x^2 u_y = 0 \tag{D.19}$$

$$R^{\tilde{q}} \equiv \nabla\cdot\tilde{\boldsymbol{u}} = 0 \tag{D.20}$$

$$\begin{aligned}R^{\tilde{\Psi}} \equiv& \frac{\partial\tilde{\Psi}}{\partial t} + u_s(\nabla_x\tilde{\Psi}\cdot\boldsymbol{p}) + \boldsymbol{u}\cdot\nabla_x\tilde{\Psi} + \xi_t(\nabla_x\tilde{\Psi}\cdot\nabla_x C) + d_x\nabla_x^2\tilde{\Psi} + \frac{1}{2}\omega\frac{\partial\tilde{\Psi}}{\partial\theta} \\ &+ \frac{\xi_r}{\rho}\frac{\partial\tilde{\Psi}}{\partial\theta}(\nabla_x C\cdot\boldsymbol{e}_\theta) + d_p\nabla_p^2\tilde{\Psi} + 2\pi\tilde{C} - \boldsymbol{S}_p : \nabla\tilde{\boldsymbol{u}} + \lambda = 0\end{aligned} \tag{D.21}$$

$$R^{\tilde{C}} \equiv \frac{\partial\tilde{C}}{\partial t} + \boldsymbol{u}\cdot\nabla_x\tilde{C} + \nabla_x^2\tilde{C} - \beta\tilde{C} - \left\langle \xi_t(\nabla_x\Psi\cdot\nabla_x\tilde{\Psi} + \Psi\nabla_x^2\tilde{\Psi}) - \frac{\xi_r}{\rho}\nabla_x\left(\Psi\frac{\partial\tilde{\Psi}}{\partial\theta}\right)\cdot\boldsymbol{e}_\theta\right\rangle_\theta = 0 \tag{D.22}$$

where the angle brackets ($\langle.\rangle$) represent the average over subscript coordinate. The surface terms captured by $BC_{\delta\Psi}, BC_{\delta C}$ are given by

$$BC_{\delta\Psi} \equiv \nabla\tilde{\Psi}\cdot\boldsymbol{e}_z = 0 \tag{D.23}$$

$$BC_{\delta C} \equiv \frac{\partial\tilde{C}}{\partial z} = \left\langle \xi_t\frac{\partial\tilde{\Psi}}{\partial z}\Psi + \frac{\xi_r}{\rho}\Psi\frac{\partial\tilde{\Psi}}{\partial\theta}\sin\theta\right\rangle_\theta = 0 \tag{D.24}$$

The only boundary condition left is the one associated with Eq. (D.13) which combines with $\delta F_D = \int_S \boldsymbol{n}\cdot\delta\boldsymbol{\sigma}\cdot\boldsymbol{t}$ term which results in

$$\begin{aligned}\delta F_{aug} =& \int_{z=1}\left(\boldsymbol{n}\cdot\delta\boldsymbol{\sigma}\cdot\boldsymbol{t} + \boldsymbol{n}\cdot\delta\boldsymbol{\sigma}\cdot\tilde{\boldsymbol{u}}\right) \\ &+ \int_V R^{\tilde{u}}\delta u + \int_V R^{\tilde{q}}\delta q + \int_{V,\theta} R^{\tilde{\Psi}}\delta\Psi + \int_V R^{\tilde{C}}\delta C \\ &+ \int_S + BC_{\delta\Psi}\delta\Psi + \int_S BC_{\delta C}\delta C \\ &+ \int_S \tilde{C}\delta A + \int_S \mu\delta A.\end{aligned} \tag{D.25}$$

In the above equation, if the adjoint flow field ($\tilde{\boldsymbol{u}}$) is chosen such than $\tilde{\boldsymbol{u}} = -\boldsymbol{t} = -\boldsymbol{e_y}$ at the surface and if the adjoint equations are satisfied i.e $R^{\tilde{u}} = R^{\tilde{q}} = R^{\tilde{\Psi}} = R^{\tilde{C}} = 0$ with boundary

condition such that the boundary terms also vanish then the gradient can be evaluated using the adjoint concentration field $\tilde{C}$ as

$$\delta F_{aug} = \int_S \tilde{C} \delta A \tag{D.26}$$

As a result, the gradient is expressed in terms of the integral of the adjoint solute field, which must be solved along with the primal governing equations.

Bibliography

[1] Jörn Dunkel, Sebastian Heidenreich, Knut Drescher, Henricus H Wensink, Markus Bär, and Raymond E Goldstein. Fluid dynamics of bacterial turbulence. *Physical review letters*, 110(22):228102, 2013.

[2] Li Zhang, Jake J Abbott, Lixin Dong, Bradley E Kratochvil, Dominik Bell, and Bradley J Nelson. Artificial bacterial flagella: Fabrication and magnetic control. *Applied Physics Letters*, 94(6), 2009.

[3] Shashi Thutupalli, Ralf Seemann, and Stephan Herminghaus. Swarming behavior of simple model squirmers. *New Journal of Physics*, 13(7):073021, 2011.

[4] Sébastien Michelin, Eric Lauga, and Denis Bartolo. Spontaneous autophoretic motion of isotropic particles. *Physics of Fluids*, 25(6), 2013.

[5] Xia Huang, Hatice Mutlu, Wenyuan Dong, and Patrick Theato. Polymeric janus nanorods via anodic aluminum oxide templating. *Soft Matter*, 19(30):5663–5667, 2023.

[6] Jeffrey L Moran and Jonathan D Posner. Phoretic self-propulsion. *Annual Review of Fluid Mechanics*, 49:511–540, 2017.

[7] Muhammad Safdar, Shahid Ullah Khan, and Janne Jänis. Progress toward catalytic micro- and nanomotors for biomedical and environmental applications. *Advanced Materials*, 30(24):1703660, 2018.

[8] Jonathan R Howse, Richard AL Jones, Anthony J Ryan, Tim Gough, Reza Vafabakhsh, and Ramin Golestanian. Self-motile colloidal particles: from directed propulsion to random walk. *Physical review letters*, 99(4):048102, 2007.

[9] Zhiyong Gao, He Li, Xiao Chen, and HP Zhang. Using confined bacteria as building blocks to generate fluid flow. *Lab on a Chip*, 15(24):4555–4562, 2015.

[10] Hugo Wioland, Enkeleida Lushi, and Raymond E Goldstein. Directed collective motion of bacteria under channel confinement. *New Journal of Physics*, 18(7):075002, 2016.

[11] Xabel Garcia, Salima Rafaï, and Philippe Peyla. Light control of the flow of phototactic microswimmer suspensions. *Physical review letters*, 110(13):138106, 2013.

[12] Jérémie Gachelin, Gastón Mino, Hélene Berthet, Anke Lindner, Annie Rousselet, and Éric Clément. Non-newtonian viscosity of escherichia coli suspensions. *Physical review letters*, 110(26):268103, 2013.

[13] Zhengyang Liu, Kechun Zhang, and Xiang Cheng. Rheology of bacterial suspensions under confinement. *Rheologica Acta*, 58:439–451, 2019.

[14] Héctor Matías López, Jérémie Gachelin, Carine Douarche, Harold Auradou, and Eric Clément. Turning bacteria suspensions into superfluids. *Physical review letters*, 115(2):028301, 2015.

[15] David Saintillan. Rheology of active fluids. *Annual Review of Fluid Mechanics*, 50:563–592, 2018.

[16] Debasmita Mondal, Ameya G Prabhune, Sriram Ramaswamy, and Prerna Sharma. Strong confinement of active microalgae leads to inversion of vortex flow and enhanced mixing. *eLife*, 10:e67663, nov 2021.

[17] Saikat Jana, Soong Ho Um, and Sunghwan Jung. Paramecium swimming in capillary tube. *Physics of Fluids*, 24(4):041901, 04 2012.

[18] Knut Drescher, Raymond E Goldstein, Nicolas Michel, Marco Polin, and Idan Tuval. Direct measurement of the flow field around swimming microorganisms. *Physical Review Letters*, 105(16):168101, 2010.

[19] Jianzhong Du and Rachel K. O'Reilly. Anisotropic particles with patchy, multicompartment and janus architectures: preparation and application. *Chem. Soc. Rev.*, 40:2402–2416, 2011.

[20] Sébastien Michelin and Eric Lauga. Phoretic self-propulsion at finite péclet numbers. *Journal of fluid mechanics*, 747:572–604, 2014.

[21] Sankalp Nambiar. *Swimmer suspensions: fluctuations, microstructure and rheology*. Phd thesis, Jawaharlal Nehru Centre for Advanced Scientific Research, Bengaluru, January 2020. Available at https://libjncir.jncasr.ac.in/xmlui/handle/123456789/3067.

[22] Daniel J Webre, Peter M Wolanin, and Jeffry B Stock. Bacterial chemotaxis. *Current Biology*, 13(2):R47–R49, 2003.

[23] Di Li and Xiangchun Xuan. Electrophoretic slip-tuned particle migration in microchannel viscoelastic fluid flows. *Physical Review Fluids*, 3(7):074202, 2018.

[24] Nicolas Waisbord, Christopher T Lefèvre, Lydéric Bocquet, Christophe Ybert, and Cécile Cottin-Bizonne. Destabilization of a flow focused suspension of magnetotactic bacteria. *Physical Review Fluids*, 1(5):053203, 2016.

[25] T Traverso and S Michelin. Collective dynamics and rheology of confined phoretic suspensions. *Journal of Fluid Mechanics*, 943:A21, 2022.

[26] M Cristina Marchetti, Jean-François Joanny, Sriram Ramaswamy, Tanniemola B Liverpool, Jacques Prost, Madan Rao, and R Aditi Simha. Hydrodynamics of soft active matter. *Reviews of modern physics*, 85(3):1143, 2013.

[27] Sriram Ramaswamy. The mechanics and statistics of active matter. *Annu. Rev. Condens. Matter Phys.*, 1(1):323–345, 2010.

[28] Thomas Surrey, François Nédélec, Stanislas Leibler, and Eric Karsenti. Physical properties determining self-organization of motors and microtubules. *Science*, 292(5519):1167–1171, 2001.

[29] FJ Ndlec, Thomas Surrey, Anthony C Maggs, and Stanislas Leibler. Self-organization of microtubules and motors. *Nature*, 389(6648):305–308, 1997.

[30] Lucy M Aplin, Damien R Farine, Richard P Mann, and Ben C Sheldon. Individual-level personality influences social foraging and collective behaviour in wild birds. *Proceedings of the Royal Society B: Biological Sciences*, 281(1789):20141016, 2014.

[31] Brian L Partridge. The structure and function of fish schools. *Scientific american*, 246(6):114–123, 1982.

[32] Francesco Ginelli, Fernando Peruani, Marie-Helène Pillot, Hugues Chaté, Guy Theraulaz, and Richard Bon. Intermittent collective dynamics emerge from conflicting imperatives in sheep herds. *Proceedings of the National Academy of Sciences*, 112(41):12729–12734, 2015.

[33] Michael E Cates, D Marenduzzo, I Pagonabarraga, and J Tailleur. Arrested phase separation in reproducing bacteria creates a generic route to pattern formation. *Proceedings of the National Academy of Sciences*, 107(26):11715–11720, 2010.

[34] Y Asano, A Jiménez-Dalmaroni, TB Liverpool, MC Marchetti, L Giomi, A Kiger, T Duke, and B Baum. Pak3 inhibits local actin filament formation to regulate global cell polarity. *HFSP journal*, 3(3):194–203, 2009.

[35] Frédéric Delsuc. Army ants trapped by their evolutionary history. *PLoS biology*, 1(2):e37, 2003.

[36] Dirk Erhard, Tertuliano Franco, and Guilherme Reis. The directed edge reinforced random walk: The ant mill phenomenon. *arXiv preprint arXiv:1911.07295*, 2019.

[37] Ria Das. Exploring the ant mill: Numerical and analytical investigations of mixed memory-reinforcement systems. *arXiv preprint arXiv:1703.06859*, 2017.

[38] Amandine Ramseyer, Alain Boissy, Bernard Thierry, and Bertrand Dumont. Individual and social determinants of spontaneous group movements in cattle and sheep. *Animal*, 3(9):1319–1326, 2009.

[39] Luis Gómez-Nava, Richard Bon, and Fernando Peruani. Intermittent collective motion in sheep results from alternating the role of leader and follower. *Nature Physics*, 18(12):1494–1501, 2022.

[40] Manfred Milinski and Rolf Heller. Influence of a predator on the optimal foraging behaviour of sticklebacks (gasterosteus aculeatus l.). *Nature*, 275(5681):642–644, 1978.

[41] Jonathan M Jeschke and Ralph Tollrian. Prey swarming: which predators become confused and why? *Animal Behaviour*, 74(3):387–393, 2007.

[42] Stefano Marras, Shaun S Killen, Jan Lindström, David J McKenzie, John F Steffensen, and Paolo Domenici. Fish swimming in schools save energy regardless of their spatial position. *Behavioral ecology and sociobiology*, 69:219–226, 2015.

[43] Christophe Hausswirth, Jean-Marc Vallier, Didier Lehénaff, Jeanick Brisswalter, Darren Smith, Grégoire Millet, and Patrick Dréano. Effect of two drafting modalities in cycling on running performance. *Medicine & Science in Sports & Exercise*, 33(3):485–492, 2001.

[44] TJ Pitcher, AE Magurran, and IJ Winfield. Fish in larger shoals find food faster. *Behavioral Ecology and Sociobiology*, 10:149–151, 1982.

[45] Elisabeth HM Sterck, David P Watts, and Carel P Van Schaik. The evolution of female social relationships in nonhuman primates. *Behavioral ecology and sociobiology*, 41:291–309, 1997.

[46] R Ethan Pride. Optimal group size and seasonal stress in ring-tailed lemurs (lemur catta). *Behavioral Ecology*, 16(3):550–560, 2005.

[47] Tamás Vicsek, András Czirók, Eshel Ben-Jacob, Inon Cohen, and Ofer Shochet. Novel type of phase transition in a system of self-driven particles. *Physical review letters*, 75(6):1226, 1995.

[48] John Toner and Yuhai Tu. Long-range order in a two-dimensional dynamical xy model: how birds fly together. *Physical review letters*, 75(23):4326, 1995.

[49] Eric Bertin, Michel Droz, and Guillaume Grégoire. Boltzmann and hydrodynamic description for self-propelled particles. *Physical Review E*, 74(2):022101, 2006.

[50] E M Purcell. Life at low reynolds number. *American Journal of Physics*, 45(1):3–11, 1977.

[51] Dennis Bray. *Cell movements: from molecules to motility*. Garland Science, 2000.

[52] Eric Lauga. Bacterial hydrodynamics. *Annual Review of Fluid Mechanics*, 48:105–130, 2016.

[53] Ganesh Subramanian and Donald L Koch. Critical bacterial concentration for the onset of collective swimming. *Journal of Fluid Mechanics*, 632:359–400, 2009.

[54] Henricus H Wensink, Jörn Dunkel, Sebastian Heidenreich, Knut Drescher, Raymond E Goldstein, Hartmut Löwen, and Julia M Yeomans. Meso-scale turbulence in living fluids. *Proceedings of the national academy of sciences*, 109(36):14308–14313, 2012.

[55] Andrey Sokolov and Igor S Aranson. Reduction of viscosity in suspension of swimming bacteria. *Physical review letters*, 103(14):148101, 2009.

[56] Neil H Mendelson, Adrienne Bourque, Kathryn Wilkening, Kevin R Anderson, and Joseph C Watkins. Organized cell swimming motions in bacillus subtilis colonies: patterns of short-lived whirls and jets. *Journal of bacteriology*, 181(2):600–609, 1999.

[57] Adama Creppy, Olivier Praud, Xavier Druart, Philippa L Kohnke, and Franck Plouraboué. Turbulence of swarming sperm. *Physical Review E*, 92(3):032722, 2015.

[58] Xiao-Lun Wu and Albert Libchaber. Particle diffusion in a quasi-two-dimensional bacterial bath. *Physical review letters*, 84(13):3017, 2000.

[59] Andrey Sokolov, Igor S Aranson, John O Kessler, and Raymond E Goldstein. Concentration dependence of the collective dynamics of swimming bacteria. *Physical review letters*, 98(15):158102, 2007.

[60] Christopher Dombrowski, Luis Cisneros, Sunita Chatkaew, Raymond E Goldstein, and John O Kessler. Self-concentration and large-scale coherence in bacterial dynamics. *Physical review letters*, 93(9):098103, 2004.

[61] Avin Babataheri, Marcus Roper, Marc Fermigier, and Olivia Du Roure. Tethered fleximags as artificial cilia. *Journal of Fluid Mechanics*, 678:5–13, 2011.

[62] Rémi Dreyfus, Jean Baudry, Marcus L Roper, Marc Fermigier, Howard A Stone, and Jérôme Bibette. Microscopic artificial swimmers. *Nature*, 437(7060):862–865, 2005.

[63] Antoine Bricard, Jean-Baptiste Caussin, Nicolas Desreumaux, Olivier Dauchot, and Denis Bartolo. Emergence of macroscopic directed motion in populations of motile colloids. *Nature*, 503(7474):95–98, 2013.

[64] Antoine Bricard, Jean-Baptiste Caussin, Debasish Das, Charles Savoie, Vijayakumar Chikkadi, Kyohei Shitara, Oleksandr Chepizhko, Fernando Peruani, David Saintillan, and Denis Bartolo. Emergent vortices in populations of colloidal rollers. *Nature communications*, 6(1):7470, 2015.

[65] Gerardo E. Pradillo, Hamid Karani, and Petia M. Vlahovska. Quincke rotor dynamics in confinement: rolling and hovering. *Soft Matter*, 15:6564–6570, 2019.

[66] Ricardo Reyes Garza, Nikos Kyriakopoulos, Zoran M Cenev, Carlo Rigoni, and Jaakko VI Timonen. Magnetic quincke rollers with tunable single-particle dynamics and collective states. *Science Advances*, 9(26):eadh2522, 2023.

[67] Ziane Izri, Marjolein N Van Der Linden, Sébastien Michelin, and Olivier Dauchot. Self-propulsion of pure water droplets by spontaneous marangoni-stress-driven motion. *Physical review letters*, 113(24):248302, 2014.

[68] W F Paxton, K C Kistler, C C Olmeda, A Sen, S K St. Angelo, Y Cao, T E Mallouk, P E Lammert, and V H Crespi. Catalytic nanomotors: autonomous movement of striped nanorods. *Journal of the American Chemical Society*, 126(41):13424–13431, 2004.

[69] Sébastien Fournier-Bidoz, André C Arsenault, Ian Manners, and Geoffrey A Ozin. Synthetic self-propelled nanorotors. *Chemical Communications*, (4):441–443, 2005.

[70] Hua Ke, Shengrong Ye, R Lloyd Carroll, and Kenneth Showalter. Motion analysis of self-propelled pt- silica particles in hydrogen peroxide solutions. *The Journal of Physical Chemistry A*, 114(17):5462–5467, 2010.

[71] Wei Gao, Allen Pei, Renfeng Dong, and Joseph Wang. Catalytic iridium-based janus micromotors powered by ultralow levels of chemical fuels. *Journal of the American Chemical Society*, 136(6):2276–2279, 2014.

[72] Stefano Palagi, Dhruv P Singh, and Peer Fischer. Light-controlled micromotors and soft microrobots. *Advanced Optical Materials*, 7(16):1900370, 2019.

[73] Linlin Wang, Andrea Kaeppler, Dieter Fischer, and Juliane Simmchen. Photocatalytic tio2 micromotors for removal of microplastics and suspended matter. *ACS applied materials & interfaces*, 11(36):32937–32944, 2019.

[74] Michael E Ibele, Paul E Lammert, Vincent H Crespi, and Ayusman Sen. Emergent, collective oscillations of self-mobile particles and patterned surfaces under redox conditions. *ACS nano*, 4(8):4845–4851, 2010.

[75] Xiankun Lin, Tieyan Si, Zhiguang Wu, and Qiang He. Self-thermophoretic motion of controlled assembled micro-/nanomotors. *Physical Chemistry Chemical Physics*, 19(35):23606–23613, 2017.

[76] Hong-Ren Jiang, Natsuhiko Yoshinaga, and Masaki Sano. Active motion of a janus particle by self-thermophoresis in a defocused laser beam. *Physical review letters*, 105(26):268302, 2010.

[77] Pierre Gaspard and Raymond Kapral. The stochastic motion of self-thermophoretic janus particles. *Journal of Statistical Mechanics: Theory and Experiment*, 2019(7):074001, 2019.

[78] BV Derjaguin, AI Storozhilova, and Ya I Rabinovich. Experimental verification of the theory of thermophoresis of aerosol particles. *Journal of Colloid and Interface Science*, 21(1):35–58, 1966.

[79] Sébastien Michelin. Self-propulsion of chemically active droplets. *Annual Review of Fluid Mechanics*, 55:77–101, 2023.

[80] Sébastien Michelin and Eric Lauga. Autophoretic locomotion from geometric asymmetry. *The European Physical Journal E*, 38:1–16, 2015.

[81] Marietta Zinner, Ilya Lukonin, and Prisca Liberali. Design principles of tissue organisation: How single cells coordinate across scales. *Current opinion in cell biology*, 67:37–45, 2020.

[82] Rebecca Heald and Orna Cohen-Fix. Morphology and function of membrane-bound organelles. *Current opinion in cell biology*, 26:79–86, 2014.

[83] Julius Adler. Chemotaxis in bacteria. *Annual review of biochemistry*, 44(1):341–356, 1975.

[84] Chih-kuan Tung, Chungwei Lin, Benedict Harvey, Alyssa G Fiore, Florencia Ardon, Mingming Wu, and Susan S Suarez. Fluid viscoelasticity promotes collective swimming of sperm. *Scientific reports*, 7(1):3152, 2017.

[85] Damien Bouffard and Alfred Wüest. Convection in lakes. *Annual Review of Fluid Mechanics*, 51:189–215, 2019.

[86] Francesco Di Nezio, Samuele Roman, Antoine Buetti-Dinh, Oscar Sepúlveda Steiner, Damien Bouffard, Anupam Sengupta, and Nicola Storelli. Motile bacteria leverage bioconvection for eco-physiological benefits in a natural aquatic environment. *Frontiers in Microbiology*, 14:1253009, 2023.

[87] U Kei Cheang, Kyoungwoo Lee, Anak Agung Julius, and Min Jun Kim. Multiple-robot drug delivery strategy through coordinated teams of microswimmers. *Applied physics letters*, 105(8), 2014.

[88] Levke Ortlieb, Salima Rafaï, Philippe Peyla, Christian Wagner, and Thomas John. Statistics of colloidal suspensions stirred by microswimmers. *Physical review letters*, 122(14):148101, 2019.

[89] Claudio Maggi, Juliane Simmchen, Filippo Saglimbeni, Jaideep Katuri, Michele Dipalo, Francesco De Angelis, Samuel Sanchez, and Roberto Di Leonardo. Self-assembly of micromachining systems powered by janus micro-motors. *arXiv preprint arXiv:1707.03630*, 2017.

[90] Salima Rafaï, Levan Jibuti, and Philippe Peyla. Effective viscosity of microswimmer suspensions. *Physical Review Letters*, 104(9):098102, 2010.

[91] John W Crawford, James A Harris, Karl Ritz, and Iain M Young. Towards an evolutionary ecology of life in soil. *Trends in ecology & evolution*, 20(2):81–87, 2005.

[92] Mohammad Reza Raveshi, Melati S Abdul Halim, Sagar N Agnihotri, Moira K O'Bryan, Adrian Neild, and Reza Nosrati. Curvature in the reproductive tract alters sperm–surface interactions. *Nature communications*, 12(1):3446, 2021.

[93] Rasika M Harshey. Bacterial motility on a surface: many ways to a common goal. *Annual Reviews in Microbiology*, 57(1):249–273, 2003.

[94] Jens Elgeti and Gerhard Gompper. Microswimmers near surfaces. *The European Physical Journal Special Topics*, 225:2333–2352, 2016.

[95] Willow R DiLuzio, Linda Turner, Michael Mayer, Piotr Garstecki, Douglas B Weibel, Howard C Berg, and George M Whitesides. Escherichia coli swim on the right-hand side. *Nature*, 435(7046):1271–1274, 2005.

[96] Guanglai Li, James Bensson, Liana Nisimova, Daniel Munger, Panrapee Mahautmr, Jay X Tang, Martin R Maxey, and Yves V Brun. Accumulation of swimming bacteria near a solid surface. *Physical Review E*, 84(4):041932, 2011.

[97] Allison P Berke, Linda Turner, Howard C Berg, and Eric Lauga. Hydrodynamic attraction of swimming microorganisms by surfaces. *Physical Review Letters*, 101(3):038102, 2008.

[98] L Rothschild. Non-random distribution of bull spermatozoa in a drop of sperm suspension. *Nature*, 198(488):1221, 1963.

[99] Sambeeta Das, Astha Garg, Andrew I Campbell, Jonathan Howse, Ayusman Sen, Darrell Velegol, Ramin Golestanian, and Stephen J Ebbens. Boundaries can steer active janus spheres. *Nature communications*, 6(1):8999, 2015.

[100] Juan P Hernandez-Ortiz, Christopher G Stoltz, and Michael D Graham. Transport and collective dynamics in suspensions of confined swimming particles. *Physical review letters*, 95(20):204501, 2005.

[101] David Saintillan and Michael J Shelley. Theory of active suspensions. *Complex Fluids in Biological Systems: Experiment, Theory, and Computation*, pages 319–355, 2015.

[102] Howard C Berg and Linda Turner. Chemotaxis of bacteria in glass capillary arrays. escherichia coli, motility, microchannel plate, and light scattering. *Biophysical Journal*, 58(4):919–930, 1990.

[103] Paul D Frymier, Roseanne M Ford, Howard C Berg, and Peter T Cummings. Three-dimensional tracking of motile bacteria near a solid planar surface. *Proceedings of the National Academy of Sciences*, 92(13):6195–6199, 1995.

[104] Eric Lauga, Willow R DiLuzio, George M Whitesides, and Howard A Stone. Swimming in circles: motion of bacteria near solid boundaries. *Biophysical journal*, 90(2):400–412, 2006.

[105] Hugo Wioland, Francis G Woodhouse, Jörn Dunkel, John O Kessler, and Raymond E Goldstein. Confinement stabilizes a bacterial suspension into a spiral vortex. *Physical review letters*, 110(26):268102, 2013.

[106] Enkeleida Lushi, Hugo Wioland, and Raymond E Goldstein. Fluid flows created by swimming bacteria drive self-organization in confined suspensions. *Proceedings of the National Academy of Sciences*, 111(27):9733–9738, 2014.

[107] Gáspár Jékely. Evolution of phototaxis. *Philosophical Transactions of the Royal Society B: Biological Sciences*, 364(1531):2795–2808, 2009.

[108] TJ Pedley and JO Kessler. Bioconvection. *Science Progress (1933-)*, pages 105–123, 1992.

[109] NA Hill and TJ Pedley. Bioconvection. *Fluid Dynamics Research*, 37(1-2):1, 2005.

[110] Björn Petri and Maria-Jesús Sanz. Neutrophil chemotaxis. *Cell and tissue research*, 371:425–436, 2018.

[111] Michael Eisenbach. Sperm chemotaxis. *Reviews of reproduction*, 4(1):56–66, 1999.

[112] Chenyu Jin, Carsten Krüger, and Corinna C Maass. Chemotaxis and autochemotaxis of self-propelling droplet swimmers. *Proceedings of the National Academy of Sciences*, 114(20):5089–5094, 2017.

[113] Elena O Budrene and Howard C Berg. Dynamics of formation of symmetrical patterns by chemotactic bacteria. *Nature*, 376(6535):49–53, 1995.

[114] Maria Tătulea-Codrean and Eric Lauga. Artificial chemotaxis of phoretic swimmers: Instantaneous and long-time behaviour. *Journal of Fluid Mechanics*, 856:921–957, 2018.

[115] Prathmesh M Vinze, Akash Choudhary, and S Pushpavanam. Motion of an active particle in a linear concentration gradient. *Physics of Fluids*, 33(3), 2021.

[116] I. Theurkauff, C. Cottin-Bizonne, J. Palacci, C. Ybert, and L. Bocquet. Dynamic clustering in active colloidal suspensions with chemical signaling. *Phys. Rev. Lett.*, 108:268303, Jun 2012.

[117] Michael E Cates and Julien Tailleur. Motility-induced phase separation. *Annu. Rev. Condens. Matter Phys.*, 6(1):219–244, 2015.

[118] Borge ten Hagen, Raphael Wittkowski, and Hartmut Löwen. Brownian dynamics of a self-propelled particle in shear flow. *Phys. Rev. E*, 84:031105, Sep 2011.

[119] Andreas Zöttl and Holger Stark. Periodic and quasiperiodic motion of an elongated microswimmer in poiseuille flow. *The European Physical Journal E*, 36:1–10, 2013.

[120] Roberto Rusconi, Jeffrey S Guasto, and Roman Stocker. Bacterial transport suppressed by fluid shear. *Nature physics*, 10(3):212–217, 2014.

[121] Marcos, Henry C Fu, Thomas R Powers, and Roman Stocker. Bacterial rheotaxis. *Proceedings of the National Academy of Sciences*, 109(13):4780–4785, 2012.

[122] Arnold JTM Mathijssen, Nuris Figueroa-Morales, Gaspard Junot, Éric Clément, Anke Lindner, and Andreas Zöttl. Oscillatory surface rheotaxis of swimming e. coli bacteria. *Nature communications*, 10(1):3434, 2019.

[123] Luis H Cisneros, Ricardo Cortez, Christopher Dombrowski, Raymond E Goldstein, and John O Kessler. Fluid dynamics of self-propelled microorganisms, from individuals to concentrated populations. *Animal Locomotion*, pages 99–115, 2010.

[124] Jane Hill, Ozge Kalkanci, Jonathan L McMurry, and Hur Koser. Hydrodynamic surface interactions enable escherichia coli to seek efficient routes to swim upstream. *Physical review letters*, 98(6):068101, 2007.

[125] Priyanka Sharan, Zuyao Xiao, Viviana Mancuso, William E Uspal, and Juliane Simmchen. Upstream rheotaxis of catalytic janus spheres. *ACS nano*, 16(3):4599–4608, 2022.

[126] Bishwa Ranjan Si, Preet Patel, and Rahul Mangal. Self-propelled janus colloids in shear flow. *Langmuir*, 36(40):11888–11898, 2020.

[127] WE Uspal, Mikhail N Popescu, S Dietrich, and M Tasinkevych. Rheotaxis of spherical active particles near a planar wall. *Soft matter*, 11(33):6613–6632, 2015.

[128] L. Gary Leal. *Basic Principles*, page 13–109. Cambridge Series in Chemical Engineering. Cambridge University Press, 2007.

[129] JC Van der Werff and CG De Kruif. Hard-sphere colloidal dispersions: the scaling of rheological properties with particle size, volume fraction, and shear rate. *Journal of Rheology*, 33(3):421–454, 1989.

[130] Toshiyuki Shikata and Dale S Pearson. Viscoelastic behavior of concentrated spherical suspensions. *Journal of Rheology*, 38(3):601–616, 1994.

[131] GK Batchelor. Sedimentation in a dilute dispersion of spheres. *Journal of fluid mechanics*, 52(2):245–268, 1972.

[132] E Guazzelli and J F Morris. *A physical introduction to suspension dynamics*, volume 45. Cambridge University Press, 2011.

[133] Élisabeth Guazzelli and Olivier Pouliquen. Rheology of dense granular suspensions. *Journal of Fluid Mechanics*, 852:P1, 2018.

[134] Jane YY Chui, Carine Douarche, Harold Auradou, and Ruben Juanes. Rheology of bacterial superfluids in viscous environments. *Soft Matter*, 17(29):7004–7013, 2021.

[135] Howard C Berg and Linda Turner. Movement of microorganisms in viscous environments. *Nature*, 278(5702):349–351, 1979.

[136] William Randolph Schneider and RN Doetsch. Effect of viscosity on bacterial motility. *Journal of bacteriology*, 117(2):696–701, 1974.

[137] Matthias Mussler, Salima Rafaï, Philippe Peyla, and Christian Wagner. Effective viscosity of non-gravitactic chlamydomonas reinhardtii microswimmer suspensions. *Europhysics Letters*, 101(5):54004, 2013.

[138] Yashodhan Hatwalne, Sriram Ramaswamy, Madan Rao, and R Aditi Simha. Rheology of active-particle suspensions. *Physical review letters*, 92(11):118101, 2004.

[139] S. Kim and S.J. Karrila. *Microhydrodynamics: Principles and Selected Applications*. Butterworth - Heinemann series in chemical engineering. Dover Publications, 2005.

[140] David Saintillan. The dilute rheology of swimming suspensions: A simple kinetic model. *Experimental Mechanics*, 50:1275–1281, 2010.

[141] David Saintillan. Extensional rheology of active suspensions. *Physical Review E*, 81(5):056307, 2010.

[142] GK Batchelor. Slender-body theory for particles of arbitrary cross-section in stokes flow. *Journal of Fluid Mechanics*, 44(3):419–440, 1970.

[143] Shing Bor Chen and Donald L Koch. Rheology of dilute suspensions of charged fibers. *Physics of Fluids*, 8(11):2792–2807, 1996.

[144] Takuji Ishikawa and TJ Pedley. The rheology of a semi-dilute suspension of swimming model micro-organisms. *Journal of Fluid Mechanics*, 588:399–435, 2007.

[145] T Ishikawa, DR Brumley, and TJ Pedley. Rheology of a concentrated suspension of spherical squirmers: monolayer in simple shear flow. *Journal of Fluid Mechanics*, 914:A26, 2021.

[146] G.M. Homsy, H. Aref, K.S. Breuer, S. Hochgreb, J.R. Koseff, B.R. Munson, K.G. Powell, C.R. Robertson, and S.T. Thoroddsen. *Multimedia Fluid Mechanics - Multilingual Version CD-ROM*. Cambridge University Press, 2004.

[147] Hassan Masoud and Howard A Stone. The reciprocal theorem in fluid dynamics and transport phenomena. *Journal of Fluid Mechanics*, 879:P1, 2019.

[148] GJ Hancock. The self-propulsion of microscopic organisms through liquids. *Proceedings of the Royal Society of London. Series A. Mathematical and Physical Sciences*, 217(1128):96–121, 1953.

[149] Geoffrey Ingram Taylor. Analysis of the swimming of microscopic organisms. *Proceedings of the Royal Society of London. Series A. Mathematical and Physical Sciences*, 209(1099):447–461, 1951.

[150] E Lauga and T R Powers. The hydrodynamics of swimming microorganisms. *Reports on Progress in Physics*, 72(9):096601, 2009.

[151] Howard C Berg and Robert A Anderson. Bacteria swim by rotating their flagellar filaments. *Nature*, 245(5425):380–382, 1973.

[152] Eamonn A Gaffney, Hermes Gadêlha, David J Smith, John R Blake, and Jackson C Kirkman-Brown. Mammalian sperm motility: observation and theory. *Annual Review of Fluid Mechanics*, 43:501–528, 2011.

[153] Christopher Brennen and Howard Winet. Fluid mechanics of propulsion by cilia and flagella. *Annual Review of Fluid Mechanics*, 9(1):339–398, 1977.

[154] Takuji Ishikawa. Fluid dynamics of squirmers and ciliated microorganisms. *Annual Review of Fluid Mechanics*, 56:119–145, 2024.

[155] Takuji Ishikawa, TJ Pedley, Knut Drescher, and Raymond E Goldstein. Stability of dancing volvox. *Journal of Fluid Mechanics*, 903:A11, 2020.

[156] Takuji Ishikawa, Tomoyuki Tanaka, Yohsuke Imai, Toshihiro Omori, and Daiki Matsunaga. Deformation of a micro-torque swimmer. *Proceedings of the Royal Society A: Mathematical, Physical and Engineering Sciences*, 472(2185):20150604, 2016.

[157] M. J. Lighthill. On the squirming motion of nearly spherical deformable bodies through liquids at very small reynolds numbers. *Communications on Pure and Applied Mathematics*, 5(2):109–118, 1952.

[158] John R Blake. A spherical envelope approach to ciliary propulsion. *Journal of Fluid Mechanics*, 46(1):199–208, 1971.

[159] Takuji Ishikawa, MP Simmonds, and Timothy J Pedley. Hydrodynamic interaction of two swimming model micro-organisms. *Journal of Fluid Mechanics*, 568:119–160, 2006.

[160] Gaojin Li, Anca Ostace, and Arezoo M Ardekani. Hydrodynamic interaction of swimming organisms in an inertial regime. *Physical Review E*, 94(5):053104, 2016.

[161] Gao-Jin Li and Arezoo M Ardekani. Hydrodynamic interaction of microswimmers near a wall. *Physical Review E*, 90(1):013010, 2014.

[162] Kenta Ishimoto and Eamonn A Gaffney. Squirmer dynamics near a boundary. *Physical Review E*, 88(6):062702, 2013.

[163] Geng Guan, Yuxiang Ying, Jianzhong Lin, and Jue Zhu. Motion characteristics of squirmers in linear shear flow. *Fluid Dynamics Research*, 56(1):015504, 2024.

[164] Tingting Qi, Jianzhong Lin, and Zhenyu Ouyang. Hydrodynamic behavior of self-propelled particles in a simple shear flow. *Entropy*, 24(7):854, 2022.

[165] Takuji Ishikawa and Timothy J Pedley. Coherent structures in monolayers of swimming particles. *Physical review letters*, 100(8):088103, 2008.

[166] Benjamin Abécassis, Cécile Cottin-Bizonne, C Ybert, A Ajdari, and L Bocquet. Boosting migration of large particles by solute contrasts. *Nature materials*, 7(10):785–789, 2008.

[167] Peter O Staffeld and John A Quinn. Diffusion-induced banding of colloid particles via diffusiophoresis: 2. non-electrolytes. *Journal of colloid and interface science*, 130(1):88–100, 1989.

[168] F.A Morrison. Electrophoresis of a particle of arbitrary shape. *Journal of Colloid and Interface Science*, 34(2):210–214, 1970.

[169] John L Anderson. Colloid transport by interfacial forces. *Annual review of fluid mechanics*, 21(1):61–99, 1989.

[170] Hassan Masoud and Howard A Stone. The reciprocal theorem in fluid dynamics and transport phenomena. *Journal of Fluid Mechanics*, 879:P1, 2019.

[171] Huan J Keh and Shing B Chen. Electrophoresis of a colloidal sphere parallel to a dielectric plane. *Journal of Fluid Mechanics*, 194:377–390, 1988.

[172] Po Y Chen and Huan J Keh. Diffusiophoresis and electrophoresis of a charged sphere parallel to one or two plane walls. *Journal of colloid and interface science*, 286(2):774–791, 2005.

[173] Suraj Shankar, Anton Souslov, Mark J Bowick, M Cristina Marchetti, and Vincenzo Vitelli. Topological active matter. *Nature Reviews Physics*, 4(6):380–398, 2022.

[174] Bharath Srinivasan. A guide to the michaelis–menten equation: steady state and beyond. *The FEBS journal*, 289(20):6086–6098, 2022.

[175] Ramin Golestanian, TB Liverpool, and A Ajdari. Designing phoretic micro-and nano-swimmers. *New Journal of Physics*, 9(5):126, 2007.

[176] Ehud Yariv. Self-diffusiophoresis of slender catalytic colloids. *Langmuir*, 36(25):6903–6915, 2019.

[177] Rodolfo Brandão, Gunnar G Peng, David Saintillan, and Ehud Yariv. Self-diffusiophoresis with bulk reaction. *Physical Review Fluids*, 9(1):014001, 2024.

[178] T. Traverso and S. Michelin. Hydrochemical interactions in dilute phoretic suspensions: From individual particle properties to collective organization. *Phyiscal Review Fluids*, 5:104203, Oct 2020.

[179] M Tătulea-Codrean and E Lauga. Artificial chemotaxis of phoretic swimmers: Instantaneous and long-time behaviour. *Journal of Fluid Mechanics*, 856:921–957, 2018.

[180] Nima Sharifi-Mood, Ali Mozaffari, and Ubaldo M Córdova-Figueroa. Pair interaction of catalytically active colloids: from assembly to escape. *Journal of Fluid Mechanics*, 798:910–954, 2016.

[181] Akhil Varma and Sébastien Michelin. Modeling chemo-hydrodynamic interactions of phoretic particles: A unified framework. *Physical Review Fluids*, 4(12):124204, 2019.

[182] Wen Yan and John F Brady. The behavior of active diffusiophoretic suspensions: An accelerated laplacian dynamics study. *The Journal of Chemical Physics*, 145(13), 2016.

[183] Takuji Ishikawa, Thanh-Nghi Dang, and Eric Lauga. Instability of an active fluid jet. *Physical Review Fluids*, 7(9):093102, 2022.

[184] Thomas D Montenegro-Johnson, Sébastien Michelin, and Eric Lauga. A regularised singularity approach to phoretic problems. *The European Physical Journal E*, 38:1–7, 2015.

[185] Ruth A Lambert, Francesco Picano, Wim-Paul Breugem, and Luca Brandt. Active suspensions in thin films: nutrient uptake and swimmer motion. *Journal of Fluid Mechanics*, 733:528–557, 2013.

[186] Amneet Pal Singh Bhalla, Boyce E Griffith, Neelesh A Patankar, and Aleksandar Donev. A minimally-resolved immersed boundary model for reaction-diffusion problems. *The Journal of chemical physics*, 139(21), 2013.

[187] Radu Balescu. *Statistical dynamics: matter out of equilibrium*. World Scientific, 1997.

[188] Robert Zwanzig. *Nonequilibrium statistical mechanics*. Oxford university press, 2001.

[189] Eric Bertin, Michel Droz, and Guillaume Grégoire. Hydrodynamic equations for self-propelled particles: microscopic derivation and stability analysis. *Journal of Physics A: Mathematical and Theoretical*, 42(44):445001, oct 2009.

[190] Dwight Roy Nicholson and Dwight R Nicholson. *Introduction to plasma theory*, volume 1. Wiley New York, 1983.

[191] Mingming Wu, John W Roberts, Sue Kim, Donald L Koch, and Matthew P DeLisa. Collective bacterial dynamics revealed using a three-dimensional population-scale defocused particle tracking technique. *Applied and environmental microbiology*, 72(7):4987–4994, 2006.

[192] Min Jun Kim and Kenneth S Breuer. Enhanced diffusion due to motile bacteria. *Physics of fluids*, 16(9):L78–L81, 2004.

[193] Alexander Morozov and Davide Marenduzzo. Enhanced diffusion of tracer particles in dilute bacterial suspensions. *Soft Matter*, 10(16):2748–2758, 2014.

[194] R Aditi Simha and Sriram Ramaswamy. Hydrodynamic fluctuations and instabilities in ordered suspensions of self-propelled particles. *Physical review letters*, 89(5):058101, 2002.

[195] David Saintillan and Michael J Shelley. Instabilities, pattern formation, and mixing in active suspensions. *Physics of Fluids*, 20(12), 2008.

[196] David Saintillan and Michael J Shelley. Instabilities and pattern formation in active particle suspensions: kinetic theory and continuum simulations. *Physical Review Letters*, 100(17):178103, 2008.

[197] J Gachelin, A Rousselet, A Lindner, and E Clement. Collective motion in an active suspension of escherichia coli bacteria. *New Journal of Physics*, 16(2):025003, 2014.

[198] Patrick T Underhill, Juan P Hernandez-Ortiz, and Michael D Graham. Diffusion and spatial correlations in suspensions of swimming particles. *Physical review letters*, 100(24):248101, 2008.

[199] Donald L Koch and Ganesh Subramanian. Collective hydrodynamics of swimming microorganisms: living fluids. *Annual Review of Fluid Mechanics*, 43:637–659, 2011.

[200] Eshel Ben-Jacob, Inon Cohen, and Herbert Levine. Cooperative self-organization of microorganisms. *Advances in Physics*, 49(4):395–554, 2000.

[201] Mitsugu Matsushita, J Wakita, H Itoh, Ismael Rafols, T Matsuyama, H Sakaguchi, and M Mimura. Interface growth and pattern formation in bacterial colonies. *Physica A: Statistical Mechanics and its Applications*, 249(1-4):517–524, 1998.

[202] Enkeleida Lushi, Raymond E Goldstein, and Michael J Shelley. Nonlinear concentration patterns and bands in autochemotactic suspensions. *Physical Review E*, 98(5):052411, 2018.

[203] Wolgang Alt. Biased random walk models for chemotaxis and related diffusion approximations. *Journal of mathematical biology*, 9:147–177, 1980.

[204] Kevin C Chen, Roseanne M Ford, and Peter T Cummings. Cell balance equation for chemotactic bacteria with a biphasic tumbling frequency. *Journal of mathematical biology*, 47:518–546, 2003.

[205] E Lushi, R E Goldstein, and M J Shelley. Collective chemotactic dynamics in the presence of self-generated fluid flows. *Physical Review E*, 86(4):040902, 2012.

[206] Jie Zhang, Bartosz A Grzybowski, and Steve Granick. Janus particle synthesis, assembly, and application. *Langmuir*, 33(28):6964–6977, 2017.

[207] Barath Ezhilan and David Saintillan. Transport of a dilute active suspension in pressure-driven channel flow. *Journal of Fluid Mechanics*, 777:482–522, 2015.

[208] Prathmesh Vinze and Sebastien Michelin. Self-organization of autophoretic suspensions in confined shear flows. *Physical Review Fluids*, 9(1):014202, 2024.

[209] W Gao and J Wang. Synthetic micro/nanomotors in drug delivery. *Nanoscale*, 6(18):10486–10494, 2014.

[210] R W Carlsen and M Sitti. Bio-hybrid cell-based actuators for microsystems. *Small*, 10(19):3831–3851, 2014.

[211] B J Nelson, I K Kaliakatsos, and J J Abbott. Microrobots for minimally invasive medicine. *Annual Review of Biomedical Engineering*, 12:55–85, 2010.

[212] E W Burkholder and J F Brady. Nonlinear microrheology of active brownian suspensions. *Soft Matter*, 16(4):1034–1046, 2020.

[213] S E Spagnolie and E Lauga. Hydrodynamics of self-propulsion near a boundary: predictions and accuracy of far-field approximations. *Journal of Fluid Mechanics*, 700:105–147, 2012.

[214] M Contino, E Lushi, I Tuval, V Kantsler, and M Polin. Microalgae scatter off solid surfaces by hydrodynamic and contact forces. *Physical Review Letters*, 115(25):258102, 2015.

[215] E Lushi, V Kantsler, and R E Goldstein. Scattering of biflagellate microswimmers from surfaces. *Physical Review E*, 96(2):023102, 2017.

[216] S E Spagnolie, G R Moreno-Flores, D Bartolo, and E Lauga. Geometric capture and escape of a microswimmer colliding with an obstacle. *Soft Matter*, 11(17):3396–3411, 2015.

[217] Y Ibrahim and T B Liverpool. How walls affect the dynamics of self-phoretic microswimmers. *The European Physical Journal Special Topics*, 225:1843–1874, 2016.

[218] A Choudhary, KVS Chaithanya, S Michelin, and S Pushpavanam. Self-propulsion in 2d confinement: phoretic and hydrodynamic interactions. *The European Physical Journal E*, 44:1–21, 2021.

[219] S S Suarez and AA Pacey. Sperm transport in the female reproductive tract. *Human Reproduction Update*, 12(1):23–37, 2006.

[220] A Costanzo, R Di Leonardo, G Ruocco, and L Angelani. Transport of self-propelling bacteria in micro-channel flow. *Journal of Physics: Condensed Matter*, 24(6):065101, 2012.

[221] N Figueroa-Morales, G L Mino, A Rivera, R Caballero, E Clément, E Altshuler, and A Lindner. Living on the edge: transfer and traffic of e. coli in a confined flow. *Soft Matter*, 11(31):6284–6293, 2015.

[222] T Kaya and H Koser. Direct upstream motility in escherichia coli. *Biophysical Journal*, 102(7):1514–1523, 2012.

[223] T Omori and T Ishikawa. Upward swimming of a sperm cell in shear flow. *Physical Review E*, 93(3):032402, 2016.

[224] Q Brosseau, F B Usabiaga, E Lushi, Y Wu, L Ristroph, J Zhang, M Ward, and M J Shelley. Relating rheotaxis and hydrodynamic actuation using asymmetric gold-platinum phoretic rods. *Physical Review Letters*, 123(17):178004, 2019.

[225] V A Martinez, E Clément, J Arlt, C Douarche, A Dawson, J Schwarz-Linek, A K Creppy, V Škultéty, A N Morozov, H Auradou, et al. A combined rheometry and imaging study of viscosity reduction in bacterial suspensions. *Proceedings of the National Academy of Sciences*, 117(5):2326–2331, 2020.

[226] M Theillard, R Alonso-Matilla, and D Saintillan. Geometric control of active collective motion. *Soft Matter*, 13(2):363–375, 2017.

[227] L Kleiser and U Schumann. Treatment of incompressibility and boundary conditions in 3-d numerical spectral simulations of plane channel flows. In *Proceedings of the Third GAMM—Conference on Numerical Methods in Fluid Mechanics*, pages 165–173. Springer, 1980.

[228] Claudio Canuto, M Yousuff Hussaini, Alfio Quarteroni, and Thomas A Zang. *Spectral methods: fundamentals in single domains*. Springer Science & Business Media, 2007.

[229] A Sen, M Ibele, Y Hong, and D Velegol. Chemo and phototactic nano/microbots. *Faraday Discussions*, 143:15, 2009.

[230] K Valiev and E N Ivanov. Rotational brownian motion. *Soviet Physics Uspekhi*, 16(1):1, 1973.

[231] W K Subczynski and J S Hyde. Diffusion of oxygen in water and hydrocarbons using an electron spin resonance spin-label technique. *Biophysical Journal*, 45(4):743–748, 1984.

[232] B Petri and M J Sanz. Neutrophil chemotaxis. *Cell and Tissue Research*, 371(3):425–436, 2018.

[233] E O Budrene and H C Berg. Complex patterns formed by motile cells of Escherichia coli. *Nature*, 349(6310):630–633, 1991.

[234] E B Jacob, I Becker, Y Shapira, and H Levine. Bacterial linguistic communication and social intelligence. *Trends in Microbiology*, 12(8):366–372, 2004.

[235] G Ariel, A Shklarsh, O Kalisman, C Ingham, and E Ben-Jacob. From organized internal traffic to collective navigation of bacterial swarms. *New Journal of Physics*, 15(12):125019, 2013.

[236] B Liebchen, D Marenduzzo, I Pagonabarraga, and M E Cates. Clustering and pattern formation in chemorepulsive active colloids. *Physical Review Letters*, 115(25):258301, 2015.

[237] G Li and J X Tang. Accumulation of microswimmers near a surface mediated by collision and rotational brownian motion. *Physical Review Letters*, 103(7):078101, 2009.

[238] D Saintillan and M J Shelley. Active suspensions and their nonlinear models. *Comptes Rendus Physique*, 14(6):497–517, 2013.

[239] M Theillard and D Saintillan. Computational mean-field modeling of confined active fluids. *Journal of Computational Physics*, 397:108841, 2019.

[240] J Buhl, D J T Sumpter, I D Couzin, J J Hale, E Despland, E R Miller, and S J Simpson. From disorder to order in marching locusts. *Science*, 312(5778):1402–1406, 2006.

[241] W E Arnoldi. The principle of minimized iterations in the solution of the matrix eigenvalue problem. *Quarterly of Applied Mathematics*, 9(1):17–29, 1951.

[242] D G Thomas. Transport characteristics of suspension: Viii. a note on the viscosity of newtonian suspensions of uniform spherical particles. *Journal of Colloid Science*, 20(3):267–277, 1965.

[243] M Neef and K Kruse. Generation of stationary and moving vortices in active polar fluids in the planar taylor-couette geometry. *Physical Review E*, 90(5):052703, 2014.

[244] R J Henshaw, O G Martin, and J S Guasto. Dynamic mode structure of active turbulence. *Physical Review Fluids*, 8(2):023101, 2023.

[245] T N Shendruk, A Doostmohammadi, K Thijssen, and J M Yeomans. Dancing disclinations in confined active nematics. *Soft Matter*, 13(21):3853–3862, 2017.

[246] A Snezhko and I S Aranson. Magnetic manipulation of self-assembled colloidal asters. *Nature Materials*, 10(9):698–703, 2011.

[247] J S Park and D Saintillan. Electric-field-induced ordering and pattern formation in colloidal suspensions. *Physical Review E*, 83(4):041409, 2011.

[248] Y Hong, N MK Blackman, N D Kopp, A Sen, and D Velegol. Chemotaxis of nonbiological colloidal rods. *Physical Review Letters*, 99(17):178103, 2007.

[249] J Palacci, S Sacanna, A P Steinberg, D J Pine, and P M Chaikin. Living crystals of light-activated colloidal surfers. *Science*, 339(6122):936–940, 2013.

[250] A Choudhary, T Renganathan, and S Pushpavanam. Inertial migration of an electrophoretic rigid sphere in a two-dimensional poiseuille flow. *Journal of Fluid Mechanics*, 874:856–890, 2019.

[251] Aditya S Khair and Jason K Kabarowski. Migration of an electrophoretic particle in a weakly inertial or viscoelastic shear flow. *Physical Review Fluids*, 5(3):033702, 2020.

[252] Egor V Yakovlev, Kirill A Komarov, Kirill I Zaytsev, Nikita P Kryuchkov, Kirill I Koshelev, Arsen K Zotov, Dmitry A Shelestov, Victor L Tolstoguzov, Vladimir N Kurlov, Alexei V Ivlev, et al. Tunable two-dimensional assembly of colloidal particles in rotating electric fields. *Scientific reports*, 7(1):1–10, 2017.

[253] Tara D Edwards and Michael A Bevan. Controlling colloidal particles with electric fields. *Langmuir*, 30(36):10793–10803, 2014.

[254] Levan Jibuti, Ling Qi, Chaouqi Misbah, Walter Zimmermann, Salima Rafaï, and Philippe Peyla. Self-focusing and jet instability of a microswimmer suspension. *Physical Review E*, 90(6):063019, 2014.

[255] Fabian R Koessel and Sara Jabbari-Farouji. Emergent pattern formation of active magnetic suspensions in an external field. *New Journal of Physics*, 22(10):103007, 2020.

[256] Ping Sheng and Weijia Wen. Electrorheological fluids: mechanisms, dynamics, and microfluidics applications. *Annual review of fluid mechanics*, 44:143–174, 2012.

[257] John P McTague. Magnetoviscosity of magnetic colloids. *The Journal of Chemical Physics*, 51(1):133–136, 1969.

[258] Xiaowei He, Shihab Elborai, Dokyung Kim, Se-Hee Lee, and Markus Zahn. Effective magnetoviscosity of planar-couette magnetic fluid flow. *Journal of applied physics*, 97(10), 2005.

[259] Howard Brenner. Rheology of a dilute suspension of dipolar spherical particles in an external field. *Journal of Colloid and Interface Science*, 32(1):141–158, 1970.

[260] LG Leal. On the effect of particle couples on the motion of a dilute suspension of spheroids. *Journal of Fluid Mechanics*, 46(2):395–416, 1971.

[261] R Alonso-Matilla and D Saintillan. Microfluidic flow actuation using magnetoactive suspensions. *Europhysics Letters*, 121(2):24002, 2018.

[262] Jacques Louis Lions. *Optimal control of systems governed by partial differential equations*, volume 170. Springer, 1971.

[263] Siva Nadarajah and Antony Jameson. A comparison of the continuous and discrete adjoint approach to automatic aerodynamic optimization. In *38th Aerospace sciences meeting and exhibit*, page 667, 2000.

[264] Hanumantha Rao Vutukuri, Maciej Lisicki, Eric Lauga, and Jan Vermant. Light-switchable propulsion of active particles with reversible interactions. *Nature communications*, 11(1):2628, 2020.

DOCTORAL SCHOOL

Titre : Dynamique collective et rhéologie des suspensions phorétiques sous forçages mécaniques et chimiques externes

Mots clés : suspension active, particules janus, chimiotaxie, comportement collectif

Résumé : La matière active est composée d'unités individuelles qui injectent de l'énergie dans le système conduisant à des dynamiques collectives non triviales. Cette thèse se concentre sur un type de micronageurs artificiels appelés particules Janus. Ces particules peuvent interagir à la fois à travers le champ d'écoulement et le champ de soluté, donnant lieu à la formation de modèles spatio-temporels complexes (tels que la formation d'asters). Des expériences rhéologiques récentes révèlent que la suspension de tels micronageurs influence fortement la réponse rhéologique de la suspension et conduit à une diminution de la viscosité effective de la suspension. La première partie de la thèse explore numériquement la dynamique et la réponse au cisaillement des particules phorétiques en suspensions diluées et confinées, qui se réorientent et dérivent vers des solutés chimiques libérés par leurs voisines à l'aide d'un modèle cinétique continu. Une distribution transitoire 1D pilotée par l'effet de confinement est une caractéristique commune aux intensités de confinement et de taux de cisaillement considérées. Cet état 1D est stable pour un confinement fort et s'observe donc en dynamique à long terme dans des canaux suffisamment étroits. Pour les canaux plus larges, l'état transitoire devient instable aux perturbations axiales dues à l'instabilité chimiotactique, conduisant à la formation d'agrégats de particules le long des parois du canal. En exerçant des contraintes sur le fluide, ces micro-nageurs modifient le comportement rhéologique des suspensions qui dépend de la répartition des particules.La deuxième partie de la thèse s'intéresse au contrôle du comportement rhéologique de la suspension. Dans cette partie, l'idée centrale est d'utiliser le forçage chimique pour déclencher l'instabilité chimiotactique de telle sorte que des agrégats de particules puissent se former et réduire la viscosité effective. Nous explorons ici le forçage chimique via un patch catalytique et montrons qu'imposer simultanément une activité et un cisaillement a des limites à des taux de cisaillement modérés, où l'instabilité chimiotactique ne peut pas se développer dans l'ensemble du domaine. Pour résoudre ce problème, nous proposons une stratégie plus robuste qui étend la région de réduction de la viscosité à des confinements plus élevés.

Title : Collective dynamics and rheology of phoretic suspensions under external mechanical and chemical forcings

Keywords : active suspension, janus particles, chemotaxis, collective behaviour

Abstract : Active matter is composed of individual units that inject energy into the system leading to nontrivial collective dynamics. This thesis focuses on a type of artificial microswimmers called as Janus particles. These particles can interact through both the flow field and the solute field, giving rise to the formation of complex spatiotemporal patterns (such as the formation of asters). Recent rheological experiments reveal that the suspension of such microswimmers strongly influences the rheological response of the suspension and leads to a decrease in the effective viscosity of the suspension. The first part of the thesis numerically explores the dynamics and shear response of dilute and confined suspensions phoretic particles, which reorient and drift towards chemical solutes released by their neighbors using a continuum kinetic model. A 1D transient distribution driven by the confinement effect is a common feature at the considered confinement and shear rate intensities. This 1D state is stable for strong confinement and is therefore observed in the long-term dynamics in sufficiently narrow channels. For wider channels, the transient state becomes unstable to axial perturbations due to chemotactic instability, leading to the formation of particle aggregates along the channel walls. As these microswimmers exter stresses on the fluid, they modify the suspensions' rheological behaviour which depends on particle distribution. The second part of the thesis focuses on controlling rheological behaviour of the suspension. In this part, the central idea is to use chemical forcing to trigger the chemotactic instability such that particle aggregates can form and reduce the effective viscosity. Here we explore the chemical forcing via a catalytic patch and show that imposing activity and shear simultaneously has limitations at moderate shear rates, where chemotactic instability cannot develop in the entire domain. To address this issue, we propose a more robust strategy that extends the viscosity reduction region to higher confinements.

Institut Polytechnique de Paris
91120 Palaiseau, France